JAAVSO

Volume 48
Number 1
2020

The Journal of the American Association of Variable Star Observers

Disk Instabilities Caused the 2018 Outburst of AG Draconis

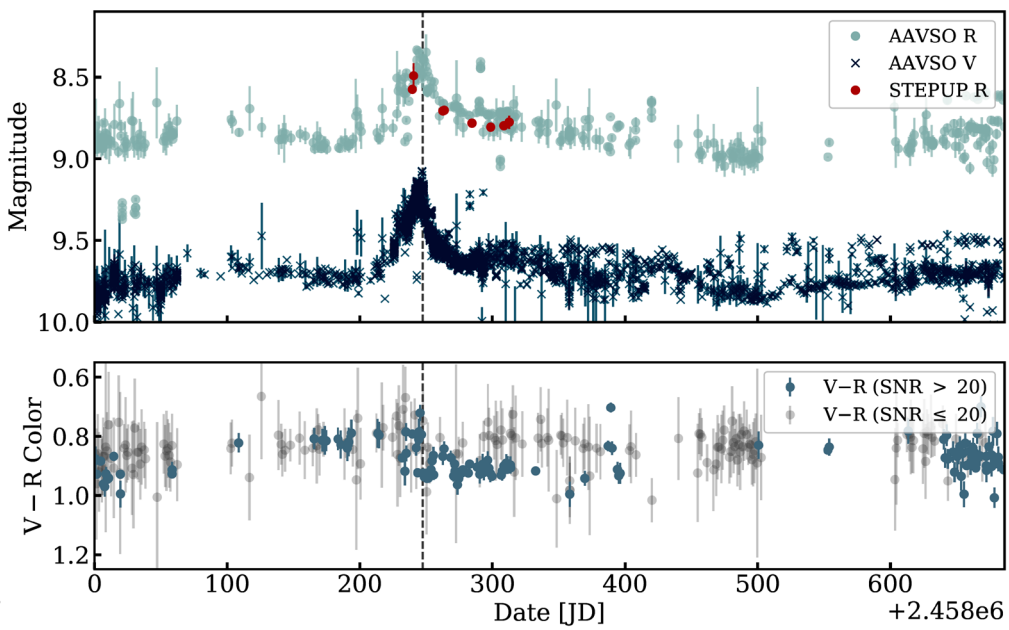

2018 outburst of AG Draconis shown by STEPUP R-band and AAVSO R- and V-band measurements. The vertical dashed line marks the peak of the outburst, which occurred on JD 2458247.448.

Also in this issue...

The American Association of Variable Star Observers
49 Bay State Road, Cambridge, MA 02138, USA

The Journal of the American Association of Variable Star Observers

The Board of the American Association of Variable Star Observers 2019–2020

ISSN 0271-9053 (print)
ISSN 2380-3606 (online)

JAAVSO

The Journal of
The American Association
of Variable Star Observers

Volume 48
Number 1
2020

ISSN 0271-9053 (print)
ISSN 2380-3606 (online)

AAVSO
49 Bay State Road
Cambridge, MA 02138
USA

Publication Schedule

The Journal of the American Association of Variable Star Observers is published twice a year, June 15 (Number 1 of the volume) and December 15 (Number 2 of the volume). The submission window for inclusion in the next issue of JAAVSO closes six weeks before the publication date. A manuscript will be added to the table of contents for an issue when it has been fully accepted for publication upon successful completion of the referee process; these articles will be available online prior to the publication date. An author may not specify in which issue of JAAVSO a manuscript is to be published; accepted manuscripts will be published in the next available issue, except under extraordinary circumstances.

Page Charges

Page charges are waived for Members of the AAVSO. Publication of unsolicited manuscripts in JAAVSO requires a page charge of US $100/page for the final printed manuscript. Page charge waivers may be provided under certain circumstances.

Publication in *JAAVSO*

With the exception of abstracts of papers presented at AAVSO meetings, papers submitted to JAAVSO are peer-reviewed by individuals knowledgeable about the topic being discussed. We cannot guarantee that all submissions to JAAVSO will be published, but we encourage authors of all experience levels and in all fields related to variable star astronomy and the AAVSO to submit manuscripts. We especially encourage students and other mentees of researchers affiliated with the AAVSO to submit results of their completed research.

Subscriptions

Institutions and Libraries may subscribe to JAAVSO as part of the Complete Publications Package or as an individual subscription. Individuals may purchase printed copies of recent JAAVSO issues via Createspace. Paper copies of JAAVSO issues prior to volume 36 are available in limited quantities directly from AAVSO Headquarters; please contact the AAVSO for available issues.

Instructions for Submissions

The *Journal of the AAVSO* welcomes papers from all persons concerned with the study of variable stars and topics specifically related to variability. All manuscripts should be written in a style designed to provide clear expositions of the topic. Contributors are encouraged to submit digitized text in MS WORD, LATEX+POSTSCRIPT, or plain-text format. Manuscripts should be submitted through the JAAVSO submission portal (https://www.aavso.org/apps/jaavso/submit/) or may be mailed electronically to journal@aavso.org or submitted by postal mail to JAAVSO, 49 Bay State Road, Cambridge, MA 02138, USA.

Manuscripts must be submitted according to the following guidelines, or they will be returned to the author for correction:

Manuscripts must be:
1) original, unpublished material;
2) written in English;
3) accompanied by an abstract of no more than 100 words.
4) not more than 2,500–3,000 words in length (10–12 pages double-spaced).

Figures for publication must:
1) be camera-ready or in a high-contrast, high-resolution, standard digitized image format;
2) have all coordinates labeled with division marks on all four sides;
3) be accompanied by a caption that clearly explains all symbols and significance, so that the reader can understand the figure without reference to the text.

Maximum published figure space is 4.5″ by 7″. When submitting original figures, be sure to allow for reduction in size by making all symbols, letters, and division marks sufficiently large.

Photographs and halftone images will be considered for publication if they directly illustrate the text.

Tables should be:
1) provided separate from the main body of the text;
2) numbered sequentially and referred to by Arabic number in the text, e.g., Table 1.

References:
1) References should relate directly to the text.
2) References should be keyed into the text with the author's last name and the year of publication, e.g., (Smith 1974; Jones 1974) or Smith (1974) and Jones (1974).
3) In the case of three or more joint authors, the text reference should be written as follows: (Smith et al. 1976).
4) All references must be listed at the end of the text in alphabetical order by the author's last name and the year of publication, according to the following format: Brown, J., and Green, E. B. 1974, *Astrophys. J.*, **200**, 765.
Thomas, K. 1982, *Phys. Rep.*, **33**, 96.
5) Abbreviations used in references should be based on recent issues of JAAVSO or the listing provided at the beginning of *Astronomy and Astrophysics Abstracts* (Springer-Verlag).

Miscellaneous:
1) Equations should be written on a separate line and given a sequential Arabic number in parentheses near the right-hand margin. Equations should be referred to in the text as, e.g., equation (1).
2) Magnitude will be assumed to be visual unless otherwise specified.
3) Manuscripts may be submitted to referees for review without obligation of publication.

Online Access

Articles published in JAAVSO, and information for authors and referees may be found online at: https://www.aavso.org/apps/jaavso/

The Journal of the American Association of Variable Star Observers
Volume 48, Number 1, 2020

Editorial

Variable Star Research

Table of Contents continued on following pages

Education and Outreach

Instruments, Methods, and Techniques

Variable Star Data

Abstracts of Papers and Posters Presented at the 108th Annual Meeting of the AAVSO, Held in Las Cruces, New Mexico, October 18–21, 2019

Table of Contents continued on following pages

Table of Contents continued on next page

Errata

Editorial

Dual-Anonymous Review

Nancy D. Morrison
Editor-in-Chief, Journal of the AAVSO

Department of Physics and Astronomy and Ritter Observatory, MS 113, The University of Toledo, 2801 W. Bancroft Street, Toledo OH 43606; jaavso.editor@aavso.org

Received June 11, 2020

Peer review—in which an independent expert critiques a research report in order to assist the author in achieving the highest possible quality—is at the core of the scientific process. Traditionally, the reviewer is anonymous in order to be able to criticize the work frankly. In recent years, however, there has arisen the practice of making the author's identity also unknown to the reviewer: double blinding or dual anonymization. The goal is to help reviewers concentrate on the scientific merits of the article rather than the merits of the authors themselves. It's difficult to assess the merits of individuals without bias, whether conscious or unconscious.

For about five years (Percy 2016), *JAAVSO* has been following this practice, asking authors not to include identifying information in the initially submitted version of their manuscripts.

Dual-anonymous review has a history going back a decade or more. As a well-known example in the world of performance art, musicians auditioning for a position in an orchestra now often play behind an opaque screen, a change that has received credit for the recent increase in the number of women who play in symphony orchestras. In just one example of what can happen in the absence of dual-anonymous review, Moss-Racusin (2012) constructed two identical resumes, one bearing a male and one a female name, and sent one or the other of them to more than a hundred university faculty members, asking them to rate the materials as if they were applications for a hypothetical laboratory manager position. Both male and female professors rated the male "applicant" significantly more highly and suggested a significantly higher starting salary for that person.

Among North American astronomy journals, *JAAVSO* is the first, to my knowledge, to institute dual-anonymous refereeing as the default. The American Astronomical Society's (AAS) journals (*The Astronomical Journal* and *The Astrophysical Journal* family) have offered it as an option for about the same length of time, but few authors select it. The explanation sometimes offered is that, since so few authors request it, referees suspect a problem when they see it and a stigma is associated with it—a vicious circle. The recently-launched *Planetary Science Journal* is the first of the AAS journals to require authors to opt out of dual-anonymous refereeing if they don't want it.

Recently, NASA has instituted mandatory dual-anonymous refereeing of proposals for observing time on NASA missions, starting gradually with the Hubble Space Telescope (HST). In proposal cycle 22 (2011), the name of the principal investigator (PI) was removed from the front page of the proposal. Two years later, the PI's full name was replaced with initials in the body of the proposal, and the following year it was made difficult to determine which of the proposal's authors was the PI. Finally, in Cycle 26, all identifying information was removed from the proposals, and authors were instructed how to mask their identities in writing their proposals. For each year, the success rates of men and women PIs were studied (Johnson and Kirk 2020). In all the years studied except the last, men had significantly higher success rates than women (the original cause of the dual-anonymization effort); only in Cycle 26 (2016), with full anonymization, were the rates equal. Subsequent years' results are still under study.

Because of the HST experience, NASA is now moving ahead with full anonymization in its proposal process for numerous guest observer missions. This program was summarized in a town hall at the recent 236th meeting of the American Astronomical Society (held virtually). NASA representatives summarized recent results of the HST experiment; for example, Iain Reid (of the Space Telescope Science Institute) mentioned dramatically improved success rates for first-time PIs. Daniel Evans (of NASA Headquarters) emphasized that the biases being addressed are not just those of gender and race but also career stage, institutional prestige, and others. Since scientific talent is found in all sorts of people and in a wide range of settings, removing personal variables from consideration is bound to improve the scientific enterprise as a whole.

The stakes are higher in proposals for observing time than in journal articles, because successful proposals receive funding to support the research and carry higher weight in assessment of scientists' careers. But it is just as important for journal authors to enable referees to be unbiased. According to the HST results on success rates, only full anonymization is effective in reducing bias. Therefore, it is important for our journal to ensure the robustness of its processes.

JAAVSO's authors vary in their efforts to hide their identities and in their success. Some potentially identifying details have to be retained because they are important for evaluating the paper, such as the setting of the observatory: mountaintop, suburban, or light-polluted urban? Northern or southern, desert or forested? Who took the data? The equipment that was used need to be described. Finally, the referee needs a complete citation list, which may need to include the authors' previous work, in order to evaluate the scientific content.

Still, some steps can be taken to obscure the authors' identities without harming, and maybe even improving, the readability of the paper. Advice from NASA includes:

• When citing your previous work, don't claim ownership. Rather than, "in our previous work, we found...," just say, for example: "previous studies (citation) demonstrated...."

• Citing your own unpublished work is not encouraged. If you must do so, say that the information was received by personal communication.

And in the *JAAVSO* context:

• Don't name your observatory, but give the relevant scientific details and fully describe the equipment used to make the observations.

• It suffices to say that the observations were made by one or more of the authors.

After the paper is accepted, you will be asked to de-anonymize the article and fill in all the needed details. These are just examples; the *JAAVSO* editorial office plans to issue more detailed guidelines soon.

Despite all efforts, it is sometimes impossible to hide the authors' identities. Indeed, if you choose to keep your identifying information in your submitted manuscript, I'll still send it out for review. But the more the reviewer's attention can be deflected away from the authors personally and toward the scientific content, the more the quality and objectivity of the review will benefit.

We thank our reviewers once again for their contributions! In virtually all cases, they do an excellent job and are fair to the authors, whether or not they know the authors' identities. Still, I am convinced that dual anonymization is helpful to them in fulfilling this role and helpful to authors in ensuring unbiased consideration of their articles.

References

Johnson, S. K., and Kirk, J. F. 2020, *Publ. Astron. Soc. Pacific*, 132, 034503.

Moss-Racusin, C. A., Dovidio, J. F., Brescoll, V. L., Graham, M. J., and Handelsman, J. 2012, *Proc. Natl. Acad. Sci.*, **109**, 16474 (https://doi.org/10.1073/pnas.1211286109).

Percy, J. R. 2016, *J. Amer. Assoc. Var. Star Obs.*, 44, 85.

QZ Carinae—Orbit of the Two Binary Pairs

Mark Blackford
Variable Stars South (VSS), Congarinni Observatory, Congarinni, NSW, Australia 2447; markgblackford@outlook.com

Stan Walker
Variable Stars South (VSS), Wharemaru Observatory, Waiharara, Northland, New Zealand 0486

Edwin Budding
Variable Stars South (VSS), Carter Observatory, Kelburn, Wellington, New Zealand 6012

Greg Bolt
Variable Stars South (VSS), Craigie Observatory, Craigie, WA, Australia 6025

Dave Blane
Variable Stars South (VSS), and Astronomical Society of Southern Africa (ASSA), Henley Observatory, Henley on Klip, Gauteng, South Africa

Terry Bohlsen
Variable Stars South (VSS), and Southern Astro Spectroscopy Email Ring (SASER), Mirranook Observatory, Armidale, NSW, Australia, 2350

Anthony Moffat
BRITE Team, Département de physique, Université de Montréal, CP 6128, Succursale Centre-Ville, Montréal, QC H3C 3J7, Canada

Herbert Pablo
BRITE Team, American Association of Variable Star Observers, 49 Bay State Road, Cambridge, MA 02138

Andrzej Pigulski
BRITE Team, Instytut Astronomiczny, Uniwersytet Wrocławski, Wrocław, Poland

Adam Popowicz
BRITE Team, Department of Automatic Control, Electronics and Informatics, Silesian University of Technology, Gliwice, Poland

Gregg Wade
BRITE Team, Department of Physics and Space Science, Royal Military College of Canada, P.O. Box 17000, Station Forces, Kingston, ON K7K 7B4, Canada

Konstanze Zwintz
BRITE Team, Universität Innsbruck, Institut für Astro- und Teilchenphysik, Technikerstrasse 25, A-6020 Innsbruck, Austria

Received September 3, 2019; revised November 18, 2019, January 12, 2020; accepted January 13, 2020

Abstract We present an updated O–C diagram of the light-time variations of the eclipsing binary (component B) in the system QZ Carinae as it moves in the long-period orbit around the non-eclipsing pair (component A). This includes new Variable Stars South members' measures from 2017 to 2019, BRITE satellite observations in 2017 and 2018, and 100 previously unpublished measures made at Auckland Observatory from 1974 to 1978. We conclude that QZ Carinae has not yet completed one orbit of the two pairs since discovery in 1971. The duration of totality of primary eclipses was measured to be 0.295 ± 0.02 day (7.08 ± 0.48 hours), rather longer than earlier values from light curve models. Other observational findings include the shape of primary and secondary eclipses and small-scale short-term brightness changes.

1. Introduction

QZ Carinae (= HD 93206, HIP 52526; V = 6.24, U–B = –0.84, B–V = 0.13; Wenger *et al.* 2000) is the brightest member of the open cluster Collinder 228 within the Great Carina Nebula region. Variability was first discovered by Brian Marino and Stan Walker at the Auckland Observatory in 1971 (Walker and Marino 1972).

Spectroscopy by Morrison and Conti (1979) revealed the system to comprise at least two pairs of very massive stars. The primary pair, non-eclipsing, has an orbital period of ~20.73 days. The less luminous eclipsing pair has a period of 5.99857 days. Leung *et al.* (1979) provided further details of these four stars, giving a total mass of 93 ± 12.6 solar masses. They also derived a mutual orbital period of several decades for the two pairs orbiting around each other.

The model arising from these early investigations is essentially similar to that of present-day understanding. According to Parkin *et al.* (2011) the brightest component of the combined spectrum is the O9.7 I type supergiant in "Component A." The secondary in Component A has not been directly observed but it is thought to be an early B-type dwarf (B2 V). "Component B" is the eclipsing binary whose brighter member is the less massive O8 III type star. Its eclipsing companion is presumed to be a more massive late O-type dwarf (O9 V). Spectral signs of this star have been mentioned in the literature, but clear evidence has been difficult to demonstrate and indications of additional variability in the system complicate the picture.

The "eclipse method" is well established as a source of empirical knowledge of stellar properties (cf. e.g. Eker *et al.* 2018). As one of the most massive close systems known, QZ Car has a special role in informing about these properties at the high end of the stellar mass range. Such young hot stars are associated with strong radiation fields and stellar winds that interact with powerful shock fronts giving rise to significant X-ray emission (Parkin *et al.* 2011). Given this context, it could be reasonably proposed that QZ Car should be an ancestor of a future gravitational wave source. This observationally challenging system may be the best test-case for checking the Roche-lobe radiative-distortion effects predicted by Drechsel *et al.* (1995).

At face value, Component B's arrangement is strongly suggestive of Case A (hydrogen core burning mass donor) type interactive binary evolution. Morrison and Conti (1980) mentioned that speckle interferometry could separate components A and B and help clarify their physical parameters. The O–C diagram from eclipse timings should also bear on this. If the full facts on a multiple stellar system such as QZ Car were available, it would offer critical tests of stellar evolution modelling, including the relationship of stars to their Galactic environment (Andersen *et al.* 1993).

In a more recent review of the system, Walker *et al.* (2017) suggested higher masses than Leung *et al.* (1979), as shown in their Tables 9 and 10 based on a value of 49.5 years for the long-period orbit. The exact period would constrain the total masses of the individual binaries and thence establish more precise parameters of the system components.

The present paper concentrates on our knowledge of the long-period orbit.

2. Ground-based observations

Ground-based measures were compiled from a variety of sources, some not previously published. Until about 1995 measures were single-channel differential photoelectric photometry, usually in UBV. Since then they were almost entirely CCD in B and V, except for some with DSLR cameras. Only the V magnitudes have been used in this study.

Due to the lack of uniformity of comparison stars in the photoelectric era no attempt has been made to correct published magnitudes. Since 1995 most measures have been linked to E Region standards although a few used the AAVSO's APASS system which has some slight divergence.

A variety of comparison stars and telescopes have been used leading to zero point offsets between the different sets of observations. This does not affect our conclusions. The unpublished measures were made in UBV at Auckland Observatory as part of a project monitoring eta Carinae. Exactly 100 in number, they extend from 1974 to 1978 and allow the determination of six new epochs which fill in the lower part of the O–C diagram very well.

Between 2017 and 2019 time series observations were collected from two sites to better define the duration of totality of primary eclipses. GB observed from the west coast of Australia (115.75833° E, 31.78917° S) through a V filter and 25-cm telescope stopped down to 8 cm. MB observed from the east coast of Australia (152.86040° E, 30.73452° S) through a V filter and 8-cm refractor stopped down to 5 cm. For both setups exposure times were limited to 10 seconds or less to avoid saturation. To reduce the effect of scintillation 5 to 7 observations were averaged to obtain the final magnitudes.

3. BRITE satellite observations

The BRIght Target Explorer (BRITE) nano-satellites (Weiss *et al.* 2014; Pablo *et al.* 2016) provide high precision photometry of bright stars (typically $V < 5$ mag) for continuous periods of up to 180 days. The un-cooled CCD cameras have an effective field of view of 24 × 20 degrees, however only a limited number of small sub-rasters, centered on pre-selected stars of interest, are downloaded for each pointing of a satellite.

BRITE images are deliberately defocussed to avoid undersampling due to the 27-arcsec/pixel resolution. In crowded regions, such as the QZ Car field, blending of multiple star images is unavoidable. Furthermore, radiation-induced defects in the sensors and other instrumental issues complicate image acquisition and analysis processes (Popowicz *et al.* 2017; Pigulski *et al.* 2018).

Although not originally selected as a target, QZ Car was included in the raster of the Wolf-Rayet star WR24 (HD 93131) which was observed between 2017 Jan 29 and Jul 1 by the red-filter BRITE-Heweliusz (BHr) satellite. Data for WR24 and QZ Car were successfully extracted and de-trended separately.

A total of 77,7783 observations were taken in chopping mode (Pablo *et al.* 2016) with exposure times of 5 seconds. Typically about 50 images were recorded over approximately 30 minutes during each 97.0972-minute orbit of the BHr satellite. QZ Car does not vary significantly on such short time scales so to improve the signal-to-noise ratio we used the orbit-averaged magnitudes (see Figure 1). The light curve phased on a period of 5.99857 d is shown in Figure 2.

QZ Car was observed again by BRITE-Heweliusz between 2018 May 16 and Jul 1, and by the red-filter BRITE-Toronto (BTr) satellite between 2018 Feb 16 and May 19.

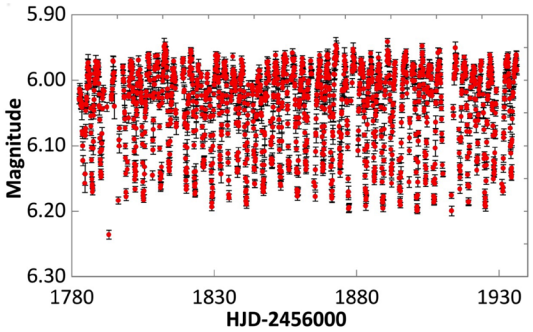

Figure 1. BRITE-Heweliusz 2017 QZ Car light curve, observations detrended and averaged per spacecraft orbit.

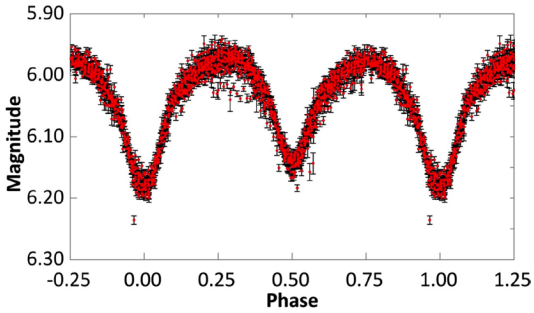

Figure 2. BRITE-Heweliusz 2017 phased light curve based on a period of 5.99857 d.

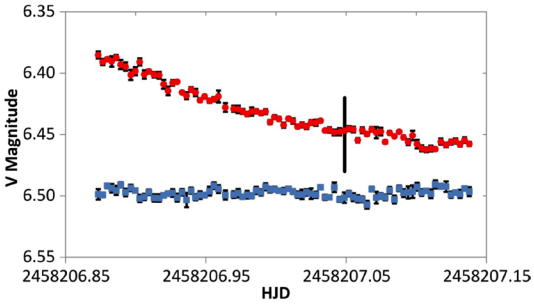

Figure 3. Ground-based light curves of QZ Car (red) and the check star HD 93191 (blue) with their error bars (black). The check star was shifted by 2 magnitudes for display purposes. Predicted start of totality based on the Leung *et al.* 1979 model is indicated by the vertical black line.

4. Determination of epochs of eclipse minima

The long-term near-continuous BRITE satellite observations allowed precise epochs of eclipse minimum to be easily measured. Determining epochs of eclipse minimum is also straightforward from ground-based observations when both ingress and egress are recorded in a single observing session. However, the long duration of totality (~5.76 hours as modelled by Leung *et al.* 1979) and small amplitude (~0.24 in V due to the more luminous non-eclipsing pair) make this difficult to apply to ground-based observations of QZ Car.

At 60° S declination QZ Car is accessible only from the southern hemisphere where experienced observers in suitable locations are relatively few. The magnitude of the star is too bright for most CCD observers. All recent CCD and DSLR measures have been made with stopped down telescopes and/or short exposures.

From latitude 30° S the system is at opposition in early March when astronomical darkness is ~10 hours, leaving only 2 hours before and after totality to measure parts of ingress and egress. The magnitude change over that time frame is very small, of the order of a few hundredths of a magnitude. Thus, second and third contact points defining the duration of totality are hard to determine accurately. An example is shown in Figure 3. Measured times of the second contact point, when ingress changes to totality, have abnormally large measurement error due to the light curve slope during totality. It was not possible to observe the end of totality in this case.

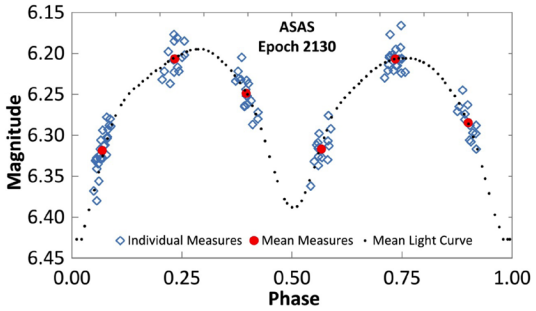

Figure 4. BRITE mean light curve (black dotted line) with 101 individual ASAS measures (open blue diamonds) between 2005 Oct and 2006 Jun. Filled red circles are average values within each group of observations.

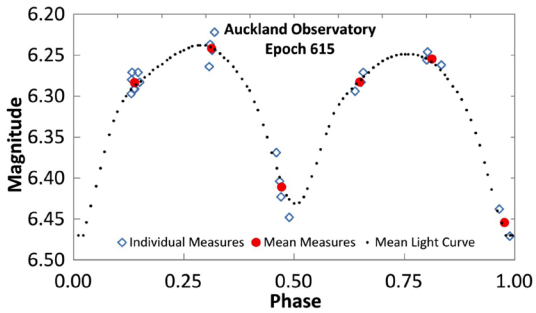

Figure 5. Similar to Figure 4 but with only 23 measures which, when averaged, fit the mean light curve well enough to determine a reliable epoch.

The period of 5.99857 days is also inconvenient. Only a narrow longitude range is suitable for observing the entire period of totality at opposition. From a given observing location eclipses occur 0.00143 d earlier each cycle, or 0.0817 d per year. So the ideal longitude moves east by 31.3° per year, taking 11.5 years to complete the cycle, although due to the light curve shape this time can be halved.

We adopted the method of fitting a mean light curve to random measures of QZ Car during annual seasons. This produces good annual epochs and is often used with longer period Cepheids. Initially we employed the symmetrical mean light curve determined by Leung *et al.* (1979) from the original observations of Walker and Marino (1972). However, Hipparcos (Perryman *et al.* 1997) and later ground-based observations indicated that the light curve is asymmetric. In particular, maxima following primary eclipses are significantly brighter than maxima following secondary eclipses. Unfortunately, a reliable mean light curve could not be constructed from the rather noisy and incomplete Hipparcos and ground-based measures.

We resolved this by constructing a mean light curve of 2017 BRITE measures. The 0.203-magnitude range of this mean light

curve is smaller than the 0.230-magnitude range measured in the V band. This results from blending with nearby stars and the non-standard red filter employed in BRITE-Heweliusz. The mean light curve was therefore scaled to match the V magnitude range and a zero point correction applied to account for different comparison stars used by each observer. Epochs derived are not affected by the zero point corrections.

The BRITE mean light curve is shown in Figure 4 along with 101 measures from one season of the All Sky Automated Survey (Pojmański 1997). It can also be used with fewer random measures as shown in Figure 5. This method provides a visual picture of the accuracy which is very useful. Much of the scatter in individual observations can be attributed to small-scale brightness variations discussed in section 7. The effect of these variations can be minimized by averaging values within each group of observations.

5. Observed-Minus-Calculated diagram of epochs of primary minimum

Mayer *et al.* (2001) presented an O–C diagram of six published times of minimum for QZ Car from discovery in 1971 to 1994. The light-time effect (LTE) due to the mutual orbit of the two pairs around each other was evident. Despite only a fraction of the orbit being covered they were able to conclude that the period is several decades.

We compiled a comprehensive set of published, historic (but previously unpublished) and new observations of QZ Car. Epochs of primary eclipses were derived from seasonal measurements (Table 1) and a more complete O–C diagram constructed in an attempt to better determine the period of the mutual orbit of the two pairs. In Figure 6 we show the O–C diagram covering 48 years since 1971 using the light elements JD 2441033.033 + 5.99857 × E, where E is the number of epochs since the initial epoch.

There are two related uncertainties in this area. Until the value of the long period orbit is determined the period derived for the eclipsing pair by Mayer *et al.* (1998) is uncertain at the fifth decimal level. This does not affect seasonal epochs. The period of the eclipsing pair will be known when one long-period orbit is completed—but the long period (and hence the correction to the eclipse period) cannot be determined until the O–C curve begins to duplicate itself.

The completion of one cycle of the long-period orbit will be seen when the O–C curve begins to run parallel to the early cycles. The period will be uncertain until the rate of approach begins to slow and the O–C curve becomes flatter.

The slope of the O–C diagram was 5.99818 days/cycle between cycles 0 and 185 and 5.99833 days/cycle between cycles 2676 and 2933. Both are shorter than the adopted period of 5.99857 days as the eclipsing system was approaching us in both cases. The period between cycles 185 and 433 had lengthened to 5.998454 days, clearly showing the curvature of the long orbit as it nears the closest point to the observer.

It is likely that the current observed trend will continue for several more years before following the curve shown from cycle 700 onward where it begins a change to the longer receding period.

6. Determining the duration of totality

6.1. Primary eclipses

For the 2019 season we organized a wider spread in longitude in an attempt to observe the two points defining the beginning and end of totality. These were made using aperture masks and V filters by GB at Craigie Observatory (115.75833° E) and MB at Congarinni Observatory (152.86040° E). Unfortunately, they were not able to observe on the same nights. Together with measures by MB in 2017 and 2018 we determined 8 ingress points and 4 egress points.

Figure 7 is a composite graph of primary eclipse totality. Measures from MB (cycle 2789) during ingress and up to mid-totality are combined with those of GB (cycle 2925) during totality and egress. GB's measures were corrected for the change in LTE between the two cycles. From these we determined duration of totality to be 0.295 ± 0.02 day. Totality is not flat, which complicates the determination of second and third contact times, although end of totality was generally clearer. This illustrates why early measures from single sites were ineffective.

Figure 8 shows the O–C values of our measured seasonal epochs and primary eclipse second and third contact points defining the start and end of totality. The scatter in the beginning and ending points illustrates the difficulty in determining exact times due to the low amplitude of eclipses.

Measures during the past three years indicate that totality lasts 7.08 ± 0.48 hours, rather longer than the 5.76 hours of the original Leung *et al.* (1979) model but a better fit to the wider eclipses of Walker *et al.* (2017).

6.2. Secondary eclipses

The most complete measures available of a secondary eclipse from one site are those of Grant Christie from Auckland Observatory in 1994 (Mayer *et al.* 1998) but these do not cover totality in full (Figure 9). Also shown is a composite light curve from ingress measures by MB in 2018 and egress measures by GB in 2019.

The considerable curvature is due to this eclipse being an annular transit by the smaller star. We were unable to identify second and third contact points of these annular transits from such light curves.

BRITE satellite data were unsuitable for determining start and end of totality. Imaging was restricted to about 30 minutes within each satellite orbit and individual measures had relatively large uncertainties. Orbit-averaged magnitudes, while more precise, had relatively poor time resolution.

7. Other brightness variations

Larger-than-normal scatter in seasonal light curves (cf. Figure 4) indicates variation over and above that due to the eclipsing pair. Hipparcos measures also showed considerable scatter (Figure 1 of Walker *et al.* 2017). The masses and spectral types of the four stars making up the system, in particular the O9 type supergiant, are such that slight variations in brightness are not unexpected. Some supergiants show relatively strong variability from surface bright spots (cf. Ramiaramanantsoa *et al.* 2018).

Table 1. Derived seasonal epochs of central primary eclipse. Values in column 2 calculated using zero epoch 41033.033 and period 5.99857 days. All measures used in this paper may be accessed at: ftp://ftp.aavso.org/public/datasets/200112_QZ_Car_Observations.xlsx

Cycle	*Calculate (HJD−2400000)*	*Derived (HJD−2400000)*	*LTE error (d)*	*Number of Source (d)*	*Observations*	*(Observer)*
0	41033.033	41033.033	0.000	0.015	41	Auckland Photoelectric Observers' Group
21	41159.003	41159.002	–0.001	0.015	41	Auckland Photoelectric Observers' Group
46	41308.967	41308.953	–0.014	0.019	17	Auckland Photoelectric Observers' Group
133	41830.843	41830.793	–0.050	0.045	12	Auckland Photoelectric Observers' Group
185	42142.768	42142.699	–0.069	0.018	53	Auckland Photoelectric Observers' Group
264	42616.655	42616.586	–0.070	0.034	12	Auckland Photoelectric Observers' Group
309	42886.591	42886.512	–0.079	0.015	14	Auckland Photoelectric Observers' Group
368	43240.507	43240.418	–0.089	0.022	5	Auckland Photoelectric Observers' Group
432	43624.415	43624.320	–0.095	0.022	15	Auckland Photoelectric Observers' Group
555	44362.239	44362.239	0.000	0.033	13	Auckland Photoelectric Observers' Group
615	44722.154	44722.037	–0.116	0.025	23	Auckland Photoelectric Observers' Group
672	45064.072	45063.962	–0.110	0.028	8	Auckland Photoelectric Observers' Group
759	45585.948	45585.828	–0.120	0.028	8	Auckland Photoelectric Observers' Group
1161	47997.373	47997.324	–0.049	0.025	38	Hipparcos
1201	48237.316	48237.274	–0.042	0.016	19	Hipparcos
1243	48489.256	48489.202	–0.054	0.032	46	Hipparcos
1278	48699.205	48699.147	–0.059	0.020	150	Pavel Mayer (La Silla Observatory)
1299	48825.175	48825.126	–0.049	0.018	24	Hipparcos
1331	49017.130	49017.091	–0.039	0.056	54	Pavel Mayer (La Silla Observatory)
1350	49131.103	49131.083	–0.020	0.019	9	Auckland Photoelectric Observers' Group
1398	49419.034	49419.022	–0.012	0.018	57	Pavel Mayer (Christie)
1398	49419.034	49419.034	0.000	0.038	20	Auckland Photoelectric Observers' Group
1948	52718.247	52718.517	0.270	0.040	21	All Sky Automated Survey
2006	53066.164	53066.444	0.280	0.010	56	All Sky Automated Survey
2015	53120.152	53120.442	0.290	0.031	43	Pavel Mayer (SAAO)
2074	53474.067	53474.368	0.301	0.013	77	All Sky Automated Survey
2129	53803.989	53804.305	0.316	0.008	101	All Sky Automated Survey
2196	54205.893	54206.190	0.297	0.019	90	All Sky Automated Survey
2253	54547.811	54548.133	0.322	0.014	108	All Sky Automated Survey
2309	54883.731	54884.071	0.340	0.017	72	All Sky Automated Survey
2324	54973.710	54974.040	0.330	0.040	26	Variable Stars South (Bohlsen)
2376	55285.635	55285.935	0.300	0.031	45	Variable Stars South (Bohlsen)
2562	56401.369	56401.639	0.270	0.018	36	Variable Stars South (Bohlsen)
2675	57079.208	57079.483	0.275	0.023	47	AAVSO (BSM South)
2676	57085.206	57085.476	0.270	0.018	122	Variable Stars South (Blackford)
2683	57127.196	57127.476	0.280	0.020	38	AAVSO (BSM Berry)
2735	57439.122	57439.372	0.250	0.021	69	Variable Stars South (Blackford)
2796	57805.035	57805.263	0.228	0.006	1681	BRITE
2799	57823.030	57823.280	0.250	0.013	121	Variable Stars South (Bolt)
2800	57829.029	57829.279	0.250	0.022	96	Variable Stars South (Blane)
2809	57883.016	57883.266	0.250	0.015	124	Variable Stars South (Blane)
2861	58194.942	58195.172	0.230	0.014	124	Variable Stars South (Blackford)
2863	58206.939	58207.169	0.230	0.008	100	Variable Stars South (Blackford)
2859	58182.945	58183.167	0.222	0.007	1197	BRITE
2922	58560.855	58561.055	0.200	0.023	53	Variable Stars South (Blane)
2926	58584.849	58585.049	0.200	0.016	150	Variable Stars South (Blackford)
2928	58596.846	58597.066	0.220	0.012	35	Variable Stars South (Blane)
2933	58626.839	58627.059	0.220	0.010	33	Variable Stars South (Blane)

QZ Car was intensely monitored over two successive cycles from La Silla Observatory in 1992 (Mayer 2001). The light curve (Figure 10) shows a puzzling feature in the later cycle which was not obvious in the preceding cycle. Similar, though less dramatic, short-term fluctuations have been recorded by other observers.

More recently the BRITE light curves from 2017 and 2018 showed long term oscillations of minimum and maximum magnitudes of the order of several percent (cf. Figure 1) and the depth of primary eclipses also varied significantly from cycle to cycle (Figure 11).

We initially thought some of the small variations may have been associated with aspect variations in the orbit of the 20.73-day pair. BRITE data were searched for such a signature. There were indications of this but at such a low level that it was not considered significant and not a source of the observed variations.

The source of these variations is unclear but may be related to wind-wind interactions, accretion disc/hot spots due to mass transfer in the eclipsing pair, and/or intrinsic variability of the bright supergiant member of the system.

8. Conclusions

Previously published and new observations combined with unpublished measures during the interval 1974 to 1978 have allowed a much more complete O–C diagram of the light-time

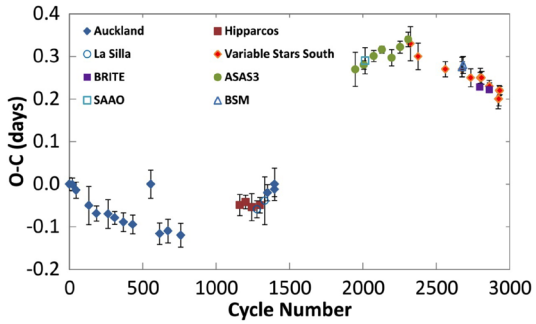

Figure 6. O–C diagram showing light-time effects due to the long-period orbit of the two pairs about each other.

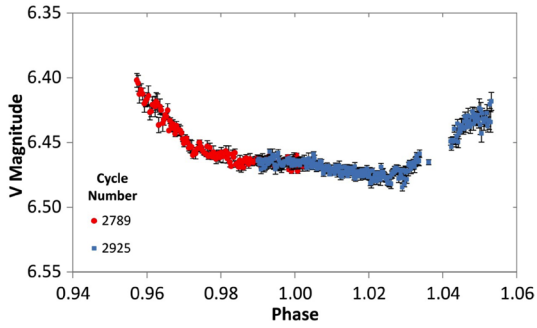

Figure 7. LTE and zero point corrected light curve of primary eclipse composed from ingress measures in 2017 and egress measures in 2019. These cover a period of ~0.57 days or 13.7 hours. The gap on egress was caused by a permanent observing obstruction which could not be removed.

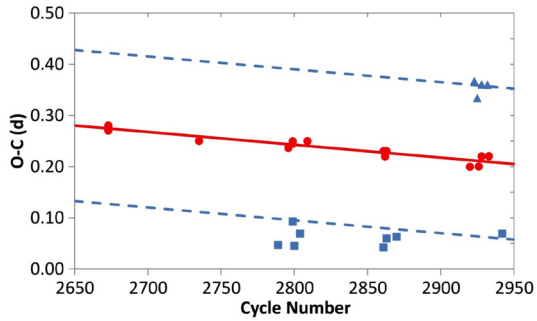

Figure 8: O–C diagram of measured seasonal epochs (red circles) from 2015 through 2019. Also plotted are O–C values determined for the start (blue squares) and end (blue triangles) of totality for primary eclipses. Dashed blue lines indicate totality lasting 0.295 day.

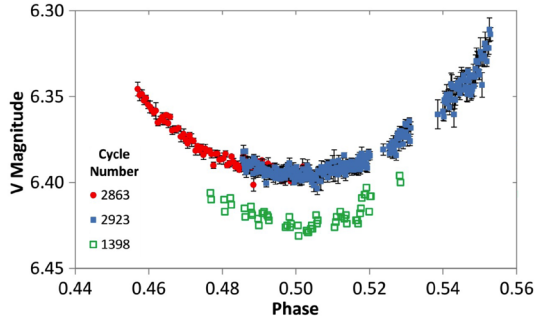

Figure 9. LTE and zero point corrected composite secondary eclipse light curve from ingress measures by MB (red circles) and egress measures by GB (blue squares). Christie's measures are plotted as empty green squares.

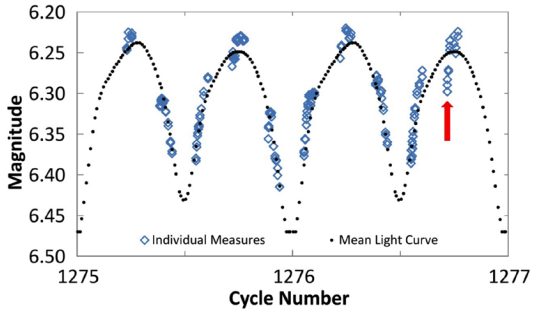

Figure 10. Two consecutive eclipse cycles measured at La Silla Observatory in 1992. Measures during cycle 1275 match the model light curve reasonably well. However, cycle 1276 shows a significant deviation (red arrow) from the model near the maximum following secondary eclipse.

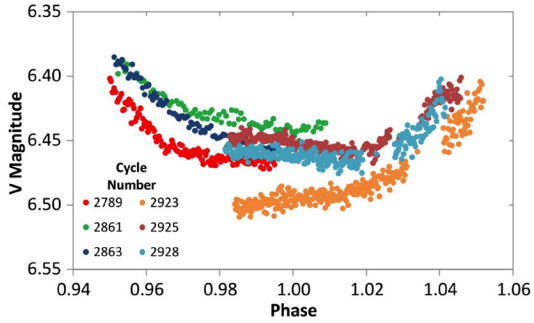

Figure 11. Three sets of primary eclipse ingress measures by MB and three of egress by GB showing significant cycle to cycle brightness variations. The downward slope during totality was consistently observed apart from cycle 2923 which showed an upward slope.

effects. The six additional early epochs define the LTE curve during most of the period when the eclipsing secondary pair was at its closest to us. This pair is presently approaching again but as yet there is no indication that this approach is slowing to parallel the earlier part of the O–C curve. We conclude that the two pairs of stars in the system have not yet completed one orbit since discovery in 1971.

BRITE satellite measures defined the true shape of the light curve which models must be able to emulate. Combined with our measures of primary and secondary eclipse shapes, we were able to produce a mean light curve to which random measures in each season could be fitted to produce reliable seasonal epochs.

Primary eclipse totality was found to last 7.08 ± 0.48 hours, which helps to explain why attempts to determine epochs from measures at this phase have been largely unsuccessful. The various figures above illustrate other aspects of the problems quite well.

QZ Car in the open cluster Collinder 228 is one of the brightest objects near the eta Carinae region and its radiation is responsible for stimulating the emission in much of the nebulosity in the southern part of that region. The system's mass and complexity are still not fully understood and continued study is extremely important.

With this in mind ingress in the 2020 season will best be studied from South America and egress from Eastern Australia. We should see the completion of one long period orbit within the next few years. Until then these epochs may help other researchers.

9. Acknowledgements

Pavel Mayer and Stan Walker exchanged data on several occasions. This included those labelled in the O–C diagram as La Silla, SAAO, and the secondary eclipse measures of Christie used in Figure 9.

This paper is based in part on data collected by the BRITE Constellation satellite mission, designed, built, launched, operated, and supported by the Austrian Research Promotion Agency (FFG), the University of Vienna, the Technical University of Graz, the University of Innsbruck, the Canadian Space Agency (CSA), the University of Toronto Institute for Aerospace Studies (UTIAS), the Foundation for Polish Science and Technology (FNiTP MNiSW), and National Science Centre (NCN).

APi acknowledges support from the NCN grant No. 2016/21/B/ST9/01126.

APo was supported by Silesian University Rector Grant no. 02/140/RGJ20/0001.

GW acknowledges support in the form of a Discovery Grant from NSERC, Canada.

We acknowledge the AAVSO for the use of AAVSOnet data and appreciate the hard work and dedication of AAVSOnet site managers Peter Nelson (BSM South) and Greg Bolt (BSM Berry).

This research has made use of the database of the All Sky Automated Survey ASAS, http://www.astrouw.edu.pl/asas/.

Members of the Auckland Astronomical Society helped with many of the observations as the Auckland Photoelectric Observers' Group, using the 50-cm Edith Winstone Blackwell telescope until epoch 759, later the Milton Road observatory with a 53-cm Cassegrain for epochs 1350 and 1398.

References

Andersen, J., Clausen, J. V., and Gimenez, A. 1993, *Astron. Astrophys.*, **277**, 439.

Drechsel, H., Haas, S., Lorenz, R., and Gayler, S. 1995, *Astron. Astrophys.*, **294**, 723.

Eker, Z., *et al.* 2018, *Mon. Not. Roy. Astron. Soc.*, **479**, 5491.

Leung, K.-C., Moffat, A. F. J., and Seggewiss, W. 1979, *Astrophys. J.*, **231**, 742.

Mayer, P. 2001, and other dates, Private communications.

Mayer, P., Lorenz, R., Drechsel, H., and Abseim, A. 2001, *Astron. Astrophys.*, **366**, 558.

Mayer, P., Niarchos, P. G., Lorenz, R., Wolf, M., and Christie, G. 1998, *Astron. Astrophys., Suppl. Ser.*, **130**, 311.

Morrison, N. D., and Conti, P. S. 1979, in *Mass Loss and Evolution of O-Type Stars*, eds. P. S. Conti, C. W. H. De Loore, Reidel Publishing Company, Dordrecht, 277.

Morrison, N. D., and Conti, P. S. 1980, *Astrophys. J.*, **239**, 212.

Pablo, H., *et al.* 2016, *Publ. Astron. Soc. Pacific*, **128**, 125001.

Parkin, E. R., *et al.* 2011, *Astrophys. J., Suppl. Ser.*, **194**, 8.

Perryman, M. A. C., European Space Agency Space Science Department, and the Hipparcos Science Team. 1997, *The Hipparcos and Tycho Catalogues*, ESA SP-1200 (VizieR On-line Data Catalog: I/239), ESA Publications Division, Noordwijk, The Netherlands.

Pigulski, A., Popowicz, A., and Kuschnig, R. 2018, in *3rd BRITE Science Conference, Lac Taureau, Canada*, eds. G. A. Wade, D. Baade, J. A. Guzik, R. Smolec, Polish Astron. Soc., Warsaw, **8**, 106.

Pojmanski, G., 1997, *Acta Astron.*, **47**, 467.

Popowicz, A., *et al.* 2017, *Astron. Astrophys.,* **605**, A26

Ramiaramanantsoa, T., *et al.* 2018, *Mon. Not. Roy. Astron. Soc.*, **473**, 5532.

Walker, W. S. G., Blackford, M., Butland, R., and Budding, E. 2017, *Mon. Not. Roy. Astron. Soc.*, **470**, 2007.

Walker, W. S. G., and Marino, B. F. 1972, *Inf. Bull. Var. Stars*, No. 681, 1.

Weiss, W. W., *et al.* 2014, *Publ. Astron. Soc. Pacific*, **126**, 573.

Wenger, M., *et al.* 2000, *Astron. Astrophys., Suppl. Ser.*, **143**, 9.

A Note on Bimodal Pulsating Red Giants

John R. Percy
Department of Astronomy and Astrophysics, and Dunlap Institute for Astronomy and Astrophysics, University of Toronto, 50 St. George Street, Toronto, ON M5S 3H4, Canada; john.percy@utoronto.ca

Received October 21, 2019; revised December 2, 2019; accepted December 2, 2019

Abstract ASAS-SN data and the AAVSO time-series analysis package VSTAR have been used to determine the pulsation periods of a sample of 23 bimodal pulsating red giants. The results have been combined with results from the literature to determine period ratios and pulsation modes, and how these vary systematically with the observed pulsation period(s). The results are consistent with previous results, and with theoretical predictions: most longer-period bimodal stars pulsate in the fundamental mode (period P0) and the first overtone mode (period P1), with P1/P0 decreasing slightly with increasing P0; most shorter-period bimodal stars pulsate in the first-overtone mode and the second-overtone mode (period P2), with P2/P1 decreasing slightly with increasing P1. Stars with period 100 to 200 days show a mixture of the two behaviors.

1. Introduction

Red giants are unstable to radial pulsation. Some red giants pulsate in two modes, usually the fundamental and first overtone mode in longer-period stars. Such bimodal pulsating red giants (PRGs) are useful in that they yield two observed periods which can be compared with theoretical predictions to provide information about the physical parameters of the star. Conventionally, Pb/Pa is plotted against log Pa in a so-called Petersen diagram (Petersen and Jorgensen 1972), where Pa and Pb are the longer and shorter periods, respectively.

Previous studies of individual bimodal PRGs (as opposed to surveys) have analyzed mostly stars with periods of 100 days or more (Mattei *et al.* 1997; Kiss *et al.*1999; Percy and Huang 2015; Fuentes-Morales and Vogt 2014). For these stars, P1/P0 is approximately 0.5. In this case, the first overtone period can be confused with the first harmonic period (P0)/2 which occurs if the light curve is not sinusoidal (Percy and Huang 2015). Theoretical models (Xiong and Deng 2007) suggest that, for shorter-period PRGs, P1/P0 increases to about 0.65 with decreasing period, and then decreases for the shortest-period stars. Short-period PRGs, studied with photoelectric photometry, have period ratios closer to 0.7 (Percy *et al.* 2008, Table 1).

The discontinuity between longer-period (greater than 100 days) PRGs with P1/P0 ~ 0.5, and shorter-period PRGs with P1/P0 ~ 0.7 might indicate that, for the shorter-period stars, the modes are not P0 and P1, but are P1 and P2. This would be consistent with recent models (Xiong *et al.*2018) which investigate the non-adiabatic oscillations and stability of PRGs in the presence of turbulent convection. They find that, for low-luminosity stars, lower-order modes are stable, while intermediate and high-order modes are unstable. As the luminosity increases, lower-order modes become unstable, and intermediate and high-order modes become stable.

In addition to the "classical" studies of indivual stars, described above, there is a large literature on Magellanic Cloud PRGs using data from the OGLE and MACHO surveys. These studies of multi-periodicy in PRGs have tended to interpret their results in terms of sequences in the period-luminosity diagram (e.g. Kiss *et al.* 1999; Wood 2000; Fuentes-Morales and Vogt 2014). Different sequences presumably correspond to stars pulsating in different modes. The horizontal spacings between the sequences are then related to period ratios. This is an extremely powerful way of visualizing the behavior of a large sample of stars.

Here, we express our results for individual stars, directly as period ratios which can be compared with theoretical values (Xiong and Deng 2007). We present period ratios Pb/Pa for a selection of PRGs with periods from 10 to 200 days, either from new analyses or from the literature. These would span the discontinuity, if indeed it was present, and choose between the two possible explanations for it. The results are then compared with theoretical predictions from Xiong and Deng (2007) and Xiong *et al.*(2018).

2. Data and analysis

Data were taken from the All-Sky Automated Survey for Supernovae (ASAS-SN: Jayasinghe *et al.* 2018, 2019) and analyzed using the AAVSO VSTAR time-series package (Benn 2013). Stars were selected to have an ASAS-SN classification of SR, periods between 10 and 200 days, and a sufficient amplitude. The light curves were first inspected for signs of bimodality; most stars were either monoperiodic or unduly scattered.

One drawback of the ASAS-SN data is that they extend for only about 2000 days—much less than e.g. the visual data of the American Association of Variable Star Observers. This limits the accuracy of any periods which are determined from the data.

Percy and Fenaux (2019) have discussed some of the problems with the automatic ASAS-SN analyses and classifications of PRGs. By carrying out the analyses manually, rather than automatically as the ASAS-SN team did, we can deal more effectively with the challenges which are presented by these complex stars.

A sample of stars with the properties described at the beginning of this section was analyzed using VSTAR. Some of the stars had many peaks of comparable height in the Fourier spectrum, and could not be interpreted. Those in Table 1 showed two clear peaks which appeared to be pulsation modes.

Those results were augmented with results for bimodal PRGs in the literature: a few shorter-period stars from Mattei *et al.* (1997) and Kiss *et al.* (1999), non-carbon stars from Percy and Huang (2015), and short-period PRGs observed by the AAVSO Photoelectric Photometry Program and by an Automated Photometric Telescope (Percy *et al.* 2008). For the purpose of plotting a Petersen diagram, the ratio of the periods and the logarithm of the longer period was calculated, and listed in Table 1. The Petersen diagram is shown in Figure 1.

3. Results

Table 1 lists the results of our time-series analysis of ASAS-SN bimodal PRGs. The columns give: the ASAS-SN name (minus ASAS-SN-V J), the longer period Pa in days and its amplitude Aa, the shorter period Pb in days and its amplitude Ab, the ratio Pb/Pa, and log Pa. Figure 1 shows a graph of Pb/Pa versus log Pa, including stars in Table 1, and from the sources mentioned in section 2.

Table 1. Pulsation properties of bimodal PRG stars from ASAS-SN V photometry.

Star Name—ASASSN-VJ	*Pa (d)*	*Aa (mag)*	*Pb (d)*	*Ab (mag)*	*Pb/Pa*	*log Pa*
191142.71+474526.6	104.47	0.31	67.69	0.15	0.648	2.02
220237.54+631351.9	100.84	0.18	52.78	0.19	0.523	2.00
080848.62-613410.2	26.70	0.07	19.95	0.04	0.747	1.43
002626.14+501637.2	142.73	0.12	87.00	0.12	0.610	2.15
112717.23+533103.7	166.92	0.20	98.34	0.24	0.590	2.22
201740.06+703651.6	173.26	0.11	104.58	0.11	0.600	2.24
071224.39-705134.9	106.42	0.19	60.41	0.14	0.568	2.03
204430.16-714817.1	91.97	0.07	61.08	0.13	0.664	1.96
111558.88-720026.6	96.61	0.10	64.67	0.12	0.669	1.99
190457.78-723524.6	83.97	0.08	55.23	0.07	0.658	1.92
105411.56-765436.6	119.49	0.18	74.77	0.18	0.628	2.08
035911.54+720905.5	44.49	0.06	31.23	0.08	0.700	1.65
003011.09+734535.8	64.03	0.16	45.33	0.09	0.708	1.87
074108.86-213820.1	16.49	0.06	9.61	0.07	0.580	1.22
175048.61-305655.3	14.58	0.11	8.15	0.11	0.559	1.16
165737.81-375858.2	18.27	0.12	9.19	0.05	0.503	1.26
155730.72-752331.0	65.05	0.08	44.15	0.05	0.679	1.81
122643.81-870158.5	106.32	0.11	67.79	0.11	0.638	2.03
085542.14-830046.9	76.78	0.12	52.83	0.12	0.688	1.88
225936.37-774536.8	72.76	0.07	49.23	0.07	0.677	1.86
035911.54+720905.5	44.49	0.06	31.23	0.08	0.702	1.65
190836.86-180124.5	34.04	0.03	17.07	0.09	0.500	1.53
180025.09-533405.9	19.15	0.05	26.76	0.05	0.715	1.43

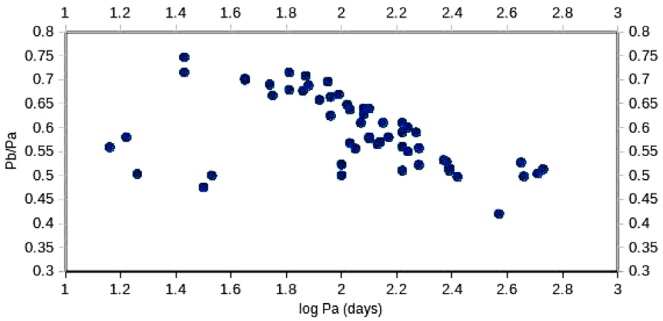

Figure 1. For bimodal PRGs: the ratio Pb/Pa of the shorter period Pb in days to the longer period Pa in days, as a function of log Pa.

4. Discussion

For stars with log Pa > 2.3, Pb/Pa is approximately 0.5, but decreases slightly from 0.52 to 0.50 or less. This is better seen in Figure 3 of Percy and Huang (2015). It is consistent with theoretical predictions if Pa and Pb are the fundamental and first overtone modes (Xiong and Deng 2007). For stars with log Pa < 2.0, Pb/Pa increases from 0.64 to 0.72 or greater with decreasing Pa. This is consistent with theoretical predictions if Pa and Pb are the first and second overtone modes (Xiong and Deng 2007). Stars with log Pa between 2.0 and 2.3 appear to be a mixture of these two groups. In that case, Pa will be a mixture of P0 and P1. Theoretical models also predict that longer-period stars should be unstable to lower-order modes, and shorter-period stars should be unstable to higher-order modes (Xiong *et al.* 2018), as we observe.

There are some shorter-period stars with Pb/Pa of about 0.5. For these, Pa and Pb may be fundamental and first overtone periods, or more likely first and third overtone modes. The latter would be more consistent with theory.

The longer-period star with a period of 350 days and Pb/Pa = 0.4 is RU Vul. This star underwent dramatic changes in both period (155 days to 100 days) and amplitude (0.85 to 0.10 magnitude), and is therefore anomalous.

The mode assignments that we have made give reasonable matches to the theoretical Petersen diagram of Xiong and Deng (2007). However, there is some ambiguity. The theoretical period ratios are moderately uncertain, especially at higher luminosities and periods, both because of uncertainties in the models, and because the period ratios are mass and composition dependent. Much depends on how well the models treat convection.

Soszyński *et al.* (2004) have plotted Petersen diagrams for PRGs in the LMC. The highest concentration of stars occurs when Pa is a long secondary period (LSP). The next largest concentration occurs for stars with log Pa < 2.0, and Pb/Pa of about 0.7. They interpret these periods as P3/P2; we interpret them as P2/P1. There is another concentration of stars with log Pa < 2 and Pb/Pa = 0.5. They interpret these as P3/P1; we could interpret them as P1/P0. We note that there are hardly any bimodal stars with log Pa > 2.0, except those with LSPs; there are no bimodal stars of the type studied by Mattei *et al.* (1997), Kiss *et al.*(1999), and Percy and Huang (2015). This suggests that there may be significant differences between the PRGs in the LMC and in our galaxy, perhaps due to composition differences.

Trabucchi *et al.* (2017) have calculated linear, radial, non-adiabatic models for PRGs in the LMC. These are reasonably successful in modeling the different sequences (corresponding to different overtones) in the PL sequences, though the theoretical periods of the higher-luminosity fundamental mode pulsators are too long. In these stars, convection and convective cells are particularly important, but difficult to treat theoretically.

A potential piece of useful information might be pulsation amplitudes. Trabucchi *et al.* (2017) showed that, in the LMC, essentially all third-overtone pulsators have amplitudes less than 0.01 mag. Similarly, in the LMC, the second-overtone pulsators have (I) amplitudes < 0.05 mag. In our Table 1, the amplitudes

corresponding to fundamental, first, second, and third overtone pulsation do not have significantly different amplitudes, but average about 0.08 mag. However, the stars in Table 1 were chosen to show evidence of bimodality in their light curves, so they are not a random sample. We would not have chosen stars with amplitudes less than 0.01 mag.

Yet another approach to pulsation modes was carried out by Percy and Bakos (2003), who summarized results on 77 small-amplitude PRGs for which radii and masses could be estimated; these are stars with periods of a few tens of days, and would lie in the left third of our Figure 1. They found that most of the stars pulsate in the first overtone, some in the fundamental, and a few in the second or third overtone. This is consistent with our interpretation of Figure 1.

5. Conclusions

Analysis of individual bimodal PRGs (Figure 1) provides detailed information about the possible pulsation modes and period ratios of these stars, and how they vary with period. The results are consistent with previous results, and with theoretical predictions. They complement results from large-scale surveys (e.g. Wood 2000) which display the results as multiple sequences in the Petersen diagram. This study also reminds us that useful work can be done by analyzing stars from the vast ASAS-SN database, by students, amateur astronomers, and others.

6. Acknowledgements

We thank the ASAS-SN team for making the photometry publicly available, in user-friendly form, and the developers of VSTAR for creating the package and making it easily available and user-friendly. We also thank the anonymous referee for helpful comments. This project made use of the SIMBAD database, maintained in Strasbourg, France. The Dunlap Institute is funded through an endowment established by the David Dunlap family and the University of Toronto.

References

Benn, D. 2013, VSTAR data analysis software (http://www.aavso.org/vstar-overview).

Fuentes-Morales, I., and Vogt, N. 2014, *Astron. Nachr.*, **335**, 1072.

Jayasinghe, T., *et al.* 2018, *Mon. Not. Roy. Astron. Soc.*, **477**, 3145.

Jayasinghe, T., *et al.* 2019, *Mon. Not. Roy. Astron. Soc.*, **486**, 1907.

Kiss, L.L., Szatmáry, K., Cadmus, R. R., Jr., and Mattei, J. A. 1999, *Astron. Astrophys.*, **346**, 542.

Mattei, J.A., Foster, G., Hurwitz, L. A., Malatesta, K. H., Willson, L. A., and Mennessier, M. O. 1997, ESA SP-402, 269.

Percy, J. R., and Bakos, A. G. 2003, in *The Garrison Festschrift*, ed. R. O. Gray, C. J. Corbally, A. G. D. Philip, L. Davis Press, Schenectady, N.Y., 49.

Percy, J. R., and Fenaux, L. 2019, *J. Amer. Assoc. Var. Star Obs.*, **47**, 202.

Percy, J. R., and Huang, D. J. 2015, *J. Amer. Assoc. Var. Star Obs.*, **43**, 118.

Percy, J. R., Mashintsova, M., Nasui, C. O., Palaniappan, R., Seneviratne, R., and Henry, G. W. 2008, *Publ. Astron. Soc. Pacific*, **120**, 523.

Petersen, J. O., and Jorgensen, H. E. 1972, *Astron. Astrophys.*, **17**, 367.

Soszyński, I. Udalski, A., Kubiak, M., Szymanski, M., Pietrzynski, G., Zebrun, K., Szewczyk, O., and Wyrzykowski, L. 2004, *Acta. Astron.*, **54**, 129.

Trabucchi, M., Wood, P. R., Montalbán, J., Marigo, P., Pastorelli, G., and Girardi, L. 2017, *Astrophys. J.*, **847**, 139.

Wood, P. R. 2000, *Publ. Astron. Soc. Australia*, **17**, 18.

Xiong, D. R., and Deng, L. 2007, *Mon. Not. Roy. Astron. Soc.*, **378**, 1270.

Xiong, D. R., Deng, L., and Zhang, C. 2018, *Mon. Not. Roy. Astron. Soc.*, **480**, 2698.

The Photometric Period of Nova V2891 Cygni

Richard E. Schmidt
Burleith Observatory, 1810 35th Street NW, Washington, DC 20007; schmidt.rich@gmail.com

Received October 29, 2019; revised December 5,2019; accepted December 6, 2019

Abstract A photometric study of the recently discovered classical nova V2891 Cyg has been undertaken at the urban Burleith Observatory in Washington, DC. A total of 887 CCD observations were obtained over a time span of 70.92 days. Analysis indicates an orbital period of 3.8755 h ± 0.0042 h, epoch (HJD) of minimal light 2458752.3860, with amplitude 0.014 magnitude (Cousins I). The long-term light curve resembles that of the F class nova DO Aql (1925).

1. Introduction

The classical nova V2891 Cyg, R.A. $21^h09^m25.53^s$, Dec. +48° 10' 52.2" (2000), was discovered by the Palomar Gattini-IR wide-field NIR survey on UT 2019 September 17.25 (De *et al.* 2019). Other catalogue names are: PGIR19brv, AT 2019qwf, ZTF 19abyukuy, 000-BNG-814, and PSO J210925.535+481052.332. A finding chart is given as Figure 1.

The present author began an observing program that detected a possible photometric period on 15 Oct. 2019. By 2019 Nov. 6, the observed period had stabilized sufficiently to report it to D. Green at the *Central Bureau for Astronomical Telegrams* (CBAT), who then requested "quick naming" by N. Samus of the *General Catalogue of Variable Stars* (GCVS). The GCVS assigned the name "V2891 Cyg" (Green 2019; Kazarovets 2019). (Note that the GCVS requires reporting of novae to the CBAT prior to assigning a GCVS designation.)

V2891 Cyg is highly reddened, at galactic latitude 0.22°. Its color index ($V–R_c$) was observed as +2.26 on 2019 September 26.1185 UT (De Young 2019). Such red objects are of special interest in light-polluted urban observatory sites, as at the Burleith Observatory in Washington, DC, where CCD imaging in the near infrared (700–900nm) remains feasible, unlike in U, B, and V bands where sky brightness dominates (Schmidt 2016).

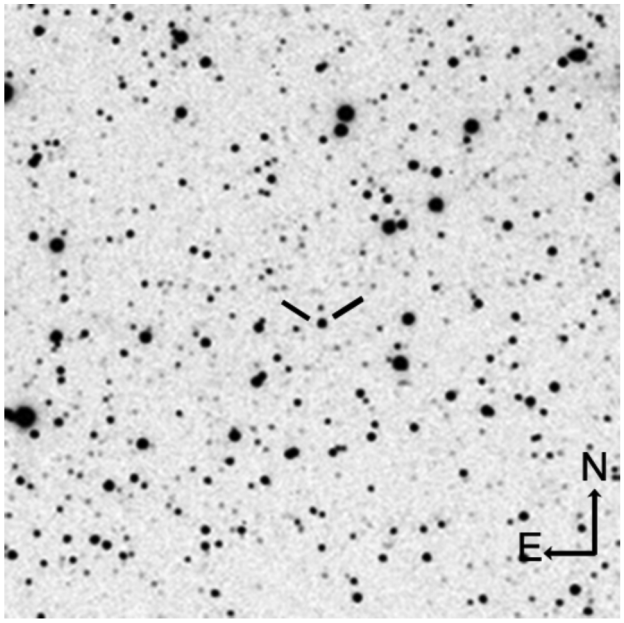

Figure 1. 10 arc-min field of V2891 Cyg.

This nova has been remarkable for its slow rise time, which had continued for 80 days by 2019 Dec. 5. In this regard its light curve resembles the F class nova DO Aql (1925) during its 70-day slow rise along the shoulder to its flat top (Vorontsov-Velyaminov 1940; Strope *et al.* 2010). Long periods of observability allow for searches for low-amplitude periodicities indicative of the nova's orbital period. At discovery the brightness of V2891 Cyg was 11.531 ABMag in J-Bessel band (De and Hankins 2019), within reach of smaller observatory instruments; continued monitoring of V2891 Cyg over the next year should aid in its classification.

2. Observations

At Burleith Observatory, CCD observations were obtained with a 0.32-m PlaneWave CDK and SBIG STL-1001E CCD camera with an Astrodon Cousins I-band filter. The KAF-1001E sensor features 24μ pixels, providing 85 dB dynamic range and scaling on the PlaneWave at 1.95 arc-sec/pixel, optimal for the typical 4 arc-sec seeing of my rooftop observatory (~2 pixels FWHM). Peak absolute quantum efficiency is ~50% in I-band.

Prior to each night's run, the acquisition computer was synchronized to the USNO NTP time service. Images (240-sec, autoguided) were sky flat-fielded, dark corrected, and aligned using SBIG CCDSOFT 5.00.12.

3. Reductions

Synthetic aperture photometry was performed using MIRA AP 7.974 (Mirametrics 2015). Cousins I-band differential ensemble photometry was performed using comparison stars from AAVSO chart sequence X24800DL (Table 1).

The resulting magnitudes of V2891 Cyg were detrended by subtracting the nightly means in order to remove the long-term light curve (De Young and Schmidt 1994). The observing log is presented in Table 2.

An example night's observing run is shown in Figure 2. Each night the individual standardized observations were uploaded to the AAVSO International Database (AID; Kafka 2019); nightly mean magnitudes are shown in Figure 3. The rising shoulder of the first 80 days of the DO Aql light curve (1925) can be seen in Figure 4.

Table 1. Comparison stars used for photometry.

AUID	R.A. (2000) h m s	Dec. (2000) ° ′ ″	C/K	Label	Ic
000-BNG-822	21 09 02.52	+48 09 51.8	1	133	12.472 (0.059)
000-BNG-823	21 09 30.71	+48 13 14.7	2	139	13.210 (0.084)
000-BNG-833	21 09 36.82	+48 07 26.6	3	143	13.193 (0.090)
000-BNG-834	21 09 46.30	+48 09 14.6	4	148	13.902 (0.117)
000-BNG-826	21 09 29.93	+48 10 17.4	K	151	14.011 (0.082)

Table 2. Observing Log.

UT	HJD 2458000+	Nr. Obs.	Mean Mag.	Mean Error (mag.)
Sep. 26.1658	752.66582	41	13.106	0.011
Sep. 27.0835	753.58348	09	13.093	0.014
Oct. 2.2099	758.70990	07	13.016	0.010
Oct. 11.0486	767.54860	32	12.924	0.011
Oct. 12.0979	768.59794	41	12.876	0.011
Oct. 15.0667	771.56667	50	12.827	0.010
Oct. 17.0619	773.56187	55	12.696	0.010
Oct. 18.0777	774.57765	44	12.652	0.009
Oct. 19.0789	775.57886	62	12.659	0.001
Oct. 24.0538	780.55384	56	12.718	0.008
Oct. 25.0513	781.55132	48	12.552	0.008
Oct. 28.0513	784.55128	57	12.529	0.008
Nov. 2.0709	789.57086	32	11.894	0.005
Nov. 3.0432	790.54322	37	11.782	0.006
Nov. 4.0576	791.55759	36	11.794	0.007
Nov. 7.0393	794.53925	33	11.922	0.008
Nov. 12.0027	799.50445	24	11.866	0.017
Nov. 13.0316	800.53156	30	11.468	0.009
Nov. 15.0509	802.55091	16	11.233	0.008
Nov. 16.9962	804.49626	18	11.447	0.008
Nov. 23.0646	810.56463	26	11.622	0.008
Nov. 24.9481	812.44807	39	11.546	0.003
Nov. 25.9566	813.51663	38	11.469	0.004
Dec. 04.9971	822.49708	15	11.527	0.005
Dec. 06.0005	823.50048	50	11.601	0.004

4. Analysis

Period analysis of reduced-by-mean observations was performed using PERANSO 2.60 software (Vanmunster 2006). Using its Date-Compensated Discrete Fourier Transform (DC-DFT) (Ferraz-Mello 1981) we derive the period 3.8755 h ± 0.0042. The resulting phased plot with spline-interpolated fit is shown in Figure 5.

The period was tested for significance using PERANSO's Fisher Monte Carlo randomization method which, while keeping observation times fixed, randomized the order of the magnitude observations over 200 permutations, searching for spectral responses due solely to observational biases (Moir 1998). The results were zero probability that no period was present in the data, and zero probability that any other significant periods were present in the data. The spectral window for all observations is shown in Figure 6. At period 6.19 cycles/day no spurious power appears, showing that the period found is not due to the sampling frequency. The resulting period information is summarized in Table 3.

Table 3. Period analysis results.

Parameter	Value
Period(h)	3.8755 (0.0042)
Period(d)	0.16148 (0.0001)
Frequency(c/h)	0.25803 (0.00028)
Mean amplitude (fit)	0.014 mag.
Number of observations	887
Time span	70.9212 days
Epoch (HJD) of light minimum	2458752.3860

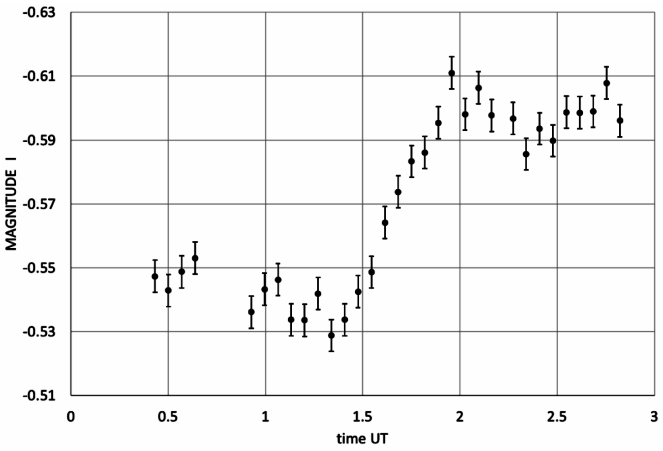

Figure 2. Observations 2019 Nov. 2.

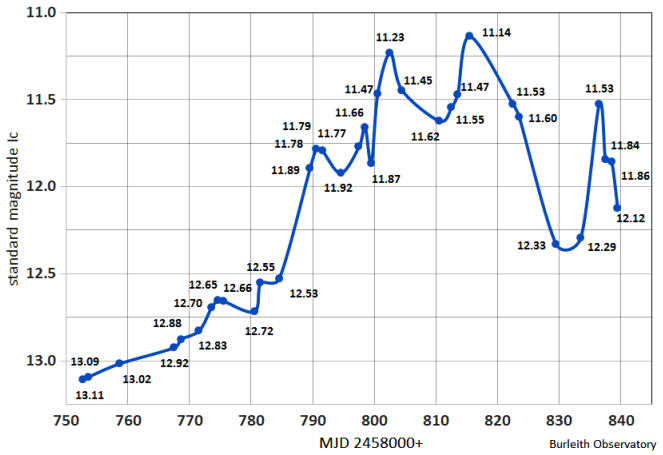

Figure 3. Nightly mean I_c magnitudes.

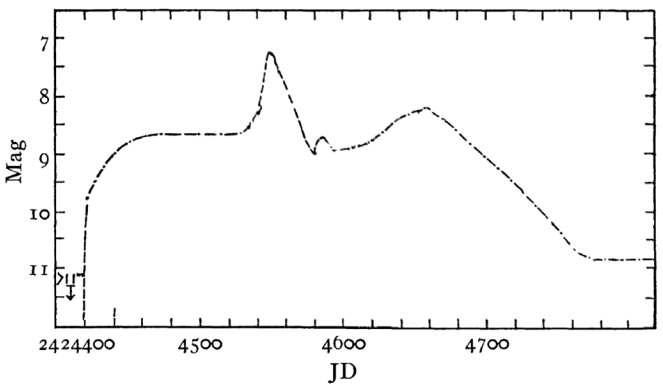

Figure 4. Light curve of DO Aql (1925; adapted from Vorontsov-Velyaminov 1940).

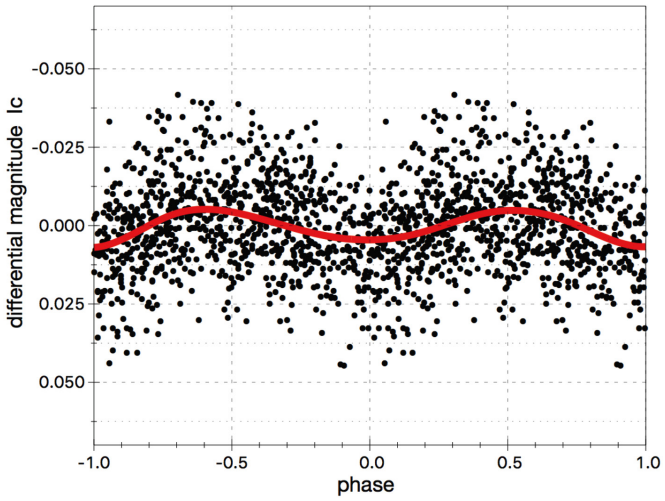

Figure 5. V2891 Cyg double phased plot with spline-interpolated fit.

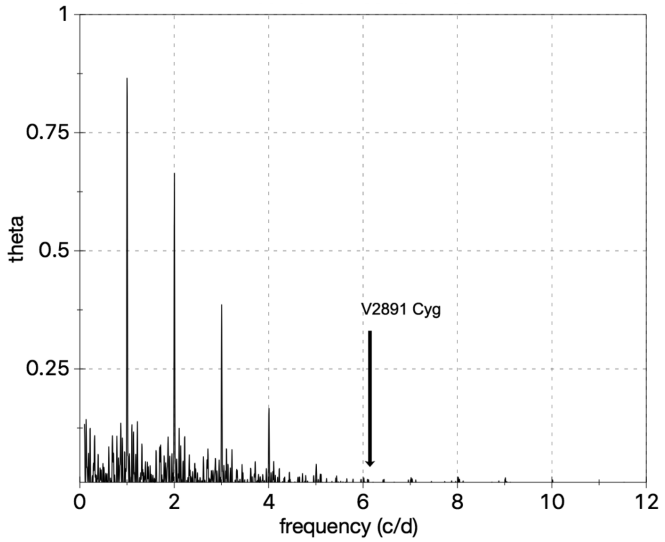

Figure 6. Spectral analysis of observational data.

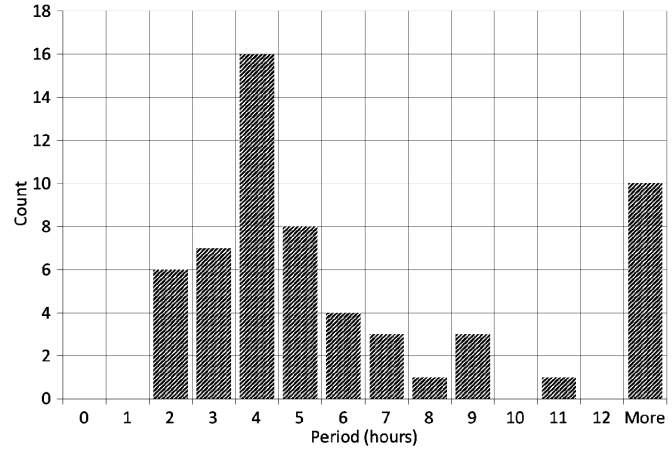

Figure 7. Histogram of novae orbital periods (Bode and Evans 2008).

5. Conclusion

The observed orbital period compares well with the median orbital period of 62 novae discussed by Bode and Evans (2008). A histogram of the orbital periods of novae from their table 2.5 in Classical Novae is shown in Figure 7. The observed period of V2891 Cyg places it in the range of most common period.

Despite its location in one of the most light-polluted urban American locations, the modest 12.5-inch telescope of the Burleith Observatory, with its ideally-matched pixel size CCD camera, is capable of quite satisfactory CCD photometry of a 13th magnitude variable observed in the near IR. The use of powerful period analysis software enables the detection of periodicity with an amplitude of only 10 milli-magnitude.

6. Acknowledgements

The author wishes to thank James A. De Young for his invaluable advice and continuing friendship since our first joint CCD photometry at the U.S. Naval Observatory in 1988, John Percy, University of Toronto, and Dipankar P. K. Banerjee, Physical Research Laboratory Ahmedabad, India, for helpful advice. Special acknowledgement is due to the AAVSO International Database for hosting photometric data from this study.

References

Bode, M., and Evans, A. 2008, *Classical Novae*, 2nd ed., Cambridge University Press, Cambridge, 26.

De, K., and Hankins, M. 2019, *Transient Name Server Astron. Transient Report*, No. 47666.

De, K., *et al.* 2019, *Astron. Telegram*, No. 13130 (http://www.astronomerstelegram.org/?read=13130).

De Young, J. A. 2019, CCD photometry with the Norfolk State University/University of Virginia 0.6-meter Rapid Response Robotic Telescope, private communication.

De Young, J. A., and Schmidt, R. E. 1994, *Astrophys. J., Lett.*, 431, L47.

Ferraz-Mello, S. 1981, *Astron. J.*, **86**, 619.

Green, D.W.E. 2019, *Cent. Bur. Electron. Telegrams*, No. 4694, 1.

Kafka, S. 2019, AAVSO International Database (https://www.aavso.org/aavso-international-database).

Kazarovets, E., Samus, N. N., Durlevich, O. V., Khruslov, A. V., Kireeva, N., and Pastukhova, E. N. 2019, *Perem. Zvezdy*, **39**, No. 3, 1.

Mirametrics. 2015, MIRA AP 7 software (http://mirametrics.com).

Moir, R. 1998, *Exp. Economics*, **1**, 87.

Schmidt, R. E. 2016, *Minor Planet Bull.*, **43**, 129.

Strope, R. J., Schaefer, B. E., and Henden, A. A. 2010, *Astron. J.*, **140**, 34.

Vanmunster, T. 2006, PERANSO period analysis software, version 2.60, CBA Belgium Observatory.

Vorontsov-Velyaminov, B. 1940, *Astrophys. J.*, **92**, 283.

The Reclassification of NSV 1586 from a Suspected Cepheid Star to a UG Class System

Stephen M. Brincat
Flarestar Observatory (MPC 171), Fl.5/B, George Tayar Street, San Gwann SGN 3160, Malta; stephenbrincat@gmail.com

Charles Galdies
Znith Observatory, Armonie, E. Bradford Street, Naxxar. NXR 2217, Malta; charles.galdies@um.edu.mt

Kevin Hills
Tacande Observatory, El Paso, La Palma, Spain; kevinhills@me.com

Winston Grech
Antares Observatory, 76/3 Kent Street, Fgura FGR 1555, Malta; wingrech@gmail.com

Received November 21, 2019; revised April 20, 2020; accepted April 21, 2020

Abstract On 2018 August 9, a contribution to the VSNET mailing list suggested that due to certain photometric attributes, NSV 1586 could possibly belong to the Dwarf Nova (DN) class. Hence, the initial classification of this star as a Cepheid variable star was put into question. This prompted the authors to investigate NSV 1586 in detail. The data obtained through our campaign suggest that the original classification of NSV 1586 as a Cepheid star is inconsistent with our findings. We determined the nature of NSV 1586 as a UG-type DN that exhibits peculiar photometric features in its light curve to possibly pertain to the UGZ/IW sub-type variable star classification. However, standstills that are indicative of this class remained undetected. The amplitude of this star was found to be of 2.9 magnitudes in the V-band, with a primary cycle period of 13.9 days. We found the color index during its cyclic permutations can range from an apparent CI of 0.5 to 1.0, corresponding to a temperature change of around 1300 K. Further research is suggested to determine the nature of this star.

1. Introduction

The star NSV 1586 was discovered as a variable star on photographic plates by C. Hoffmeister and its variable nature was announced in volume 289 of *Astronomische Nachrichten* (Hoffmeister 1966). NSV 1586 was initially designated as SON 8560 and was listed as a short-period variable, possibly belonging to the δ Cepheid class with a magnitude range of 15.5 to 16.5. No reference period was then quoted for this star. SON 8560 was included in the *New Catalogue of Suspected Variable Stars* (Kukarkin *et al.* 1982) and was designated as NSV 1586.

On 2018 August 9, a contribution by Taichi Kato to VSNET mailing list (2018) stated that data downloaded from the ASAS-SN Survey indicate that NSV 1586 could possibly be a Dwarf Nova (DN), as the star's color index is compliant with this class of objects and no definite period could be determined. Hence, the classification of this star as a Cepheid variable star was put into question.

This prompted the authors to investigate NSV 1586 in detail. An observational campaign was initiated by the authors through the observatories mentioned in Table 1. The data obtained through our campaign suggest that the original classification of NSV 1586 as a Cepheid star is also inconsistent with our findings. We determined the nature of NSV 1586 as a UG-type DN that exhibits peculiar photometric features in its light curve to possibly pertain to the UGZ/IW sub-type variable star classification. However, standstills that are indicative of this class remained undetected.

NSV 1586 is also designated as UCAC4 690-030039 and has been listed in a number of catalogues under other

Table 1. Equipment and observatories details.

Observatory	*Location*	*Observer*	*Telescope*	*Filter*	*CCD Sensor*	*Field-of-View (arcmin)*	*Binning (arcsec/pixel)*	*Pixel Scale*
Antares	Fgura, Malta	W. Grech	0.279-m SCT	C	SBIG STL-11000/ KAI-11000M	45.9×30.6	2×2	1.37
Flarestar	San Gwann, Malta	S. M. Brincat	0.254-m SCT	C	Moravian G2-1600/ KAF 1603ME	25.5×17.0	1×1	0.99
Tacande	La Palma, Spain	K. Hills	0.500-m Optimised Dall Kirkham	V	FLI ML3200/ KAF3200ME	35.7×24.1	1×1	0.98
Znith	Naxxar, Malta	C. Galdies	0.203-m SCT	C	Moravian G2-1600/ KAF 1603ME	30.0×20.0	1×1	1.17

Note: CCD cameras were operated at sensor temperature ranging from –20° to –15° C. All images were calibrated through dark frame and flat field subtraction.

designations. The GAIA DR2 catalogue (Gaia Collaboration *et al.* 2018) designated the star's unique source identifier as "2580466216051418888." The GAIA DR2 catalogue has listed this star at the following coordinates (2000.0): R.A. $04^h\ 24^m\ 17.9677655784^s$, Dec. +47° 52' 12.620239643" with a stellar effective temperature of 5628.54 K. The GAIA DR-2 lists the distance of this star as 573.564 pc with a higher and lower bound of confidence interval of 595.069 and 553.534 pc, respectively.

2. Observations

2.1. Multiband photometric data

Most of the photometric data during our campaign were acquired from the observatories listed in Table 1. Our dataset was supplemented by archival photometry gathered by the "All-Sky Automated Survey for Supernovae" (ASAS-SN; Kochanek *et al.* 2017) spanning the duration of our observations campaign. The ASAS-SN images utilized by this research were those taken through V and g-bands. An offset for g-band photometry was applied.

All photometric magnitudes were obtained through differential aperture photometry with zero-points calibrated to the APASS Catalog (Henden *et al.* 2016). Observations by ASASS-SN were usually taken in batches of two or three images in one night and they were repeated with intervals ranging from 1 to 5 days. There have been occasions where the interval period was longer due to unfavorable weather conditions.

In order to minimize scatter in our light curve, all of our images had a minimum exposure of 5 minutes to enable a good signal-to-noise ratio. In some cases when the star was observed to be at minimum, 10-minute exposures were utilized by Flarestar, Znith, and Antares Observatories. Tacande Observatory employed 5-minute exposures throughout our campaign and all of our observations were predominantly carried out under an airmass of less than two atmospheres. We utilized differential aperture photometry for all image analysis. The source of comparison stars (i.e. 000-BMT-664, 000-BMT-665, 000-BMT-666 extracted from AAVSO chart X23245AX) used were those supplied by the AAVSO Sequence Team. These comparison stars were used by all observatories involved except for the ASAS-SN data that may have made use of the same APASS source but possibly utilizing different comparison stars. Our monitoring campaign commenced on 2018 August 8 and was concluded on 2019 April 11, spanning a 246-day monitoring period as acquired from the observatories listed in Table 1.

2.2. Results

In order to investigate the behavior of NSV 1586, we commenced our research through the acquisition of the data from the ASAS-SN survey (Kochanek *et al.* 2017) that was taken prior to our campaign. Using PERANSO (v2.60) (Paunzen and Vanmunster 2016), we performed a period search on this data ranging from 2014 December 16 up to 2018 October 10. A total of 425 V-band observations derived from the ASASS-SN Survey were analyzed for any periodicity; however, no clear periodicity was obtained from this dataset using Lomb-Scargle, Fourier Analysis of light curves (FALC), Phase Dispersion Minimization (PDM), and Phase-binned Analysis of Variance algorithms. The light curve based on the ASAS-SN survey data is shown in Figure 1.

A total of 411 observations were acquired in the V-band from Tacande Observatory in addition to a small number of B-filtered observations in the Johnson system to obtain color photometry. A total of 101 V-band and 606 CV-band observations were gathered from Flarestar Observatory. Znith and Antares Observatories contributed 94 and 76 observations respectively through a C-filter reduced to a V standard. Heliocentric JD corrections have been applied to all observations. This observational campaign yielded a total of 1432 observations.

Observations acquired during our observation window (HJD 2458338 to 2458585) revealed that the star underwent several cycles during which the brightness varied from magnitude ~15.2 to ~18.1 mv. The light curve shown in Figure 2 illustrates our contributions along those gathered from the ASASSN survey to monitor the photometric activity of NSV 1586. During the initial period (i.e. HJD 2458338 to 2458385.4), we observed three cycles each with a period of 12.55 d, 13.8 d, and 11.0 d, and with a mean cycle of 12.45 d. Despite our expecting the next cycle to complete by reaching the minimum, the cycle did not materialize and the star remained brighter than 16.2 mv. The next "unsubdued" minimum occurred on HJD 2458461.41 at magnitude 17.67 mv, 30.12 d later. The next deep minimum was recorded on HJD 245488.44 at ~18.0 mv, 27.03 d after the previously-mentioned minimum. A short cycle of 10.80 d was then recorded after this minimum when the star declined in brightness down to magnitude 17.03 mv on HJD 2458499.24. Due to weather constraints, we could not maintain our previous coverage density. Notwithstanding this, we managed to record two additional short cycles that started on HJD 2458530.27 and HJD 2458543.28, with a quasi-periodic duration of 13.01 d and 12.97 d, respectively.

The light curve morphology of V513 Cassiopeiae (Figure 3) produced by Stubbings and Simonsen (2016) shows similarities to those observed following our observational campaign. Hence, it seems plausible that NSV 1586 belongs to the UGZ/IW class. However, the peaks of super outbursts are not readily apparent in our light curve and therefore we could not be certain that this star belongs to the UGZ/IW class.

A period analysis using the ANOVA, Lomb-Scargle (Lomb 1976; Scargle 1982), and PDM methods (PERANSO) of the lightcurve in Figure 2 yielded two combined cycle periods; PI of 13.94 ± 0.19 d and PII of 11.50 ± 0.15 d. The resultant Lomb-Scargle period spectrum (periodogram) is shown in Figure 4. The main cycle period identified for NSV 1586 is 13.9 d (± 0.2) with a secondary period of 11.5 d (± 0.2).

In order to evaluate the nature of NSV 1586, histogram analysis based on 1-day binned data was carried out and showed a distribution of the magnitude regime consistent with the UGZ/IW class.

An investigation for the presence of periodic humps was also carried-out over four nights through high cadence data (5 or 6 minutes) when the star was near maximum light. Using PERANSO software, a search was made from 0.1 to 25 cycles per day during which no significant peak was detected when using the Lomb-Scargle algorithm. The Phase Dispersion

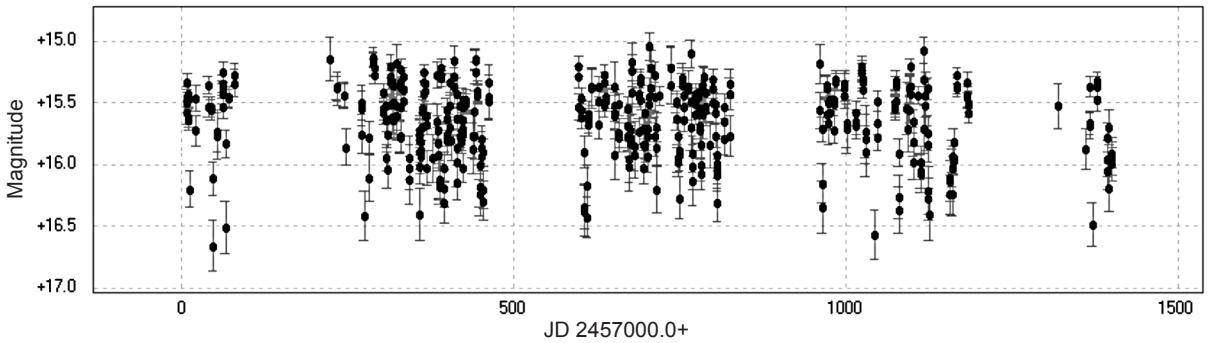

Figure 1. V-band data derived from the ASAS-SN Survey for the period 2014 December 16 to 2018 October 14.

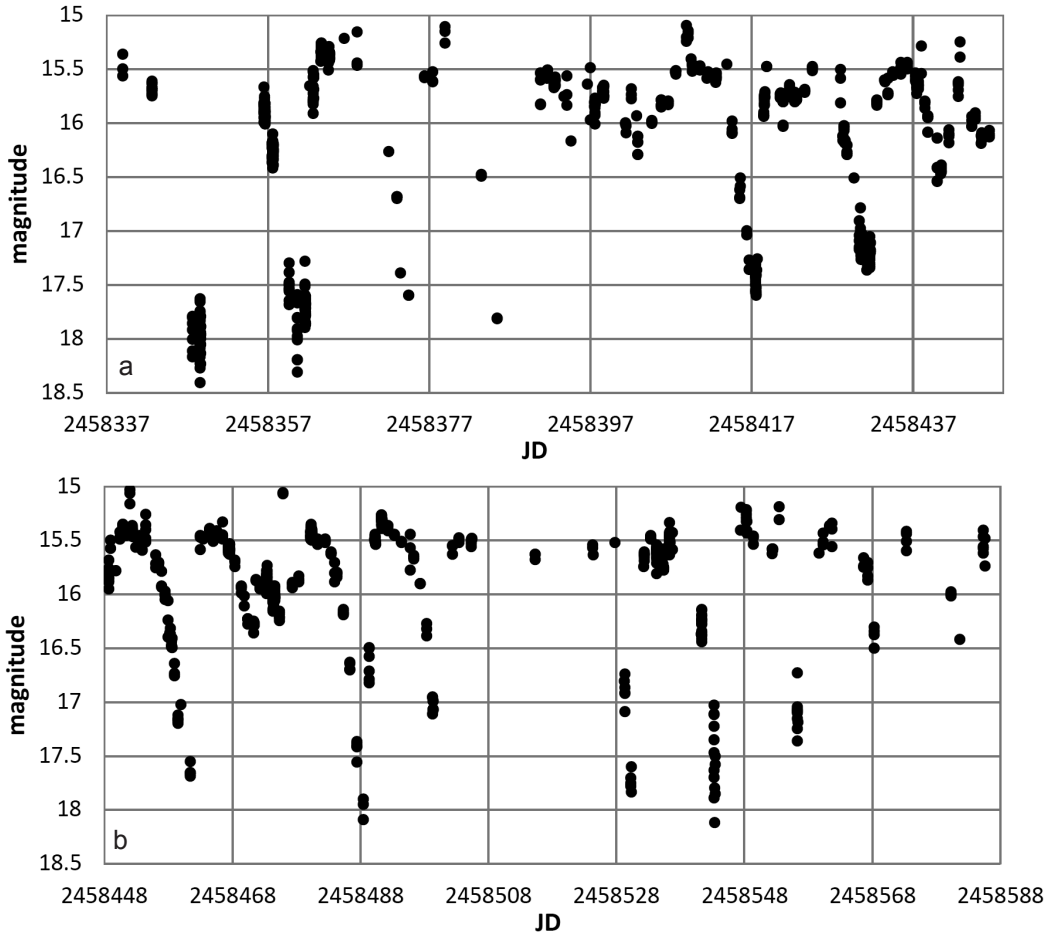

Figure 2. NSV 1586 light curve in two panels showing the light changes in V-band during the observational campaign ranging from HJD 2458338 to HJD 2458585, spanning a period of 247 days.

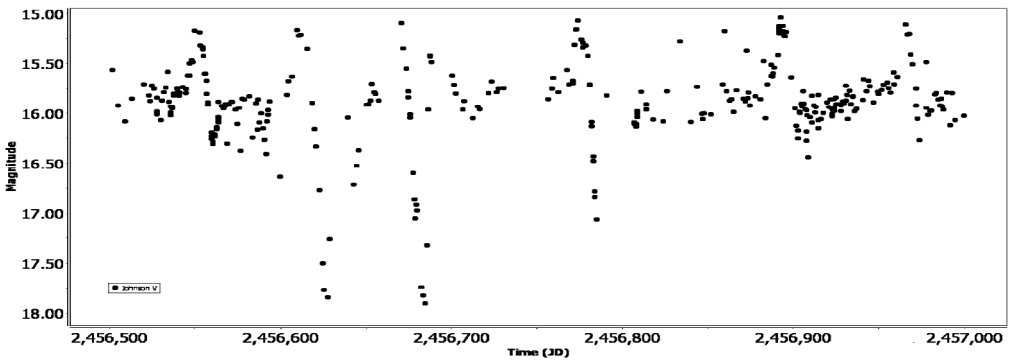

Figure 3. The AAVSO light curve of V513 Cas spanning from JD 2456500–2457000 (July 2013–December 2014) (from Stubbings and Simonsen (2016)).

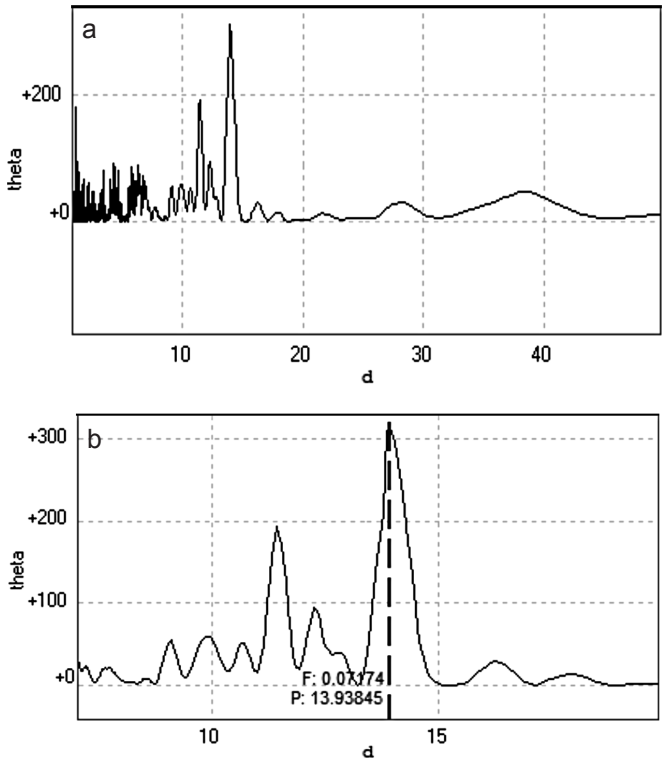

Figure 4. Lomb-Scargle periodogram of NSV 1586 showing the primary cycle of 13.94 d and a secondary cycle of 141.46 d. Figure (a) shows the periodogram ranging from 0 to 50 days. Figure (b) shows a zoomed part of Figure (a) centered on the primary cycle (F = cycles/day, 0.07).

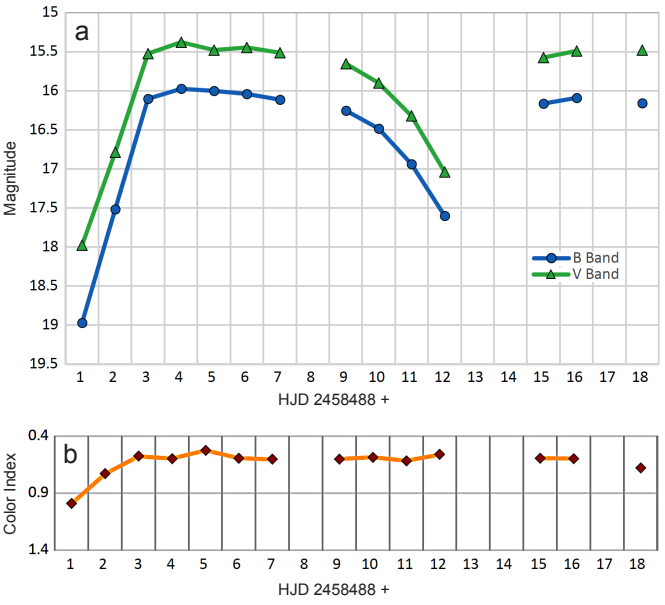

Figure 5. B, V light curves (a) and color evolutions (b). Blue (circles) and green (triangles) symbols represent B and V, respectively. Red (diamonds) symbols represent the color index B–V.

Minimization (PDM) and ANOVA algorithms yielded identical results.

An additional verification analysis was carried out during February and March 2020, to ascertain any stochastic behavior during different phases of NSV 1586 (N = 403). However, orbital brightness variations remained undetected. Instead stochastic brightness variations (flickering) were noted that are characteristic of many cataclysmic variable stars (Bruch 2000). These variations were observed down to a cadence of 90 seconds with amplitudes ranging from 0.02 to 0.2 magnitude. Results acquired through the 0.5-m telescope at La Palma from Tacande Observatory during quiescence showed stochastic variations up to 0.7 magnitude.

2.3. Color photometry

During the period from 2019 January 4 to January 23, we have obtained color photometry from Tacande Observatory (Table 1). This period coincided with an interval when NSV 1586 was at quiescence and rose to maximum light. We have obtained photometric measurements through B and V bands. In most cases, we acquired multiple readings per night that were averaged to improve precision and reduce any scatter in our data.

Figure 5a–b shows the light curve of a cycle from minimum light that started from HJD 2458488.442 (at magnitudes 18.96 and 17.97 for B and V bands, respectively) to maximum light that occurred on HJD 2458491.391 at B magnitude 15.97 and V magnitude 15.38.

Our Color Index (CI) results obtained through B–V bands indicate that at quiescence the light from the star system emits most of its light with an apparent CI of 1.0. Four days after an outburst was recorded, the CI decreased to 0.5 d, suggesting an increase in temperature. From the 9th day post-quiescence, the star started to decline in brightness but despite this, CI readings showed that the system's B–V radiative output remained somewhat constant. It is important to note that these CI readings did not include compensation for galactic dust extinction as we have observed some inconsistences with estimates of dust concentrations in this region.

Using the methods applied by Flower (1996) and Torres (2010), we obtained an observed CI temperature difference between the quiescent and outburst phases of 4867 K and 6182 K, respectively. Hence, our observations suggest a temperature change of the combined light output by the system of around 1300 K.

Upon examination of the morphology of our light curve, we deduce that NSV 1586 exhibits a puzzling light curve and it is difficult to classify the variable with any degree of certainty. From the evidence gathered above, we believe that the star belongs to the UG type of cataclysmic variables. Although we observed similarities to the UGZ/IW systems, further observations are needed to determine its sub-class, especially in the light that no clear standstill periods have been found throughout the period of this study including the period monitored by the ASSAS-SN survey, where observations go back to 2014 December 16 (HJD 2457007).

The absence of brighter and longer superoutbursts indicates that this is not an SU UMa type star. The damping oscillations

observed at maximum light are possibly similar to those observed by Kato (2018) for other CV systems that may be due to giant flares occurring near the secondary star surface. However, in this case, more data are needed to confirm such hypothesis. The dampening phenomenon has further complicated matters as any "intrinsic" signal by this system may have been hidden by such oscillations.

In consideration of the above, it is suggested that more research is needed to unravel this intriguing star. Further spectroscopic analysis may reveal the underlying mechanisms that drive the photometric variation exhibited by NSV 1586.

3. Conclusions

We report that the original classification of NSV 1586 in the General Catalogue of Variable Stars (GCVS; Kukarkin *et al.* 1982) is inconsistent with our findings and suggest that this star is likely to be a UG class system. Over the course of its observational campaign, NSV 1586 did not yield any photometric behavior that is consistent with the former classification. The amplitude of this star was found to be of 2.9 magnitudes in the V-band, with a primary cycle period of 13.9 days and a secondary period of 11.5 d. We found that the color index during its cyclic permutations can range from an apparent CI of 0.5 to 1.0, corresponding to a temperature change of around 1300 K. No orbital variations were detected by this study. Further research is suggested, including spectroscopic analysis.

4. Acknowledgements

We acknowledge with special thanks the guidance provided by Sebastián Otero of the AAVSO in the analysis of our data and for providing a way forward in the publication of this manuscript. We are also grateful to Paul Layland for helping us in this analysis.

This research has made use of the AAVSO Photometric All-Sky Survey (APASS), funded by the Robert Martin Ayers Sciences Fund and NSF AST-1412587.

References

Bruch, A. 2000, *Astron. Astrophys.*, **359**, 998.

Flower, P. J. 1996, *Astrophys. J.*, **469**, 355.

Gaia Collaboration, *et al.* 2018, *Astron. Astrophys.*, **616A**, 1.

Henden, A. A., Templeton, M., Terrell, D., Smith, T. C., Levine, S., and Welch, D. 2016, VizieR Online Data Catalog: AAVSO Photometric All Sky Survey (APASS) DR9, II/336.

Hoffmeister, C. 1966, *Astron. Nachr.*, **289**, 139.

Kato, T. 2018, arXiv:1811.05038.

Kochanek, C. S., *et al.* 2017, *Publ. Astron. Soc. Pacific*, **129**, 104502.

Kukarkin, B. V., *et al.* 1982, *New Catalogue of Suspected Variable Stars*, Nauka, Moscow.

Lomb, N. R. 1976, *Astrophys. Space Sci.*, **39**, 447.

Paunzen, E., and Vanmunster, T. 2016, *Astron. Nachr.*, **337**, 239.

Scargle, J. D. 1982, *Astrophys. J.*, **263**, 835.

Stubbings, R., and Simonsen, M. 2016, *J. Amer. Assoc. Var. Star Obs.*, **44**, 128.

Torres, G. 2010, *Astron. J.*, **140**, 1158.

VSNET. 2018, VSNET Online Mailing List, Department of Astronomy, Kyoto University (http://www.kusastro.kyoto-u.ac.jp/vsnet).

Disk Instabilities Caused the 2018 Outburst of AG Draconis

Helena M. Richie
W. M. Wood-Vasey
Lou Coban
Physics and Astronomy Department, University of Pittsburgh, 3941 O'Hara Street, Pittsburgh, PA 15260; her45@pitt.edu; wmwv@pitt.edu; coban@pitt.edu

Received November 27, 2019; revised May 14, 2020; accepted May 14, 2020

Abstract The symbiotic binary AG Draconis (AG Dra) has a well-established outburst behavior based on an extensive observational history. Usually, the system undergoes a 9- to 15-year period of quiescence with a constant average energy emitted, during which the system's orbital period of ~550 d can be seen at shorter wavelengths (particularly in the U-band) as well as a shorter period of ~355 d thought to be due to pulsations of the cool component. After a quiescent period, the marker of an active period is usually a major (cool) outburst of up to V = 8.4 mag, followed by a series of minor (hot) outbursts repeating at a period of approximately 1 year. However, in 2016 April after a 9-year period of quiescence, AG Dra exhibited unusual behavior: it began an active phase with a minor outburst followed by two more minor outbursts repeating at an interval of ~1 year. We present R-band observations of AG Dra's 2018 April minor outburst and an analysis of the outburst mechanism and reports on the system's activity levels following the time of its next expected outburst. By considering the brightening and cooling times, the scale of the outburst, and its temperature evolution we have determined that this outburst was of disk instability in nature.

1. Background

1.1. Symbiotics

Symbiotic binary systems, also known as symbiotics, are a type of cataclysmic variable star (CV) that consist of an interacting cool giant star and a hot compact object, most commonly a white dwarf (WD). Interaction between the cool and hot component results from an outflow of matter from the cool component that accretes onto the hot component. Matter outflow can be due to stellar wind off of the cool component or the cool component overfilling its Roche-lobe. In many cases, the rate of mass loss off of the cool component can be sufficient to fuel hydrogen burning in a thermonuclear shell around the hot component (Sokoloski *et al.* 2006 and references therein). As a result of mass outflow, symbiotics often exist inside of a gas cloud that can be fully or partially ionized by the hot component (Kenyon 1986).

Symbiotics undergo periods of quiescence and activity, driven by the state of equilibrium between mass outflow, accretion, and ionization of the gas cloud. In quiescence, symbiotics emit energy at a constant average rate. During an active phase where this equilibrium is disturbed, symbiotics can be observed to undergo outbursts that feature an optical brightening of the system by 2 to 3 magnitudes with amplitude decreasing at longer wavelengths (Skopal and Baludanský 2003). This classical symbiotic outburst (or classical novae) is the most common type of outburst and commonly recurs on timescales of a decade (Kenyon 1986). The driving mechanism behind a classical symbiotic outburst is the shedding of material off of the cool component onto the hot component as it overfills its Roche lobe, triggering thermonuclear runaway in a shell on the surface of the hot component. Another common type of outburst observed in CV systems containing red dwarfs (as opposed to giants) is the dwarf nova, which is driven by instability in accretion disks surrounding the WD that causes an increase in mass flow through the disk, resulting in temporary heating and brightening. These types of outbursts necessarily have smaller peak magnitudes and timescales than those observed in classical symbiotic outbursts.

Though these mechanisms are reasonable explanations of some outbursts observed in symbiotics, there are many outbursts that have been observed that, due to their the scales and recurrence times, cannot be explained by these mechanisms alone (Kenyon 1986; Mikolajewska *et al.* 1995; Sion *et al.* 1979). To this end, Sokoloski *et al.* (2006) proposed a *combination nova* model to describe outbursts in symbiotics that exhibit qualities of both classical symbiotic outbursts and dwarf novae. This model suggests that outbursts in symbiotics are due to enhanced thermonuclear burning with disk instability as a trigger event. This model can account for the peak luminosities and short recurrence times of outbursts seen in many symbiotics, particularly for Z Andromedae, as described in Sokoloski *et al.* (2006).

On a larger scale, studying symbiotics is important in the context of their being a possible progenitor of Type Ia supernovae. As such, we would like to understand the true nature of these outbursts in order to predict their activity patterns. For most symbiotics, we have not been able to observe state transitions from quiescence to activity due to their irregular outburst behavior. An interesting exception is the system known as AG Draconis (AG Dra). This symbiotic has cyclical activity patterns, making it possible to predict and observe its state transitions.

1.2. AG Draconis

AG Dra is one of the best-studied symbiotics, with observations spanning the last century. Like most symbiotics, AG Dra has been observed to alternate between phases of quiescence and activity, undergoing a series of outbursts during its active phases. According to González-Riestra *et al.* (1999), such outbursts can be of both hot and cool type. Cool outbursts are caused by the expansion of the hot component's pseudo-atmosphere and a subsequent drop in WD temperature,

which can be seen as an anticorrelation between optical/UV and X-ray emission. Hot outbursts occur when the WD's radius remains fixed and its temperature increases or remains the same. Outbursts of this nature show consistencies with disk instability-driven dwarf novae outbursts, as well as with the Sokoloski *et al.* (2006) combination nova model where the thermonuclear burning pseudo-atmosphere of the WD expands after exceeding a threshold accretion rate triggered by disk instabilities. Evidence of the existence of an accretion disk surrounding the WD has recently been provided in a study done by Lee *et al.* (2019). Over the course of its observation, certain periods have been discovered that characterize the system's orbital motion and outburst behavior. With its semi-regular state transitions, AG Dra is a useful subject to study in order to characterize the mechanisms of symbiotic outbursts that are generally unclear.

The system consists of a K3 III red giant (Kenyon and Fernandez-Castro 1987) and white dwarf that are 1.5 $M_\odot$ and 0.4–0.6 $M_\odot$ (Mikolajewska *et al.* 1995), respectively. The hot component has a luminosity of ~10^3 $L_\odot$ and a temperature of ~80–150 × 10^3 K (Mikolajewska *et al.* 1995). The components have been observed to be at an orbital separation of 400 $R_\odot$ (Garcia 1986) and are enveloped in a partially ionized circumbinary nebula (Mikolajewska *et al.* 1995). Lee *et al.* (2019) showed that the upper limit in accretion disk size is 0.3 au or ~65 $R_\odot$. Radio observations of emission from the circumbinary nebula give a rate of mass loss of 10^{-7} $M_\odot$ yr^{-1} (Mikolajewska *et al.* 1995). There is also evidence of thermonuclear shell burning on the WD's surface at a rate of 3.2×10^{-8} $M_\odot$ yr^{-1} (González-Riestra *et al.* 1999). From a study of the historical UBV light curve of AG Dra done by Hric *et al.* (2014), the time between active periods has been observed to be anywhere from 12 to 16 years. Additionally, two periods for the system have been clearly established: an orbital period of ~550 d and a period of ~355 d thought to be a result of pulsations of the cool component (Galis *et al.* 1999). AG Dra's orbital period becomes prominent at shorter wavelengths, showing itself most clearly in the U-band during quiescence. Its pulsation period can be seen during both quiescent and active phases and is most visible in B and V-bands (Galis *et al.* 2016).

In its observed active phases, AG Dra exhibits outbursts with consistent peak magnitudes, but irregular multitudes and shapes. They are spaced anywhere from 359 to 375 days (Galis *et al.* 2015). Normally, after an extended period of quiescence at V = 9.8 mag, AG Dra begins its active phases with a major cool outburst with peak magnitude of about B = 8.8 mag and V = 8.4 mag (Galis *et al.* 2017), followed by a series of minor hot outbursts. It has not been confirmed, but the combination nova outburst model seems like a promising explanation of the underlying mechanism for a number of these outbursts. However, in May of 2015 AG Dra exhibited very unusual behavior as it entered its most recent active phase. The activity began with a minor outburst with peak magnitude of V = 9.6 mag, followed (at the usual cadence of ~360 d) by two more minor outbursts with peak magnitude of B = 9.1 mag and V = 9.6 mag (Galis *et al.* 2017). This study showed that during these minor outbursts the system exhibited signs of both hot and cool type outbursts by examining the equivalent widths of certain emission lines and observing the disappearance of the Raman scattered O VI lines, respectively. In early April of 2018, AG Dra began its fourth minor outburst of its 2015–2018 active phase. The Survey of Transiting Extrasolar Planets at the University of Pittsburgh (STEPUP) has monitored this outburst by conducting R-band photometric observations to examine an understudied band-pass of the system's outbursts. With these measurements, we seek to characterize the nature of AG Dra's most recent outburst.

2. STEPUP

STEPUP (http://pitt.edu/~stepup/) has used the Meade Instruments f/8, 16" RCX400 Keeler Telescope at the Allegheny Observatory in Pittsburgh, Pennsylvania, to conduct photometric observations of a variety of objects since its inception in 2009 (Good 2011). The main camera is a Santa Barbara Instruments Group (SBIG) STL-6303e and the field of view is 29.2 arcminutes by 19.5 arcminutes. Founded by Melanie Good, STEPUP's original mission was to discover and study new transiting exoplanets and has recently expanded its reach to observing variable stars. STEPUP records their data and processes them with an image analysis program, STEPUP Image Analysis (SIA) (https://github.com/mwvgroup/STEPUP_image_analysis), written in the PYTHON programing language by lead undergraduate, Helena Richie. SIA is responsible for removing instrument signatures from STEPUP's data, generating WCS information for each file, and performing differential aperture photometry to generate a light curve of the target object. SIA uses the ASTROPY PYTHON package (Astropy Collaboration 2018) throughout the routine as well as the WCSTOOLS (Mink 1997) software package and Astrometry.net (Lang *et al.* 2010) in the process of plate-solving the images. STEPUP has contributed to several publications (Shporer *et al.* 2010; Fleming *et al.* 2012) on exoplanet transit timing variations and discovery.

3. Observations

To monitor AG Dra's outburst behavior, STEPUP began conducting observations of the system in late 2018 April and continued through 2018 July using the Cousins R filter. Observations were made using a variety of exposure times ranging from 5 to 30 seconds. We removed saturated data points using a square aperture centered around each target, check, and comparison star to ensure that no pixels had met or exceeded the expected saturation level. If a pixel in the aperture met or exceeded this level, the data point corresponding to the image containing the object was removed from analysis. Subsequent observations had shortened exposure times (15 s and 5 s) to avoid saturation. All data were recorded in the FITS file format (Wells *et al.* 1981) and processed by SIA. These results can be seen in Table 1. The full table is available through the AAVSO ftp site at ftp://ftp.aavso.org/public/datasets/richie481-sia-agdra-output.txt (if necessary, copy and paste link into the address bar of a web browser). In addition to our own photometric measurements, we included observations from the AAVSO International Database (AID; Kafka 2020) in our analysis.

Table 1. Sample first ten data points of SIA output for STEPUP AG Dra observations.

Date	*Date (JD)*	*Exp Time (s)*	*Target R (mag)*	*Uncertainty (mag)*	*Filter*	*Check Label*	*Check R (mag)*	*Airmass*
2018-04-30	2458239.611990740	30	8.5960	0.0008672	R	345	11.8312	1.3478
2018-04-30	2458239.616747690	30	8.5818	0.0008344	R	345	11.6420	1.3338
2018-04-30	2458239.623541670	30	8.5725	0.0008411	R	345	11.6270	1.3148
2018-04-30	2458239.624884260	30	8.5966	0.0008593	R	345	11.6529	1.3111
2018-04-30	2458239.625578700	30	8.5749	0.0008360	R	345	11.6265	1.3093
2018-04-30	2458239.626250000	30	8.5678	0.0008362	R	345	11.6211	1.3075
2018-04-30	2458239.627615740	30	8.5854	0.0008440	R	345	11.6348	1.3038
2018-04-30	2458239.628287040	30	8.5789	0.0008348	R	345	11.6345	1.3020
2018-04-30	2458239.629641200	30	8.5690	0.0008288	R	345	11.6299	1.2985
2018-04-30	2458239.630324070	30	8.5812	0.0008463	R	345	11.6208	1.2968

Note: First ten data points from STEPUP's observations of AG Dra's 2018 outburst. The full table is available through the AAVSO ftp site at ftp://ftp.aavso.org/public/datasets/richie481-sia-agdra-output.txt (if necessary, copy and paste link into the address bar of a web browser).

Table 2. Comparison stars used to process AG Dra data.

AUID	*Label*	*R.A. h m s*	*Dec. ° ‘ “*	*R (mag)*
000-BCY-347	129	16 00 08.77	66 49 20.0	12.555
000-BCY-346	123	16 00 24.08	66 49 29.6	11.980
000-BJS-730	111	16 02 54.40	66 41 33.9	10.708
000-BCY-344	119	16 00 11.22	66 39 14.2	11.575
000-BCY-348	132	16 01 08.41	66 55 21.4	12.900

Note: Comparison stars used for photometric analysis of AG Dra data. These stars were given by the AAVSO Variable Star Plotter Photometry Table with VSP code X24880AIL.

Table 3. Observations of AG Dra by STEPUP.

Date	*ExpTime (s)*	*R (mag)*	*Uncertainty (mag)*
2018-04-30	30	8.5762	0.0008
2018-05-01	30	8.4682	0.0008
2018-05-23	30	8.7039	0.0009
2018-05-24	15	8.7393	0.0018
2018-06-14	15	8.7904	0.0013
2018-06-28	5	8.8538	0.0023
2018-07-08	10	8.7884	0.0015
2018-07-12	10	8.8002	0.0016

Note: Median magnitudes of AG Dra for each night of observation by STEPUP. An outburst depth of $\Delta R = 0.518 \pm 0.011$ mag was observed using STEPUP and AAVSO measurements over a period of 161 d.

4. Image processing

We used our STEPUP Image Analysis code to process the photometric data taken by STEPUP of the 2018 outburst of AG Dra. SIA works in three main steps: (1) instrument signature removal (ISR); (2) astrometric calibration (ASTROM); and (3) differential photometry (PHOT). As input, SIA takes raw science images in the FITS file format, three types of calibration images, a plate-solved science image (generated by Astrometry.net (Lang *et al.* 2010)), and an input file that includes coordinates of the target, check, and comparison stars and the magnitudes of the comparison stars. We list the comparison stars used for AG Dra's analysis in Table 2 given by the AAVSO Variable Star Plotter tool. All three steps of SIA were performed to process the AG Dra data and are summarized as follows.

For ISR, SIA writes a data set of files that have been corrected for dead pixel columns, uneven CCD illumination, and thermal noise using flat, bias, and dark calibration images. To generate master calibration files, SIA takes the median across the image set of each pixel for the dark and bias. For the master flat, the array is normalized with respect to the center region of the image that is evenly illuminated. The raw science images have the master bias and dark subtracted from them and are divided by the flat. The result is an instrument-signature-removed data set.

In the next step, ASTROM, SIA takes the instrument signature removed files generated by ISR and a plate-solved image generated by Astrometry.net to write a set of files with the WCS FITS header keywords of the plate-solved image to the headers of the rest of the dataset. Then, SIA uses the WCSTools software package (Mink 1997) to adjust this information to accurately represent the coordinates of each pixel in each individual file. The result is a dataset with instrument signature-removed, plate-solved images.

The final step of SIA is to perform differential aperture photometry. This places apertures at the positions of the target, check, and several comparison stars to get the sum of counts in the aperture for each object in every image of the dataset. A background rate per square pixel (s_{bkgd}) for the region of the image is determined by placing an annulus around the aperture and dividing its count sum by its area. The aperture and annulus sizes are as follows: $r_{aper} = 4$ arcsec, $r_{in} = 25$ arcsec, and $r_{out} = 27$ arcsec. Subtracting the product of s_{bkgd} and the area of the aperture (A_{aper}) from the aperture sum gives the net counts of the object. A 2D-Gaussian fit is applied for aperture centroiding. This process is used to get the net counts for all objects of interest in each image. The uncertainty in net counts for an object is given by

$$N = \sqrt{S_* + s_{bkgd} A_{aper}} \quad (1)$$

where S_* is the net count value in the aperture around the object.

The net count values are then calibrated to magnitudes using the relation,

$$m_* = m_c - 2.5 \log_{10}\left(\frac{S_*}{S_c}\right), \quad (2)$$

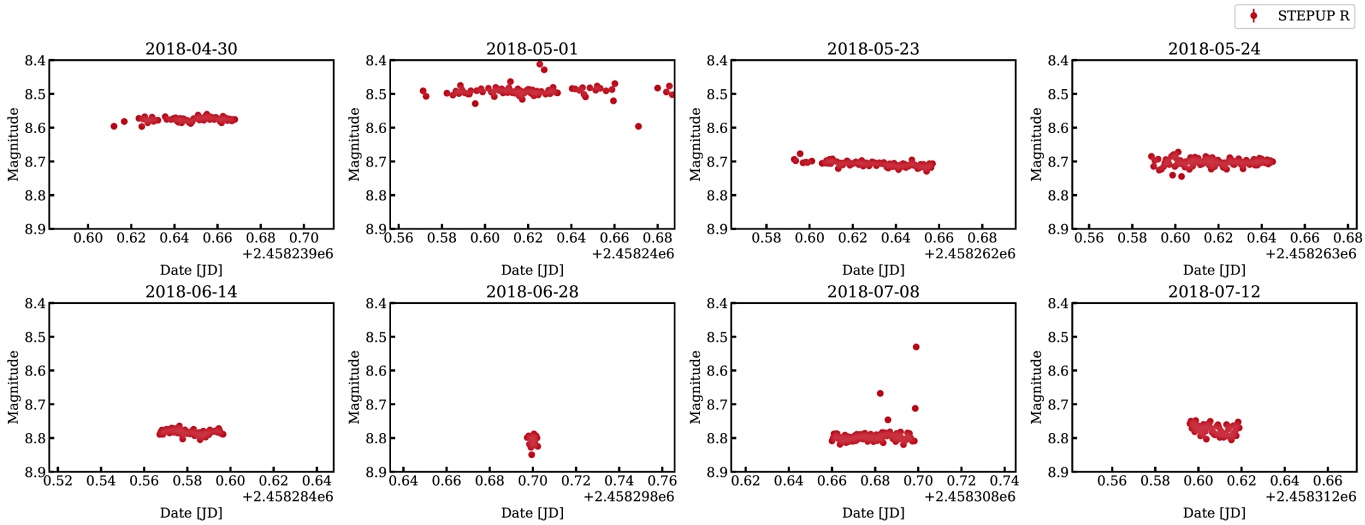

Figure 1. STEPUP R observations of AG Dra 2018 outburst. Figures are shown on a 0.13183 d = 3.1639 h timescale. These observations show no obvious variation in brightness and thus put a lower limit on the brightening timescale of AG Dra during outburst.

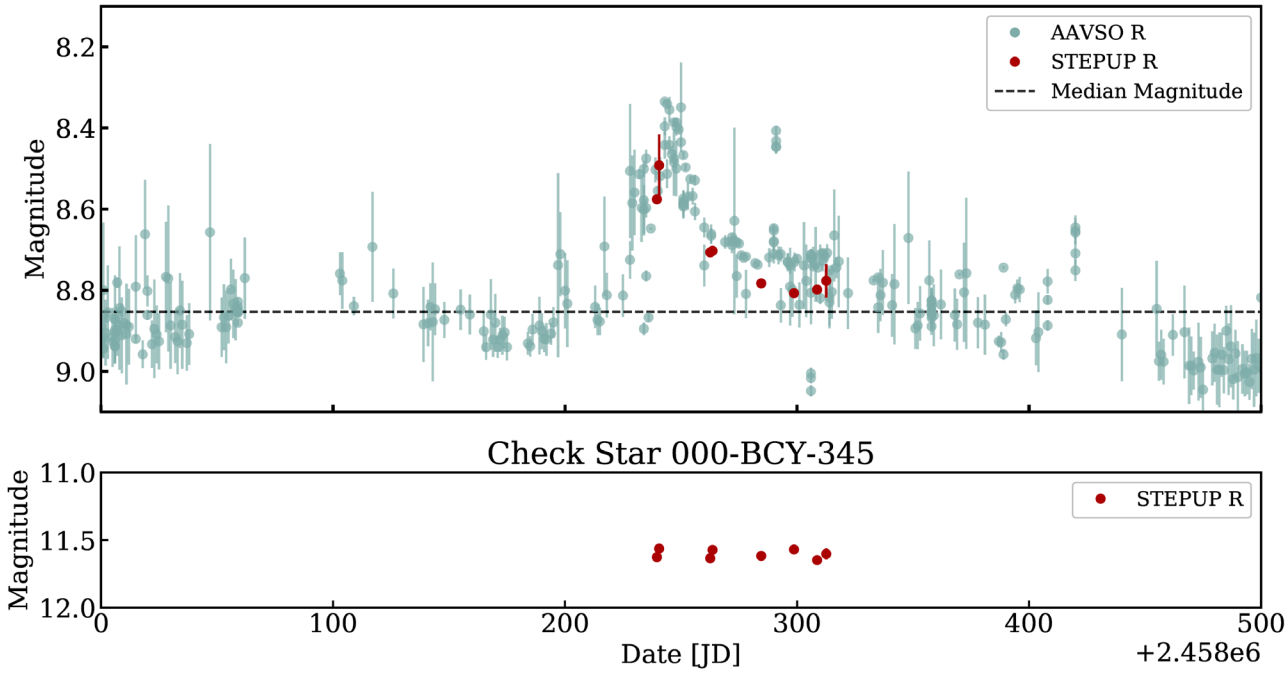

Figure 2. (Top) 2018 outburst of AG Dra shown by AAVSO and STEPUP R-band measurements. The system has an orbital period of T_{orbit} = 549.73 d and the cool component has a pulsation period of T_{pulse} = 355.27 d (Galis *et al.* 1999), which are visible during quiescence. (Bottom) Light curve of check star 000-BCY-345.

where m_* and S_* are the magnitude and counts of the target star, respectively, and for the comparison star the same values given by m_c and S_c. SIA outputs a light curve of the target and check star as well as output files giving magnitude values and net count values for both objects, as well as unscaled light curves of comparison stars and a summary of aperture position corrections.

5. Analysis

We used data collected by STEPUP as well as R-band and V-band observations available from the AID to analyze AG Dra's 2018 outburst behavior. SIA was used to analyze each night of STEPUP data on the outburst and, assuming a Gaussian distribution, the median of observed magnitudes was taken to be the system's magnitude for a given night. The measurements for all eight nights of observation can be seen in Table 3 and a plot of STEPUP's measurements in Figure1. We took the uncertainty in each night's magnitude, σ_i to be the standard error of the data set,

$$\sigma_i = \frac{\sigma_i}{\sqrt{n}}, \quad (3)$$

where σ is the sample standard deviation from the median, and n is the total number of data points. The light curve of the outburst including AAVSO and STEPUP data can be seen in Figure 2.

We included AAVSO data to analyze the outburst depth and start and end date. The AID points used in our analysis are the median of all R-band observations in bins of 1 day.

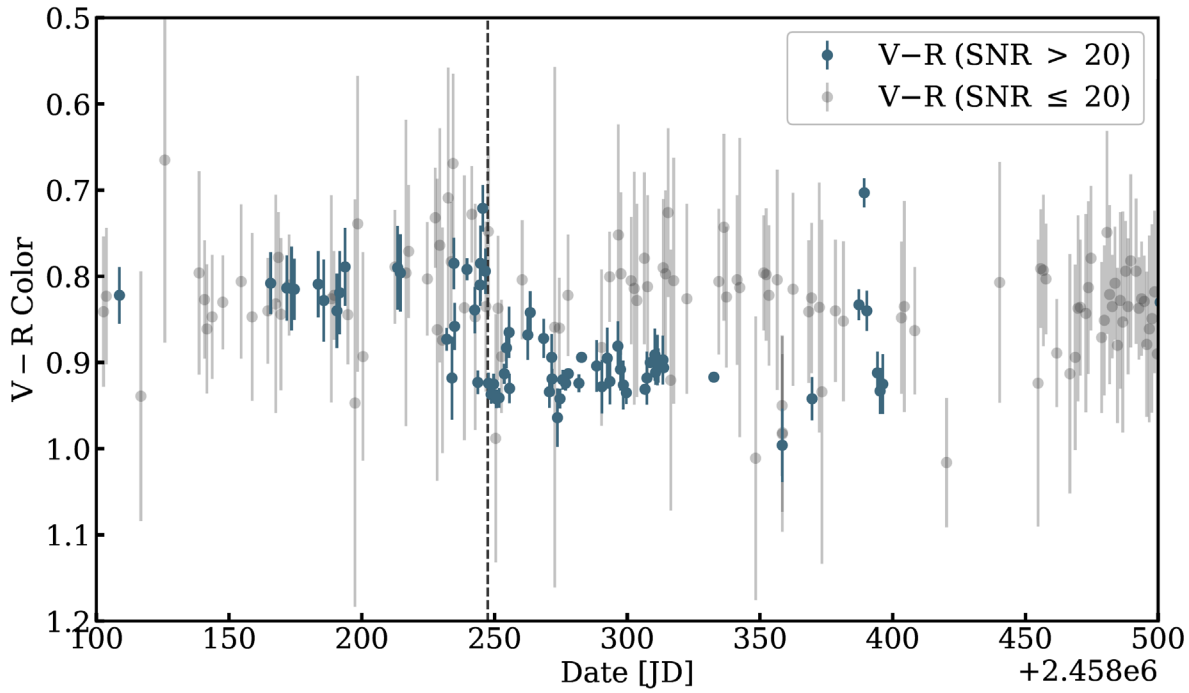

Figure 3. Color evolution of AG Dra's 2018 outburst. The system's behavior exhibits chromaticity of amplitude V−R = 0.112 ± 0.015 mag. A slight increase in temperature can be seen leading up to the outburst's peak followed by a larger reddening as the system returns to quiescence.

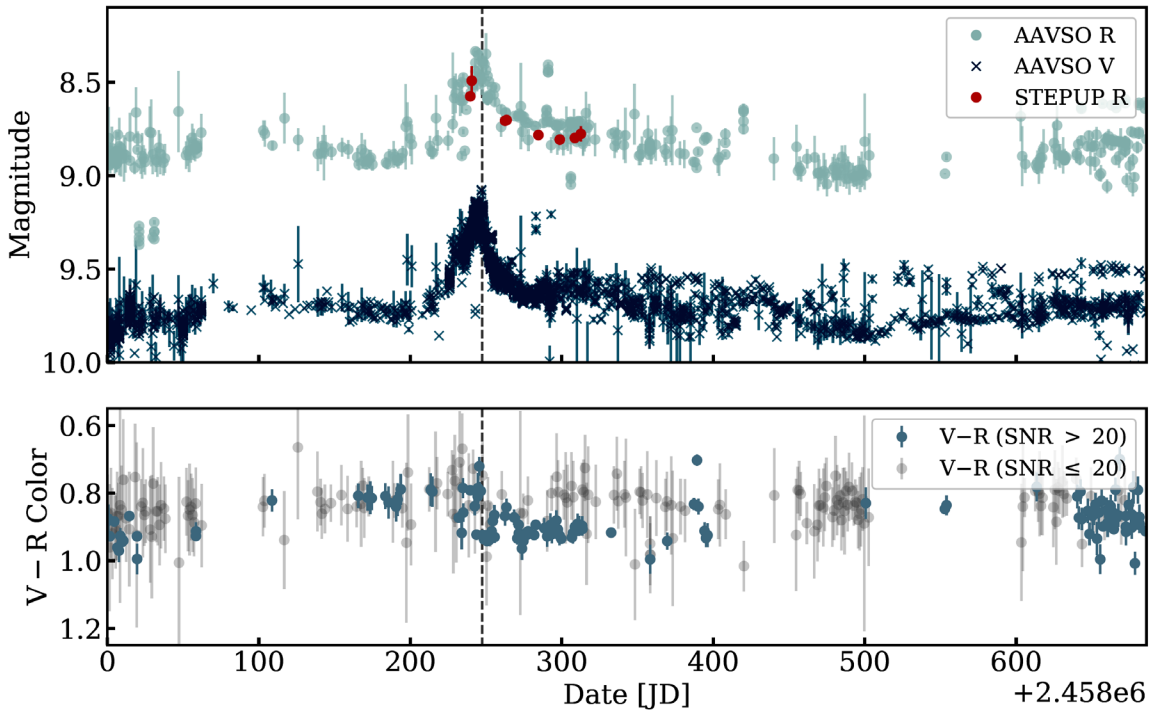

Figure 4. 2018 outburst of AG Dra shown by STEPUP R-band and AAVSO R and V-band measurements. This shows all measurements available in the AID, instead of the median 1-day binned data as used in the analysis described in section 5. The R-band amplitude of the outburst was observed to be ΔR = 0.518 ± 0.011 mag and the V-band amplitude was observed to be ΔV = 0.781 ± 0.003 mag. Below this is the V−R light curve over the course of the outburst, showing an amplitude of 0.100 mag as the system returns to quiescence. The vertical dashed line marks the peak of the outburst, which occurred on JD 2458247.448.

We took the quiescence value of AG Dra to be the median of these resulting magnitudes, giving a value of R = 8.853 mag. Using this value as a threshold to distinguish between in-outburst and out-of-outburst data points, the outburst start and end dates are JD 2458190 and JD 2458351, respectively, giving an outburst duration of 161 d. Taking the difference of the minimum and maximum magnitude values during this period, we found an outburst depth of $\Delta R = 0.518 \pm 0.011$ mag. Figure 4 presents the full outburst with AAVSO V and R observations as well as STEPUP R observations.

To determine the nature of the outburst, we next performed a color analysis of AG Dra's 2018 outburst. All STEPUP R and AAVSO V and R observations were used to give V – R color during the outburst period. To get a higher-resolution light curve, instead of using 1-day bins as was used in the R-band analysis, we divided the light curves into intervals of 0.3 d (~7.2 h) where the median of all points in each interval was taken to be the value of that interval's magnitude. Each value's associated uncertainty was propagated to give the uncertainty in each interval's magnitude. Then, the color light curve and its uncertainty values were determined by subtracting the values in each band for each interval and propagating their uncertainties. To determine the amplitude of the color light curve, all points in the outburst interval with SNR > 20 were considered. By taking the difference in the median of the pre-outburst values and the post-outburst values we found a color of $V - R = 0.112 \pm 0.015$ mag. This result can be seen in Figure 3.

6. Results

The AG Draconis system was observed by STEPUP and AAVSO observers to outburst by $\Delta R = 0.518$ mag over the course of 161 d, lasting from JD 2458190 until JD 2458351. The outburst peaked in the R-band on JD 2458242.749 and in the V-band on JD 2458247.448. This outburst exhibited color change of V – R = 0.112 mag. This color change coincided with the V-band outburst's peak, so we will take JD 2458247.448 to be the date of the outburst's peak. The V-band depth of this outburst is similar to that of previous minor outbursts of AG Dra, such as the system's 2016 outburst that peaked at around V = 9.1 mag. Galis *et al.* (2017) studied this outburst by examining the system's equivalent widths of certain emission lines and the disappearance of the Raman scattered O VI lines. This study shows evidence of the outburst being of both hot and cool type. Our analysis of AG Dra's 2018 outburst may suggest a similar temperature evolution, with the primary feature being a large reddening (and potentially a drop in temperature) following the outburst's peak, as shown in Figure 4. Additionally, before AG Dra began descending back to quiescence, a slightly bluer V – R color can be seen as the system approaches its peak outburst value.

There are three main pieces of evidence that suggest that this outburst was a disk instability: (1) the sharp increase in brightness followed by a longer descent to quiescence; (2) the scale of the outburst; and (3) the color evolution of the event. The system rose to outburst in 55.1 d. After a small amount of brightening for the first ~20 days of the outburst, the system began to rapidly brighten, with its magnitude increasing linearly at a rate of V = –0.018 mag per day. A constraint on the timescale of this brightening can be seen in Figure 1, which shows no change in magnitude on the order of ~1.5 hr. Following the outburst's peak, the system's brightness dropped off rapidly at first, declining at a rate of V = 0.033 mag per day for the first ~15 d, followed by a slower rate of decline for the duration of the system's return to quiescence. This exponential fall in brightness provides evidence against outbursts that typically have linear rates of decline, such as classical novae (Hachisu and Kato 2015). The system took ~105.9 d to completely return to quiescence. It is quite typical of disk instability-driven dwarf novae to have brightening times that are shorter than the timescale of their decline, as is seen in this outburst. This model would suggest that the system's brightness declines due to the propagation of a cooling wave inward through the disk at the local sound speed. Lee *et al.* (2019) provides an upper limit on the size of the WD's accretion disk of 65 $R_\odot$. For a rate of propagation of 0.7 $R_\odot$ per 7–10 d (Sokoloski *et al.* 2006), this is reasonable, though it would suggest a much smaller disk size than the provided upper limit.

Furthermore, the amplitudes of $\Delta R = 0.518$ mag and $\Delta V = 0.781$ mag are too small to be caused by the thermonuclear runaways that drive classical symbiotic outbursts. Viewing the color evolution of the system, we see that the system became slightly bluer as the peak of the outburst occurred, followed by sizable reddening corresponding to the V – R = 0.112 mag amplitude of the light curve after the outburst's peak. This provides evidence against classical novae since these types of outbursts usually show a negative color (i.e. B – V color < 0 mag and U – B color < 0 mag, according to Hachisu and Kato (2015)) following the peak of the event. Given our unresolved photometric data of the entire system, it is impossible to know which component of AG Dra was responsible for this increase in temperature. In the disk instability-type outburst, we see a rise in accretion disk temperature that triggers a change in the disk's viscosity as it reaches a critical temperature. This change in viscosity causes an increase in mass flow through the disk and subsequent heating and brightening, which could be responsible for the behavior of the color light curve as the outburst reaches its peak. Then, as the event ends, the system cools until its normal temperature is restored by the lower rate of mass flow supplied by the cool component's mass loss, which could in theory be responsible for the increase in V – R color seen in Figure 3. If it were confirmed that this temperature change corresponds to a change in the disk temperature, then this would provide further evidence for the disk instability nature of this outburst.

Another model that is less suited to describe this event is the combination nova outburst. The combination nova outburst is also triggered by disk instabilities, but is followed by a large decrease in temperature and increase in brightness as the white dwarf expels a surrounding shell of material after enhanced thermonuclear burning has commenced. This seems less likely to have caused this event, as the peak luminosity caused by enhanced shell burning would be much higher than that observed in AG Dra's outburst. Also, a combination nova type outburst would most probably not have a linear rise to peak luminosity, as is seen in this event. While the

available evidence favors the disk instability model, further data would be useful to distinguish among the temperatures of the disk, hot component, and cool component. In the case of a disk instability outburst, we would expect an increase in temperature and luminosity of the accretion disk, while the other components remain fixed in these parameters. While the shape and timescales of this 2018 event are generally consistent with those of typical dwarf novae, the expected linear decline corresponding to the propagation of a cooling wave through the disk is not visible. The system's R-band and V-band brightness both fall off exponentially, indicating that there may be further activity involved in the system's cooling and decline in brightness. Additionally, if the size of the disk is as large as the upper limit provided by Lee *et al.*'s (2019) study, this cooling time would not be consistent with the cooling rate described by Sokoloski *et al.* (2006). Further data that resolves the activity of individual components of the system may be illuminating in consideration of this cooling mechanism.

7. Discussion

Since the conclusion of this event, AG Dra has not exhibited any further outbursts, with a notable lack of activity in 2019 May during the time when the next outburst of AG Dra was expected. This suggests that the 2015–2018 active phase of the system has concluded. Though this active stage's outburst frequency has remained consistent with previous active stages, continuous UBVR photometric monitoring of the system is still necessary to determine if AG Dra has truly returned to quiescence or if it will continue to exhibit abnormal outburst behavior. In particular, monitoring the temperature evolution of the hot component and accretion disk individually would be especially helpful in looking for signs of combination nova-type outbursts.

Though this event was probably triggered by disk instabilities, it remains unclear what caused the discrepancy between this outburst's exponential fall-off and the typical dwarf novae's linear decline. For the typical major outbursts exhibited by AG Dra in its active phase the combination nova model shows strong potential for explaining the underlying mechanism for at least some of the outbursts, though it has not been confirmed as conclusively as in Sokoloski *et al.*'s (2006) study of Z And. What remains unclear about the system is the connection between the minor outbursts exhibited by AG Dra in its 2015–2018 active phase and its typical behavior during major outbursts. Whether or not there is a connection between this activity and previous outbursts has yet to be determined. Knowing the temperature and individual luminosities of each component would clarify whether this is indicative of a different outburst mechanism (e. g., a combination nova-type outburst) or if this behavior is due to system properties of AG Dra, such as having a small disk size or interference of thermal pulsations by the cool component, allowing us to connect this activity into the grand scheme of AG Dra's outburst behavior.

8. Acknowledgments

We acknowledge with thanks the variable star observations from the AAVSO International Database contributed by observers worldwide and used in this research. We also would like to thank both Scott Kenyon and the anonymous referee for their helpful comments that improved this paper.

This research was funded by the NASA Pennsylvania Space Grant Consortium Research Scholarship Award and the University of Pittsburgh Department of Physics and Astronomy.

References

Astropy Collaboration; Price-Whelan, A. M., *et al.* 2018, *Astron. J.*, **156**, 123.

Fleming, S. W., *et al.* 2012, *Astron. J.*, **144**, 72.

Gális, R., Hric, L., Friedjung, M., and Petrík, K. 1999, *Astron. Astrophys.*, **348**, 533.

Gális, R., Hric, L., Leedjärv, L., and Merc, J. 2016, *Open Eur. J. Var. Stars*, **176**, 22.

Gális, R., Hric, L., and Smelcer, L. 2015, *Open Eu. J. Var. Stars*, **169**, 4

Gális, R., Merc, J., and Leedjärv, L. 2017, *Open Eur. J. Var. Stars*, **180**, 24.

Garcia, M. R. 1986, *Astron. J.*, **91**, 1400.

González-Riestra, R., Viotti, R., Iijima, T., and Greiner, J. 1999, *Astron. Astrophys.*, **347**, 478.

Good, M. L. 2011, Master's thesis, University of Pittsburgh (http://d-scholarship.pitt.edu/9073/).

Hachisu, I., and Kato, M. 2015, *Astrophys. J.*, **798**, 76.

Hric, L., Gális, R., Leedjärv, L., Burmeister, M., and Kundra, E. 2014, *Mon. Not. Roy. Astron. Soc.*, **443**, 1103.

Kafka, S. 2020, variable star observations from the AAVSO International Database (https://www.aavso.org/aavso-international-database-aid).

Kenyon, S. J. 1986, *The Symbiotic Stars*, Cambridge University Press, Cambridge.

Kenyon, S. J., and Fernandez-Castro, T. 1987, *Astron. J.*, **93**, 938.

Lang, D., Hogg, D. W., Mierle, K., Blanton, M., and Roweis, S. 2010, *Astron. J.*, **139**, 1782.

Lee, Y.-M., Lee, H.-W., Lee, H.-G., and Angeloni, R. 2019, *Mon. Not. Roy. Astron. Soc.*, **487**, 2166.

Mikolajewska, J., Kenyon, S. J., Mikolajewski, M., Garcia, M. R., and Polidan, R. S. 1995, *Astron. J.*, **109**, 1289.

Mink, D. J. 1997, in *Astronomical Data Analysis Software and Systems VI*, eds. G. Hunt, H. Payne, Astron. Soc. Pacifc Conf. Ser. 125, Astronomical Society of the Pacific, San Francisco, 249.

Shporer, A., *et al.* 2010, *Astrophys. J.*, **722**, 880.

Sion, E. M., Acierno, M. J., and Tomczyk, S. 1979, *Astrophys. J.*, **230**, 832.

Skopal, A., and Baludanský, D. 2003, in *Symbiotic Stars Probing Stellar Evolution*, eds. R. L. M. Corradi, J. Mikolajewska, T. J. Mahoney, Astron. Soc. Pacific Conf. Ser. 303, Astronomical Society of the Pacific, San Francisco, 249.

Sokoloski, J. L., *et al.* 2006, *Astrophys. J.*, **636**, 1002.

Wells, D. C., Greisen, E. W., and Harten, R. H. 1981, *Astron. Astrophys., Suppl. Ser.*, **44**, 363.

Continued Period Changes in BW Vulpeculae

David E. Cowall
Member, American Association of Variable Star Observers; 20361 Nanticoke Drive, Nanticoke, MD 21840; cowall@comcast.net

Brian A. Skiff
Research Assistant, Lowell Observatory, 1400 West Mars Hill Road, Flagstaff, AZ 86001; bas@lowell.edu

Andrew P. Odell *(deceased May 2019)*
Emeritus Associate Professor of Physics and Astronomy, Northern Arizona University

Received December 4, 2019; revised February 7, 2020; accepted February 14, 2020

Abstract BW Vulpeculae (BW Vul) has the largest amplitude of the β Cephei stars. Over almost 80 years of observations, BW Vul has closely followed a parabolic ephemeris and possibly a light-travel-time effect. This parabola, with excursions on either side, also could be viewed as a sequence of straight lines (constant period) with abrupt period increases. This paradigm predicted a period increase around 2004, which did not occur. A recent observing campaign on this star using the AAVSOnet's Bright Star Monitor telescopes as well as the 0.7-m Lowell Observatory telescope has been undertaken. A period analysis of our data suggests that the period may have paradoxically decreased beginning around 2009. Further observations are necessary to confirm this analysis.

1. Introduction

β-Cephei stars (β Cep) are pulsating variables with periods of 0.1–0.3 day with masses 10–20 $M_{\odot}$. They exhibit large radial velocities but small visual amplitudes with the greatest flux and amplitude in the ultraviolet (UV). They have spectral types B0.5-B2. The largest amplitude β Cep star is the monoperiodic BW Vulpeculae (BW Vul) (aliases: HR 8007 and HD 199140; R.A. 20 54 22.4, Dec. +28 31 19). Its mass is ~15 $M_{\odot}$ and it is ~10^3 times more luminous than the Sun. The V band amplitude is 0.24, but almost 1 magnitude in UV (Percy 2007).

There has been extensive literature published regarding period increases in BW Vul. Based upon spectroscopy, Petrie (1954) first suggested a constant rate of period increase, dP/dt = +3.7 seconds/century. Cherewick and Young (1975) confirmed this with photometry, albeit with a rate approximately half as large. If due to the evolution of the star, then these large positive dP/dt would indicate that BW Vul is in the shell hydrogen burning phase. This contradicts evidence that β Cep stars in clusters are in the late core burning phase where the period change is well under one clock-second per century. This seemingly rules out the contraction phase where the period should decrease.

Another proposed interpretation of the data was a piecewise linear ephemeris with abrupt period changes, suggested by the following investigations: Tunca (1978) suggested a constant period with a dP/dt = +0.5 second/century in 1972. Chapellier (1985) offered a similar interpretation with abrupt period changes in 1931 and 1945 as well. Chapellier and Garrido (1990) documented another period increase around 1980–1981. An international campaign to monitor BW Vul during the 1982 observing season unfortunately yielded only one timing (Sterken *et al.* 1986). Chapellier and Garrido (1990) offered no physical explanation for the period changes but suggested that a convective process could be responsible. They posited that both the amplitude and timings became unstable for three years during the 1980–1981 change.

Odell (1984) noted an apparent periodic variation superimposed on the quadratic ephemeris and attributed it to the light-travel time effect (LTTE) of a small-mass companion, or to two pulsation modes beating with a period of about 25 years. Pigulski (1993) solved for this postulated binary orbit. With reasonable assumptions for the mass of the primary and the inclination of the orbit, the mass of the secondary should be less than 2.5 $M_{\odot}$, and therefore not detectable in extant observations. All this uncertainty surrounding BW Vul was mostly ignored due to the seemingly predictive power of LTTE and the case was considered settled (Horvath *et al.* 1998). Two excellent review papers, Zhou (1999) and Sterken (2005), both used BW Vul as the illustrative example of a star demonstrating LTTE. However, the LTTE model predicted a dP/dt = +0.5 second/century around 2002 which did not happen and thus appears to rule out this explanation for the period variation in this star (Odell 2012).

2. Methods

2.1. AAVSOnet

B-band and V-band images of BW Vul were obtained using the American Association of Variable Star Observers network (AAVSOnet) telescopes (Henden 2014) in Cambridge, Massachusetts (BSM-HQ), New Mexico (BSM-NM), and Hawaii (BSM-Hamren). All AAVSO images were calibrated each observing night using twilight flat-fields as well as bias and dark frames.

Ensemble photometry was done using comparison stars HD 199221 and HD 335322 and check star HD 199418 obtained from the AAVSO Comparison Star Database. Mathematical analyses were performed using VPHOT (AAVSO 2012), VSTAR (Benn 2013), and an EXCEL spreadsheet. Results were air mass corrected, transformed, and submitted to the AAVSO International Database (AID; Kafka 2015).

2.2. Lowell Observatory

Images of BW Vul were obtained using the 0.7-m robotic

telescope at Lowell Observatory's Anderson Mesa Station. The CCD field is 15' × 15' with image-scale 0.46"/pixel. Because of the star's brightness, data were taken with narrowband filters approximating the B, V, R wavelengths. These were centered at 4450 Å, 5260 Å, and 7128 Å, and all about 60 Å width. These filters are normally used to subtract out continuum flux from other filters used to measure emission bands in comets. They have the additional use of allowing bright stars to be observed with the telescope in reasonable exposure times. Twilight flat-field and bias frames were obtained each observing night. The CCD camera is cooled using a CryoTiger chiller to –110° C, so dark frames are not required for calibration.

Similar frames of the B-giant HD 198820 = HR 7996 (B3III), 4 degrees north of BW Vul, were interleaved with the variable to serve as the sole comparison star. This procedure worked only on bona-fide photometric (cloud-free) nights. More recently the BW Vul field center has been adjusted to include three rather faint on-chip comparison stars, so that useful data could be obtained when the sky was unexpectedly "cirrus-y."

Seasonal observations continue using the on-chip comparisons, omitting the red filter, but substituting a narrow-band filter in the far-red (8900 Å), near the center of the Sloan z filter passband.

The data prior to Andy Odell's death were analyzed by him using IRAF scripts. We do not know the details of those reductions. However, we know that he necessarily needed to be a finicky photometrist in order to seek the subtle effects in the stars on which he worked.

3. Results

Observed Timings (T_o) of maximum/minimum light were determined using the parabolic method. To for the AAVSO data represent the mean of the B-band and V-band data. Calculated Timings (T_c) are from Sterken's (1993) equation:

$$T_c = 28802.5487 + (0.201038)(\text{Cycle\#}) \quad (1)$$

These data are included in the ephemerides of Table 1 (AAVSO) and Table 2 (Lowell). To are reported in the columns labeled HJD in days. Cycle numbers ending in .45 represent minima. (O–C)s are the residuals to a linear fit of data and are in clock-minutes.

The BW Vul B-band phase plot from the AAVSO data is shown in Figure 1. Mean scatter on the fit is ~0.05 mag.

A residuals plot combining our data with historical results dating back to 1982 is shown in Figure 2 showing best linear fits.

4. Discussion

Over almost 80 years of observations, BW Vul has closely followed a parabolic ephemeris (period increasing by 2.4 seconds/century) with perhaps LTTE induced by a hypothetical companion. This parabola with excursions on either side also could be viewed as a sequence of straight lines (constant period) with abrupt period increases. This paradigm predicted a necessary period increase around 2004, which did not occur. To the contrary, our data, as seen graphically in the Figure 2 residuals plot, suggest that the period may have paradoxically decreased around 2009 by ~0.0006%. There are insufficient data at present to determine if this proposed period change is real, or if this assumed change is linear plus/minus a sine wave accounting for LTTE. Therefore, both the AAVSOnet and the Lowell Observatory have committed to further observations of this star.

Table 1. BW Vul timings, AAVSO.

Cycle	*HJD (2450000+)*	*(O–C)*
134114.45	5764.8898	–0.6
142048.45	7359.9608	–7.8
143727.45	7697.524	9.2
143772.45	7706.553	–16.6
144500.45	7852.927	4.4
144530.45	7858.954	–1.8
144535.45	7859.948	–17.9
144540.45	7860.962	–5.3
144644.45	7881.8682	–8.6
144659.45	7884.8877	–3
144667.45	7886.4961	–2.9
144684.45	7889.9154	–0.7
144694.45	7891.9294	4.5
144704.45	7893.9389	3.1

Table 2. BW Vul timings, Lowel Observatory.

Cycle	*HJD (2450000+)*	*(O-C)*
142056.45	7361.5800	10.1
142948.45	7540.9025	-1.3
143028	7556.9002	4.6
143166.45	7584.7314	0
143167	7584.8436	2.3
143171.45	7585.7355	-1.6
143172	7585.8468	-0.6
143311	7613.7982	8.6
143519.45	7655.7021	3.5
143623.45	7676.6111	4.3
143624	7676.7239	7.5
143772.45	7706.5655	2.8
143773	7706.6729	-1.8
143777.45	7707.5730	6.1
143778	7707.6872	11.3
144674	7887.8166	3.9
144674.45	7887.9027	-2.5
144679	7888.8262	10.1
144679.45	7888.9116	2.8
144793.45	7911.8321	5.1
144794	7911.9437	6.6
144798.45	7912.8384	6.6
144799	7912.9480	5.2
145354.45	8024.6133	0.2
145355	8024.7316	10.5

5. Acknowledgements

The impetus for this paper comes, in large part, from the passion that Andy Odell had for BW Vul. Unfortunately, he passed away suddenly from a heart attack in May of 2019. He was convinced that this star had much more to teach us and that new surprises awaited us if we continued to observe it. When he was asked what he thought those surprises might

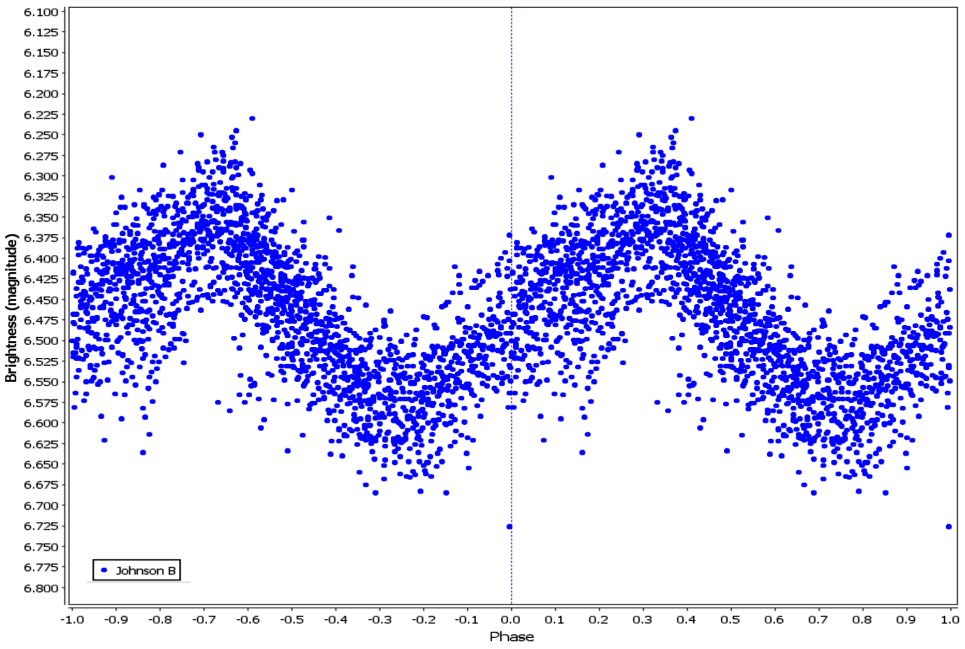

Figure 1. BW Vul B-band phase plot from the AAVSO data.

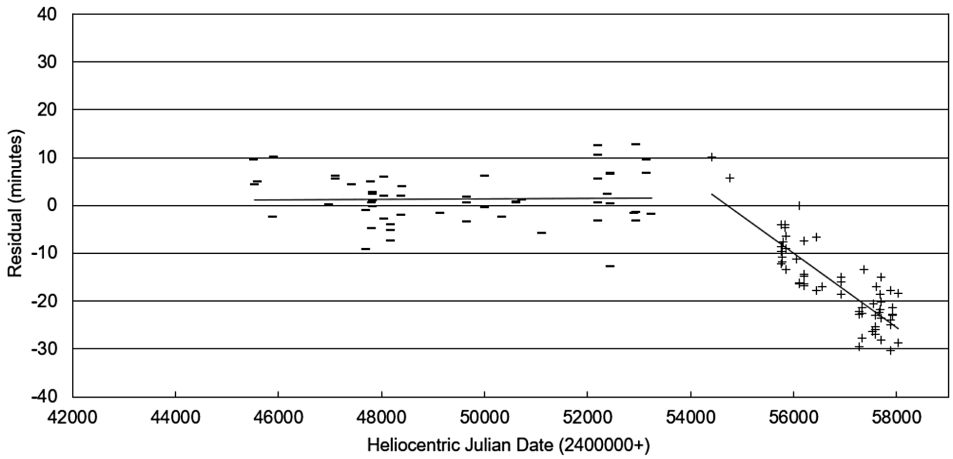

Figure 2. BW Vul O–C HJD (2400000+). "-": 1982–2004 (historical); "+": 2007–2017 (AAVSO and Lowell).

be he said, "Ask me again in 50 years." Rest in peace, Andy, amongst the stars. We acknowledge with thanks the variable star observations from the AAVSO International Database contributed by observers worldwide and used in this research.

References

AAVSO. 2012, VPHOT AAVSO photometric software (http://www.aavso.org/vphot).

Benn, D. 2013, VSTAR data analysis software (http://www.aavso.org/vstar-overview).

Chapellier, E. 1985, *Astron. Astrophys.*, **147**, 145.

Chapellier, E., and Garrido, R. 1990, *Astron. Astrophys.*, **230**, 304.

Cherewick, T., and Young, A. 1975, *Publ. Astron. Soc. Pacific*, **87**, 311.

Henden, A. 2014, AAVSOnet (https://www.aavso.org/aavsonet).

Horvath., A., Gherega, O., and Farkas, L. 1998, *Romanian Astron. J.*, **8**, 89.

Kafka, S. 2015, variable star observations from the AAVSO International Database (https://aavso.org/aavso-international-database-aid).

Odell, A. P. 1984, *Publ. Astron. Soc. Pacific*, **96**, 657.

Odell, A. P. 2012, *Astron. Astrophys.*, **544A**, 28.

Percy, J. 2007, *Understanding Variable Stars*, Cambridge University Press, New York, 186.

Petrie, R. M. 1954, *Publ. Dom. Astrophys. Obs.*, **10**, 39.

Pigulski, A. 1993, *Astron. Astrophys.*, **274**, 269.

Sterken, C. 1993, *Astron. Astrophys.*, **270**, 259.

Sterken, C. 2005, in *The Light Time Effect in Astrophysics*, ed. C. Sterken, ASP Conf. Ser. 335, Astronomical Society of the Pacific, San Francisco, 3.

Sterken, C., *et al.* 1986, *Astron. Astrophys., Suppl. Ser.*, **66**, 11.

Tunca, Z. 1978, *Inf. Bull. Var. Stars*, No. 1386, 1.

Zhou, A. 1999, *Astrophys. Rep.*, *Publ. Bejing Astrophys. Obs.*, No. 33, 17.

ASAS-SN Observations of Long Secondary Periods in Pulsating Red Giants

John R. Percy
Anthony Mark Wallace
Department of Astronomy and Astrophysics, and Dunlap Institute for Astronomy and Astrophysics, University of Toronto, 50 St. George Street, Toronto, ON M5S 3H4, Canada; john.percy@utoronto.ca

Received December 12, 2019; revised February 25, 2020; accepted February 25, 2020

Abstract About a third of all pulsating red giants (PRGs) have long secondary periods (LSPs), an order of magnitude longer than their pulsation periods (P). Although LSPs have been known for many decades, their nature and cause are uncertain. We have analyzed data on 45 PRGs, from the All-Sky Automated Survey for Supernovae (ASAS-SN), and combined the results with data from the literature to draw a few new conclusions about this phenomenon. LSPs have V amplitudes of up to 0.45 mag. The ratio LSP/P has a peak at 10 ± 1, and a broader distribution at 7 ± 1. There is no obvious correlation between LSP/P and LSP itself. Previous studies have suggested that the pulsation amplitude does not vary around the LSP cycle, but varies on longer time scales of 20–45 P. However, we find smaller variations in pulsation amplitude around the LSP cycle, which may be partly due to the effect of the LSP variations on the pulsation amplitude determination, but otherwise appear to be real and common.

1. Introduction

Red giant stars are unstable to pulsation, but their variability is complex, with "wandering" periods (Eddington and Plakidis 1929), variable pulsation amplitudes (Percy and Abachi 2013), and, in about a third of stars, "long secondary periods" (LSPs) of unknown cause (Wood 2000). Percy and Deibert (2016) and Percy and Leung (2017) used data from the American Association of Variable Star Observers (AAVSO) International Database (AID) to study the LSP phenomenon, following on the work of Mattei *et al.* (1998) and Kiss *et al.* (1999), and Fuentes-Morales and Vogt (2014) who used data from the original ASAS survey. Important studies of PRGs in the LMC have also been carried out by Wood (2000) and others, using data from other automated surveys.

In the present study, we supplement those studies of PRGs with new results from the analysis of data from the All-Sky Automated Survey for Supernovae—ASAS-SN (Jayasinghe *et al.* 2018, 2019). We look especially at the amplitudes of both the pulsation periods and the LSPs, since more attention has been paid to the periods than to the amplitudes.

Percy and Fenaux (2019) have recently analyzed data on PRGs from ASAS-SN, and pointed out some problems with the automated analysis and classification of PRGs by the ASAS-SN project. These arise from the complexity of PRGs' variability, as mentioned above. Knowing of and accounting for this complexity, it would now be possible to extract useful information from this very large sample (175,000!) of PRGs. In the present paper, we continue to explore the use of the ASAS-SN data to understand more about these stars.

2. Data and analysis

We analyzed the 45 ASAS-SN stars in Table 1, all of which were selected because their light curves showed the clear presence of both an LSP and variability on a time scale an order of magnitude shorter which was presumed to be pulsational variability. For this specific project, we restricted ourselves to stars with LSP ~ 500 days. Given the finite length of the ASAS-SN database (about 2,000 days), longer LSPs cannot be reliably identified and studied. The data were downloaded, and analyzed using the AAVSO VSTAR time-series package (Benn 2013), which includes a Fourier and a wavelet analysis routine.

3. Results

3.1. Pulsation periods and LSPs

Pulsation periods, LSPs, and their amplitudes were determined for a sample of 45 stars which were classified by ASAS-SN as SR, and which had LSPs of approximately 500 days as determined by a cursory inspection of their light curves. The results are given in Table 1. The columns list: the star name minus ASAS-SN-V-J, the pulsation amplitude, the LSP amplitude, the pulsation period P, the LSP, the apparent time scale for smaller pulsation amplitude variations (see sections below), and LSP/P. Here, "amplitude" is defined as the coefficient of the sine curve, corresponding to the period. The peak-to-peak "range" would be twice that.

3.2. LSP amplitudes

The amplitude of the LSP and its upper limit provide some information and constraints on possible causes for the phenomenon. Figure 1 shows a histogram of the amplitudes of all the LSPs in our new sample, as well as those in Percy and Deibert (2016), Percy and Leung (2017), and Fuentes-Morales and Vogt (2014).

3.3. Ratios of LSP to pulsation period

Figure 2 shows a histogram of values of LSP/P. The peak is at 9–10, and there is also a broad, shallower distribution around 6–7. For the stars in Table 1, half have LSP/P = 10 ± 1, with the smaller broad distribution at 7 ± 1. For the stars analyzed by Fuentes-Morales and Vogt (2014) having LSPs, the peak values of LSP/P are 9 ± 1 and 5 ± 1, which is not inconsistent with our results.

3.4. A relation between LSP/P and LSP?

Previous studies have shown that shorter-period PRGs are more likely to be pulsating in an overtone mode, and longer

Table 1. Analysis of ASAS–SN observations of pulsating red giants.

Name (ASAS–SN–V)	*A(P)*	*A(LSP)*	*P(d)*	*LSP(d)*	*tA (d)*	*LSP/P*
191616.35+475823.7	0.21	0.08	54	506	428	9.4
200906.21–360621.9	0.27	0.08	50	502	460	10.0
102404.50–424432.1	0.07	0.04	43	534	600	12.4
092133.94–302421.6	0.41	0.11	53	500	—	9.4
073356.87–761029.5	0.19	0.08	50	537	453	10.7
101642.40–324246.4	0.09	0.05	47	497	500	10.6
221339.54+250026.2	0.18	0.06	70	510	550	7.3
175204.29–505333.5	0.06	0.04	51	530	458	10.4
201618.11–514426.6	0.29	0.08	63	449	680	7.1
181621.36–624528.8	0.15	0.07	67	408	437	6.1
072611.52–051112.8	0.21	0.17	120	526	—	4.4
165443.03–674130.3	0.22	0.11	52	521	—	10.0
061244.28–494217.4	0.06	0.04	52	511	—	9.8
071807.32–580600.5	0.32	0.06	60	485	406	8.1
223902.01+210756.5	0.20	0.10	84	511	1060	6.1
041209.77–581525.7	0.06	0.04	49	497	660	10.1
190736.39–283252.1	0.17	0.10	51	513	1010	10.1
200517.75+152705.5	0.29	0.14	87	494	—	5.7
043744.566+535304.7	0.28	0.09	67	667	—	10.0
183140.63–342342.4	0.17	0.09	54	530	580	9.8
185021.64–372919.3	0.07	0.04	55	504	—	9.2
050943.86+072725.6	0.09	0.05	50	530	—	10.6
073046.65–642648.2	0.24	0.09	55	523	—	9.5
195637.80+073255.0	0.28	0.10	84	537	650	6.4
042558.31+224004.7	0.33	0.08	63	511	530	8.1
024353.42+383555.7	0.24	0.08	62	510	—	8.2
060912.35–142851.3	0.10	0.06	52	538	—	10.3
202651.30+192639.8	0.17	0.06	62	493	460	8.0
202346.72+230928.2	0.20	0.10	65	486	—	7.5
173343.90–491900.9	0.10	0.05	60	489	—	8.2
202507.66+131360.0	0.26	0.09	55	520	—	9.5
075229.72–065927.9	0.34	0.10	66	506	—	7.7
065430.46–024530.5	0.16	0.08	69	507	400	7.3
180342.74–541714.9	0.20	0.09	56	527	940	9.4
160247.19–262523.7	0.09	0.19	54	547	—	10.1
120733.34–572501.6	0.14	0.20	56	377	430	6.7
192322.36+132404.5	0.15	0.17	47	349	—	7.4
200830.55–024558.2	0.21	0.14	44	700	750	15.9
165027.59–670623.6	0.16	0.18	42	512	440	12.2
190727.12–115432.9	0.07	0.19	25	346	—	13.8
184135.31–074400.7	0.10	0.15	27	415	—	15.4
201749.96+101629.5	0.15	0.15	50	374	367	7.5
085241.14–390810.0	0.20	0.11	29	290	290	10.0
143922.74–622255.9	0.20	0.18	30	365	265	12.2
042659.04–705401.3	0.10	0.08	35	344	920	9.8

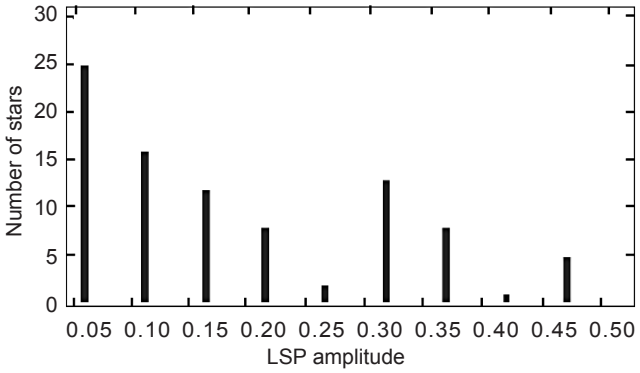

Figure 1. Histogram of the amplitudes, in magnitudes, of LSPs for PRGs in our sample. As described in the text, there are biases against small to medium amplitudes, and for medium to large ones. Amplitudes of up to 0.45 magnitude are found in these stars.

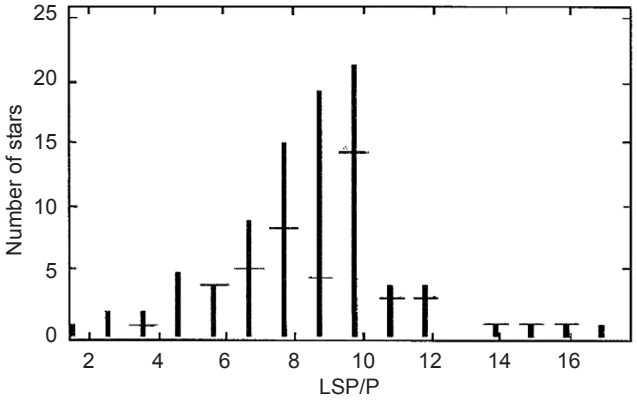

Figure 2. Histogram of ratios of LSP/P for PRGs in our sample, and PRGs in the sources given in section 3.2. There is a strong peak at 10 ± 1, a small number at 7 ± 1, and a very few larger than 12. The horizontal bars are the results for the ASAS-SN stars listed in Table 1.

period PRGs (such as Mira stars) are more likely to pulsate in the fundamental mode. If the LSP was correlated with, for example, the radius of the star, then LSP/P might be expected to be larger in short-period, first-overtone stars, and smaller in longer-period, fundamental-mode stars. Figure 3 shows the relation between LSP/P and LSP. No such trend is obvious.

3.5. Does pulsation amplitude vary around the LSP cycle?

If the LSP produces significant changes in the *physical* properties of the pulsating star, then it is possible that these produce changes in the pulsation amplitude around the LSP cycle. The time scales of amplitude variation in PRGs tend to be 20–45 times the pulsation period (Percy and Abachi 2013; Percy and Deibert 2016), whereas the LSPs tend to be 5–10 times the pulsation period. This suggests that the pulsation amplitude does *not* vary significantly on the LSP time scale. Percy and Di (2018), using AAVSO data, also found this to be the case in four stars, for which there was sufficiently dense coverage in the AID.

These studies, however, used decay parameters of 0.001 in VSTAR to average out the scatter in the AAVSO visual data. ASAS-SN data do not have this scatter, and are reasonably dense, so we have used them, with a decay parameter of 0.01, to investigate this question in more detail. The significance of the decay parameter is discussed by Templeton (2004) and in more detail by Foster (1996), who created the WWZ wavelet analysis tool. The decay parameter sets the width of the Gaussian window function. To quote Templeton (2004): "The algorithm fits a sinusoidal wavelet to the data, but as it does so, it weights the data points by applying the sliding window function to the data; points near the center of the window have the heaviest weights in the fit, while those near the edges have smaller weights. The window slides along the data set, giving us a representation of the spectral content of the signal at times corresponding to the center of that window." A slow decay averages the spectral properties over a longer time span. A fast decay averages them over a shorter time span, and therefore gives finer detail, though based on fewer data points, and therefore with potentially lower accuracy.

We found the situation to be somewhat more complicated. Smaller amplitude variations are found on a shorter time scale.

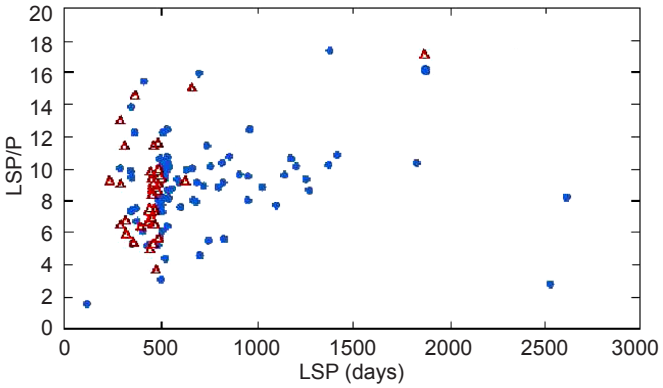

Figure 3. The relationship between LSP/P and LSP. There is no obvious relation. See text for discussion. The red triangles are the results for the stars listed in Table 1. The blue filled circles are the results for other stars, in the sources given in section 3.2.

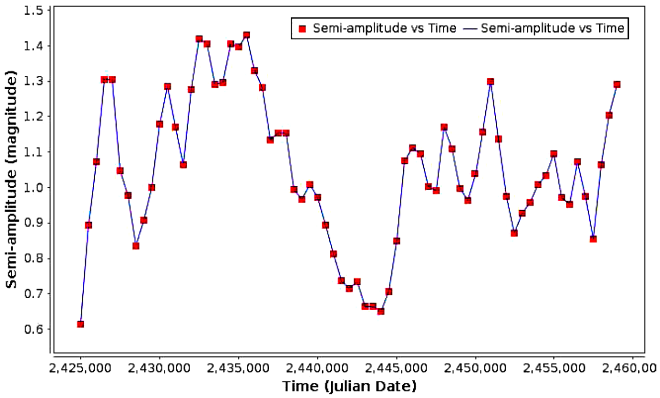

Figure 4. For T Ari: the pulsation amplitude in magnitudes versus time, using a decay parameter of 0.01 in vstar, showing both the slow variations (tens of thousands of days) and the smaller variations on a time scale comparable to the LSP, which is 2600 days in this star (Percy and Deibert 2016).

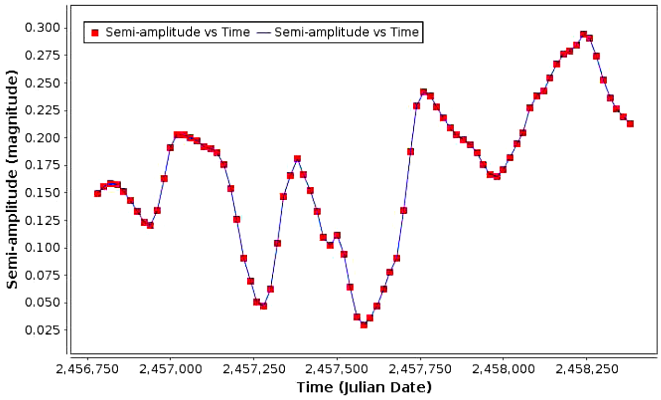

Figure 5. For ASASSN-V J165027.59-670623.6: the pulsation amplitude in magnitudes versus time, using a decay parameter of 0.01 in vstar, showing both the slow variations (time scale two thousand days) and the substantial variations on a time scale comparable to the LSP, which is about 500 days in this star (Table 1).

The second-last column in Table 1 lists the time scales (tA in days) of these variations, as determined by wavelet analysis. This will be discussed in more detail in section 4.

4. Discussion

4.1. Periods and LSPs

The stars were chosen to have LSPs of *approximately* 500 days, but the derived values range between 300 and 700 days, though the statistical uncertainty of these is obviously large, since the lengths of the datasets are only about 2,000 days. Most of the pulsation periods are about 50 days. In this sense, our star sample is not an unbiased one.

4.2. LSP amplitudes

There are several biases in the histogram of LSP amplitudes (Figure 1). The ASAS-SN stars in Table 1 were chosen to have a conspicuous LSP, as well as visible shorter-period variations which were presumed to be due to pulsation. Stars with LSPs from Percy and Deibert (2016), Percy and Leung (2017), and Fuentes-Morales and Vogt (2014) are less biased, but LSPs with amplitudes below 0.10 are still less likely to be detected. So the true shape of Figure 1 is more likely to be a smooth drop-off from 0.00 to the apparent upper limit of 0.45. This upper limit provides some constraint on the possible LSP mechanism, which remains uncertain. Figure 1, when compared with Figure 3 in Percy and Deibert (2016), confirms that there is no shortage of large-amplitude (~0.3–0.4 mag) LSPs, even for LSPs as low as 500 days.

We note that Trabucchi *et al.* (2017) found that, in the Large Magellanic Cloud, LSPs seem to have an upper limit to their amplitude of 0.4 mag, or slightly higher, shown in their Figure 7.

It is possible that some stars have a large LSP amplitude and a small pulsation amplitude, so that the LSP is then interpreted as a pulsation period. Percy and Fenaux (2019) identified a few such stars.

It is also possible that all PRGs—even including Mira stars—have LSPs, but that most of them have amplitudes which are too small to be detected. This is a possibility that is worth investigating—if it is practically possible.

4.3. Ratios of LSPs to pulsation period

One possible interpretation is that the larger values of LSP/P occur when P is a first-overtone pulsation mode (P1), and the smaller values occur when P is the fundamental mode (P0). In that case, the large number of LSP/P values around 10 suggests that about half of the stars are pulsating in the first overtone, whereas the stars with LSP/P around 7 are pulsating in the fundamental mode. The ratio P1/P0 varies between 0.45 and 0.65 for these stars (Xiong and Deng 2007; Percy 2020).

4.4. A relation between LSP/P and LSP?

Since shorter-period PRGs are known to pulsate in the first overtone, whereas longer-period ones pulsate in the fundamental, there might be a trend between LSP/P and LSP. Figure 3, which includes data from Percy and Deibert (2016) and Morales-Fuentes and Vogt (2014), shows no evidence for that. Figure 5 in Percy and Deibert (2016), which includes LSPs

up to 3,000 days, confirms this lack of a trend. Our result is also consistent with Fuentes-Morales and Vogt (2014), Figure 4.

4.5. Does pulsation amplitude vary around the LSP cycle?

The *a priori* reasons for believing that the pulsation amplitude does not vary significantly around the pulsation cycle are: (1) the dominant time scale for pulsation amplitude is 20–45 pulsation periods, whereas the time scale of the LSP is 5–10 pulsation periods; and (2) Percy and Di (2018) did not find any significant variation in pulsation amplitude during the LSP cycles of four stars.

We have re-examined this question. In particular: we have reduced the decay parameter in the VSTAR wavelet analysis. This gives finer resolution for study of the period and amplitude variation though, because it determines these over shorter intervals—typically one pulsation cycle—it does not have the advantage of averaging out the scatter over more than one pulsation cycle. We find that the individual pulsation cycles are affected (sometimes significantly) by the LSP variability, so this effect may be *partly* due to the method of analysis. The longer-time-scale variations are still present. Figures 4 and 5 show two examples. Table 1, column 6 gives the time scale τA, in days, of the smaller, shorter-period variations in pulsation amplitude. These shorter-period variations may have been averaged out in our previous studies. In this column, a blank entry indicates that there were no detectable amplitude variations.

A detailed comparison of the LSP light curve and the pulsation amplitude variability as determined by wavelet analysis with a short decay parameter shows clearly that the two are *not in phase*; they indeed have similar but unequal time scales. This can be seen in the AAVSO data for U Del and Y Lyn, which are especially densely covered. There is no consistent relation between the times of maximum pulsation amplitude and the phase in the LSP cycle.

5. Conclusions

This study provides an example of how data from the ASAS-SN survey, because of their accuracy and density, can provide useful information about the behavior of PRGs, including the poorly-understood LSP phenomenon. Specifically, we have derived information about the amplitudes of the LSPs, and their upper limit, and about the relationship between LSP/P and LSP (assuming it to be related to radius). We have also been able to study variations in pulsation amplitude on time scales of the LSP to tens of pulsation periods.

One limitation of the ASAS-SN survey is that the datasets are only about 2,000 days long. This limits the precision of the derived periods, and limits the extent to which we can study very long time scale phenomena in these stars. There are also the inevitable seasonal gaps in the data, which can lead to confusing aliases in the Fourier spectrum.

This project is also an example of the kind of project which can be carried out by an undergraduate student, who can develop and integrate their science and math skills, motivated by doing real science with real data.

6. Acknowledgements

This paper made use of ASAS-SN photometric data. We thank the ASAS-SN project team for their remarkable contribution to stellar astronomy, and for making the data freely available on-line. We acknowledge and thank the University of Toronto Work-Study Program for financial support. The Dunlap Institute is funded through an endowment established by the David Dunlap Family and the University of Toronto.

References

Benn, D. 2013, VSTAR data analysis software (http://www.aavso.org/vstar-overview).

Eddington, A. S., and Plakidis, S. 1929, *Mon. Not. Roy. Astron. Soc.*, **90**. 65.

Foster, G. 1996, *Astron. J.*, **112**, 1709.

Fuentes-Morales, I., and Vogt, N. 2014, *Astron. Nachr.*, **335**, 1072.

Jayasinghe, T., *et al.* 2018, *Mon. Not. Roy. Astron. Soc.*, **477**, 3145.

Jayasinghe, T., *et al.* 2019, *Mon. Not. Roy. Astron. Soc.*, **486**, 1907.

Kiss, L. L., Szatmary, K., Cadmus, R. R., Jr., and Mattei, J. A. 1999, *Astron. Astrophys.*, **346**, 542.

Mattei, J. A., Foster, G., Hurwitz, L. A., Malatesta, K. H., Willson, L. A., and Mennessier, M. O. 1998, in *Proceedings of the ESA Symposium "Hipparcos-Venice '97"*, ESA SP-402, ESA Publications Division, Noordwijk, The Netherlands, 269.

Percy, J. R. 2020, *J. Amer. Assoc. Var. Star Obs.*, **48**, in press.

Percy, J. R., and Abachi, R. 2013, *J. Amer. Assoc. Var. Star Obs.*, **41**, 193.

Percy, J. R., and Deibert, E. 2016, *J. Amer. Assoc. Var. Star Obs.*, **44**, 94.

Percy, J. R., and Di, K. 2018, arXiv: 1807.05095.

Percy, J. R., and Fenaux, L. 2019, *J. Amer. Assoc. Var. Star Obs.*, **47**, 202.

Percy, J. R., and Leung, H. 2017, *J. Amer. Assoc. Var. Star Obs.*, **45**, 30.

Templeton, M. R. 2004, *J. Amer.. Assoc. Var. Star Obs.*, **32**, 41.

Trabucchi, M., Wood, P. R., Montalbán, J., Marigo, P., Pastorelli, G., and Girardi, L. 2017, *Astrophys. J.*, **847**, 139.

Wood, P. R. 2000, *Publ. Astron. Soc. Australia*, **17**, 18.

Xiong, D. R., and Deng, L. 2007, *Mon. Not. Roy. Astron. Soc.*, **378**, 1270.

HD 121620: A Previously Unreported Variable Star with Unusual Properties

Roy A. Axelsen
AAVSO; Astronomical Association of Queensland; Variable Stars South, P.O. Box 706, Kenmore, Queensland 4069, Australia; reaxelsen@gmail.com

Received December 20, 2019; revised February 11, 14, 2020; accepted February 14, 2020

Abstract During a study of the δ Scuti star V1393 Centauri by digital single lens reflex photometry, it was found that two of the chosen comparison stars were variable. This paper reports the subsequent investigation of one of them, HD 121620, which revealed irregular light variations of 0.8 magnitude in V within a time frame of approximately 24 hours. Photometry in the Hipparcos and Tycho databases from December 1989 to February 1993 revealed an average VT magnitude of 7.25 and little scatter in the data, indicating that the star was then either constant or only slightly variable. Photometry in the ASAS-3 V database between January 2001 and September 2009 showed a similar pattern, with an average magnitude of 7.1. Variability is documented in the ASAS-SN V database from February 2016 to September 2019, and in the ASAS-SN g database from June 2018 to September 2019. Inspection of the author's light curves and Fourier analysis of the author's data show a time frame of one day, but no regular periodicity. Since HD 121620 has a spectral type of G6/8III, it belongs to a population of stars which are least likely to be variable. The nature of its variability has not been determined.

1. Introduction

During a digital single lens reflex (DSLR) photometric study of the δ Scuti star V1393 Cen, the light curves of the variable and check stars were found to have anomalous features, indicating that the comparison star is variable. Photometry of several stars in the field of view revealed that two of them, HD121191 and HD121620, are variable. HD121191 is a previously unreported δ Scuti star (Axelsen 2019). HD121620, a 7th magnitude G6/8III high proper-motion star at R.A. 13 57 56.44, Dec. –53 42 15.34 (ICRS, J2000 from SIMBAD) (Wenger *et al.* 2000) was found to have unusual features of variability, which are reported herein.

2. Methods

Time series photometry was performed on 12 nights from 26 May to 23 June 2019. RAW format images were captured with a Canon EOS 500D DSLR camera through an 80-mm f/7.5 refractor on an equatorial mount. Autoguided exposures of 180 seconds were taken at ISO 400, with a 5-second gap between consecutive exposures.

Images were converted to the FITS format and pre-processed in IRIS (Buil 1999–2018) using dark, bias, and flat frames. Images from the blue and green channels were extracted and imported into ASTROIMAGEJ (Collins *et al.* 2017) for aligning and aperture photometry. Comparison and check stars were HD 120858 and HD 121277, respectively. Data listed in SIMBAD for the variable, comparison, and check stars are shown in Table 1.

Flux values from ASTROIMAGEJ were imported into an EXCEL spreadsheet. Instrumental magnitudes and transformed magnitudes in B and V were calculated using transformation coefficients derived from photometry of images of standard stars from the E regions (Menzies *et al.* 1989). Atmospheric extinction corrections were not applied. The data were analyzed in VSTAR (Benn 2012).

Position searches in SIMBAD (http://simbad.u-strasbg.fr/simbad/sim-fid), the SAO/NASA ADS Custom Query Form (http://adsabs.harvard.edu/abstract_service.html), and the *General Catalogue of Variable Stars* (GCVS; Samus *et al.* 2017, http://www.sai.msu.su/gcvs/cgi-bin/search.htm) failed to find any specific report of variability in HD 121620.

Evidence for variability of HD 121620 was also sought in *The Hipparcos and Tychco Catalogues* (Perryman *et al.* 1997) via the I/239/hip_main table in Vizier (http://vizier.u-strasbg.fr/viz-bin/VizieR-3), in the All Sky Automated Survey (ASAS-3 V) database (Pojmanski 2002), and in the All-Sky Automated Survey for Supernovae (ASAS-SN, http://www.astronomy.ohio-state.edu/~assassin/index.shtml) (Shappee *et al.* 2014; Kochanek *et al.* 2017).

3. Results

3.1. New photometry of HD 121620

The transformed V magnitude of HD 121620 from the author's data was determined for 1,439 time points over the 12 nights of observation, during a total observing time of 78 hr 50 min. The shortest duration of observation during one night was 3 hr 16 min and the longest 8 hr 38 min. The magnitudes

Table 1. Data from SIMBAD for the variable, comparison, and check stars.

Star	*Component*	*R.A.* *h m s*	*Dec.* ° ′ ″	*V*	*B*	*B–V*
HD 121620	Variable star	13 57 56.44	–53 42 15.34	7.088 (0.010)	8.043 (0.015)	0.955
HD 120858	Comparison star	13 53 21.11	–53 14 29.96	8.71 (0.01)	10.00 (0.03)	1.29
HD 121277	Check star	13 55 55.68	–53 14 58.72	9.16 (0.02)	10.04 (0.04)	1.24

ranged from 7.05 to 7.83, but were not distributed uniformly across the observing nights. During the first six nights, the magnitude ranged from 7.05 to 7.37, whereas the range during the last six nights was 7.34 to 7.83.

Light curves are shown in Figures 1 and 2. Figure 1 includes all observations in B and V and shows their distribution in time across the twelve nights. When the star was brighter, during the first six nights, B–V was greater than it was during the last six nights. Figure 2 illustrates in more detail the light curves for each of the twelve nights. It should be noted that the check star light curves in Figure 2 are shifted so that in each panel the variable and check star light curves are both optimally visualized. HD 121620 brightened during the five nights from 26–27 May to 30–31 May. The observations for the night of 11–12 June exhibit a pattern suggesting the light curve may have been approaching a peak. On the nights of 12–13 and 13–14 June the light curves are descending. Troughs are present for the nights of 17–18 and 18–19 June. The light curve is again descending for the short period of observation before midnight on 19 June. A pronounced trough is seen in observations from 22–23 June. Thus, although no regular periodicity is evident from inspection of the light curves, there is variability with a time frame of about 24 hours.

Another feature is the presence of short, low amplitude flares, seen on 27–28 May just after the beginning of the light curve, and on 30–31 May, possibly at the beginning of the light curve, and again about two thirds of the way along its length. At least two and probably more flares are seen on 13–14 June.

3.2. Photometry of HD 121620 in published databases

The light curve of all data on HD 121620, from the author's observations and from professional sky surveys, is plotted in Figure 3. The sources of the data are: The Hipparcos and Tycho Database (VT magnitudes); ASAS-3 V; ASAS-SN V and g; and the author's V data.

The Hipparacos and Tycho Database contains 129 observations of the VT magnitude of HD 121620 between December 1989 and February 1993. The magnitude varies between 7.21 and 7.28, with 87% of the observations lying in the range 7.23 to 7.26. Thus, the star was either constant, or varied only slightly during this time.

Observations were sourced from the ASAS-3 V database between December 2000 and September 2009. Saturation in survey images between December 2000 and September 2001 resulted in large scatter. These observations are unreliable and were not used. From 2002 onwards exposure times were reduced, thereby avoiding saturation. From these, 615 observations between January 2001 and September 2009 were extracted for analysis in this paper. These observations had little scatter and a mean magnitude of 7.1.

ASAS-SN yielded data in the V and g photometric systems. At the time the data were accessed on 12 December 2019, 813 V-band observations were found from February 2016 to September 2018 and 776 g-band observations were found from June 2018 to September 2019. Thus, only ASAS-SN g-band data are available for the time the personal observations were made. ASAS-SN V magnitudes range from 7.066 to 8.170, with 80% of the observations lying in the range 7.4 to 7.7, whereas the g magnitudes vary from 7.487 to 9.219 (excluding two 11th magnitude outliers), with only 5% of observations being brighter than magnitude 7.9. In comparison with the ASAS-SN V data, the g magnitude range is greater, since the g passband is roughly equivalent to the combined Johnson B and V passbands. There is also a larger scatter in the data, particularly for the fainter magnitudes.

A note of caution is needed concerning ASAS-SN data for bright stars, because the sensors usually saturate between magnitudes 10 and 11 in V. ASAS-SN uses a procedure that improves the data for saturated stars and enables useful photometric information to be obtained, although the degree of improvement is conditional. The best improvement occurs when the charge bleeding from saturated pixels is conservative, and the saturated star is relatively isolated (Kochanek *et al.* 2017). We consider that the improvement in the ASAS-SN photometry for HD 121620 does yield valid data, because inspection of Figure 3 herein reveals that the amplitude of the author's V data is similar to that of the ASAS-SN V data.

3.3. Period analysis

Inspection of Figure 1 suggests a time scale of approximately 24 hours, since light curves taken on consecutive nights are in several instances approximately parallel. Period analysis using Date Compensated Discrete Fourier Transform (DC DFT) in VStar for the period range 0 to 10 days and a resolution of 0.01 reveals the most prominent period to be 1 day with semi-amplitude of 0.35 magnitude (Figure 4).

Analysis of the ASAS-SN V data within a period range of 0 to 50 d and a resolution of 0.01 reveals that the most prominent period is 29.66 d, with a low amplitude of 0.042 magnitude (Figure 5). Analysis of the same data but for the period range 0 to 6 d and a higher resolution (0.001) reveals a prominent peak representing a period of 0.997 d with a low amplitude of 0.053 magnitude (Figure 6).

A similar analysis of the ASAS-SN g observations reveals three peaks close to the noise level of the data. They represent periods of 0.99 d, 6.44 d, and 0.2 d, respectively, with amplitudes of 0.073, 0.071, and 0.064 magnitude (Figure 7). Their significance is uncertain, and they are not considered further in this paper.

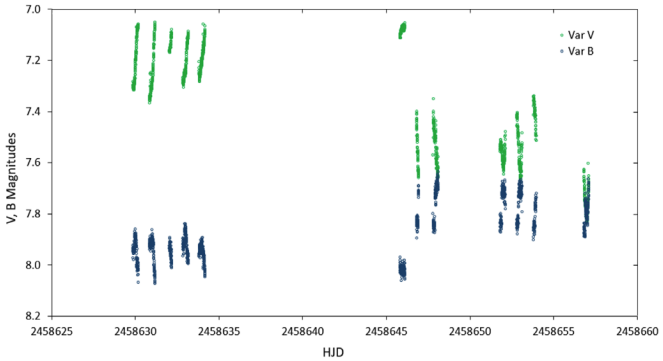

Figure 1. Light curve of HD 121620 from the author's DSLR photometric data obtained during 12 observing nights from 26 May to 23 June 2019. Green and blue represent Johnson V and B data, respectively. This illustration gives an overall view of the entire dataset, showing the magnitude range and the distribution of data across time.

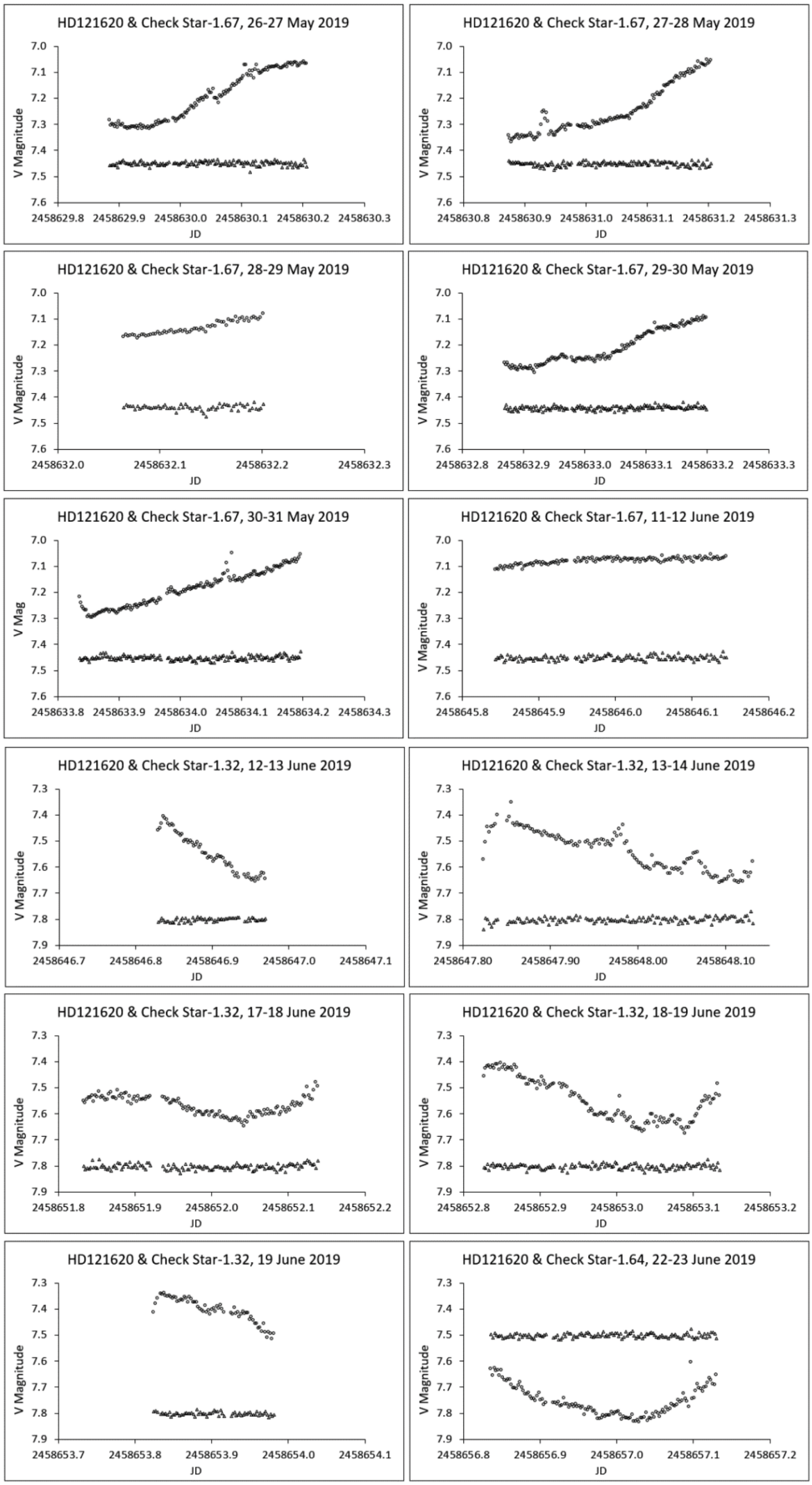

Figure 2. V Light curves of HD 121620 and the check star from the author's data for each of the 12 observing nights. The check star magnitude is offset by various values to allow optimal visualization of the data. The value of the offset is shown in the title of each panel.

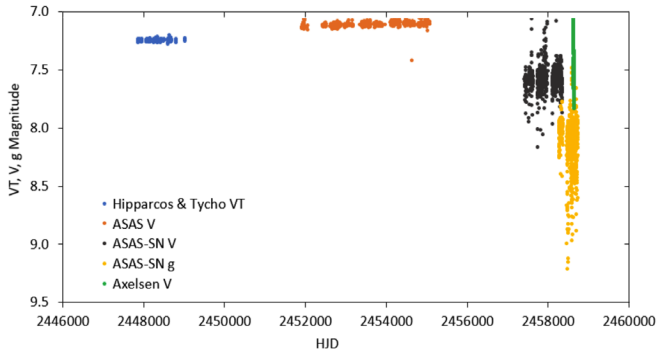

Figure 3. Light curve of HD 121620 from all data sources, 1989–2019. Two outlying 11th magnitude data points have been omitted from the ASAS-SN g data. The author's data are in green.

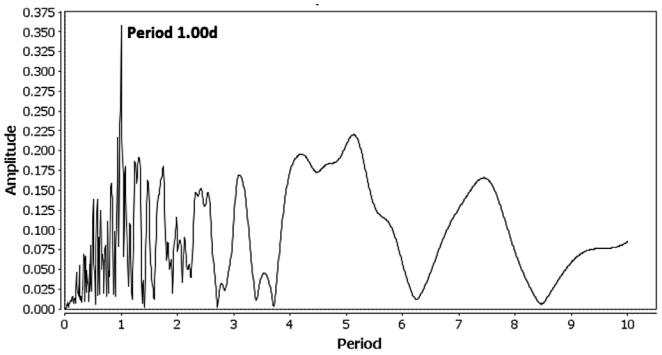

Figure 4. Amplitude versus period plot for HD 121620 at a resolution of 0.01 day from VSTAR using the author's observations. A period of 1 day is most prominent, with amplitude of about 0.35 magnitude.

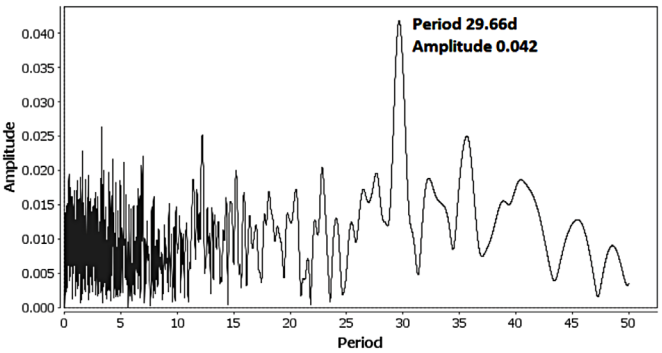

Figure 5. Amplitude versus period plot from 0 to 50 days at a resolution of 0.01 day for HD 121620 from VSTAR using the Johnson V data from ASAS-SN. The amplitude of the data is small. The most prominent peak, 29.66 d, is close to the synodic period of the Moon, and is likely to be spurious (see text).

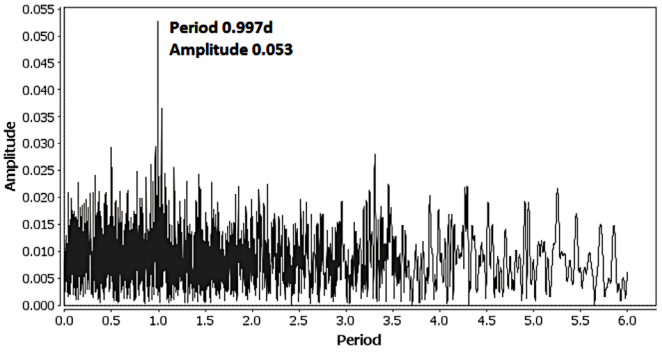

Figure 6. Amplitude versus period plot from 0 to 6 days at a resolution of 0.001 day for HD 121620 from VSTAR using the Johnson V data from ASAS-SN. The amplitude is small. The most prominent peak represents a period 0.997 d.

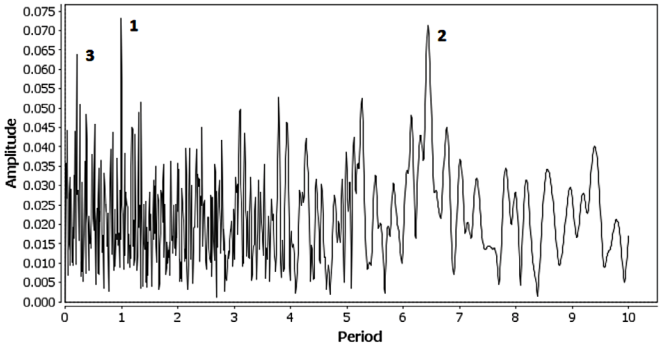

Figure 7. Amplitude versus period plot from 0 to 10 days at a resolution of 0.01 day for HD 121620 from VSTAR using the Sloan g data from ASAS-SN. The three most prominent peaks, numbered 1 to 3 in the above, are not far above the noise level of the data. They represent periods of 0.99d, 6.44d, and 0.2d respectively, with amplitudes of 0.073, 0.071, and 0.064 magnitude, respectively.

4. Discussion

Photometry of HD 121620 is available in five datasets: The Hipparcos and Tycho Database from December 1989 to September 1993; the ASAS-V data from December 2000 to September 2009; the ASAS-SN V band data from January 2017 to September 2018; the ASAS-SN g band data from June 2018 to September 2019; and the author's V data, from 26 May to 23 June 2019.

Perhaps the most remarkable thing about this star is that it was either constant or variable with a very low amplitude when the Hipparcos observations were made, and for most of the time during which ASAS-3 V data is available. Seven years and four months after the last ASAS-3 observations, at the time of the earliest ASAS-SN data in January 2017, variability of HD 121620 was evident, with an amplitude of several tenths of a magnitude in V. This behavior has continued through to the most recent data, with the author's data showing similar overall amplitude to that seen in the ASAS-SN V data. The amplitude of the ASAS-SN g data is greater, and the mean magnitude fainter. These differences would be expected, since the ASAS-SN g passband approximates the combined passbands of Johnson V and B filters, and since the B-V color index varied from 1 to 0 approximately in the author's data.

The cadences of the ASAS-SN V and g data vary from one to several days, with three closely spaced observations about 105 to 110 seconds apart on each day that observations are made. The cadence of the author's data is about 185 seconds for time series photometry over several hours each observing night. Thus, the latter data captures properties of variability that are not revealed by the professional surveys.

Visual inspection and period analysis of the author's and ASAS-SN light curves did not find a consistent regular period; hence a phased light curve could not be constructed. There is, however, a time frame of variation of approximately 24 hours, clearly evident in Figure 1, where several light curves are approximately parallel. Period analysis of the author's data also shows a period of 1 day (Figure 4). This could be an artefact imposed on the data by the time frame inherent in the nightly observing schedule, but the results of the Fourier analysis are supported by the visual evidence from the light curves themselves.

A period of 29.66 d was revealed by Fourier analysis of the ASAS-SN Johnson V data (Figure 5). This duration is very close to the synodic period of the Moon. Percy (2015) has shown that a period of this length is likely to be spurious, representing an alias of much shorter periods. A similar period was also found on analysis of the ASAS-SN g data, but has not been illustrated in this paper.

A period of 0.997d was found in the ASAS-SN V data, but with low amplitude of 0.053 magnitude (Figure 6). The period very close to one day supports a similar value found on visual inspection of the author's light curves, and by Fourier analysis of the author's data. However, as the ASAS-SN observation schedule has an inherent time frame of one day and as the amplitude of the 0.997 d period is very low, it may not reflect a true period.

Analysis of the ASAS-SN g data reveals three peaks representing periods of 0.99 d, 6.44 d, and 0.2 d respectively, all with low amplitudes (0.064 to 0.073 magnitude) and all close to the noise level of the data (Figure 7). The comments applied to the low amplitude period of 0.997d from the ASAS-SN V data in the previous paragraph also apply to the 0.99 d period in the ASAS-SN g data. The other periods, 6.44 d and 0.2 d, have not been found in any other analysis. Because of this and because of their low amplitudes they are not considered to be significant. The type of variability exhibited by HD 121620 has not been determined. Henry *et al.* (2000) found variability in only 19% of G6 to G9 giants, the least variable spectral classes. In contrast he found that 100% of K5 and later type giants in a large sample were variable. From Table 1 of Henry *et al.* (2000), the shortest time scale of variability of a G type star was 25 days, and the periods of variable rotating G6/8 stars from Kepler data are reported to be about 9 to 15 days (from Figure 2 of Nielsen *et al.* 2013). These periods are much longer than the time frame of about one day found in the author's data.

Flares seen in the author's data from three of the twelve nights that HD 161620 was observed would be expected in G type stars (Maehara *et al.* 2012; Shibayama *et al.* 2013).

5. Conclusion

The variability of HD 121620 is unusual. First, Hipparcos observations between December 1989 and February 1993 and ASAS-3 V observations between January 2001 and September 2009 indicate the star was either constant or variable with very low amplitude at those times. Second, despite the fact that this is a bright star of 7th magnitude, its variability is not recorded in either the GCVS or SIMBAD, nor does it appear to receive any specific mention in the searchable publications of the NASA Astrophysics Data System. Third, a time frame of about 1d, without regular periodicity, is strongly suggested by the author's data, both from inspection of the light curves and from period analysis. However, a period as short as this would not be expected in variable G type stars. The nature of variability of HD 121620 is therefore not defined.

6. Acknowledgements

This research has made use of NASA's Astrophysics Data System and the SIMBAD database, operated by CDS, Strasbourg, France.

The author acknowledges with thanks the generous assistance of John Percy in the preparation of this publication.

References

Axelsen, R. A. 2019, *J. Amer. Assoc. Var. Star Obs.*, **47**, 173.

Benn, D. 2012, *J. Amer. Assoc. Var. Star Obs.*, **40**, 852.

Buil, C. 1999–2018, IRIS astronomical images processing software (http://www.astrosurf.com/buil/iris-software.html).

Collins, K. A., Kielkopf, J. F., Stassun, K. G., and Hessman, F. V. 2017, *Astron. J.*, **153**, 77.

Henry, G. W., Fekel, F. C., Henry, S. M., and Hall, D. S. 2000. *Astrophys. J., Suppl. Ser.*, **130**, 201.

Kochanek, C. S. *et al.* 2017, *Publ. Astron. Soc. Pacific*, **129**, 104502.

Maehara, H., *et al.* 2012, *Nature* **485**, 478.

Menzies, J. W., Cousins, A. W. J., Banfield, R. M., and Laing, J. D. 1989, *S. Afr. Astron. Obs. Circ.*, **13**, 1.

Nielsen, M. B., Gizon, L., Schunker, H., and Karoff, C. 2013, *Astron. Astrophys.*, **557**, L10.

Percy, J. R. 2015, *J. Amer. Assoc. Var. Star Obs.*, **43**, 223.

Perryman, M. A. C., European Space Agency Space Science Department, and the Hipparcos Science Team. 1997, *The Hipparcos and Tycho Catalogues*, ESA SP-1200 (VizieR On-line Data Catalog: I/239), ESA Publications Division, Noordwijk, The Netherlands.

Pojmanski, G. 2002, *Acta Astron.*, **52**, 397.

Samus, N. N., Kazarovets, E. V., Durlevich, O. V., Kireeva, N. N., and Pastukhova, E. N. 2017, *Astron. Rep.*, **61**, 80.

Shappee, B. J. *et al.* 2014, *Astrophys. J.*, **788**, 48.

Shibayama, T., *et al.* 2013, *Astrophys. J., Suppl. Ser.*, **209**, 5.

Wenger, M., *et al.* 2000, *Astron. Astrophys., Suppl. Ser.*, **143**, 9.

CCD Photometry, Light Curve Modeling, and Period Study of the Overcontact Binary Systems NSVS 7245866 and V685 Pegasi

Kevin B. Alton
UnderOak Observatory, 70 Summit Avenue, Cedar Knolls, NJ; mail@underoakobservatory.com

Received January 1, 2020; revised February 27, 2020; accepted March 2, 2020

Abstract Precise time-series multi-color (B, V, and I_c) light curve data were acquired at UnderOak Observatory (UO) from NSVS 7245866 (2017) and V685 Peg (2016). Prior to this investigation only monochromatic CCD data for both variables were available from automated surveys which employ sparse sampling strategies. Each target produced new times-of-minimum from data acquired at UO as well as values extrapolated from the SuperWASP survey. These results along with other eclipse timings from the literature were used to generate new ephemerides. Roche modeling of the observed light curve data was accomplished using the Wilson-Devinney code. Each system exhibits a total eclipse, therefore a reliable photometrically derived value for the mass ratio (q_{ptm}) was determined which consequently provided initial estimates for the physical and geometric elements of both variable systems.

1. Introduction

Overcontact binaries (OCs), also known as eclipsing W UMa-type (EW) variables, have stellar components that are in varying degrees of physical contact and therefore share a common atmosphere. They represent at least 25% of all eclipsing binaries found in photometric surveys conducted in both Northern and Southern hemispheres (Kepler (Prša *et al.* 2011); ASAS (Paczyński *et al.* 2006); New South Wales Survey (Christiansen *et al.* 2008)). Despite their relatively high abundance, many questions about energy and mass transfer within and between stars remain unanswered. Since OCs have short orbital periods (0.25–1 d) they are attractive targets for photometric study using modestly sized telescopes equipped with CCD cameras. Their corresponding light curves (LCs) typically exhibit eclipse minima of nearly equal depth that show little color change, thereby suggesting that surface temperatures are similar. Radial velocity studies reveal that the majority of OCs have mass ratios ($q = m_2/m_1$) that diverge considerably from unity and have been observed as low as 0.065–0.08 (Sriram *et al.* 2016; Mochnacki and Doughty 1972; Paczyński *et al.* 2007; Arbutina 2009). Overcontact binaries spend most of their evolutionary lifetimes in physical contact (Stępień 2006; Gazeas and Stępień 2008; Stępień and Kiraga 2015). Depending on many factors, including rate of angular momentum loss, mass ratio, total mass, orbital period and metallicity, OCs are destined to merge into fast rotating stars or to alternatively produce exotic objects such as blue stragglers (Qian *et al.* 2006; Stępień and Kiraga 2015), double degenerate binaries, supernovae, or even double black holes (Almeida *et al.* 2015).

Monochromatic CCD-derived photometric data for NSVS 7245866 were first acquired from the ROTSE-I survey between 1999 and 2000 (Akerlof *et al.* 2000; Wozniak *et al.* 2004; Gettel *et al.* 2006). Later on this system was also captured by the Catalina Sky (Drake *et al.* 2014), and SuperWASP (Butters *et al.* 2010) surveys. Similarly, sparsely sampled photometric data for V685 Pegasi (TYC 2258-1489-1) had been acquired from the ROTSE-I, ASAS (Pojmański *et al.* 2005), Catalina, and SuperWASP surveys. The SuperWASP findings for both systems proved to be a rich source of time (HJD) vs. magnitude data and were further examined to extract out new times-of-minimum (ToM) light and generate period-folded light curves. Although other ToM values have been sporadically reported, this paper marks the first detailed period analyses leading to new ephemerides. Data gathered from the Gaia DR2 release of stellar parameters (Andrae *et al.* 2018) and LAMOST DR5 (Zhao *et al.* 2012; Wang *et al.* 2019) improved the reliability of an effective temperature (T_{eff1}) assigned to each primary star. These refined values were subsequently used for Roche modeling of LCs for NSVS 7245866 and V685 Peg using newly acquired multi-color photometric data. As a result, this investigation also provides the first published photometric mass ratio estimates along with preliminary physical and geometric characteristics for each system.

2. Observations and data reduction

Precise time-series photometric data were acquired at UnderOak Observatory (UO; 74.456217 W, 40.825229 N) with a 0.28-m Schmidt-Cassegrain telescope and an ST-8XME CCD camera installed at the Cassegrain focus. Automated imaging was performed with photometric B-, V-, and I_c filters manufactured to match the Johnson-Cousins Bessell prescription. Computer time was updated immediately prior to each session and exposure time for all images adjusted to 60 s (NSVS 7245866) or 75 s (V685 Peg). Details regarding image acquisition (science frames, darks, and flats), calibration, and registration can be found elsewhere (Alton 2016). Only data from images taken above 30° altitude (airmass < 2.0) were used, consequently, error due to differential refraction and color extinction was minimized and not corrected. Instrumental readings were reduced to MPOSC3 catalog-based magnitudes (Warner 2007) built into MPO CANOPUS v10.7.1.3 (Minor Planet Observer 2011).

3. Results and discussion

Further photometric reduction to LCs was accomplished using an ensemble of at least three non-varying comparison stars in the same field of view (FOV). The identities, J2000

coordinates, V-mags, and MPOSC3 color indices (B–V) for these stars are listed in Table 1. CCD images annotated with the location of target and comparison stars are shown for NSVS 7245866 (Figure 1) and V685 Peg (Figure 2). Uncertainty in comparison star measurements made in the same FOV with NSVS 7245866 or V685 Peg typically stayed within ± 0.007 mag for V- and I_c- and ± 0.010 mag for B-passbands. All photometric data from both systems can be downloaded from the AAVSO archives (https://www.aavso.org/data-download).

3.1. Photometry and ephemerides

Times of minimum (ToM) were calculated using the method of Kwee and van Woerden (1956) as implemented in PERANSO v2.6 (Paunzen and Vanmunster 2016). Curve fitting all eclipse timing differences (ETD) was accomplished using scaled Levenberg-Marquardt algorithms (QtiPlot 2013). The results from these analyses are separately discussed for each binary system in the subsections below.

3.1.1. NSVS 7245866

A total of 333 photometric values in B-, 339 in V-, and 337 in I_c-passbands were acquired at UO from NSVS 7245866 between February 18, 2017, and March 6, 2017. Included in these determinations were four new ToM measurements which are summarized in Table 2. The SuperWASP survey (Butters *et al.* 2010) provided a wealth of photometric data taken (30-s exposures) at modest cadence that repeats every 9 to 12 min. Unfiltered data acquired in 2004 and broadband (400–700 nm) measurements made between 2006 and 2008 were offset relative to V-mag data produced at UO (2017) and then folded together (Figure 3; P = 0.406543 d) by applying periodic orthogonals (Schwarzenberg-Czerny 1996) to fit observations and analysis of variance to assess fit quality (PERANSO v2.6). In some cases (n = 41) the SuperWASP data were amenable to further analysis using the method of Kwee and van Woerden (1956) to estimate ToM values. These results (2006–2008), along with other eclipse timings acquired at UO in 2017 (Table 2), were used to calculate a linear ephemeris (Equation 1):

$$\text{Min.I (HJD)} = 2457818.5685\,(8) + 0.4065432\,(1)\,\text{E}. \quad (1)$$

When all ToM data were included (2004–2017), plotting (Figure 4) the difference between the observed eclipse times and those predicted by the linear ephemeris against epoch (cycle number) reveals what appears to be a quadratic relationship (Equation 2) where:

$$\text{ETD} = -1.47 \cdot 10^{-4} + 2.03 \cdot 10^{-6}\text{E} + 2.13 \cdot 10^{-10}\text{E}^2. \quad (2)$$

In this case the ETD residuals vs. epoch can be described by an expression with a positive quadratic coefficient ($+2.13 \cdot 10^{-10}$), suggesting that the orbital period may have been slowly increasing over time at the rate of 0.033 (7) $\text{s} \cdot \text{y}^{-1}$.

It would be remiss, however, not to note that eclipse timing data for NSVS 7245866 are only available since 2004, with a large time gap between 2008 and 2017. Despite the apparent quadratic fit of the ETD residuals illustrated in Figure 4, the best fit simultaneous LC solution (Figure 3) using SuperWASP (2004–2008) and UO (2017) ToM values had very small uncertainty (P = 0.406543 ± 0.000004 d). Arguably, if there is a secular change in the orbital period, the rate would be similar to many other contact systems reported in the literature (Giménez *et al.* 2006). Furthermore, given the paucity of data, it is not surprising that no other underlying variations in the orbital period stand out, such as those that might be caused by magnetic cycles (Applegate 1992) or the presence of an additional gravitationally bound stellar-size body. At a minimum, another decade of precise times of minimum will be needed to reveal whether the orbital period of this system is changing in a predictable fashion.

3.1.2. V685 Peg

A total of 304 photometric values in B-, 303 in V-, and 313 in I_c-passbands were acquired from V685 Peg between October 18, 2016, and November 8, 2016. Included with the ToM data summarized in Table 3 are five new values acquired at UO, 24 times estimated from the SuperWASP survey, as well as three other published times that were used to calculate a new linear ephemeris (Equation 3):

$$\text{Min.I (HJD)} = 2457700.6725\,(4) + 0.3172596\,(4)\,\text{E}. \quad (3)$$

These data, shown in Figure 5, suggest that the orbital period of V685 Peg has not meaningfully changed since 2004. Furthermore, as can be seen (Figure 6), TAMMAG2 values from SuperWASP, which were offset to match the mean V-mag observed in 2016, produced the best fit LC when P = 0.317260 ± 0.000004 d.

3.2. Effective temperature estimation

The primary star is defined as the more massive member of each binary system throughout this paper. The effective temperature of the primary star (T_{eff1}) was derived from a composite of astrometric (USNO-A2.0, USNO-B1.0, and UCAC4) and photometric (2MASS, SDSS-DR8, and APASS) survey measurements (B–V), low resolution spectra obtained from LAMOST-DR5 (Zhao *et al.* 2012; Wang *et al.* 2019), the Gaia DR2 release of stellar parameters (Andrae *et al.* 2018), and color index (B–V) data acquired at UO. Interstellar extinction (A_V) was calculated using the reddening value (E(B–V)) estimated from the median of six Galactic dust map models (Amôres *et al.* 2011) reproduced within the GALExtin VO-service (http://www.galextin.org/v1p0/).

Intrinsic color, $(B–V)_0$, for NSVS 7245866 calculated from measurements made at UO and those determined from five other sources are listed in Table 4. The median value (0.505 ± 0.093) indicates a primary star with an effective temperature (6260 ± 333 K) that probably ranges in spectral class between F6V and F7V. Houdashelt *et al.* (2000) reported an improved color-temperature relation for cool dwarf stars ($0.32 \leq (B–V) \leq 1.35$) wherein T_{eff1} was calculated to be 6204 ± 380 K. These results, when combined with other T_{eff1} estimates from Gaia DR2 (6066^{+202}_{-140} K) and LAMOST DR5 (6254 ± 14), produced a median value of 6230 ± 267 K which was used for subsequent Roche modeling. Notably, this determination is consistent with the spectral type assigned (F5V) to NSVS 7245866 based on

Table 1. Astrometric coordinates (J2000), V-mags and color indices (B–V) for NSVS 7245866 (Figure 1), V685Peg (Figure 2), and their corresponding comparison stars used in this photometric study.

Star Identification	*R. A. (J2000)* *h m s*	*Dec. (J2000)* *° ′ ″*	*V-mag*[a]	*(B-V)*[a]
(T) NSVS 7245866	07 36 53.06	+34 40 20.60	11.253	0.443
(1) GSC 02461-02062	07 36 57.76	+34 41 58.03	11.230	0.478
(2) GSC 02461-02214	07 36 43.07	+34 39 32.47	12.271	0.482
(3) GSC 02461-01637	07 36 23.34	+34 36 56.22	10.379	0.258
(4) GSC 02461-01381	07 36 41.69	+34 42 37.69	11.999	0.442
(5) GSC 02461-01073	07 37 01.50	+34 44 48.88	12.188	0.569
(T) V685 Peg	23 53 19.50	+28 23 49.68	11.707	0.685
(1) GSC 02258-01111	23 53 59.13	+28 26 57.01	10.116	0.653
(2) GSC 02258-01840	23 53 01.00	+28 18 39.27	11.690	0.738
(3) GSC 02258-01581	23 53 41.07	+28 19 21.59	11.977	1.005

[a]*V-mag and (B–V) for comparison stars derived from MPOSC3 database described by Warner (2007).*

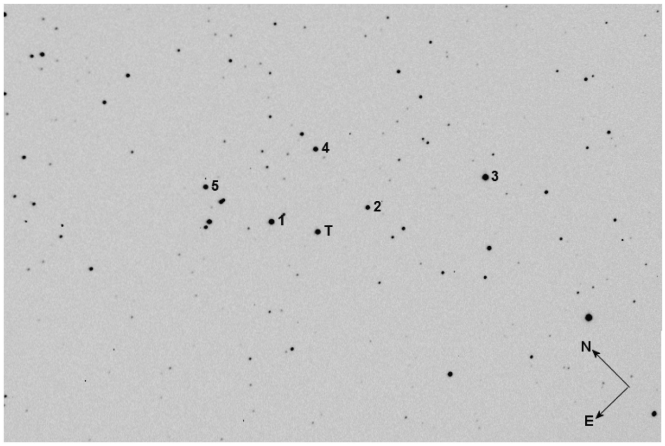

Figure 1. CCD image (V-mag) of NSVS 7245866 (T) showing the location of comparison stars (1–5) used to generate MPOSC3-derived magnitude estimates.

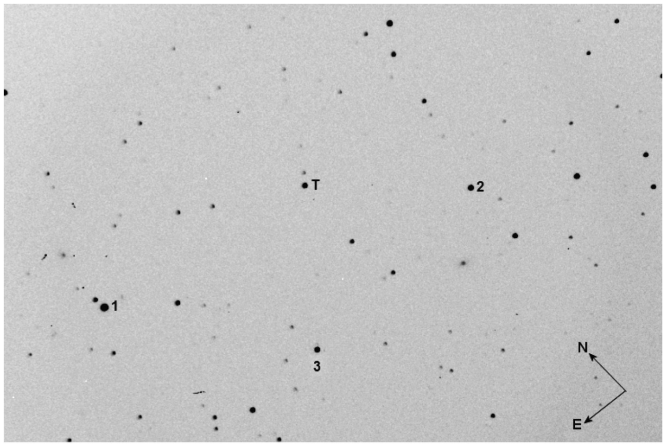

Figure 2. CCD image (V-mag) of V685 Peg (T) showing the location of comparison stars (1–3) used to generate MPOSC3-derived magnitude estimates.

low-resolution spectra taken in 2017 and reported in LAMOST DR5 (http://dr5.lamost.org/spectrum/view?obsid=535813088).

Similarly, dereddened color indices from UO and five other sources are summarized for V685 Peg in Table 5. The median value (0.718 ± 0.047) corresponds to a primary star with an effective temperature (5520 ± 186 K) that likely ranges in spectral class between G7V and G8V. As above, this result, when combined with the value (T_{eff1} = 5521 ± 270 K) calculated according to Houdashelt *et al.* (2000), the Gaia DR2 estimate (5355^{+149}_{-92} K), and that reported (5582 ± 23 K) in LAMOST DR5, yielded a median of 5521 ± 168 K which was adopted for ensuant Roche modeling. Based on a low resolution spectrum (http://dr5.lamost.org/spectrum/view?obsid=490308235) reported in LAMOST DR5, the spectral classification of the primary star is G7V, a result consistent with the V685 Peg color-temperature data presented herein.

Table 2. NSVS 7245866 times-of-minimum (September 29, 2004–March 6, 2017), cycle number and residuals (ETD) between observed and predicted times derived from the updated linear ephemeris (Equation 1).

HJD (2400000 +)	*HJD Error*	*Cycle Number*	*Eclipse Time Difference*	*Reference*
53277.68797	0.0005	–11169.5	0.00349	1
53278.70647	0.0007	–11167	0.00564	1
54056.62331	0.0007	–9253.5	0.00206	1
54057.63575	0.0009	–9251	–0.00186	1
54067.59702	0.0003	–9226.5	–0.00090	1
54070.64627	0.0003	–9219	–0.00072	1
54083.65866	0.0006	–9187	0.00229	1
54084.67078	0.0004	–9184.5	–0.00196	1
54085.68981	0.0002	–9182	0.00072	1
54092.6018	0.0008	–9165	0.00148	1
54098.70019	0.0005	–9150	0.00171	1
54099.51119	0.0003	–9148	–0.00037	1
54099.71531	0.0005	–9147.5	0.00048	1
54100.52696	0.0004	–9145.5	–0.00096	1
54101.54608	0.0004	–9143	0.00181	1
54111.50419	0.0002	–9118.5	–0.00040	1
54115.57181	0.0006	–9108.5	0.00180	1
54118.61771	0.0007	–9101	–0.00138	1
54120.65221	0.0003	–9096	0.00040	1
54122.47948	0.0004	–9091.5	–0.00177	1
54135.48954	0.0006	–9059.5	–0.00109	1
54139.55809	0.0007	–9049.5	0.00202	1
54140.57325	0.0008	–9047	0.00083	1
54141.38471	0.0004	–9045	–0.00080	1
54141.58998	0.0010	–9044.5	0.00120	1
54142.40159	0.0005	–9042.5	–0.00028	1
54142.60458	0.0009	–9042	–0.00056	1
54145.45119	0.0003	–9035	0.00025	1
54146.4653	0.0009	–9032.5	–0.00200	1
54150.53261	0.0005	–9022.5	–0.00012	1
54153.37728	0.0005	–9015.5	–0.00125	1
54153.58513	0.0005	–9015	0.00333	1
54154.39456	0.0005	–9013	–0.00033	1
54155.40972	0.0004	–9010.5	–0.00153	1
54156.42874	0.0005	–9008	0.00113	1
54162.52576	0.0003	–8993	0.00001	1
54163.53846	0.0007	–8990.5	–0.00366	1
54168.41671	0.0009	–8978.5	–0.00392	1
54170.45072	0.0009	–8973.5	–0.00263	1
54171.46803	0.0007	–8971	–0.00167	1
54539.38955	0.0001	–8066	–0.00176	1
57804.54332	0.0001	–34.5	0.00028	2
57805.55905	0.0001	–32	–0.00035	2
57815.51906	0.0001	–7.5	–0.00065	2
57818.56878	0.0001	0	0.00000	2

References: 1. SuperWASP (Butters et al. *2010); 2. This study at UO.*

3.3. Roche modeling approach

Roche modeling of LC data from NSVS 7245866 and V685 Peg was performed with PHOEBE 0.31a (Prša and Zwitter

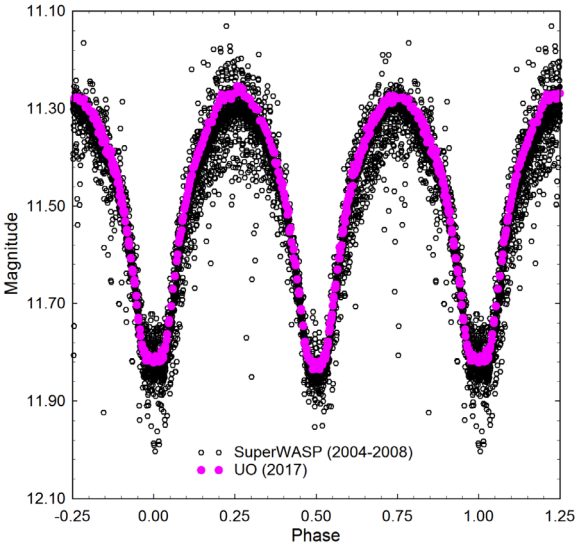

Figure 3. Period folded (P = 0.406543 ± 0.000004 d) light curve data (TAMMAG2 vs. HJD) for NSVS 7245866 acquired from the SuperWASP Survey (2004–2008) and V-mag measurements made at UO in 2017.

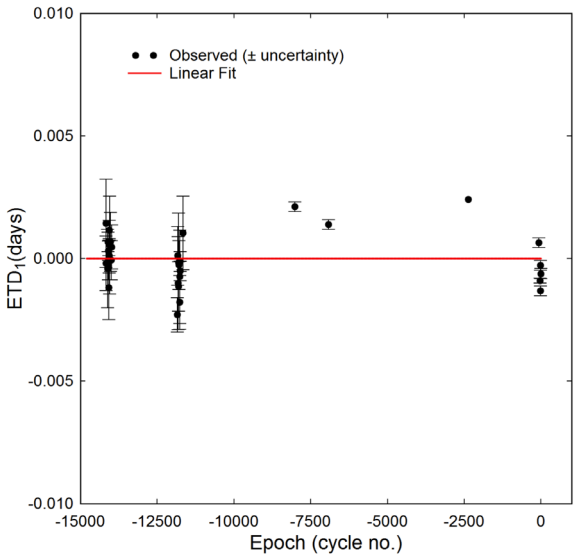

Figure 5. Eclipse timing differences (ETD) vs. epoch for V685 Peg calculated using the updated linear (Equation 3). Measurement uncertainty is denoted by the hatched vertical lines. The solid red line within the figure indicates the Levenberg-Marquardt derived linear fit.

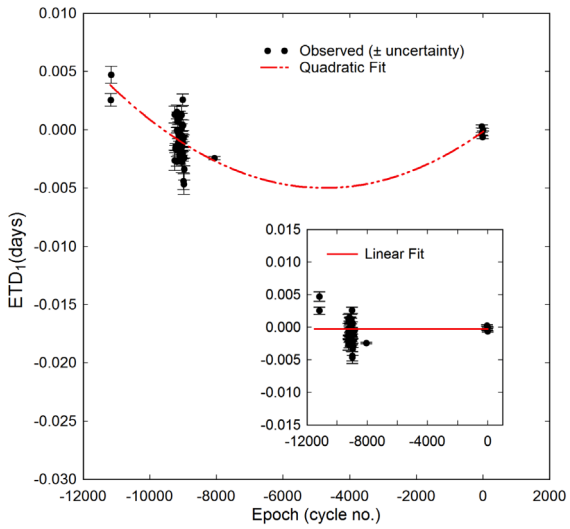

Figure 4. Eclipse timing differences (ETD) vs. epoch for NSVS 7245866 calculated using the updated linear (Equation 1) and quadratic ephemerides (Equation 2). Measurement uncertainty is denoted by the hatched vertical lines. The dashed red line represents the quadratic fit while the solid red line within the figure insert indicates the linear fit.

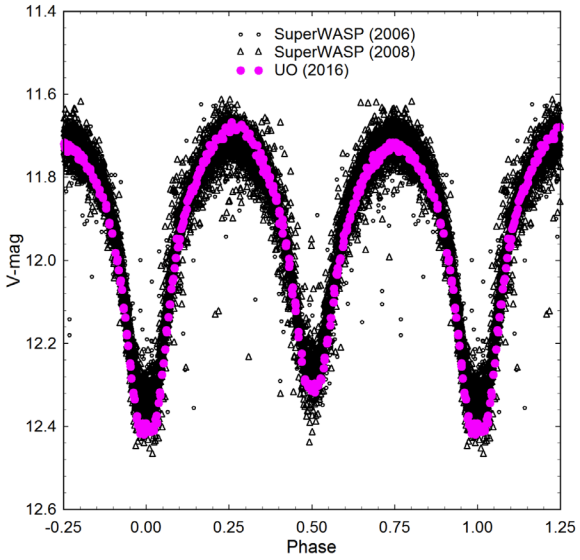

Figure 6. Period folded (P = 0.317260 ± 0.000004 d) light curve data (TAMMAG2 vs. HJD) for V685 Peg acquired from the SuperWASP Survey in 2006 and 2008 and V-mag measurements made at UO in 2016.

2005) and WDWINT56A (Nelson 2009). Both programs feature a MSWINDOWS-compatible GUI interface to the Wilson-Devinney WD 2003 code (Wilson and Devinney 1971; Wilson 1979; Wilson 1990). WDWINT56A incorporates Kurucz's atmosphere models (Kurucz 2002) that are integrated over BVR$_c$I$_c$ passbands. In both cases, the selected model was Mode 3 for an overcontact binary. Other modes (detached and semi-detached) were explored but never approached the goodness of fit achieved with Mode 3. Since the internal energy transfer to the surface of both variable systems is driven by convective (< 7500 K) rather than radiative processes, the value for bolometric albedo ($A_{1,2}$ = 0.5) was assigned according to Ruciński (1969) while the gravity darkening coefficient ($g_{1,2}$ = 0.32) was adopted from Lucy (1967). Logarithmic limb darkening coefficients (x_1, x_2, y_1, y_2) were interpolated (Van Hamme 1993) following each change in the effective temperature (T_{eff2}) of the secondary star during model fit optimization using differential corrections (DC). All but the temperature of the more massive star T_{eff1}, $A_{1,2}$, and $g_{1,2}$ were allowed to vary during DC iterations. In general, the best fits for T_{eff2}, i, q, and Roche potentials ($\Omega_1 = \Omega_2$) were collectively refined (method of multiple subsets) by DC using the multicolor LC data until a simultaneous solution was found. LCs from NSVS 7245866 (Figures 7 and 8) and V685 Peg (Figures 9 and 10) exhibit asymmetry during quadrature (Max I ≠ Max II) which is often called the O'Connell effect (O'Connell 1951). Both systems required the addition of spots to obtain the

Table 3. V685 Peg times-of-minimum (July 17, 2004–November 8, 2016), cycle number and residuals (ETD) between observed and predicted times derived from the updated linear ephemeris (Equation 3).

HJD (2400000 +)	*HJD Error*	*Cycle Number*	*Eclipse Time Difference*	*Reference*
53203.6776	0.0018	–14174.5	0.00144	1
53207.6417	0.0011	–14162	–0.00020	1
53220.6492	0.0016	–14121	–0.00042	1
53228.5817	0.0004	–14096	0.00068	1
53229.5328	0.0008	–14093	–0.00007	1
53232.5471	0.0004	–14083.5	0.00031	1
53235.5596	0.0013	–14074	–0.00119	1
53238.5748	0.0007	–14064.5	0.00011	1
53239.5277	0.0004	–14061.5	0.00115	1
53242.5410	0.0020	–14052	0.00054	1
53253.4866	0.0012	–14017.5	0.00068	1
53259.5138	0.0008	–13998.5	–0.00007	1
53263.6387	0.0009	–13985.5	0.00047	1
53944.6337	0.0007	–11839	–0.00230	1
53947.6501	0.0012	–11829.5	0.00011	1
53952.5665	0.0019	–11814	–0.00101	1
53953.6768	0.0010	–11810.5	–0.00114	1
53954.6295	0.0020	–11807.5	–0.00016	1
53961.6091	0.0010	–11785.5	–0.00027	1
53967.6355	0.0011	–11766.5	–0.00179	1
53968.5883	0.0019	–11763.5	–0.00075	1
53970.6512	0.0004	–11757	–0.00012	1
53973.6647	0.0004	–11747.5	–0.00051	1
54003.4887	0.0015	–11653.5	0.00104	1
55158.6320	0.0002	–8012.5	0.00211	2
55503.6511	0.0002	–6925	0.00138	3
56947.9765	[a]	–2372.5	0.00241	4
57679.5754	0.0002	–66.5	0.00064	5
57690.5193	0.0001	–32	–0.00091	5
57693.5339	0.0002	–22.5	–0.00028	5
57697.4986	0.0002	–10	–0.00132	5
57700.6719	0.0002	0	–0.00062	5

[a] *Not reported. References: 1. SuperWASP; 2. Diethelm (2010); 3. Diethelm (2011); 4. Nagai (2015); 5. This study at UO.*

best fit LC simulations. A hot spot on the secondary star was incorporated during Roche modeling of NSVS 7245866 (Figure 11), while a cool spot on each component was necessary to achieve the best fit of LC data for V685 Peg (Figure 12). A statistically meaningful ($l_3 > 0$) third light contribution was evident in all bandpasses during DC optimization for NSVS 7245866. Since each system clearly undergoes a total eclipse, Roche model convergence to a unique value for q is self-evident, thereby obviating the need for any "q-search" exercise. These general findings are described in more detail within the subsections for each variable that follow.

3.4. Roche modeling results

In general, it is not possible to unambiguously determine the mass ratio, subtype (A or W), or total mass without radial velocity (RV) data. Nonetheless, since a total eclipse is observed in the LCs from both systems, a unique mass ratio value for each system could be found (Terrell and Wilson 2005). Standard errors reported in Tables 6 and 7 are computed from the DC covariance matrix and only reflect the model fit to the observations which assumes exact values for any fixed parameter. These errors are generally regarded as unrealistically small, considering the estimated uncertainties associated with the mean adopted T_{eff1} values along with basic assumptions about $A_{1,2}$, $g_{1,2}$ and the influence of spots added to the Roche model. Normally, the value for T_{eff1} is fixed with no error during modeling with the WD code despite measurement uncertainty which can arguably approach 10% relative standard deviation (R.S.D.) without supporting spectral data. The effect that such uncertainty in T_{eff1} would have on modeling estimates for q, i, $\Omega_{1,2}$, and T_{eff2} has been investigated with other overcontact binaries including A- (Alton 2019) and W-subtypes (Alton and Nelson 2018). As might be expected, any change in the fixed value for T_{eff1} results in a corresponding change in the T_{eff2}. These results are notably consistent whereby the uncertainty in the model fit for T_{eff2} would be essentially the same as that established for T_{eff1}. For example, with NSVS 7245866, the expected uncertainty for T_{eff2} would be ±267 K. Furthermore, varying T_{eff1} by as much as 10% did not appreciably affect the uncertainty estimates (R.S.D. < 2%) for i, q, or $\Omega_{1,2}$ (Alton 2019; Alton and Nelson 2018). Assuming that the actual T_{eff1} values for NSVS 7245866 and V685 Peg fall within 10% of the adopted values used for Roche modeling (a reasonable presumption according to results presented in section 3.2), then uncertainty estimates for i, q, or $\Omega_{1,2}$ along with spot size, temperature, and location would likely not exceed 2% R.S.D.

The fill-out parameter (f) which corresponds to the outer surface shared by each star was calculated according to Equation 4 (Kallrath and Milone 1999; Bradstreet 2005) where:

$$f = (\Omega_{inner} - \Omega_{1,2})/(\Omega_{inner} - \Omega_{outer}), \quad (4)$$

wherein Ω_{outer} is the outer critical Roche equipotential, Ω_{inner} is the value for the inner critical Roche equipotential, and $\Omega = \Omega_{1,2}$ denotes the common envelope surface potential for the binary system. In both cases the systems are considered overcontact since $0 < f < 1$.

3.4.1. NSVS 7245866

LC parameters and geometric elements derived from WDWINT56A are summarized in Table 6. According to Binnendijk (1970) the deepest minimum (Min I) of an A-type overcontact system occurs when the cooler and less massive constituent transits across the face of the hotter and more massive star. Therefore, the flat-bottomed dip in brightness at Min II is indicative of a total eclipse of the secondary. It was evident that NSVS 7245866 is most likely an A-type overcontact binary given other diagnostic clues such as its spectral class (F5V) and orbital period (P > 0.4 d). Consequently, WD modeling proceeded under this assumption. It became immediately apparent that model-simulated LCs at Min I and Min II were consistently deeper than the observed values in all three bandpasses. This result was remediated by allowing the third light parameter (l_3) to freely vary during DC optimization. These findings (Table 6) suggest the presence of a blue-rich ($l_3(B) > l_3(V)$ or $l_3(I_c)$) field star in the distant background that has contaminated the light from NSVS 7245866. Analysis of potential secular changes in the orbital period that might arise from the influence of a third gravitational body is not possible at this time due to the limited availability of precise eclipse timing data. Despite the lack of supporting evidence for a stellar body in close

Table 4. Estimation of effective temperature (T_{eff1}) of NSVS 7245866 based upon dereddened (B–V) data from five surveys and the present study.

	USNO-B1.0	*USNO-A2.0*	*2MASS*	*APASS DR9*	*UCAC4*	*Present Study*
$(B–V)_0$[a]	0.651	0.628	0.399	0.505	0.505	0.425
T_{eff1}[b] (K)	5766	5824	6684	6260	6260	6574
Spectral Class[b]	G2V-G3V	G1V-G2V	F3V-F4V	F6V-F7V	F6V-F7V	F4V-F5V

[a] *Intrinsic $(B–V)_0$ determined using reddening value E(B–V) = 0.027 ± 0.004.*
[b] *T_{eff1} interpolated and spectral class range estimated from Pecaut and Mamajek (2013). Median value, $(B–V)_0$ = 0.505 ± 0.093, corresponds to an F6V-F7V primary star (T_{eff1} = 6260 ± 333 K).*

Table 5. Estimation of effective temperature (T_{eff1}) of V685 Peg based upon dereddened (B–V) data from five surveys and the present study.

	USNO-A2.0	*2MASS*	*SDSS-DR8*	*UCAC4*	*APASS DR9*	*Present Study*
$(B–V)_0$[a]	0.808	0.657	0.708	0.728	0.826	0.687
T_{eff1}[b] (K)	5293	5740	5562	5505	5244	5641
Spectral Class[b]	G9V-K0V	G2V-G3V	G6V-G7V	G7V-G8V	K0V-K1V	G5V-G6V

[a] *Intrinsic $(B–V)_0$ determined using reddening value E(B–V) = 0.028 ± 0.001.*
[b] *T_{eff1} interpolated and spectral class range estimated from Pecaut and Mamajek (2013). Median value, $(B–V)_0$ = 0.718 ± 0.047, corresponds to a G7V-G8V primary star (T_{eff1} = 5520 ± 186 K).*

Table 6. Light curve parameters evaluated by Roche modeling and the geometric elements derived for NSVS 7245866 assuming it is an A-type W UMa variable.

Parameter	*No spot*	*Hot spot*
T_{eff1} (K)[b]	6230 (267)	6230 (267)
T_{eff2} (K)	6366 (3)	6351 (3)
q (m_2 / m_1)	0.359 (1)	0.350 (1)
A[b]	0.5	0.5
g[b]	0.32	0.32
$\Omega_1 = \Omega_2$	2.526 (2)	2.504 (2)
i°	87.1 (3)	87.2 (3)
$A_S = T_s / T_\star$[c]	—	1.08 (1)
Θ_S (spot co-latitude)[c]	—	90 (7)
φ_S (spot longitude)[c]	—	351 (1)
r_S (angular radius)[c]	—	23 (1)
$L_1 / (L_1 + L_2)_B$[d]	0.6855 (3)	0.6925 (2)
$L_1 / (L_1 + L_2)_V$	0.6923 (1)	0.6986 (1)
$L_1 / (L_1 + L_2)_{Ic}$	0.6985 (1)	0.7040 (1)
l_3 (B)[e]	0.7372 (64)	0.8820 (56)
l_3 (V)	0.5357 (27)	0.5400 (27)
l_3 (I_c)	0.2702 (17)	0.2677 (17)
r_1 (pole)	0.4548 (3)	0.4578 (2)
r_1 (side)	0.4902 (4)	0.4941 (3)
r_1 (back)	0.5215 (5)	0.5255 (5)
r_2 (pole)	0.2886 (8)	0.2874 (2)
r_2 (side)	0.3028 (10)	0.3017 (3)
r_2 (back)	0.3474 (19)	0.3474 (5)
Fill-out factor (%)	30.6	32.6
RMS (B)[f]	0.00781	0.00755
RMS (V)	0.00561	0.00511
RMS (I_c)	0.00451	0.00432

[a] *All uncertainty estimates for T_{eff2}, q, $\Omega_{1,2}$, i, $r_{1,2}$, and L_1 from WDWINT56a (Nelson 2009).*
[b] *Fixed with no error during DC.*
[c] *Secondary star spot parameters in degrees (Θ_S, φ_S and r_S) or A_S in fractional degrees (K).*
[d] *L_1 and L_2 refer to scaled luminosities of the primary and secondary stars, respectively.* [e] *Fractional percent luminosity of third light parameter (l_3) at φ = 0.25.*
[f] *Monochromatic residual mean square error from observed values.*

Table 7. Lightcurve parameters evaluated by Roche modeling and the geometric elements derived for V685 Peg assuming it is a W-type W UMa variable.

Parameter	*No spot*	*Cool spots*
T_{eff1} (K)[b]	5521 (168)	5521 (168)
T_{eff2} (K)	5842 (5)	5774 (2)
q (m_2 / m_1)	0.386 (1)	0.404 (1)
A[b]	0.5	0.5
g[b]	0.32	0.32
$\Omega_1 = \Omega_2$	2.620 (2)	2.643 (3)
i°	89.8 (2)	87.0 (4)
$A_P = T_s / T_\star$[c]	—	0.79 (1)
Θ_P (spot co-latitude)	—	90 (1)
φ_P (spot longitude)	—	189 (1)
r_P (angular radius)	—	12.0 (1)
$A_S = T_s / T_\star$[d]	—	0.78 (1)
Θ_S (spot co-latitude)	—	90 (1)
φ_S (spot longitude)	—	103 (1)
r_S (angular radius)	—	19.9 (1)
$L_1 / (L_1 + L_2)_B$[e]	0.6260 (4)	0.6317 (2)
$L_1 / (L_1 + L_2)_V$	0.6468 (3)	0.6482 (1)
$L_1 / (L_1 + L_2)_{Ic}$	0.6627 (2)	0.6609 (1)
r_1 (pole)	0.4413 (6)	0.4398 (4)
r_1 (side)	0.4727 (7)	0.4712 (5)
r_1 (back)	0.5014 (8)	0.5011 (5)
r_2 (pole)	0.2859 (17)	0.2915 (9)
r_2 (side)	0.2988 (20)	0.3051 (11)
r_2 (back)	0.3359 (36)	0.3439 (20)
Fill-out factor (%)	12.9	17.3
RMS (B)[f]	0.01622	0.00943
RMS (V)	0.01520	0.00735
RMS (I_c)	0.01249	0.00590

[a] *All uncertainty estimates for T_{eff2}, q, $\Omega_{1,2}$, i, $r_{1,2}$, and L_1 from WDWINT56a (Nelson 2009).*
[b] *Fixed with no error during DC.*
[c] *Primary star spot parameters in degrees (Θ_P, φ_P and r_P) or A_P in fractional degrees (K).*
[d] *Secondary star spot parameters in degrees (Θ_S, φ_S and r_S) or A_S in fractional degrees (K).*
[e] *L_1 and L_2 refer to scaled luminosities of the primary and secondary stars, respectively.*
[f] *Monochromatic residual mean square error from observed values.*

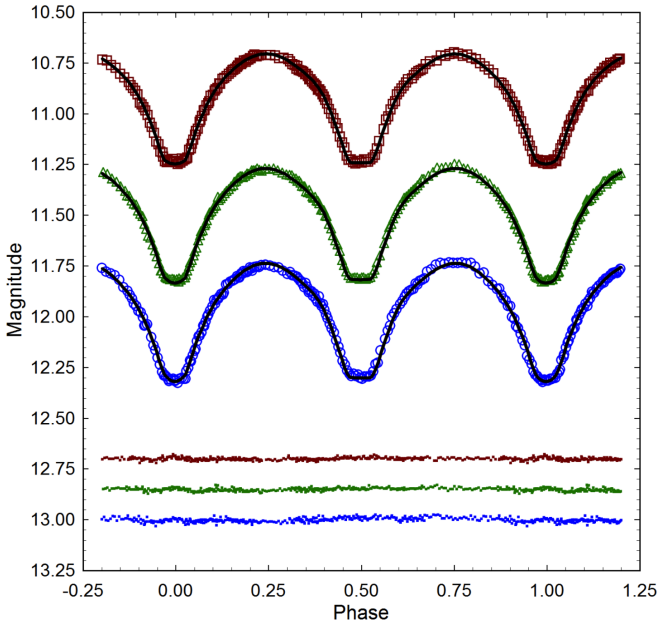

Figure 7. Folded CCD light curves for NSVS 7245866 produced from photometric data obtained between February 18, 2017, and March 6, 2017. The top (I_c), middle (V), and bottom curve (B) shown above were reduced to MPOSC3-based catalog magnitudes using MPO CANOPUS. In this case, the Roche model assumed an A-type overcontact binary with a third light contribution and no spots; residuals from the model fits are offset at the bottom of the plot to keep the values on scale.

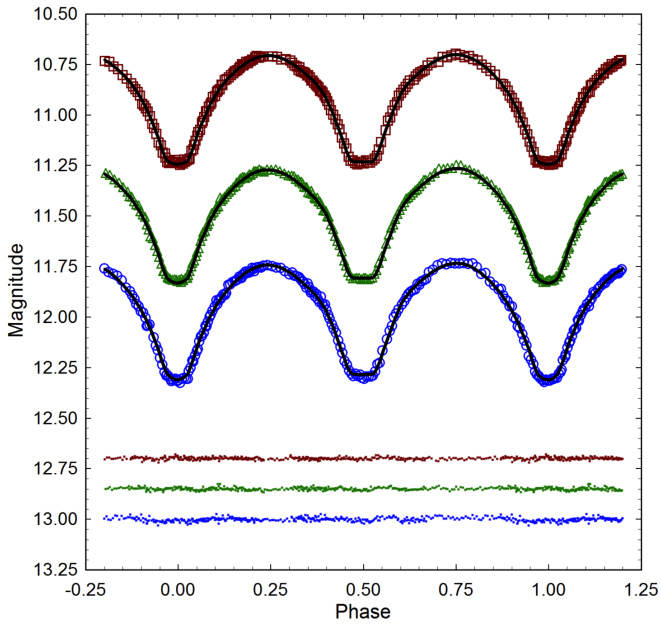

Figure 8. CCD light curves for NSVS 7245866 as shown in Figure 7 except that this case, the Roche model assumed an A-type overcontact binary with a hot spot on the secondary star.

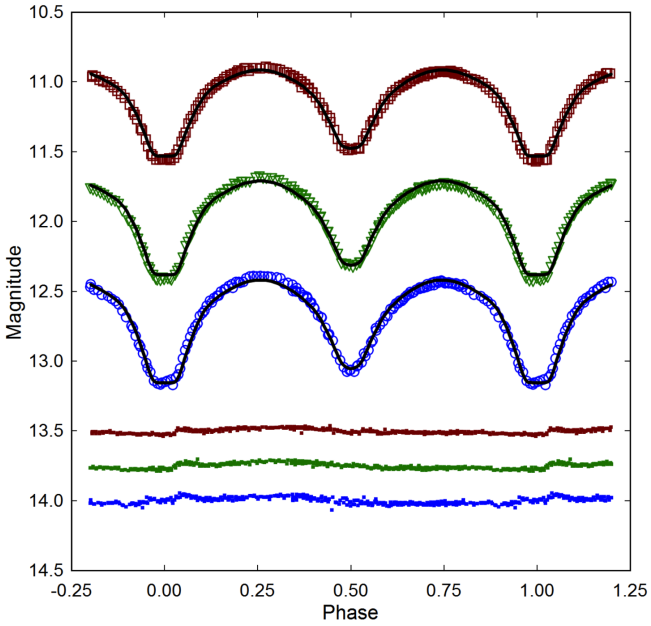

Figure 9. Folded CCD light curves for V685 Peg produced from photometric data obtained between October 18, 2016, and November 8, 2016. The top (I_c), middle (V), and bottom curve (B) shown above were reduced to MPOSC3-based catalog magnitudes using MPO CANOPUS. In this case, the Roche model assumed a W-type overcontact binary with no spots; residuals from the model fits are offset at the bottom of the plot to keep the values on scale.

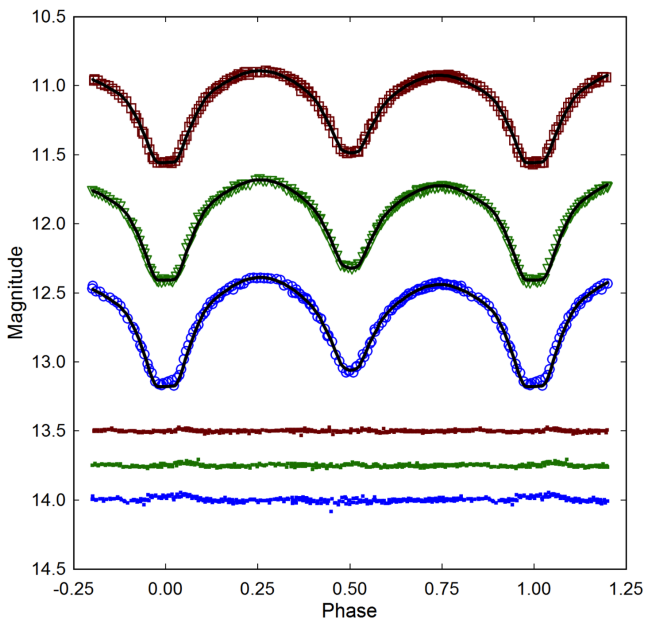

Figure 10. CCD light curves for V685 Peg as in Figure 9, however in this case, the Roche model assumed a W-type overcontact binary with a cool spot on both stars.

proximity, the presence of a hot main sequence star in the same neighborhood as NSVS 7245866 would likely overwhelm any photometric measurement, thereby discounting this possibility. However unlikely, a nearby faint blue object such as a white dwarf could satisfactorily explain the blue-rich third light.

In order to address the slight asymmetry observed during maximum light (Max I < Max II), a hot spot was added near the neck of the secondary star. This provided a modest improvement to the light curve fits during Min II (Figure 8) as reflected in the lower residual mean square error compared to that obtained from the unspotted fit (Table 6). A three-dimensional image rendered (Figure 11) using BINARY MAKER 3 (BM3; Bradstreet and Steelman 2004) illustrates the secondary star transit across the primary face during Min I ($\varphi = 0$) and the hot spot location on the secondary star ($\varphi = 0.68$). Also, it should be noted that contrary to expectations for an A-type system, the best fit of the LC data occurred when the effective temperature of the secondary star (T_{eff2}) was higher (121–136 K) than the primary

Table 8. Fundamental stellar parameters for NSVS 7245866 using the mean photometric mass ratio ($q_{ptm} = m_2/m_1$) from the spotted Roche model fits of LC data (2017) and the estimated mass based on empirically derived M-PRs for overcontact binary systems.

Parameter	*Primary*	*Secondary*
Mass ($M_\odot$)	1.38 ± 0.08	0.48 ± 0.03
Radius ($R_\odot$)	1.34 ± 0.02	0.83 ± 0.01
a ($R_\odot$)	2.84 ± 0.04	2.84 ± 0.04
Luminosity ($L_\odot$)	2.43 ± 0.42	1.01 ± 0.03
M_{bol}	3.79 ± 0.03	4.74 ± 0.03
Log (g)	4.32 ± 0.03	4.28 ± 0.03

Table 9. Fundamental stellar parameters for V685 Peg using the mean photometric mass ratio ($q_{ptm} = m_2 / m_1$) from the spotted Roche model fits of LC data (2016) and the estimated mass based on empirically derived M-PRs for W UMa type variable stars.

Parameter	*Primary*	*Secondary*
Mass ($M_\odot$)	1.17 ± 0.07	0.47 ± 0.03
Radius ($R_\odot$)	1.06 ± 0.02	0.70 ± 0.01
a ($R_\odot$)	2.31 ± 0.03	2.31 ± 0.03
Luminosity ($L_\odot$)	0.94 ± 0.12	0.49 ± 0.01
M_{bol}	4.81 ± 0.03	5.52 ± 0.03
Log (g)	4.46 ± 0.03	4.42 ± 0.03

(T_{eff1}) component (Table 6). Not without precedence, this phenomenon has also been observed for EK Com (Deb *et al.* 2010), HV Aqr (Gazeas *et al.* 2007), BO CVn (Zola *et al.* 2012), and TYC 1664-0110-1 (Alton and Stępień 2016).

3.4.2. V685 Peg

V685 Peg would appear to be a W-subtype overcontact binary system based on its spectral classification (G7V), orbital period ($P < 0.4$ d), and LC behavior. As shown in Figures 9 and 10, the flattened bottom at the deepest minimum (Min I) results from the occultation of the hotter secondary by the larger, but cooler primary star. Since according to the convention used herein where the primary star is the most massive ($m_2/m_1 \leq 1$), a phase shift (0.5) was introduced to properly align the LC for subsequent Roche modeling. LC parameters and geometric elements with their associated uncertainty were derived using WDWINT56A (Table 7). The best LC fits were obtained by the addition of a single cool spot on each star. A three-dimensional rendering produced using BM3 (Figure 12) shows a transit of the hotter secondary across the face of the primary star during Min II ($\varphi = 0.5$) and the location of each spot on the binary pair ($\varphi = 0.83$).

3.5. Absolute parameters

Fundamental stellar parameters were estimated for each binary system using results from the best fit spotted LC simulations. However, without the benefit of RV data which define the orbital motion, mass ratio, and total mass of the binary pair, these results should be more accurately described as "relative" rather than "absolute" parameters and considered preliminary in that regard.

3.5.1. NSVS 7245866

Three empirically derived mass-period relationships (M-PR) for W UMa-binaries have been published. The first M-PR was reported by Qian (2003) while two others followed from Gazeas and Stępień (2008) and then Gazeas (2009). According to Qian (2003) when the primary star is less than 1.35 $M_\odot$ or the system is W-type its mass can be determined from Equation 5:

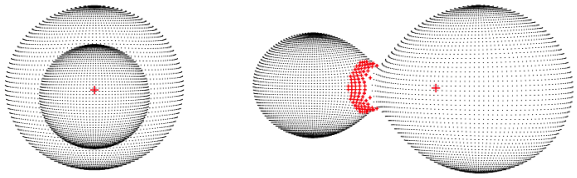

Figure 11. Three-dimensional spatial model of NSVS 7245866 illustrating the transit of the secondary star across the primary star face at Min I ($\varphi = 0$) and hot spot location ($\varphi = 0.68$) near the neck region of the secondary star.

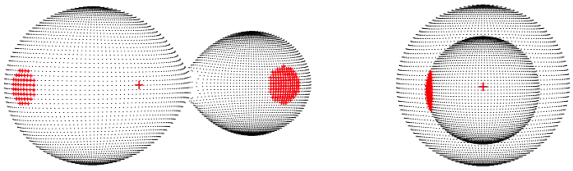

Figure 12. Three-dimensional spatial model of V685 Peg showing a transit of the hotter secondary across the face of the cooler primary star at Min II ($\varphi = 0.5$) and the locations of a single cool spot on each of the binary constituents ($\varphi = 0.83$).

$$\log(M_1) = 0.391\,(59) \cdot \log(P) + 1.96\,(17), \quad (5)$$

or alternatively when $M_1 > 1.35\ M_\odot$ or A-type then Equation 6:

$$\log(M_{-1}) = 0.761\,(150) \cdot \log(P) + 1.82\,(28), \quad (6)$$

where P is the orbital period in days. Using the most appropriate relationship (Equation 6) leads to $M_1 = 1.50 \pm 0.19\ M_\odot$ for the primary. The M-PR (Equation 7) derived by Gazeas and Stępień (2008):

$$\log(M_1) = 0.755\,(59) \cdot \log(P) + 0.416\,(24), \quad (7)$$

corresponds to a W UMa system where $M_1 = 1.32 \pm 0.10\ M_\odot$. Gazeas (2009) reported another empirical relationship (Equation 8) for the more massive (M_1) star of a contact binary such that:

$$\log(M_1) = 0.725\,(59) \cdot \log(P) - 0.076\,(32) \cdot \log(q) + 0.365\,(32), \quad (8)$$

from which $M_1 = 1.30 \pm 0.13\ M_\odot$. The mean of three values ($M_1 = 1.38 \pm 0.08\ M_\odot$) estimated from empirical models (Equations 6, 7, and 8) was used for subsequent determinations of M_2, semi-major axis a, volume-radii r_L, and bolometric magnitudes (M_{bol}) for NSVS 7245866.

The secondary mass $= 0.48 \pm 0.03\ M_\odot$ and total mass ($1.86 \pm 0.09\ M_\odot$) of the system were consequently determined using the mean photometric mass ratio (0.350 ± 0.001) from the spotted Roche model. By comparison, a single MS star with a mass similar to the secondary (late K-type) would likely be much smaller ($R_\odot \sim 0.54$), cooler ($T_{eff} \sim 3900$ K), and far less luminous ($L_\odot \sim 0.06$). The semi-major axis, $a(R_\odot) = 2.84 \pm 0.04$, was calculated from Newton's version (Equation 9) of Kepler's third law where:

$$a^3 = (G \cdot P^2 (M_1 + M_2)) / (4\pi^2). \quad (9)$$

The effective radius of each Roche lobe (r_L) can be calculated over the entire range of mass ratios ($0 < q < \infty$) according to an expression (Equation 10) derived by Eggleton (1983):

$$r_L = (0.49q^{2/3}) / (0.6q^{2/3} + \ln(1 + q^{1/3})), \quad (10)$$

from which values for r_1 (0.4917 ± 0.0002) and r_2 (0.2928 ± 0.0002) were determined for the primary and secondary stars, respectively. Since the semi-major axis and the volume radii are known, the radii in solar units for both binary components can be calculated where $R_1 = a \cdot r_1 = 1.34 \pm 0.02\,R_\odot$ and $R_2 = a \cdot r_2 = 0.83 \pm 0.01\,R_\odot$.

Luminosity in solar units ($L_\odot$) for the primary (L_1) and secondary stars (L_2) was calculated from the well-known relationship derived from the Stefan-Boltzmann law (Equation 11) where:

$$L_{1,2} = (R_{1,2} / R_\odot)^2 (T_{1,2} / T_\odot)^4. \quad (11)$$

Assuming that $T_{eff1} = 6230$ K, $T_{eff2} = 6351$ K, and $T_\odot = 5772$ K, then the solar luminosities ($L_\odot$) for the primary and secondary are $L_1 = 2.43 \pm 0.42$ and $L_2 = 1.01 \pm 0.03$, respectively. According to the Gaia DR2 release of stellar parameters (Andrae *et al.* 2018), the reported T_{eff} (6066^{+202}_{-140} K) is probably not meaningfully different from the adopted T_{eff1} (6230 ± 136 K) value. However, the predicted size ($R_\odot = 1.64^{+0.08}_{-0.10}$) and luminosity ($L_\odot = 3.30^{+0.101}_{-0.102}$) for the primary star in NSVS 7245866 are greater than the corresponding values generated by the study herein. Based on the Bailer-Jones (2015) correction for parallax data in Gaia DR2 this system can be found at a distance of $391.2^{+8.7}_{-8.4}$ pc. By comparison, using values (V_{max}, A_V, and M_V) independently derived herein, the distance modulus equation corrected for interstellar extinction places NSVS 7245866 about 13% closer (341 ± 31 pc) to the Gaia DR2 determination which is presently regarded as the "gold-standard" for Galactic distances.

3.5.2. V685 Peg

To estimate the primary star mass for V685 Peg (Table 9) the same approach described for NSVS 7245866 was used. In this case, the M-PRs (Equations 5, 7, 8) lead to a mean value of $1.17 \pm 0.07\,M_\odot$ for the primary star. The secondary mass ($0.47 \pm 0.03\,M_\odot$) and total mass ($1.65 \pm 0.07\,M_\odot$) of the system were derived from the spotted model photometric mass ratio (0.404 ± 0.001). Assuming solar-like metallicity, a solitary main sequence star with a similar mass (late K-type to early M-type) would probably be much smaller ($R_\odot \sim 0.52$), cooler ($T_{eff} \sim 3600$ K), and much less luminous ($L_\odot < 0.06$). The semi-major axis ($a(R_\odot)$), the effective radius of each Roche lobe (r_L), the radii in solar units ($R_\odot$), and the luminosities in solar units ($L_\odot$) were calculated as described for NSVS 7245866. According to the Gaia DR2 release of stellar parameters (Andrae *et al.* 2018), the reported Teff (5355^{+149}_{-92} K) is not meaningfully different from the adopted value ($T_{eff1} = 5521 \pm 168$ K) used herein. Likewise, the Gaia DR2 reported size ($R_\odot = 1.12^{+0.04}_{-0.06}$) and luminosity ($L_\odot = 0.925^{+0.018}_{-0.018}$) of the primary star are comparable to values estimated by the study herein (Table 9). According to the Bailer-Jones (2015) correction for parallax-derived distances reported in Gaia DR2 (Gaia Collab. *et al.* 2018) this system is $257.3^{+2.62}_{-2.56}$ pc away. A value independently derived from the distance modulus equation using data generated at UO places V685 Peg at a similarly distant 262 5 pc.

4. Conclusions

New times of minimum for NSVS 7245866 (n = 45) and V685 Peg (n = 32) based on multicolor CCD data (BVI_c) acquired at UO and values extrapolated from the SuperWASP survey are reported herein. These along with a few other published values led to a new linear ephemeris for each system. Eclipse timings from NSVS 7245866 also produced what appears to be a quadratic relationship suggesting that the orbital period might be increasing at a rate of $0.033\ s \cdot y^{-1}$. Both systems will require many more years of precise eclipse timing data to further substantiate any potential change(s) in orbital period. The adopted effective temperatures (T_{eff1}) for NSVS 7245866 (6230 ± 267 K) and V685 Peg (5521 ± 168 K) were based on a composite of four sources that notably included values from the Gaia DR2 release of stellar characteristics (Andrae *et al.* 2018) and estimates from LAMOST DR5 spectral data (Zhao *et al.* 2012; Wang *et al.* 2019). Both overcontact systems clearly experience a total eclipse which is evident as a flattened bottom during minimum light. Since NSVS 7245866 is most likely an A-type W UMa variable, this feature is observed during Min II. By contrast, V685 Peg exhibits a flattened bottom during its deepest minimum light (Min I) as would be expected from a W-type overcontact eclipsing binary. The photometric mass ratios for NSVS 7245866 ($q_{ptm} = 0.350$) and V685 Peg ($q_{ptm} = 0.404$) determined by Roche modeling of each totally eclipsing system should prove to be reliable substitutes for mass ratios derived from RV data. Nonetheless, spectroscopic studies (RV and high resolution classification spectra) will be required to unequivocally determine a total mass and spectral class for both systems.

5. Acknowledgements

This research has made use of the SIMBAD database operated at Centre de Données astronomiques de Strasbourg, France. In addition, the Northern Sky Variability Survey hosted by the Los Alamos National Laboratory (https://skydot.lanl.gov/nsvs/nsvs.php), the All Sky Automated Survey Catalogue of Variable Stars (http://www.astrouw.edu.pl/asas/?page=acvs), and the Catalina Surveys Data Release 2 archives maintained at http://nesssi.cacr.caltech.edu/DataRelease/ were mined for essential information. This work also presents results from the European Space Agency (ESA) space mission Gaia. Gaia data are being processed by the Gaia Data Processing and Analysis Consortium (DPAC). Funding for the DPAC is provided by national institutions, in particular the institutions participating in the Gaia MultiLateral Agreement (MLA). The Gaia mission website is https://www.cosmos.esa.int/gaia. The Gaia archive website is https://archives.esac.esa.int/gaia. This paper makes use of data from the first public release of the WASP data as

provided by the WASP consortium and services at the NASA Exoplanet Archive, which is operated by the California Institute of Technology, under contract with the National Aeronautics and Space Administration under the Exoplanet Exploration Program. The use of public data from LAMOST is also acknowledged. Guoshoujing Telescope (the Large Sky Area Multi-Object Fiber Spectroscopic Telescope LAMOST) is a National Major Scientific Project built by the Chinese Academy of Sciences. Funding for the project has been provided by the National Development and Reform Commission. LAMOST is operated and managed by the National Astronomical Observatories, Chinese Academy of Sciences.

The careful review and helpful commentary provided by Dr. Joel Eaton is gratefully acknowledged.

References

Akerlof, C., *et al.* 2000, *Astron. J.*, **119**, 1901.
Almeida, L. A., *et al.* 2015, *Astrophys. J.*, **812**, 102.
Alton, K. B. 2016, *J. Amer. Assoc. Var. Star Obs.*, **44**, 87.
Alton, K. B. 2019, *J. Amer. Assoc. Var. Star Obs.*, **47**, 7.
Alton, K. B., and Nelson, R. H. 2018, *Mon. Not. Roy. Astron. Soc.*, **479**, 3197.
Alton, K. B., and Stępień, K. 2016, Acta Astron., 66, 357.
Amôres, E. B., Moitinho, A., Arsenijevic, V., and Sodré, L 2011, in *Star Clusters in the Era of Large Surveys*, eds. A. Moitinho, J. Alves, Springer, Berlin-Heidelberg, 93.
Andrae, R., *et al.* 2018, *Astron. Astrophys.*, **616A**, 8.
Applegate, J. H. 1992, *Astrophys. J.*, **385**, 621.
Arbutina, B. 2009, *Mon. Not. Roy. Astron. Soc.*, **394**, 501.
Bailer-Jones, C. A. L. 2015, *Publ. Astron. Soc. Pacific*, **127**, 994.
Binnendijk, L. 1970, *Vistas Astron.*, **12**, 217.
Bradstreet, D. H. 2005, in *The Society for Astronomical Sciences 24th Annual Symposium on Telescope Science*, Society for Astronomical Science, Rancho Cucamonga, CA, 23.
Bradstreet, D. H., and Steelman, D. P. 2004, BINARY MAKER 3, contact software (http://www.binarymaker.com).
Butters, O. W., *et al.* 2010, *Astron. Astrophys.*, **520**, L10.
Christiansen, J. L., *et al.* 2008, *Mon. Not. R. Astron. Soc.*, **385**, 1749.
Deb, S., Singh, H. P., Seshadri, T. R., and Gupta, R. 2010, *New Astron.*, **15**, 662.
Diethelm, R. 2010, *Inf. Bull. Var. Stars*, No. 5920, 1.
Diethelm, R. 2011, *Inf. Bull. Var. Stars*, No. 5960, 1.
Drake, A. J., *et al.* 2014, *Astrophys. J., Suppl. Ser.*, **213**, 9.
Eggleton, P. P. 1983, *Astrophys. J.*, **268**, 368.
Gaia Collaboration, Brown, A.G.A., *et al.* 2018, *Astron. Astrophys.*, **616A**, 1.
Gazeas, K. D. 2009, *Commun. Asteroseismology*, **159**, 129.
Gazeas, K. D., Niarchos, P. G., and Zola, S. 2007, in *Solar and Stellar Physics Through Eclipses*, ASP Conf. Ser. 370, Astronomical Society of the Pacific, San Francisco, 279.
Gazeas, K., and Stępień, K. 2008, *Mon. Not. Roy. Astron. Soc.*, **390**, 1577.
Gettel, S. J., Geske, M. T., and McKay, T. A. 2006, *Astron. J.*, **131**, 621.
Giménez, A., Guinan, E., Niarchos, P., and Ruciński, S., eds. 2006, *Close Binaries in the 21st Century: New Opportunities and Challenges*, Springer, Dordrecht.
Houdashelt, M. L., Bell, R. A., and Sweigart, A. V. 2000, *Astron. J.*, **119**, 1448.
Kallrath, J., and Milone, E. F. 1999, *Eclipsing Binary Stars: Modeling and Analysis*, Springer, New York.
Kurucz, R. L. 2002, *Baltic Astron.*, **11**, 101.
Kwee, K. K., and van Woerden, H. 1956, *Bull. Astron. Inst. Netherlands*, **12**, 327.
Lucy, L. B. 1967, *Z. Astrophys.*, **65**, 89.
Minor Planet Observer. 2011, MPO Software Suite (http://www.minorplanetobserver.com), BDW Publishing, Colorado Springs.
Mochnacki, S. W., and Doughty, N. A. 1972, *Mon. Not. Royal Astron. Soc.*, **156**, 51.
Nagai, K. 2015, *Bull. Var. Star Obs. League Japan*, **59**, 7.
Nelson, R. H. 2009, WDWINT56A: Astronomy Software by Bob Nelson (https://www.variablestarssouth.org/bob-nelson).
O'Connell, D. J. K. 1951, *Publ. Riverview Coll. Obs.*, **2**, 85.
Paunzen, E., and Vanmunster, T. 2016, *Astron. Nachr.*, **337**, 239.
Paczyński, B., Sienkiewicz, R., and Szczygiel, D. M. 2007, *Mon. Not. Roy. Astron. Soc.*, **378**, 961.
Paczyński, B., Szczygiel, D. M., Pilecki, B. and Pojmański, G. 2006, *Mon. Not. Royal Astron. Soc.*, **368**, 1311
Pecaut, M., and Mamajek, E. E. 2013, *Astrophys. J., Suppl. Ser.*, **208**, 9.
Pojmański, G., Pilecki, B., and Szczygiel, D. 2005, *Acta Astron.*, **55**, 275.
Prša, A., and Zwitter, T. 2005, *Astrophys. J.*, **628**, 426.
Prša, A., *et al.* 2011, *Astron. J.*, **141**, 83
Qian, S-B. 2003, *Mon. Not. Roy. Astron. Soc.*, **342**, 1260.
Qian, S., Yang, Y., Zhu, L., H., He, J., and Yuan, J. 2006, *Astrophys. Space Sci.*, **304**, 25
QtiPlot. 2013, QTIPLOT v0.9.9-rc9, Data analysis and scientific visualisation (https://www.qtiplot.com/).
Ruciński, S. M. 1969, *Acta Astron.*, **19**, 245.
Wang, R., *et al.* 2019, *Pub. Astron. Soc. Pacifc*, **131**, 024505
Schwarzenberg-Czerny, A. 1996, *Astrophys. J., Lett.*, **460**, 107.
Sriram, K., Malu, S., Choi, C.S., and Vivekananda Rao, P. 2016, *Astron. J.*, **151**, 69.
Stępień, K. 2006, *Acta Astron.*, **56**, 199.
Stępień, K., and Kiraga, M. 2015, *Astron. Astrophys.*, **577A**, 117.
Terrell, D., and Wilson, R. E. 2005, *Astrophys. Space Sci.*, **296**, 221.
van Hamme, W. 1993, *Astron. J.*, **106**, 2096.
Warner, B. D. 2007, *Minor Planet Bull.*, **34**, 113.
Wilson, R. E. 1979, *Astrophys. J.*, **234**, 1054.
Wilson, R. E. 1990, *Astrophys. J.*, **356**, 613.
Wilson, R. E., and Devinney, E. J. 1971, *Astrophys. J.*, **166**, 605.
Wozniak, P. R., *et al.* 2004, *Astron. J.*, **127**, 2436.
Zhao, G., Zhao, Y.-H., Chu, Y.-Q., Jing, Y.-P, and Deng, L.-C. 2012, *Res. Astron. Astrophys.*, **12**, 723.
Zola, S., Nelson, R. H., Şenavcı, H. V., Szymanski, T., Kuźmicz, A., Winiarski, M., and Jableka, D. 2012, *New Astron.*, **17**, 673.

Period Analysis of All-Sky Automated Survey for Supernovae (ASAS-SN) Data on a Sample of "Irregular" Pulsating Red Giants

John R. Percy
Department of Astronomy and Astrophysics, and Dunlap Institute for Astronomy and Astrophysics, University of Toronto, 50 St. George Street, Toronto, ON M5S 3H4, Canada; john.percy@utoronto.ca

Received January 22, 2020; revised March 13, 2020; accepted March 17, 2020

Abstract All-Sky Automated Survey for Supernovae (ASAS-SN) data and, for some stars, AAVSO visual and V data have been used to study the possible periodicity of 74 "irregular" pulsating red giants (PRGs) in the AAVSO observing program. Results have been obtained and tabulated for 41 of them. For most of the tabulated stars, the new data provide more and/or better results than AAVSO data alone. All have small amplitudes. Several of the stars appear to have a long secondary period, as well as a pulsation period. A very few may be bimodal. Only about half of the periods that we derive are consistent with the periods in the VSX catalogue. We recommend that the AAVSO consider which of these small-amplitude "irregular" stars should continue to be observed, and how.

1. Introduction

Red giant stars are unstable to pulsation. In the *General Catalogue of Variable Stars* (GCVS; Samus *et al.* 2017), pulsating red giants (PRGs) are classified according to their light curves. Mira (M) stars have reasonably regular light curves, with visual ranges greater than 2.5 magnitudes. Semiregular (SR) stars are classified as SRa if there is appreciable periodicity, and SRb if there is little periodicity. Irregular (L) stars have very little or no periodicity. These divisions are arbitrary; there is a smooth spectrum of behavior in these stars, in amplitude, in period, and in degree of periodicity or irregularity. This paper deals with the "irregular" end of the spectrum.

There are hundreds of PRGs in the AAVSO visual observing program which are classified as SR or L type, but which have not been well-analyzed—usually because the number and distribution of measurements is insufficient. Percy and Terziev (2011), following on the work of Percy and Long (2010), analyzed data on "neglected" L-type stars in the AAVSO International Database (Kafka 2020) and, in their Table 2, recommended which stars might benefit from further observations—preferably photoelectric or CCD—and which would not.

Data from the All-Sky Automated Survey for Supernovae (ASAS-SN: Jayasinghe *et al.* 2018, 2019) is now available for almost all of these L-type stars, and can potentially provide additional information about their variability and periodicity. In the present paper, we use the ASAS-SN data and the AAVSO time-series package VSTAR (Benn 2013) to study the periods and amplitudes of as many of these stars as possible. We also analyze AAVSO visual and PEP/CCD data on these stars where available, to complement the ASAS-SN data. The purposes of this project are (1) to determine whether any of these "irregular" variables show sufficient periodicity to be reclassified as semiregular, (2) to determine the amplitudes of variability and, based on these and the degree of periodicity, recommend whether they should continue to be observed by the AAVSO and, if so, how, and (3) to compare our results with those given by the AAVSO VSX catalogue (Watson *et al.* 2014). The purpose was not to undertake astrophysical analysis of these stars; they are not suited for that purpose.

2. Data and analysis

Data were downloaded from the ASAS-SN website, and Fourier-analyzed using the AAVSO time-series analysis package vstar (Benn 2013). Where possible, AAVSO visual or Johnson V data (Kafka 2020) were analyzed also, though this paper reports only on stars which had usable ASAS-SN data. Note that ASAS-SN data are not suitable for stars brighter than V = 7 or fainter than V = 17. The precision of the period(s) that we determined was limited by the length of the dataset which, in the case of the ASAS-SN data, was about 2,000 days, so the uncertainty in the periods was typically about one percent. Pulsation periods of red giants are also known to "wander" by a few percent (Eddington and Plakadis 1929). The data available to us were often sparse, especially in the case of the AAVSO data. These limitations must be kept in mind when comparing results from ASAS-SN and AAVSO data with each other, and with results from the VSX catalogue and other results in the literature. As usual, we had to be alert for alias and harmonic periods, to distinguish them from overtone periods, which can be astrophysically useful (Percy and Huang 2015). Percy and Fenaux (2019) have discussed some other problems with ASAS-SN automated analysis and classification of pulsating red giants.

3. Results

The initial sample of stars was taken from Table 2 in Percy and Terziev (2011). There were some stars which were not observed by ASAS-SN, usually because they were too bright. For others, the ASAS-SN data were too sparse or scattered for analysis. For yet others, the combined ASAS-SN and AAVSO data did not produce any meaningful period results, either because the data were insufficient, or because the star's amplitude was too small, or because the star was truly irregular. In this paper, amplitude refers to the coefficient of the best-fit sine curve with the period under discussion; the peak-to-peak range would be twice this.

WY Gem, BU Gem, KK Per, and PR Per are actually classified as red supergiants, but it is still important to know

Table 1. Analysis of ASAS-SN data on irregular pulsating red giants.

Star Name	*P(days)*	*A (mag.)*	*PVSX (days)*	*Notes*
V338 Aql	47 ± 3	0.09	75.499374	LSP 760 d, A 0.1
HM Aur	270 ± 5	0.34	—	also 742 d, A 0.28
DK Boo	63	0.05	60.23	
UX Cam	94	0.11	—	LSP 920 ± 20 d, A 0.22
AA Cam	75 ± 25	0.08	—	LSP 650 d, A 0.13
UV Cnc	150 ± 50	0.16	148.520266	
RU Car	111	0.06	359	
BO Car	145	0.19	130.7	
WW Cas	400	0.13	—	also 233 d, A 0.11
AA Cas	80	0.14	—	LSP 800 d, A 0.15
PY Cas	55:	0.10	111	possible LSP 566 d, A 0.13
V396 Cen	220 ± 10	0.18	230.769226	also P 400 d, A 0.18?
SW Cet	80.5	0.19	53.93228	possible LSP 1150 ± 100 d, A 0.20
AO Cru	290	0.12	—	results uncertain
SV Cyg	410 ± 10	0.20:	196	also P 200 ± 10 d, A 0.15
AX Cyg	370 ± 10	0.16	361:	also P 188 d, A 0.13
BI Cyg	800 ± 50	0.18	—	also P 319 d, A 0.13
V485 Cyg	55 ± 5	0.09	—	
V1152 Cyg	118	0.17	—	
V2429 Cyg	503	0.27	—	
CT Del	82.2	0.12	83.5	LSP 350 ± 10 d, A 0.16
KP Del	27 ± 2	0.27	—	
AZ Dra	367	0.23	357	AAVSO data give 357 d
AV Eri	232	0.22	78.6	also P 123 d, A 0.12 overtone?
WY Gem	344	0.05	23550	
FI Gem	149	0.10	95.89142	also P 70 d? results uncertain
GN Her	91.7	0.09	—	LSP 533 d, A 0.17
V939 Her	67.6	0.13	—	LSP 417: d, A 0.14
TU Lyr	146.5	0.19	—	also P 278: d, A 0.16
PX Lyr	66	0.14	—	LSP 500 ± 100 d, 0.18
EX Ori	112:	0.19	115	LSP 910 d, A 0.15
V352 Ori	114 ± 5	0.10	118.6	
GO Peg	75 ± 5	0.09	79.3	
PV Peg	36.9	0.11	520	LSP also present?
FR Per	218.5	0.12	—	
ST Psc	822	0.28	540	also P 75–100 d?
V727 Sco	390:	0.09	—	
CP Tau	273	0.09	—	LSP 1365 d, A 0.12
V TrA	250	0.08	—	
FI Vel	40.4	0.02	—	not a PRG?
NSV 14284	85.9	0.20	87.7	

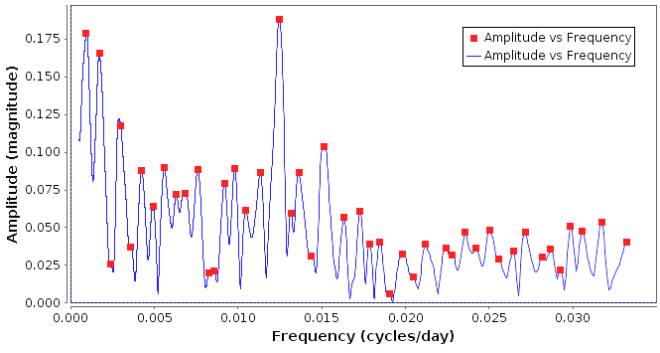

Figure 1. The Fourier spectrum of SW Cet, using ASAS-SN data. There appears to be a pulsation period of 80.5 days (frequency 0.0124 cycle / day), with an amplitude of 0.19 mag, and also a long secondary period of about a thousand days and an amplitude of 0.18 mag. The latter is not inconsistent with the period derived from AAVSO visual data, namely 1,280 days with an amplitude of 0.20. The VSX period is 53.93228 days. There is no evidence for this period, above the noise level, in the ASAS-SN Fourier spectrum.

whether these stars are truly "irregular" and/or should be removed from the AAVSO observing program—especially the visual program.

The following stars are probably non-variable: SV Aur, DR Boo, IZ Cas, UW Dra, KK Per, HU Sge, and NSV 14213. For the following stars, we were not able to obtain any results, usually because the ASAS-SN data were sparse or non-existent: NO Aur, VY UMa, NQ Cas, V391 Cas, AD Cen, AS Cep, T Cyg, RY Cyg, TV Cyg, CY Cyg, LW Cyg, QZ Cyg, V449 Cyg, V1173 Cyg, AC Dra, AT Dra, BU Gem, OP Her, TT Leo, T Lyr, X Lyr, XY Lyr, SY Peg, PR Per, X TrA, and RW Vir.

Table 1 lists stars for which we obtained some evidence of a coherent period. All these stars had ASAS-SN data, and all except RU Car, V352 Ori, V727 Sco, V TrA, and FI Vel had usable AAVSO data. Given the low amplitude of most of these stars, and their complexity—wandering periods, variable amplitudes, long secondary periods (LSPs)—the periods can usually not be specified precisely. Likewise, the amplitudes in Table 1 are "typical" values; somewhat different values might be obtained over different time periods. These amplitudes are

almost all less than 0.2 mag. We also list the VSX period, PVSX, in days. The fourth column gives notes on some of the stars. Figure 1 shows the Fourier spectrum of a typical star, SW Cet. It has a pulsation period of 80.5 days which is well-defined, and much different than the VSX period of 53.93228 days. It also appears to have a long secondary period.

Detailed notes on the stars which were analyzed can be found on the following permanent, open-access website, maintained by the author's university: http://hdl.handle.net/1807/99842

4. Discussion

None of the stars in Table 1 appear to be strictly periodic, but they are candidates for reclassification as semiregular. The search for any degree of periodicity was challenging. The amplitudes were small. The ASAS-SN data were limited in length. The AAVSO visual data were limited in accuracy. Any AAVSO V data were sporadic, at best. Many of the stars that we studied did not yield any results. Many of the stars in Table 1 show evidence for long secondary periods, and the AAVSO data were useful in confirming some of these periods. It is significant that long secondary periods are reasonably common in irregular stars (or stars classified as such).

Among the stars with periods in the VSX catalogue, about half of our periods are inconsistent with the VSX periods, whereas the other half appear to be consistent. We note that a few of our stars have VSX periods which are expressed to 7 or 8 significant figures. This is not appropriate for these stars, which are semiregular at best, with "wandering" periods, and finite datasets.

Most of these stars continue to be observed visually—even the stars with amplitudes of 0.1 or less, including stars which are probably non-variable. For example: in the last decade, there have been dozens of visual measurements of NO Aur, which is probably non-variable. The AAVSO should consider how the observers' efforts can be used more productively. A few of the stars could continue to be observed photometrically but, for most of them, there is no scientific value in continuing to observe them.

5. Conclusions

The ASAS-SN data have been helpful in confirming that many of these "irregular" stars have some degree of periodicity, and should be reclassified as semiregular. For most of the stars in Table 1, the new data provide more and/or better results than obtained by Percy and Long (2010) or Percy and Terziev (2011) using AAVSO data alone. Not all of the periods of these stars are consistent with the periods in the VSX catalogue; the latter should be used with caution. Some of the stars appear to be non-variable, and almost all have small amplitudes—0.2 mag or less. Nevertheless, almost all of these stars continue to be observed visually, which is only marginally useful, at best. The AAVSO should address the question of whether and/or how these program stars should continue to be observed.

6. Acknowledgements

This paper made use of ASAS-SN photometric data. We thank the ASAS-SN project team for their remarkable contribution to stellar astronomy, and for making the data freely available on-line. This paper also made use of AAVSO data. We thank the observers and HQ staff for making and archiving the data, and the developers of VSTAR for creating this useful package, and making it publicly available. The Dunlap Institute is funded through an endowment established by the David Dunlap Family and the University of Toronto.

References

Benn, D. 2013, VSTAR data analysis software (http://www.aavso.org/vstar-overview).

Eddington, A. S., and Plakidis, S. 1929, *Mon. Not. Roy. Astron. Soc.*, **90**, 65.

Jayasinghe, T. *et al.* 2018, *Mon. Not. Roy. Astron. Soc.*, **477**, 3145.

Jayasinghe, T. *et al.* 2019, *Mon. Not. Roy. Astron. Soc*., **486**, 1907.

Kafka, S. 2020, variable star observations from the AAVSO International Database (https://www.aavso.org/aavso-international-database-aid).

Percy, J. R., and Long, J. 2010, *J. Amer. Assoc. Var. Star Obs.*, **38**, 161.

Percy, J. R., and Terziev, E. 2011, *J. Amer. Assoc. Var. Star Obs.*, **39**, 1.

Percy, J. R., and Huang, D. J. 2015, *J. Amer. Assoc. Var. Star Obs.*, **43**, 118.

Percy, J. R., and Fenaux, L. 2019, *J. Amer. Assoc. Var. Star Obs.*. **47**, 202.

Samus N. N., Kazarovets E. V., Durlevich O. V., Kireeva N. N., and Pastukhova E. N. 2017, *Astron. Rep.*, **61**, 80 (*General Catalogue of Variable Stars*: version GCVS 5.1, http://www.sai.msu.su/groups/cluster/gcvs/gcvs).

Watson, C., Henden, A. A., and Price, C. A. 2014, AAVSO International Variable Star Index VSX (Watson+, 2006–2014; http://www.aavso.org/vsx).

The Photometric Period of V392 Persei (Nova Persei 2018)

Richard E. Schmidt
Burleith Observatory, 1810 35th Street NW, Washington, DC 20007; schmidt.rich@gmail.com

Received January 25, 2020; revised March 10, 2020; accepted March 10, 2020

Abstract A photometric study of V392 Per (Nova Per 2018) has been undertaken at the urban Burleith Observatory in Washington, DC. A total of 1,010 CCD observations were obtained over a time span of 78.06 days. Analysis indicates an orbital period of 1.5841 h ± 0.0004 h, epoch (JD) of minimal light 2458839.52275, with amplitude 0.019 magnitude (Cousins I).

1. Introduction

The dwarf nova V392 Per (Nova Persei 2018), R.A. 04^h 43^m 21.37^s, Dec. +47° 21' 25.9" (2000), was first reported 50 years ago by Gerold A. Richter, Sonneberg Observatory, as a possible type U Gem variable of magnitude range 15–17 m_{pg} (Richter 1970). It was assigned type Z Cam (UGZ:) by (Liu and Hu 2000). Other catalogue names for this object are: S 10653, 2MASS J04432138+4721257, GSC2.3 NCFD013562, WISE J044321.38+472125.8. On 2018 April 29.4740 UT Yuji Nakamura, Kameyama, Japan, reported a magnitude 6.2 nova outburst (Nakamura 2018). Numerous follow-up observations confirmed this first thermonuclear eruption, which was accompanied by strong gamma-ray and X-ray emission (Murphy-Glaysher *et al.* 2019). The quiescent spectral energy distribution of V392 Per appears to rule out a red giant donor (Darnley and Starrfield 2018). The intensity of [NeV] 3426 neon lines suggests that this is an O-Ne-Mg white dwarf, or neon nova, as is Nova Cyg 1992 (Warner 2006; Munari and Ochner 2018). A preliminary orbital period was reported on 25 Jan. 2020 by (Schmidt 2020).

2. Observations

At Burleith Observatory, CCD observations were obtained with a 0.32-m PlaneWave CDK and SBIG STL-1001E CCD camera with an Astrodon Cousins I_c filter. This observatory is located in Washington, D. C., one of the brightest light polluted areas of the East Coast. In 2015 December, the sky background was measured as 18.50 ± 0.04 mag / arcsec^2 (I_c) (Schmidt 2016). From this location photometry in bands other than far-red optical is not feasible.

Prior to each night's run, the acquisition computer was synchronized to the USNO NTP time service. Images (240 sec, autoguided) were sky flat-fielded and dark corrected using The SKYX Professional Edition (Software Bisque 2020). An observing summary is given in Table 1.

3. Reductions

Synthetic aperture photometry was performed using MIRA PRO X64 version 8 (Mirametrics 2020). Aperture radii in 1.95 arc-second pixels were: object, 4; inner sky, 8; outer sky, 15. The field star Gaia DR2 2543617458239086 08 lies 8.6 arc seconds (4.4 pixels) north of V392 Per. It is reportedly stable at m_I = 13.977, m_v = 14.970 (Munari *et al.* 2020; Henden *et al.* 2016). This star was removed from each image prior to measurement, using the interactive pixel repair function of the aperture photometry package (Figure 1).

Table 1. Observation log. Time are UTC, not corrected for light travel time.

MJD start	*MJD end*	*Hours*	*Number of Observations*
58839.53131	58839.77779	5.92	54
58846.50502	58846.66373	3.81	33
58850.54891	58850.75502	4.95	44
58855.48628	58855.73133	5.88	62
58857.48038	58857.70976	5.51	60
58861.48409	58861.56303	1.89	23
58865.48278	58865.68026	4.74	50
58868.50348	58868.70290	4.79	49
58869.47865	58869.70119	5.34	57
58870.48553	58870.72153	5.66	64
58871.48648	58871.55852	1.73	21
58882.53477	58882.64854	2.73	39
58888.47759	58888.66063	4.39	59
58894.48230	58894.66850	4.47	63
58897.48101	58897.64268	3.88	46
58899.48560	58899.63067	3.48	48
58901.48301	58901.65186	4.05	51
58902.49476	58902.63006	3.25	37
58907.48439	58907.63131	3.53	49
58910.48860	58910.59473	2.55	38
58916.49398	58916.58354	2.15	32
58917.49434	58917.59207	2.35	31

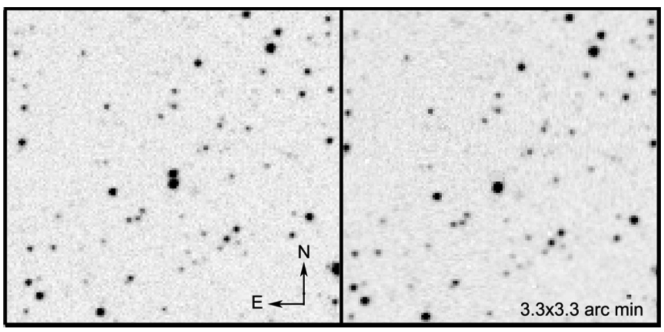

Figure 1. Removal of close field star.

Cousins I-band differential ensemble photometry was performed using the comparison stars from AAVSO chart sequence X24928QD (Table 2; C = comparison, K = check, Label = chart label).

The resulting magnitudes of V392 Per were detrended by subtracting the nightly means in order to remove the long-term

Table 2. Comparison stars.

AUID	R.A. (2000) h m s	Dec. (2000) ° ′ ″	C/K	Label	I_c	Mag. Error
000-BMQ-811	04 43 59.51	+47 24 18.6	1	130	11.720	(0.085)
000-BBH-307	04 43 07.45	+47 26 08.4	2	132	12.219	(0.186)
000-BBH-320	04 43 27.65	+47 25 49.4	3	135	12.421	(0.083)
000-BBH-306	04 43 04.85	+47 24 20.9	K	139	12.916	(0.161)

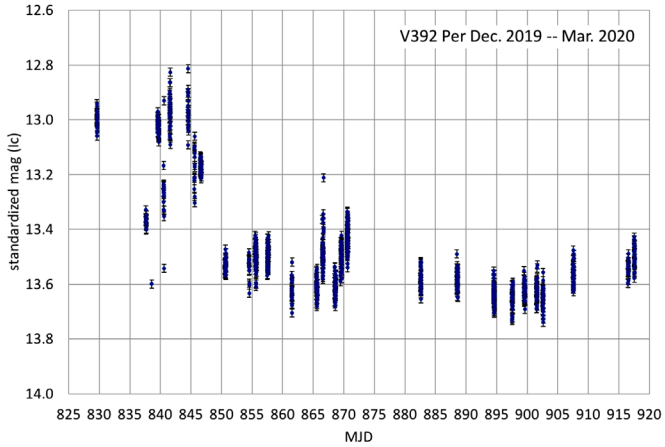

Figure 2. Observed I_c magnitudes, Dec. 2019–Mar. 2020.

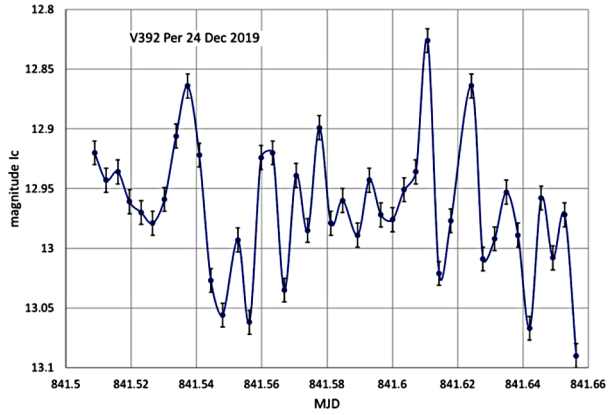

Figure 3a. Example session, 24 Dec. 2019.

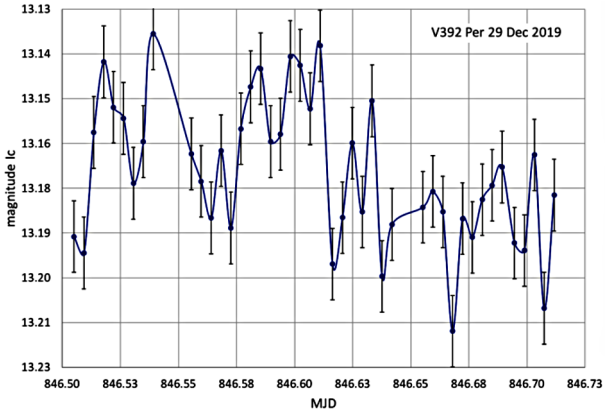

Figure 3b. Example session, 29 Dec. 2019.

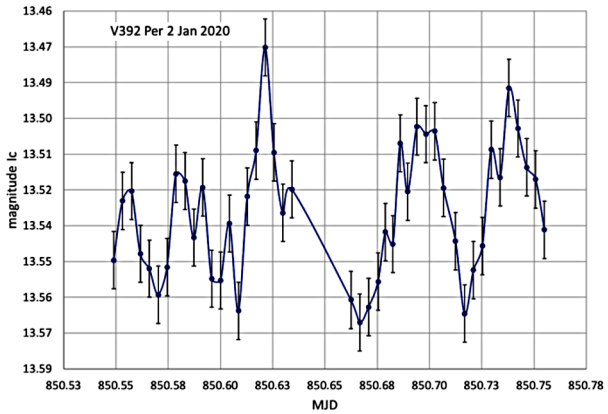

Figure 3c. Example session, 2 Jan. 2020.

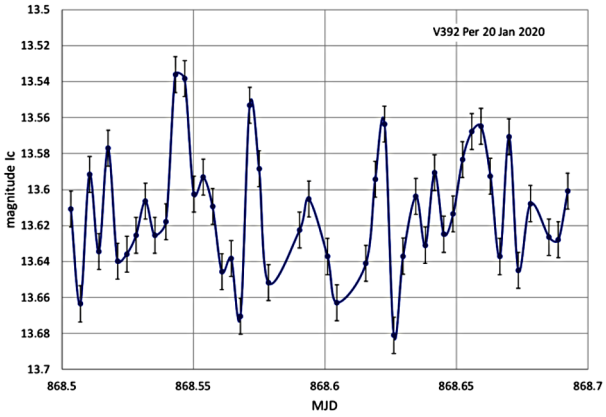

Figure 3d. Example session, 20 Jan. 2020.

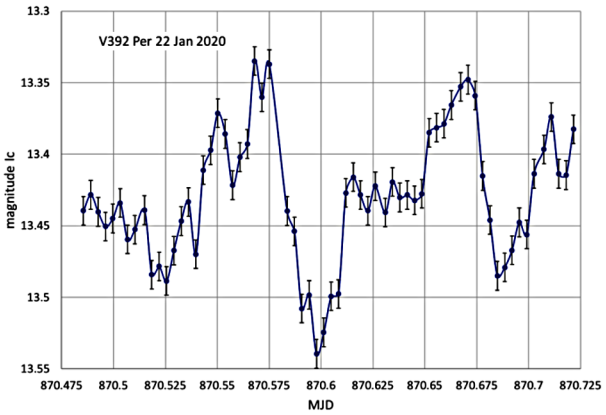

Figure 3e. Example session, 22 Jan. 2020.

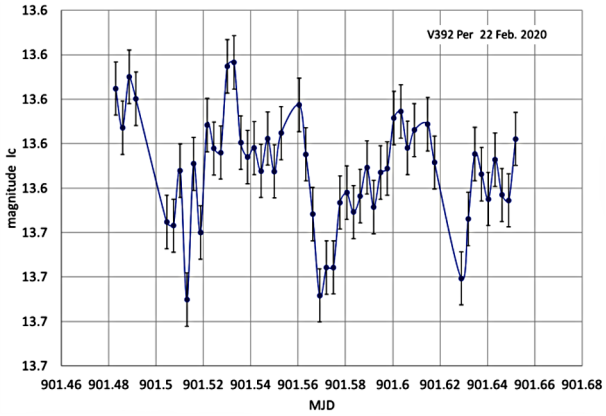

Figure 3f. Example session, 22 Feb. 2020.

light curve. Nightly observations, including unused sessions, are shown in Figure 2. Example observing sessions are shown in Figure 3.

4. Analysis

Period analysis of reduced-by-mean observations was performed using PERANSO 2.60 software (Vannmuster 2006). Using in turn both date-compensated discrete Fourier transform and Lomb-Scargle periodogram analyses, each gave the resulting period 1.5841 h ± 0.0004. Note that the error is a formal error of solution only, and not an indicator of the probability of reality of the observed period. The Lomb-Scargle periodogram is shown in Figure 4. Window aliases appear at about a frequency of 10 cycles per day (see VanderPlas 2018).

The most prominent period, 15.15 c / d, appears also in the minimum of the phase dispersion minimization (PDM) spectrum (Stellingwerf 1978), shown in Figure 5.

The most prominent period, 15.15 c / d, is shown in the folded double phase plot (Figure 6). A 225-point average with 128-point spline interpolation is shown (solid line), with amplitude 0.018 magnitude I_c.

The period was tested for significance using the PERANSO Fisher Monte Carlo randomization method which, while keeping observation times fixed, randomized the order of the magnitude observations over 200 permutations, searching for spectral responses due solely to observational biases (Moir 1998). The results were 0.005 ± 0.005 probability that no period was present in the data, and zero probability that any other significant periods were present in the data. The spectral window for all observations is shown in Figure 7. At frequency 15.15 cycles/day (dashed line), no spurious power appears, indicating that the period found is not due to the sampling frequency.

Table 3 summarizes the resulting period information.

5. Conclusion

The observed period of 95.05 minutes places Nova Persei 2018 squarely within the histogram of orbital periods of pre-cataclysmic variables found by (Nelson *et al.* 2018) and of the

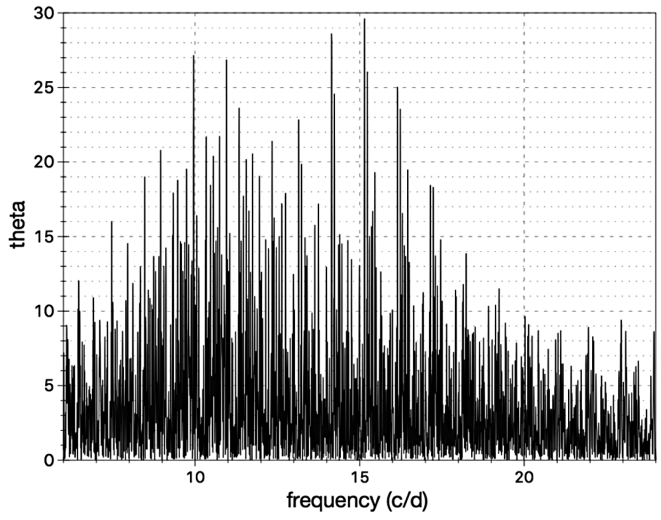

Figure 4. Lomb-Scargle periodogram.

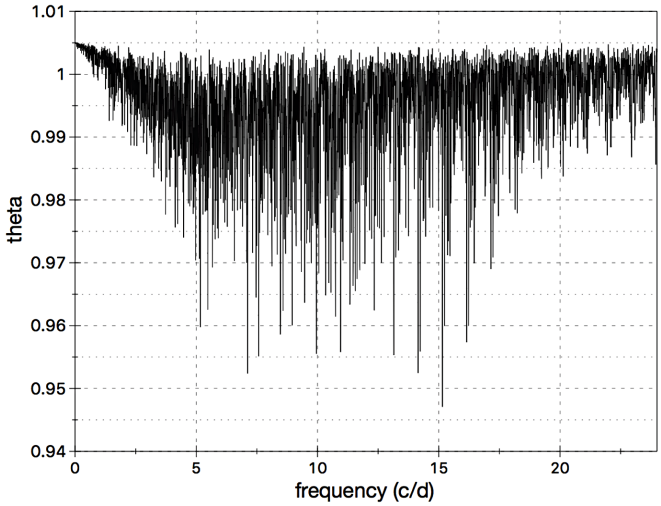

Figure 5. PDM spectrum.

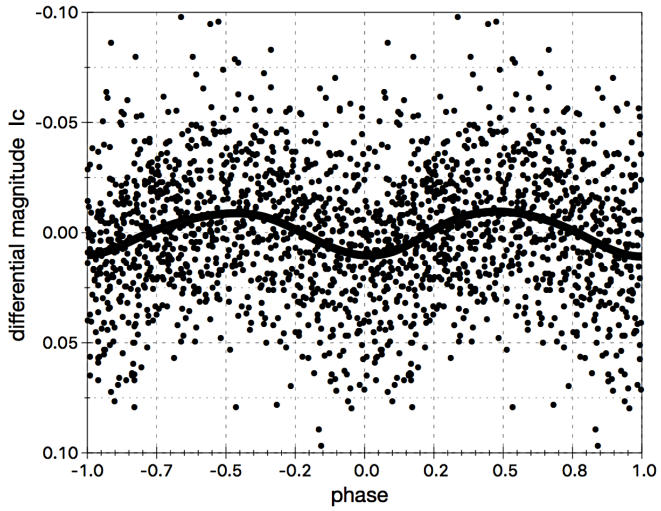

Figure 6. V392 Per, double phased plot with spline interpolated fit.

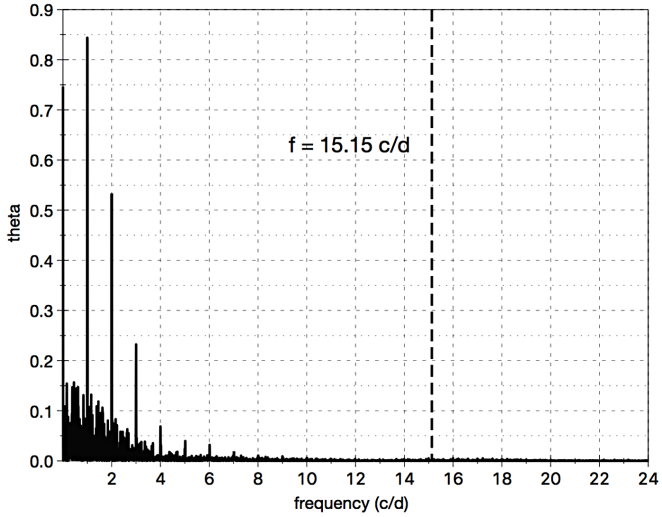

Figure 7. Spectral analysis for observational time aliases.

Table 3. Period analysis results for V392 Per.

Parameter	*Result*
Period(h)	1.5841 (0.0004)
Period(d)	0.06600 (0.00002)
Frequency(c/d)	15.15057 (0.0036)
Mean amplitude (fit)	0.019
Number of observations	1,010
Time span	78.0608 days
Epoch (JD) of minimum	2458839.52275

CVs found by the Sloan Digital Sky Survey (Southworth *et al.* 2012). V392 Per shows strong night-to-night flickering typical of cataclysmic variables, and this contributes much noise to the observations. If the observed photometric period is indeed orbital rather than a superhump period, the mass of a nova's Roche-lobe-filling main sequence secondary (M_2) would be uniquely determined as approximately $M_2 / M_\odot = 0.065\, P^{5/4}$ (Bode and Evans 2008).

For V392 Persei, $M_2 = 0.11\, M_\odot$. The orbital radius from Kepler's third law ("… it is absolutely certain and exact that the proportion between the periodic times of any two planets is precisely the sesquialterate [3/2] proportion of their mean distances…" (Kepler 1619)) for a primary mass of $1.2\, M_\odot$, for example, is 0.0034 AU, or about one-third that of the U Gem variable SS Cygni.

As was shown with Nova Cyg 1992 (V1974 Cyg), observations in Cousins I_c are effective in detecting photometric periodicity (DeYoung and Schmidt 1994), even near time of maximum. This implies that the nova shell may not be perfectly opaque in the red (Schaefer 2020). Further studies are warranted.

6. Acknowledgements

As modern astronomy stands upon the shoulders of giants, and of their supporting staff, we do well to pay tribute to the tireless observers of the Sonneberg Observatory's all-sky patrol which commenced in 1925 under C. Hoffmeister: G. A. Richter, Paul Ahnert, Nikolaus Richter, Johannes Hoppe, Sergej Gaposchkin, Heribert Schneller, Rudolf Brandt, Otto Morgenroth, Artur Teichgraeber, Hans Huth, and others. The author wishes to thank James A. DeYoung, NRL/USNO (ret.) for his invaluable advice. Special thanks to the AAVSO International Database for providing photometric standards for this study.

References

Bode, M., and Evans, A. 2008, *Classical Novae*, 2nd ed., Cambridge University Press, Cambridge, 25.

Darnley, M. J., and Starrfield, S. 2018, arXiv:1805.00994v2.

De Young, J. A., and Schmidt, R. E. 1994, *Astrophys. J., Lett.*, **431**, L47.

Henden, A. A., Templeton, M., Terrell, D., Smith, T. C., Levine, S., and Welch, D. 2016, AAVSO Photometric All Sky Survey (APASS) DR9, VizieR On-line Data Catalog II/336.

Kepler, J. 1619, *Harmonices Mundi*, Book V, Chapter III, Linz, Austria, Johannes Planck, 189–190.

Liu, W., and Hu, J. Y. 2000, *Astrophys. J., Suppl. Ser.*, **128**, 387.

Mirametrics, MIRA PRO X64 software, 2020 (http://www.mirametrics.com).

Moir, R. 1998, *Exp. Economics*, **1**, 87.

Munari, U., Moretti, S., and Maitan, A. 2020, *Astron. Telegram*, No. 13381, 1.

Munari, U., and Ochner, P. 2018, *Astron. Telegram*, No. 11926, 1.

Murphy-Glaysher, F. J., Darnley, M. J., Page, K. L. 2019, *Astron. Telegram*, No. 12951, 1.

Nakamura, Y. 2018, *Cent. Bur. Astron. Telegrams* "Transient Object Followup Reports," TCP J04432130+4721280 (www.cbat.eps.harvard.edu/unconf/followups/J04432130+4721280.html).

Nelson, L., Schwab, J., Ristic, M., and Rappaport, S. 2018, *Astrophys. J.*, **866**, 88.

Richter, G. A. 1970, *Mitt. Veränderl. Sterne*, **5**, 99.

Schaefer, B. E. 2020, private communication.

Schmidt, R. E. 2016, *Minor Planet Bull.*, **43**, 129.

Schmidt, R. E. 2020, IAU Circ., No. 4718, 1 (www.cbat.eps.harvard.edu/iau/cbet/004700/CBET004718.txt).

Software Bisque. 2020, THE SKY X Professional Edition (www.bisque.com).

Southworth, J., Gänsicke, B. T., and Breedt, E. 2012, in *Interacting Binaries to Exoplanets: Essential Modelling Tools*, eds. M. Richards, I. Hubeny, Proc. IAU Symp. 282, Cambridge University Press, Cambridge, 123.

Stellingwerf, R. F. 1978, *Astrophys. J.*, **224**, 953.

VanderPlas, J. T., 2018, *Astrophys. J., Suppl. Ser.*, **236**, 16.

Vannmuster, T., 2006, PERANSO period analysis software, v.2.60, CBA Belgium Observatory (http://www.cbabelgium.com/peranso).

Warner, B. 2006, *J. Amer. Assoc. Var. Star Obs.*, **35**, 98.

Light Curve Asymmetries in Three Short Period Eclipsing Binary Stars

Gage Hahs
Charlyn Ortmann
Vayujeet Gokhale
Truman State University, Department of Physics, Kirksville, MO 63501; gokhale@truman.edu

Received February 19, 2020; revised April 10, 2020; accepted April 23, 2020

Abstract We present light curve analysis of three variable stars, NSVS 10384295 (P = 0.297899 d), NSVS 7347726 (P = 0.43394 d), and NSVS 13251721 (P = 0.23340 d), using data collected at the 31-inch NURO telescope at the Lowell Observatory in Flagstaff, Arizona, in three filters: Bessell B, V, and R. We quantify the asymmetries in these systems by generating a twelve-term Fourier fit and using the resulting Fourier coefficients to calculate ΔI (the difference in the heights of the primary and secondary maxima), the "Light Curve Asymmetry" (LCA), and the "O'Connell Effect Ratio" (OER). Our analysis shows that of the three systems studied, NSVS 13251721 has the most asymmetric light curve, and that NSVS 7347726 has the most symmetric light curve. We also observe that for all three systems, the asymmetries are most pronounced in the B filter, and the least in the R filter. Additionally, we use the Fourier coefficients to confirm NSVS 10384295 and NSVS 13251721 as W UMa type systems, and NSVS 7347726 to be a β Lyrae type system.

1. Introduction

We present results for three eclipsing binary systems selected from Hoffman *et al.* (2008), namely, NSVS 10384295 (P = 0.297899d), NSVS 7347726 (P = 0.43394d), and NSVS 13251721 (P = 0.23340d). This project is part of an effort at Truman State University to introduce undergraduate students to differential aperture photometry by following three to four eclipsing binaries per semester with the aim of generating light curves, classifying these systems as either β Lyrae, Algol, or W UMa type systems, and quantifying the asymmetries in the light curves of these objects. Following Gardner *et al.* (2015) and Akiba *et al.* (2019), we focus on the asymmetries in the light curves in each of the filters by calculating the difference in the heights of the primary and secondary maxima (ΔI), the "Light Curve Asymmetry" (LCA), and the "O'Connell Effect Ratio" (OER; McCartney 1999; O'Connell 1951). The OER is the ratio of the area under the curves between phases φ = 0.0 to φ = 0.5 and phases φ = 0.5 to φ = 1.0 (see section 3 below). An OER > 1 implies that the first half of the light curve has more total flux than the second half. The LCA, on the other hand, measures the deviance from symmetry of the two halves of the light curve. If both halves are perfectly symmetric, then we would expect the LCA to be zero. We refer the reader to Gardner *et al.* (2015) for a more detailed discussion on the LCA and OER. We are interested in studying these asymmetries since their origin is not well studied or understood—the two most popular explanations, the "starspot" model and the "hotspot" model, are not entirely satisfactory (Akiba *et al.* 2019).

We do not attempt to model these systems—that would require access to spectroscopic data, which we do not have. Instead, we superpose the two halves of an appropriately phased light curve to identify the phase at which the light curves are asymmetric (see section 3). In the starspot model, this phase information can be used to constrain the location and characteristics of the starspots for a given orbital cycle. This, however, has limited utility given that astronomers usually only have one or two orbital cycles of data. We are working on using uninterrupted data from the Kepler (Prša *et al.* 2011) and Transiting Exoplanet Survey Satellite (TESS) missions (Ricker *et al.* 2015) to constrain the system parameters even without access to spectroscopic data. In particular, we aim to investigate the time evolution of "starspots" on the surface of one, or both, components in the binary system. From this, we want to determine what role these starspots play in the observed, and as yet, not well understood asymmetries in the light curves of eclipsing binary star systems.

In the following, section 2 outlines our observational data acquisition and data reduction methods, section 3 contains our results and analysis of the light curves, and section 4 is a discussion of our results.

2. Observations

We present BVR photometry of eclipsing variable stars NSVS 10384295 (P = 0.297899 d), NSVS 7347726 (P = 0.43394 d), and NSVS 13251721 (P = 0.23340 d). The data were collected using the 2 k × 2 k Loral NASACam CCD attached to the 31-inch NURO telescope at Lowell Observatory, Flagstaff, Arizona. The filters used are Bessell BVR (see Table 1). We follow the procedure outlined in Gardner *et al.* (2015) for data collection and reduction: Bias subtraction and

Table 1. Observation dates, instrument, and filters for the targets.

Target	*Date of Observation*	*Telescope*	*Filters*
NSVS 10384295	08 March 2016	NURO	Bessell BVR
	09 March 2016	NURO	Bessell BVR
NSVS 7347726	09 March 2016	NURO	Bessell BVR
	10 March 2016	NURO	Bessell BVR
	11 March 2016	NURO	Bessell BVR
NSVS 13251721	10 March 2016	NURO	Bessell BVR
	10 March 2016	NURO	Bessell BVR

Table 2. Target, comparison, and check star coordinates and comparison star B and V magnitudes used for data from the NURO telescope.

Star	*Name*	*R.A. (J2000)* h m s	*Dec. (J2000)* ° ′ ″	*V*	*B*
Target	NSVS 10384295	12 32 49.94	+15 17 35.21		
Comparison	BD+16 2388	12 32 39.29	+15 13 36.83	10.4	11.5
Check	BD+16 2387	12 32 28.36	+15 18 19.49		
Target	NSVS 7347726	08 08 57.97	+37 12 05.62		
Comparison	TYC 2481-548-1	08 08 42.65	+37 09 08.45	12.10	12.73
Check	TYC 2481-26-1	08 08 32.02	+37 06 14.04		
Target	NSVS 13251721	13 32 28.07	–02 30 56.52		
Comparison	UCAC2 30863052	13 32 02.04	–02 33 13.11	11.877	12.517
Check	—	13 32 02.45	–02 33 51.20		

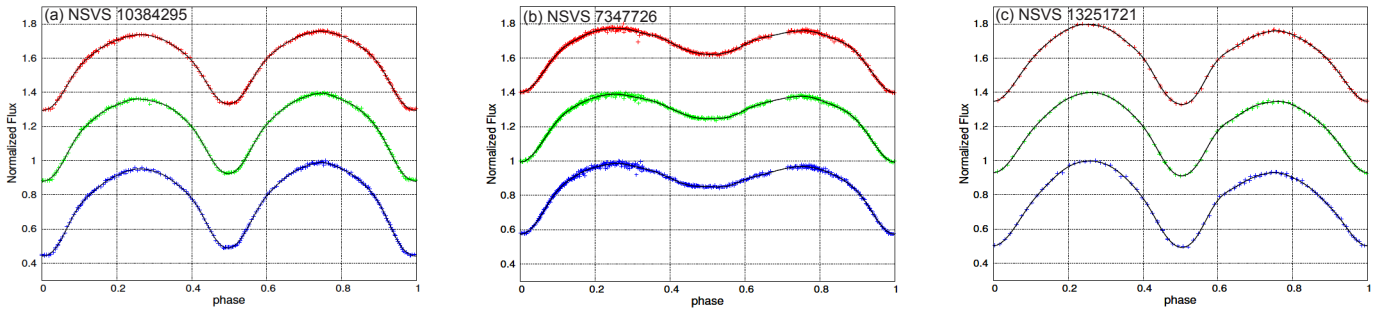

Figure 1. Differential magnitudes ("+" symbols) for each of the systems. The Fourier fit (black continuous curve) is plotted along with the red, green, and blue curves corresponding to R, V, and B filters, respectively. Note that these curves are generated after the data for each object had been shifted so that the primary eclipse occurs at phase 0. The average error in flux for NSVS 10384295 and NSVS 13251721 in each of the three filters is about 0.007, and for NSVS 7347726 it is about 0.01. Error bars are not shown for the sake of clarity.

Table 3. Classification of systems based on Fourier coefficients.

Target	*Filter*	a_1	a_2	a_4	$a_2(0.125–a_2)$	*Classification*
NSVS 10384295	B	0.0301 ± 0.0005	–0.2367 ± 0.0005	–0.0577 ± 0.0005	–0.0856 ± 0.0002	W UMa
	V	0.0268 ± 0.0005	–0.2225 ± 0.0006	–0.0556 ± 0.0005	–0.0773 ± 0.0002	W UMa
	R	0.0227 ± 0.0005	–0.2039 ± 0.0005	–0.0511 ± 0.0005	–0.0670 ± 0.0002	W UMa
NSVS 7347726	B	0.0780 ± 0.0004	–0.1248 ± 0.0005	–0.0267 ± 0.0005	–0.0312 ± 0.0001	β Lyrae
	V	0.0726 ± 0.0003	–0.1234 ± 0.0004	–0.0269 ± 0.0004	–0.0306 ± 0.0001	β Lyrae
	R	0.0636 ± 0.0003	–0.1203 ± 0.0004	–0.0272 ± 0.0004	–0.0295 ± 0.0001	β Lyrae
NSVS 13251721	B	0.0083 ± 0.0009	–0.2199 ± 0.0009	–0.0441 ± 0.0010	–0.0759 ± 0.0004	W UMa
	V	0.0022 ± 0.0006	–0.2119 ± 0.0006	–0.0446 ± 0.0007	–0.0714 ± 0.0003	W UMa
	R	–0.0023 ± 0.0007	–0.2066 ± 0.0006	–0.0436 ± 0.0007	–0.0685 ± 0.0003	W UMa

(sky) flat fielding is done using the software package MAXIMDL (v6.16; Diffraction Limited 2020). No dark subtraction was performed since for the nitrogen cooled camera at NURO, the dark current is negligible. Differential photometry is then performed on the target with a suitable comparison and check star using the ASTROIMAGEJ software (v3.2; Collins *et al.* 2017) (Differential photometry data are available on request via email: gokhale@truman.edu and at http://gokhale.sites.truman.edu/asymmetries/.) The aperture size was set to two times the full width at half maximum (FWHM) of the brightest object on which photometry was performed. The radius of the inner annulus was chosen to exclude any other stars close to the target, whilst the outer radius was set to ensure that the annulus contains approximately 4 times the number of pixels that are in the aperture, following the procedure outlined by Conti (2018). We searched for any comparison stars from the Tycho (Høg *et al.* 2000) catalogue that are present in the image frame, and used these stars to determine the B and V magnitudes of each of the targets. Since we could not find the R magnitude of any of the comparison stars, differential photometry was performed on the R-filter data using instrumental magnitudes. The details for the target, comparison, and check star are provided in Table 2.

3. Results and analyses

3.1. Light curves

We phase fold the time axis of each of the light curves using the equation:

$$\Phi = \frac{T - T_0}{P} - \text{Int}\quad\frac{T - T_0}{P} \tag{1}$$

where P is the period of the system (Hoffman *et al.* 2008) and T_0 is an arbitrarily chosen epoch. Following Warner and Harris (2006), we convert the differential magnitude measured in each filter to the normalized flux by using:

$$I(\Phi)_{\text{obs}} = 10^{-0.4 \times (m(\Phi) - m(\max))} \tag{2}$$

where $m(\Phi)$ is the magnitude at a certain phase Φ and $m(\max)$ is the maximum magnitude observed for the object. We perform Fourier fit analyses on the light curves by generating a truncated twelve-term Fourier fit (Wilsey and Beaky 2009):

$$I(\Phi)_{\text{fit}} = a_0 + \sum_{n=1}^{12}(a_n \cos(2\pi n\Phi) + b_n \sin(2\pi n\Phi)) \tag{3}$$

where a_0, a_n, and b_n are the Fourier coefficients of the fit, and Φ is the phase (Hoffman *et al.* 2009). Note that the Fourier fit is accomplished using WOLFRAM MATHEMATICA (Wolfram Res. Co. 2019). The phase-folded light curves, along with the corresponding Fourier fits, are shown in Figures 1a, 1b and 1c.

3.2. Classification of systems

We follow the procedure outlined by Rucinski (1997) and Wiley and Beaky (2009) and summarized in Akiba *et al.* (2019) (see their section 3.2) to classify the three systems under consideration. The Fourier coefficients, and the associated errors, are extracted from the Fourier fits generated using MATHEMATICA (Wolfram Res. Co. 2019) and are tabulated in Table 3. Each filter gives us consistent results which match with the expected classification based on a visual inspection of the light curves: NSVS 10384295 and NSVS 13251721 are confirmed to be of the W UMa type, whilst NSVS 7347726 is confirmed to be of the β Lyrae type.

3.3. Asymmetries in the light curve: Quantifying the O'Connell Effect

We again follow the procedure outlined by Akiba *et al.* (2019) to quantify the asymmetries in the light curves of each of these objects in each filter. We first calculate the difference in the normalized flux near the primary and secondary maxima as ΔI_{ave} and ΔI_{fit} using our data and fit, respectively. Also, the coefficient b_1 associated with the first sine term of the Fourier fit is the half-amplitude of the sine wave, and therefore $|2b_1|$ is a good approximation to ΔI (Wilsey and Beaky 2009). The calculated values of $|2b_1|$, ΔI (Fourier), andΔI (Average) are shown in Table4.

Then, we evaluate the O'Connell Effect Ratio (OER) and the Light Curve Asymmetry (LCA) as described by McCartney (1999) as follows:

$$\text{OER} = \frac{\int_{0.0}^{0.5}(I(\Phi)_{\text{fit}} - I(0.0)_{\text{fit}})d\Phi}{\int_{0.5}^{1.0}(I(\Phi)_{\text{fit}} - I(0.0)_{\text{fit}})d\Phi} \tag{4}$$

and,

$$\text{LCA} = \sqrt{\int_{0.0}^{0.5}\frac{(I(\Phi)_{\text{fit}} - I(1.0 - \Phi)_{\text{fit}})^2}{I(\Phi)^2_{\text{fit}}}\,d\Phi} \tag{5}$$

where $I(\Phi)_{\text{fit}}$ is given by Equation 3. The values for these parameters are tabulated in Table 5. The uncertainties of the OER and LCA are calculated according to the formal proofs outlined in the appendices of Akiba *et al.* (2019).

It is instructive to superpose the two halves of an eclipsing binary light curve to visually appreciate the asymmetries in them. In addition, we calculate the difference in the two halves of the light curve as:

$$\Delta I(\Phi)_{\text{fit}} = I(\Phi)_{\text{fit}} - I(1 - \Phi)_{\text{fit}} \tag{6}$$

Figure 2 shows the "half-phase plot" for each of our systems in the B filter. The $\Delta I(\Phi)_{\text{fit}}$ function is plotted in the bottom panel. Figure 3 shows the difference in the two halves of the light curve in each of the filters for all the three systems under consideration. The plots show certain similarities in the asymmetries in the three filters. For example, in all three filters $\Delta I(\Phi)_{\text{fit}}$ is largely negative for NSVS 10384295, in keeping with the fact that the maxima after the secondary eclipse is brighter than the maximum after the primary eclipse for this system. $\Delta I(\Phi)_{\text{fit}}$ values for NSVS 7347726 and NSVS 13251721 are largely positive, with the latter showing a significantly larger asymmetry than the former system. It is also clear that the discrepancy in flux is greatest in the B filter and least in the R filter, which is also a trend we notice in other asymmetry parameters like the OER, LCA, and the ΔIs.

As mentioned earlier, we are in the process of generating similar plots and animations for eclipsing binary systems over several orbital cycles using data obtained from the TESS and Kepler missions. This will allow us to study the changes in the asymmetry as a function of time, which will be valuable in modeling these systems (Koogler *et al.* 2019).

4. Discussion

4.1. NSVS 10384295

From Table 3 for NSVS 10384295, we see that $a_4 > I_2(0.125 - a_2)$ in all filters, which suggests that the system is an overcontact W UMa or β Lyrae type eclisping binary system. Since $|a_1| < 0.05$ in all filters we classify NSVS 10384295 as a W UMa type system, following the criteria summarized in Akiba *et al.* (2019). This is consistent with the shape of its light curve (Figure 1a).

By visual inspection of the light curve, we see that NSVS 10384295 exhibits the O'Connell Effect with the peak magnitude after the primary eclipse being less than the peak magnitude after the secondary eclipse. This is reflected in the negative ΔI values in Table 4. Similarly, the OER is less than 1 for each filter (Table 5), suggesting again that the peak after the secondary eclipse is brighter than the peak after the primary eclipse. Also note that the O'Connell Effect, quantified in terms of ΔI, is most prominent in the B filter and least prominent in the R filter (Table 4). This is also reflected in Table 5—the OER

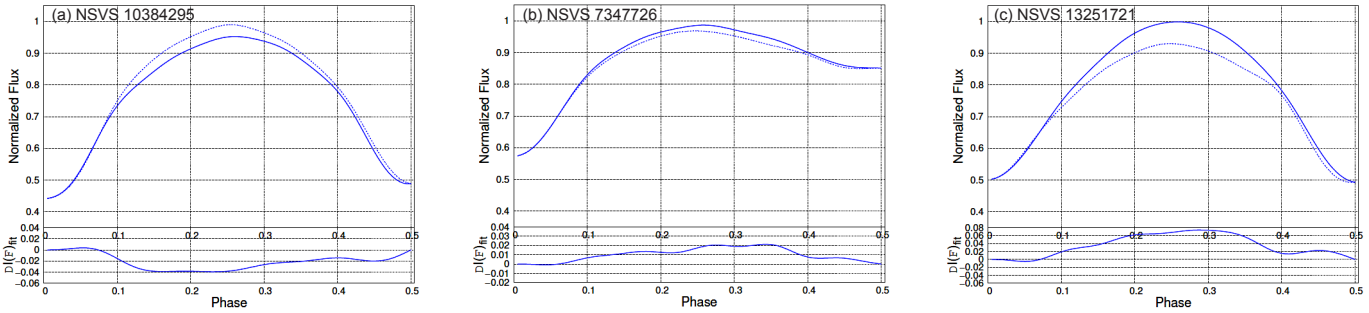

Figure 2. Superposed phased plots of the primary half (solid line) and the secondary half (dotted line) of the light curves in the B filter for each of the systems. The bottom panel shows the difference between the two halves of the light curve. In the absence of any asymmetry, the two curves should coincide, and the solid blue curve in the bottom panel would be a flat line at "0."

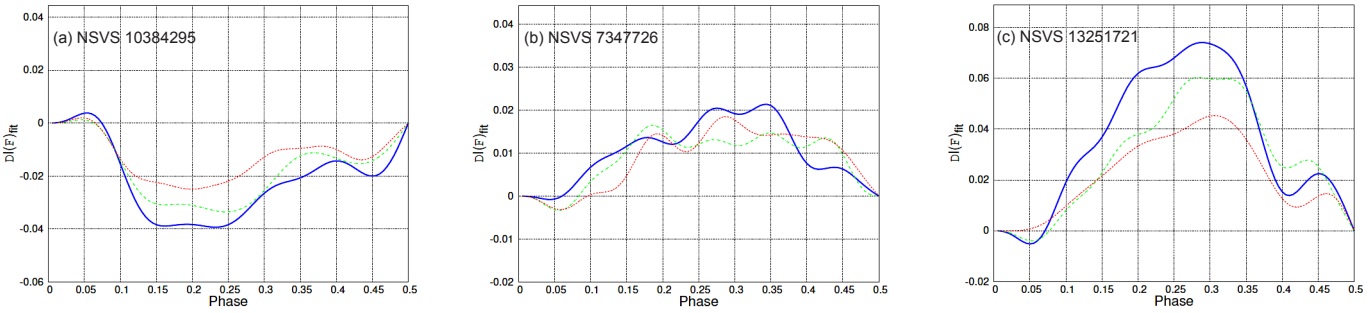

Figure 3. Difference in normalized flux in the B (blue solid curve), V (green dashed), and R (red dotted) filters for each of the systems. See text for details.

Table 4. Quantifying the O'Connell Effect in terms of difference in maxima.

Target	*Filter*	$\|2b_1\|$	*ΔI (Fourier)*	*ΔI (Average)*
NSVS 10384295	B	0.034 ± 0.001	–0.037 ± 0.004	–0.036 ± 0.001
	V	0.028 ± 0.001	–0.033 ± 0.004	–0.033 ± 0.002
	R	0.020 ± 0.001	–0.021 ± 0.004	–0.019 ± 0.001
NSVS 7347726	B	0.017 ± 0.001	0.018 ± 0.003	0.017 ± 0.001
	V	0.014 ± 0.001	0.012 ± 0.003	0.013 ± 0.002
	R	0.014 ± 0.001	0.013 ± 0.003	0.014 ± 0.002
NSVS 13251721	B	0.060 ± 0.002	0.069 ± 0.007	0.071 ± 0.004
	V	0.047 ± 0.002	0.052 ± 0.005	0.052 ± 0.003
	R	0.035 ± 0.016	0.038 ± 0.005	0.042 ± 0.002

Table 5. Quantifying the O'Connell Effect in terms of OER and LCA.

Target	*Filter*	*OER*	*LCA*
NSVS 10384295	B	0.938 ± 0.010	0.021 ± 0.002
	V	0.946 ± 0.011	0.017 ± 0.002
	R	0.957 ± 0.012	0.013 ± 0.002
NSVS 7347726	B	1.034 ± 0.011	0.009 ± 0.002
	V	1.031 ± 0.010	0.008 ± 0.001
	R	1.034 ± 0.010	0.008 ± 0.001
NSVS 13251721	B	1.137 ± 0.028	0.033 ± 0.003
	V	1.113 ± 0.021	0.027 ± 0.003
	R	1.087 ± 0.021	0.020 ± 0.003

value deviates from unity the most in the B filter and least in the R filter. Note that the OER is the ratio of the total flux from the object in the "primary" and the `secondary' halves of the light curve (Equation 4), and thus a perfectly symmetric curve corresponds to an OER = 1 (Gardner *et al.* 2015).

4.2. NSVS 7347726

From Table 3 for NSVS 7347726, we see that $a_4 > a_2(0.125 - a_2)$ in each filter, which suggests that the system is either a W UMa or a β Lyrae type system. Inspection of the a_1 coefficient further classifies NSVS 7347726 as a β Lyrae since $a_1 > 0.05$ (Akiba *et al.* 2019). This result based on the Fourier coefficients supports the characteristic β Lyrae light curve shape seen in Figure 1b.

By visual inspection of the light curve, we see that NSVS 7347726 exhibits a less prominent O'Connell Effect with the peak magnitude after the primary eclipse being slightly greater than the peak magnitude after the secondary eclipse. This is reflected by the positive ΔI values in Table 4. Moreover, the difference in maxima (ΔI's, see Table 4) is largest in the B filter and practically identical in the V and R filters. Similarly, the OER and LCA values in the three filters for this object are practically identical. As can be seen in Figure 1b, both maxima, as well as the secondary minimum, are very nearly flat. The OER > 1 consistently in each filter though, allowing us to state that the peak after the primary is greater than the peak after the secondary in magnitude. We note that, in this study, the average LCA for NSVS 7347726 is the smallest of the three objects, which implies a more symmetric light curve.

4.3. NSVS 13251721

For NSVS 13251721, we see that $a_4 > a_2(0.125 - a_2)$, which suggests a close contact W UMa or β Lyrae type system. Additionally, $a_1 < 0.05$, which leads to an overall classification of W UMa that is visually verified through inspection of Figure 1c. Upon further inspection of Figure 1c, we see that NSVS 7347726 exhibits an O'Connell Effect with the peak magnitude after the primary eclipse being greater than the peak magnitude following the secondary eclipse. This is reflected by the positive ΔI values in Table4 and by the OER values in Table 5. Also, we note the familiar pattern where the OER and LCA are most prominent in the B filter and least prominent in the R filter.

5. Acknowledgements

We have made extensive use of the tools avaliable on the AAVSO website, in particular, the VSP (Variable Star Plotter) tool to generate star charts. In addition, we have used the SIMBAD database, operated at CDS, Strasbourg, France, and NASA's Astrophysics Data System. We are thankful for the support provided by the Office of Student Research at Truman State University, and to the Missouri Space Grant Consortium. The authors would also like to thank the anonymous referee for useful comments and suggestions, which greatly improved the manuscript.

References

Akiba, T., Neugarten, A., Ortmann, C., and Gokhale, V. 2019, *J. Amer. Assoc. Var. Star Obs.*, **47**, 186.

Collins, K. A., Kielkopf, J. F., Stassun, K. G., and Hessman, F. V. 2017, *Astron. J.*, **153**, 77.

Conti, D. M. 2018, *A Practical Guide to Exoplanet Observing*, rev. 4.2 (https://astrodennis.com).

Diffraction Limited. 2020 MAXIMDL image processing software (http://www.cyanogen.com).

Gardner, T., Hahs, G., and Gokhale, V. 2015, *J. Amer. Assoc. Var. Star Obs.*, **43**, 186.

Hoffman, D. I., Harrison, T. E., Coughlin, J. L., McNamara, B. J., Holtzman, J. A., Taylor, G. E., and Vestrand, W. T. 2008, *Astron. J.*, **136**, 1067.

Hoffman, D. I., Harrison, T. E., and McNamara, B. J. 2009, *Astron. J.*, **138**, 466.

Høg, E.,*et al.* 2000, *Astron. Astrophys.*, **355**, L27.

Koogler, B., Shroyer, K., and Gokhale, V. 2019, B*ull. Amer. Astron. Soc.*, **51**, id. 207.02 (aas234-aas.ipostersessions.com/Default.aspx?s=C4-8F-61-93-39-B1-84-E0-B1-57-42-ED-CA-46-8B-77).

McCartney, S. A. 1999, Ph.D. dissertation, University of Oklahoma.

O'Connell, D. J. K. 1951, *Riverview Coll. Obs. Publ.*, **2**, 85.

Prša A.,*et al.* 2011, *Astron. J.*, **141**, 83.

Ricker G. R.,*et al.* 2015, *J. Astron. Telesc. Instrum. Syst.*, **1**, 014003.

Rucinski, S. M. 1997, *Astron. J.*, **113**, 407.

Warner, B. D., and Harris, A. W. 2006 *A Practical Guide to Lightcurve Photometry and Analysis*, Springer, New York.

Wilsey N. J., and Beaky M. M. 2009, in *The Society for Astronomical Sciences 28th Annual Symposium on Telescope Science*, Society for Astronomical Sciences, Rancho Cucamonga, CA, 107.

Wolfram Research Co. 2019, "How to Fit Models with Measurement Errors" (https://reference.wolfram.com/language/howto/FitModelsWithMeasurementErrors.html).

TYC 2402-0643-1: First Precision Photometric Observations and Analyses of the Totally Eclipsing, Solar Type Binary

Ronald G. Samec
Faculty Research Associate, Pisgah Astronomical Research Institute, 1 PARI Drive, Rosman, NC 28772; ronaldsamec@gmail.com

Daniel B. Caton
Dark Sky Observatory, Physics and Astronomy Department, Appalachian State University, 525 Rivers Street, Boone, NC 28608-2106; catondb@appstate.edu

Danny R. Faulkner
Johnson Observatory, 1414 Bur Oak Court, Hebron, KY 41048; dfaulkner@answersingenesis.org

Received March 28, 2020; revised April 22, May 11, 2020; accepted May 11, 2020

Abstract CCD BVRI light curves of TYC 2402-0643-1 were taken on 21, 22, and 23 January 2020 at the Dark Sky Observatory, Boone, North Carolina, with the 0.81-m reflector of Appalachian State by Daniel Caton. The variability of TYC 2402-0643-1 ([GGM2006] 6868894, NSVS 4382530) was discovered in the sky patrol data taken by the ROTSE-I telescope. It is classified as a contact variable with a maximum V magnitude of 11.373, an amplitude of V = 0.442, and a period of 0.399579 d. Three times of minimum light were determined from our present observations, which include one primary eclipse and two secondary eclipses. We selected three times of low light from ASAS observations and Gettel sent us some ROTSE data. From these we determined a 20-year study and a quadratic ephemeris. Thus, from our study, the period is found to be increasing. This could be due to mass transfer making the mass ratio ($q = M_2 / M_1$) decrease. A Wilson-Devinney analysis reveal that the system is an A-type W UMa binary (the hotter component is the more massive) with a somewhat extreme mass ratio, $q = 0.2079 \pm 0.0003$ (star 1 is the more massive, primary component, $1/q = M_1/M_2 = 4.8$). Its Roche Lobe fill-out is ~22%. No spots were needed in the solution. The temperature difference of the components is only ~70 K, so it is in strong thermal contact. The inclination is high, $83.4 \pm 0.1°$, resulting in a total eclipse. As a result, the secondary minimum has a time of constant light with an eclipse duration of some 43 minutes.

1. Introduction

Many times, extreme mass ratio contact binaries (EMRBs, solar type, $q \lessapprox 0.2$, Samec *et al.* 2011) tend to become more extreme. In this case, the primary component is the gainer and the secondary component decreases in mass. In conservative mass exchange (Nelson and Alton 2019),

$$\frac{dM}{dt} = \frac{(dP/dt)\,(M_1\,M_2)}{[3P\,(M_1 - M_2)]} \quad . \qquad (1)$$

However, besides mass exchange, the mass is decaying from the system due to magnetic braking (Guinan and Bradstreet 1988). Magnetic braking happens in rotating solar type stars and binaries (Gharami *et al.* 2018). Solar type stars (roughly type FV to MV type stars) have deep convective envelopes made up of swirling plasmas that are magnetic in nature with strong dipole magnetic fields and magnetic phenomena, notably star spots (Mullen 1975; Vant'veer 1994). Stellar plasma winds escape from the North and South poles out to the Alfvén radius of the stars (about 15 solar radii). This allows the transport of mass particles on stiffly rotating magnetic field lines rotating with increasing radii, transferring angular momentum (L) into space (for a single particle, moving on radius, r, $L = mvr$) with expanding r. This continuously removes angular momentum, ΔL, from the binary causing angular momentum loss (AML, Loukaidou and Gazeas 2020). This effectively torques the star, $\tau = dL/dt$. For a single star, this causes the star's rotation to slow, finally resulting in a slow rotating star (from periods of a few days to about a month) like our present sun (Melendez *et al.* 2017; Guinan and Engle 2009). For a solar type binary system (two stars co-orbiting about a center of mass or barycenter), the same magnetic braking occurs but the orbital radius of the binary shrinks (Bradstreet and Guinan 1994) and by Kepler's third law, the orbital period shortens. When the atmospheres of the stars touch, the stars are called contact binaries. The stars continue to coalesce (Guinan *et al.* 1987) until they violently form, by a *red novae event* (Tylenda and Kamiński 2016; Molnar *et al.* 2017), fast-rotating single stars such as A-type stars, magnetic stars, or subgiants, similar to the spotted FK Comae stars in globular clusters (Schneider *et al.* 2019). An unpublished, extreme mass ratio binary, TYC 2402-0643-1, is reported on in this paper.

2. History and observations

The variability of TYC 2402-0643-1 ([GGM2006] 6868894, NSVS 4382530) was discovered in the sky patrol data taken by the ROTSE-I telescope (Gettel *et al.* 2006). They classified it as a contact variable with a maximum magnitude of $V_{max} = 11.373$, an amplitude of 0.442 V_{mag}, J–K = 0.467, and a period of 0.399579 d. ROTSE curves are shown in Figure 1. The binary appears in the automated variable star classification of variable stars (Hoffman *et al.* 2009) using the Northern Sky Variability Survey (NSVS; Hoffman *et al.* 2009). The system was also observed by the All

Sky Automated Survey as ASASSN-V J051858.09+365806.2 (Pojmański 2002). They give a $V_{mean} = 11.33$, an amplitude of 0.4, and EW designation, J–K = 0.467. Their ephemeris is:

$$\text{HJD Min I} = 2457070.80679 + 0.3995827\text{E d} \times \text{E} \qquad (2)$$

The ASAS curves are shown in Figure 2. From the ASAS and ROTSE curves we were able to phase the data with Equation 1 and the ROTSE period (0.399579 d) and construct parabola fits to the primary and secondary minima to locate several times of minimum light within 0.001 phase of each minimum.

This system was observed as a part of our professional collaborative studies of interacting binaries at Pisgah Astronomical Research Institute from data taken from DSO observations. The observations were taken by D. Caton, R. Samec, and D. Faulkner. Reduction and analyses were done by R. Samec.

Our BVRI light curves were taken at Dark Sky Observatory, on 21, 22, and 23 January 2020 with a thermoelectrically cooled (–35° C) 1K × 1K FLI camera and Bessel *BVRI* filters.

Individual observations included 264 images in Johnson-Cousins B, 282 in V, 311 in R_c, and 306 in I_c. The BVRI observations are given in Table 1. The probable error of a single observation was 4 mmag in B, V, and R, and 3 mmag in I. The nightly C–K values stayed constant throughout the observing run with a precision of about 1%. Exposure times varied from 45s in B, 20s in V, to 15s in R and I. To produce these results, nightly images were calibrated with 25 bias frames, at least five flat frames in each filter, and ten 300-second dark frames.

3. Photometric targets and finding chart

The photometric targets are given in Table 2. A finder chart of the field is given as Figure 3. The B, V, and B–V nightly light curves from 22 and 23 January 2020 are displayed in Figures 4 and 5.

4. Period study

Three mean times (from BVRI data) of minimum light were calculated and averaged from our present observations, one primary and two secondary eclipses:

$$\text{HJD I} = 2457870.51294 \pm 0.00078,$$
$$\text{HJD II} = 2457870.713587 \pm 0\ 0.00052,$$
$$2457871.512445 \pm 0.00078.$$

These minima were weighted as 1.0 in the period study. In addition, four times of minimum light were calculated ASAS data and were weighted 0.1. Six other times of minimum light were taken from ROTSE data. These were not available publicly but were supplied by Dr. Sara Gettel (2020) at one author's request (Samec) and we wish to thank her for these data so that we were able to put together a reasonable period study.

From these timings, ephemerides have been calculated, a linear and a quadratic one:

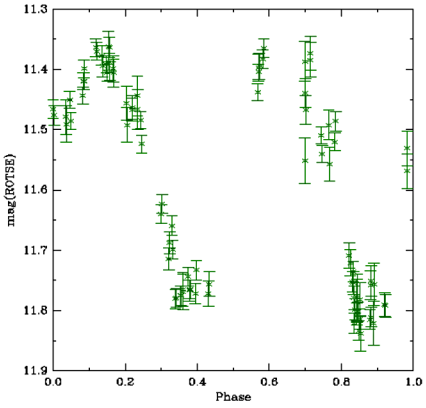

Figure 1. ROTSE light curves (Gettel *et al.* 2006).

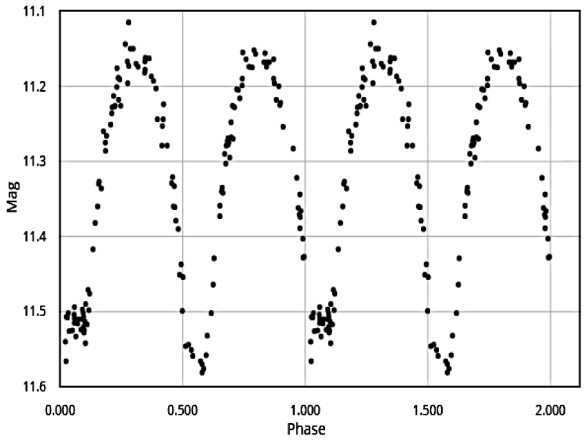

Figure 2. ASAS light curves (Pojmański 2002).

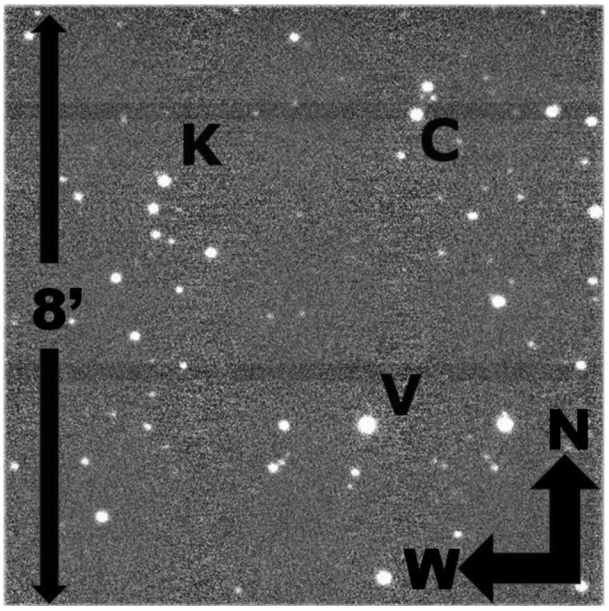

Figure 3. Finder chart: TYC 2402-0643-1 (V), comparison star (C), and check (K).

$$\text{JD Hel Min I} = 2458870.51289 \pm 0.00045\,\text{d} + 0.399578304 \pm 0.000000064 \times E \quad (3)$$

$$\text{JD Hel Min I} = 2458870.51346 \pm 0.00019\text{d} + 0.39958073 \pm 0.00000021 \times E + 0.000000000134 \pm 0.000000000012 \times E^2 \quad (4)$$

The study given here covers a time interval of ~20 years. It does show an orbital period that is increasing. If this effect is found to be correct, it might be due to mass transfer to the more massive, primary component making the mass ratio more extreme. The residuals are given in Table 3. The linear residuals are shown in Figure 6 and a plot of the quadratic term overlying the linear term residuals is given in Figure 7. The quadratic term B, V with B–V color curves and R, I curves with R–I color curves phased with Equation 3 are given in Figures 8 and 9, respectively.

The quadratic ephemeris yields a $\dot{P} = 8.77 \times 10^{-7}$ d / yr, or a mass exchange rate of

$$\frac{dM}{dt} = \frac{\dot{P} M_1 M_2}{3P (M_1 - M_2)} = \frac{-1.65 \times 10^{-8}\, M_\odot}{d}. \quad (5)$$

in a conservative scenario (the primary component is the gainer.)

5. Light curve characteristics

Averages of BVRI magnitudes from each quarter phase cycles, 0.0, 0.25, 0.50, and 0.75, are given in Table 4. From these, we can determine interesting characteristics of the curves. The curves are of good accuracy, averaging better than 1% photometric precision. The amplitude of the light curves varies from 0.35 to 0.47 mag. The O'Connell effect, a possible indicator of spot activity, averages less than the noise level. The differences in minima are small, 0.0–0.07 mag, indicating overcontact light curves in good thermal contact. A time of constant light occurs at our secondary minimum and lasts some 43 minutes.

6. Temperature and light curve solution

The 2MASS, J–K = 0.47 ± 0.02 for the binary star. These magnitudes correspond to ~K0V ± 2.5, which yields a temperature of 5250 ± 200 K. We use this temperature as the primary component's temperature in the light curve analysis. Fast rotating binary stars of this type are noted for having strong magnetic activity, so the binary is of solar type with a convective atmosphere.

7. Light curve solution

The B, V, R_c, and I_c curves were pre-modeled with BINARY MAKER 3.0 (Bradstreet and Steelman 2002). Fits were determined in all filter bands, which were very stable. The solution was that of an over contact eclipsing binary. The parameters were then averaged (q = 0.21, fill-out = 0.15, i = 80.25, T_2 = 5100, with one cool spot) and input into a four-color simultaneous

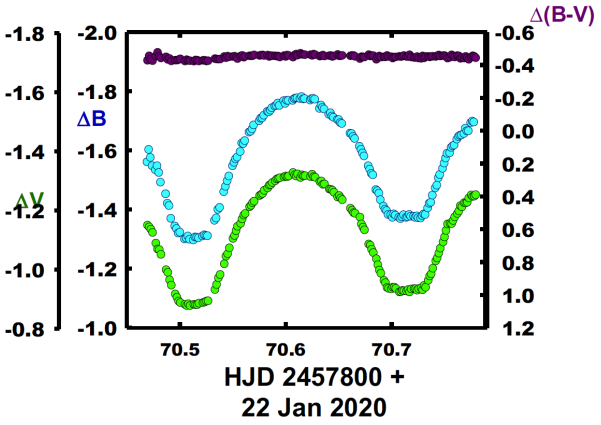

Figure. 4. TYC 2402-0643-1 B,V, B–V color curves from the evening of 22 January 2020.

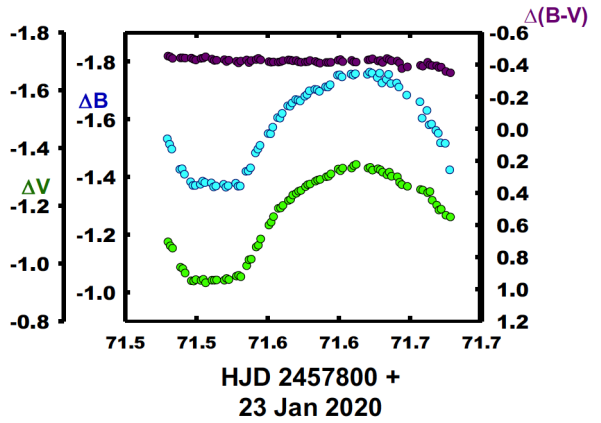

Figure. 5. TYC 2402-0643-1 B, V, B–V color curves from the evening of 23 January 2020.

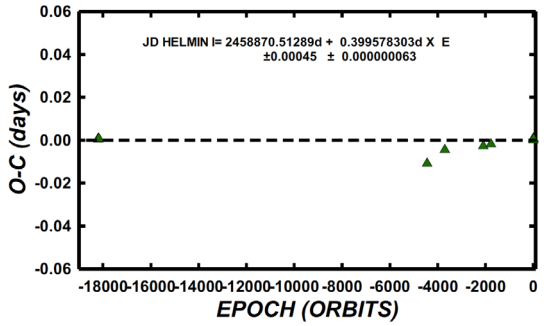

Figure 6. A plot of the linear residuals from Equation 3. The interval of the observations is some 20 years.

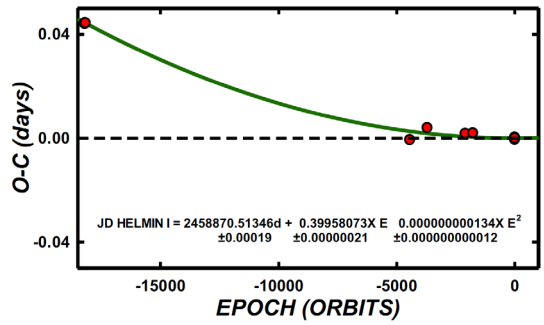

Figure 7. A plot of the quadratic term overlying the linear term residuals of Equation 4. The interval of the observations is some 20 years.

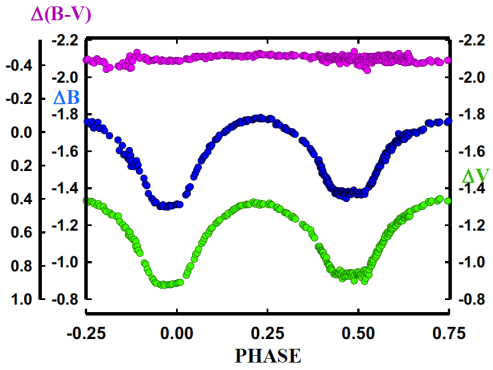

Figure 8. TYC 2402-0643-1 B,V plots and B–V color curves phased with Equation 1.

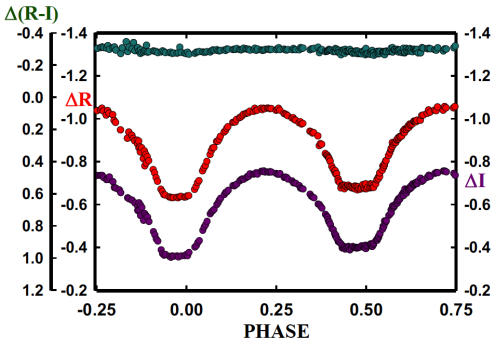

Figure 9. TYC 2402-0643-1 R, I plots and R–I color curves phased with Equation 1.

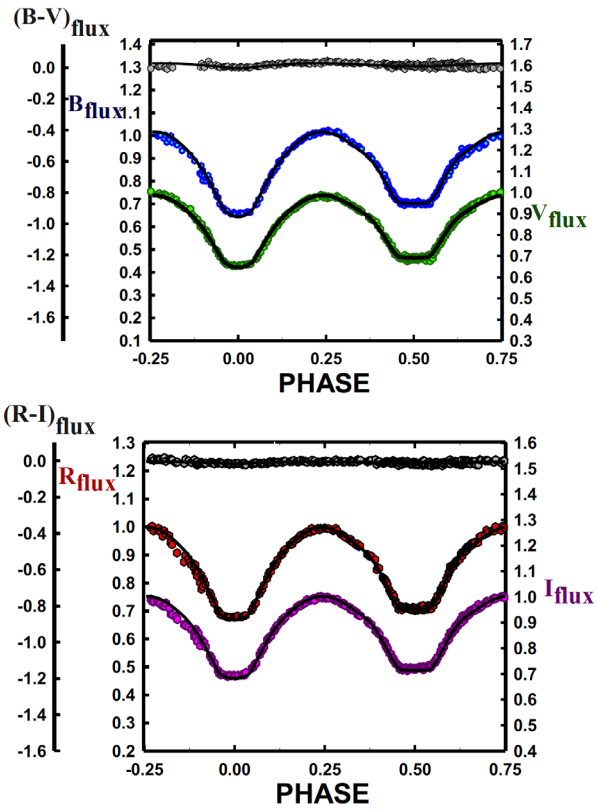

Figure 10. TYC 2402-0643-1: (a, upper plot) B, V normalized fluxes and the B–V color curves overlaid by the detached solution for TYC 2402-0643-1; (b, lower plot) R_c, I_c normalized fluxes and the R_c–I_c color curves overlaid by the over contact solution of TYC 2402-0643-1.

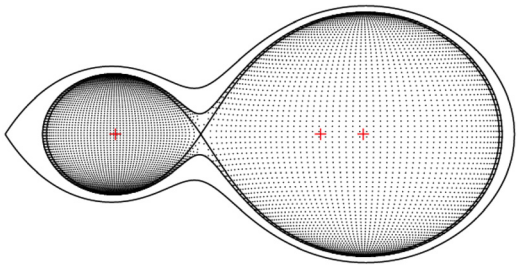

Figure 11. Solution of TYC 2402-0643-1 in cross-section showing the inner and outer Lagrangian surfaces and the fill-out (Bradstreet and Steelman 2002, BINARY BAKER 3.0).

light curve calculation using the Wilson-Devinney program (Wilson and Devinney 1971; Wilson 1979, 1990, 1994, 2008, 2012; Wilson *et al.* 2010; Van Hamme and Wilson 1998; Wilson and Van Hamme 2014). The solution was computed in Mode 3 and converged to a solution. Convective parameters g = 0.32, A = 0.5 (Lucy 1967; Ruciński 1969) were used.

An eclipse duration of ~43 minutes was determined for our secondary eclipse and the light curve solution. The more massive component is the hotter, making the system an A-type W UMa contact binary. We tried third light but that did not solve any fitting issues. The solution parameters follow in Table 5. The light curves of the BVRI solution with the solution curves overlay the mean flux values in Figures 10a and 10b. Figure 11 shows the geometric solution of TYC 2402-0643-1 in cross-section with the inner and outer Lagrangian surfaces and the fill-out.

TYC 2402-0643-1 is an A-type, W UMa binary. Since the eclipses were total, the mass ratio, q, is well determined (Terrell and Wilson 2005) with a fill-out of 22(1)%. The system has an extreme mass ratio of ~0.208, and a component temperature difference of only ~68 K, so it is in good thermal contact. No spots were needed in the final modeling. But there are various fluctuations about the smooth solution curve that indicate activity. Of the 25 EMRBs in Samec *et al.* (2011), three did not have modeled spots. However, for a solar-type binary such as this, that does not mean that there is no magnetic activity. Likely, the surface is saturated with magnetic activity, but is averaging out in flux level so the light curves are not a good means of detecting them. Doppler imaging of systems with fairly symmetric curves has shown many spots are actually present (Senavcı *et al.* 2011; Xiang *et al.* 2015). The inclination of ~83.4° resulted in a time of constant light in the secondary eclipse. Its photometric spectral type indicates a surface temperature of ~5250 K for the primary component, making it a solar type binary. Such a main sequence star would have a mass of ~0.86 $M_\odot$ and the secondary (from the mass ratio) would have a mass of ~0.18 $M_\odot$, making it very much undersized. The temperature (~5180 K) of a single main sequence star would make it of type K1V instead of M4.5V as indicated by its mass. At present the period study indicates that it is increasing. This could be due to mass exchange with the flow toward the primary, more massive component. Radial velocity curves are needed to obtain absolute (not relative) system parameters.

References

Bradstreet E. F., and Guinan, E. F. 1994, in *Interacting Binary Stars*, ed. A. W. Shafter, ASP Conf. Ser. 56, 228, Astronomical Society of the Pacific, San Francisco.

Bradstreet, D. H., and Steelman, D. P. 2002, *Bull. Amer. Astron. Soc.*, **34**, 1224.

Gaia Collaboration, Prusti, T., *et al.* 2016, *Astron. Astrophys.*, **595**, 1.

Gettel, S. J. 2020, Personal communication.

Gettel S. J., Geske M. T., and McKay T. A. 2006, *Astron. J.*, **131**, 621.

Gharami, P., Ghosh, K., and Rahaman, F. 2018, *Bull. Calcutta Math. Soc.*, **110**, 309.

Guinan, E. F., and Bradstreet, D. H. 1988, in *Formation and Evolution of Low Mass Stars*, eds. A. K. Dupree, M. T. V. T. Lago, NATO Adv. Sci. Inst. (ASI) Ser. C, 241, Kluwer, Dordrecht, 345.

Guinan, E. F., Bradstreet, D. H., and Robinson, C. R. 1987, *Bull. Amer. Astron. Soc.*, **19**, 1085.

Guinan, E. F., and Engle, E. G. 2009, in *The Ages of Stars*, eds. J. Th. van Loon, J. M. Oliveira, IAU Symp. 258, Cambridge Univ. Press, Cambridge, 395.

Hoffman, D. I., Harrison, T. E., and McNamara, B. J. 2009, *Astron. J.*, **138**, 466.

Loukaidou, G., and Gazeas, K. 2020, *Contrib. Astron. Obs. Skalnaté Pleso*, **50**, 461.

Lucy, L. B. 1967, *Z. Astrophys.*, **65**, 89.

Meléndez, J., dos Santos, L. A., and Freitas, F. C. 2017, in *Living Around Active Stars*, eds. D. Nandy, A. Valio, P. Petit, IAU Symp. 328, Cambridge Univ. Press, Cambridge, 274.

Molnar, L. A., *et al.* 2017, *Astrophys. J.*, **840**, 1.

Mullan, D. J. 1975, *Astrophys. J.*, **198**, 563.

Nelson, R. H., and Alton, K. B. 2019, *Inf. Bull. Var. Stars*, No. 6266, 1.

Ochsenbein, F., Bauer, P., and Marcout, J. 2000, *Astron. Astrophys., Suppl. Ser.*, **143**, 23.

Pojmański, G. 2002, *Acta. Astron.*, **52**, 397.

Ruciński, S. M. 1969, *Acta Astron.*, **19**, 245.

Samec, R. G., Labadorf, N. C., Hawkins, D. R., Faulkner, and Van Hamme, W. 2011, *Astron. J.*, **142**, 117.

Schneider, F. R., Ohlmann, S. T., Podsiadlowski, P., Röpke, F. K., Balbus, S. A., Pakmor, R., and Springel, V. 2019, *Nature*, **574**, 211.

Şenavcı, H. V., Hussain, G. A. J., O'Neal, D., and Barnes, J. 2011, *Astron. Astrophys.*, **529A**, 11.

Skrutskie, M. F., *et al.* 2006, *Astron. J.*, **131**, 1163.

Terrell D., and Wilson R. E. 2005, *Astrophys. Space Sci.*, **296**, 221.

Tylenda, R., and Kamiński, T. 2016, *Astron. Astrophys.*, **592A**, 134.

U.S. Naval Observatory. 2012, UCAC-3 (http://www.usno.navy.mil/USNO/astrometry/optical-IR-prod/ucac).

Van Hamme, W., and Wilson, R. E. 1998, Bull. Amer. Astron. Soc., 30, 1402.

Vant'veer, F. 1994, *Mem. Soc. Astron. Ital.*, **65**, 105.

Wilson, R. E. 1979, *Astrophys. J.*, **234**, 1054.

Wilson, R. E. 1990, *Astrophys. J.*, **356**, 613.

Wilson, R. E. 1994, *Publ. Astron. Soc. Pacific*, **106**, 921.

Wilson, R. E. 2008, *Astrophys. J.*, **672**, 575.

Wilson, R. E. 2012, *Astron. J.*, **144**, 73.

Wilson, R. E., and Devinney, E. J. 1971, *Astrophys. J.*, **166**, 605.

Wilson, R. E., and Van Hamme, W. 2014, *Astrophys. J.*, **780**, 151.

Wilson, R. E., Van Hamme, W., and Terrell, D. 2010, *Astrophys. J.*, **723**, 1469.

Xiang, Y., Gu, S., Collier Cameron, A., and Barnes, J. R. 2015, *Mon. Not. Roy. Astron. Soc.*, **447**, 567.

Table 1. TYC 2402-0643-1 observations, ΔB, ΔV, ΔR_c, and ΔI_c, variable star minus comparison star.

Δ*B*	*BHJD 2458800+*	Δ*B*	*BHJD 2458800+*	Δ*B*	*BHJD 2458800+*	Δ*B*	*BHJD 2458800+*	Δ*B*	*BHJD 2458800+*
–1.552	69.481	–1.322	70.500	–1.774	70.614	–1.377	70.724	–1.367	71.531
–1.509	69.483	–1.299	70.505	–1.781	70.615	–1.371	70.725	–1.418	71.535
–1.479	69.484	–1.302	70.506	–1.773	70.617	–1.370	70.728	–1.419	71.536
–1.479	69.486	–1.309	70.508	–1.774	70.618	–1.378	70.729	–1.430	71.538
–1.434	69.489	–1.298	70.509	–1.769	70.623	–1.384	70.731	–1.482	71.542
–1.446	69.491	–1.296	70.513	–1.774	70.625	–1.382	70.732	–1.495	71.543
–1.412	69.492	–1.306	70.515	–1.775	70.626	–1.404	70.734	–1.508	71.545
–1.398	69.494	–1.305	70.516	–1.772	70.628	–1.420	70.736	–1.549	71.550
–1.370	69.499	–1.303	70.518	–1.741	70.632	–1.423	70.737	–1.548	71.552
–1.386	69.500	–1.309	70.522	–1.752	70.634	–1.447	70.739	–1.571	71.554
–1.381	69.502	–1.313	70.523	–1.744	70.635	–1.472	70.742	–1.604	71.557
–1.358	69.503	–1.311	70.525	–1.739	70.637	–1.481	70.743	–1.602	71.559
–1.381	69.506	–1.310	70.526	–1.721	70.641	–1.506	70.744	–1.619	71.560
–1.368	69.509	–1.362	70.533	–1.726	70.643	–1.517	70.746	–1.645	71.564
–1.380	69.514	–1.370	70.535	–1.715	70.644	–1.538	70.748	–1.644	71.566
–1.364	69.516	–1.399	70.536	–1.711	70.645	–1.556	70.750	–1.655	71.567
–1.378	69.518	–1.406	70.538	–1.703	70.649	–1.573	70.751	–1.667	71.570
–1.388	69.519	–1.459	70.542	–1.703	70.650	–1.589	70.753	–1.665	71.571
–1.372	69.524	–1.477	70.543	–1.693	70.652	–1.591	70.755	–1.662	71.573
–1.362	69.527	–1.496	70.545	–1.690	70.653	–1.609	70.757	–1.678	71.576
–1.430	69.539	–1.512	70.547	–1.657	70.661	–1.614	70.758	–1.684	71.578
–1.442	69.540	–1.547	70.550	–1.656	70.663	–1.617	70.759	–1.697	71.579
–1.456	69.542	–1.559	70.551	–1.646	70.664	–1.637	70.762	–1.702	71.583
–1.473	69.544	–1.570	70.553	–1.639	70.665	–1.646	70.763	–1.701	71.585
–1.519	69.547	–1.576	70.554	–1.613	70.670	–1.650	70.765	–1.695	71.586
–1.518	69.549	–1.595	70.557	–1.602	70.671	–1.651	70.766	–1.711	71.591
–1.547	69.551	–1.624	70.559	–1.590	70.673	–1.656	70.769	–1.710	71.592
–1.570	69.552	–1.622	70.560	–1.580	70.674	–1.674	70.770	–1.718	71.594
–1.592	69.556	–1.632	70.562	–1.547	70.678	–1.665	70.771	–1.751	71.599
–1.619	69.558	–1.661	70.566	–1.535	70.680	–1.665	70.773	–1.752	71.601
–1.625	69.560	–1.664	70.567	–1.521	70.681	–1.693	70.775	–1.745	71.602
–1.626	69.561	–1.672	70.569	–1.516	70.683	–1.698	70.777	–1.755	71.609
–1.653	69.565	–1.685	70.570	–1.466	70.685	–1.695	70.778	–1.751	71.610
–1.658	69.567	–1.699	70.575	–1.462	70.687	–1.531	71.480	–1.756	71.612
–1.693	69.569	–1.708	70.577	–1.454	70.688	–1.512	71.481	–1.754	71.620
–1.677	69.570	–1.709	70.578	–1.432	70.690	–1.495	71.483	–1.762	71.622
–1.681	69.573	–1.718	70.580	–1.410	70.693	–1.425	71.488	–1.758	71.623
–1.691	69.575	–1.731	70.583	–1.400	70.694	–1.427	71.490	–1.743	71.627
–1.560	70.469	–1.729	70.584	–1.395	70.696	–1.408	71.492	–1.758	71.629
–1.602	70.471	–1.735	70.586	–1.382	70.697	–1.382	71.496	–1.724	71.630
–1.575	70.472	–1.743	70.587	–1.381	70.700	–1.369	71.498	–1.737	71.633
–1.547	70.474	–1.749	70.590	–1.372	70.701	–1.369	71.499	–1.754	71.635
–1.533	70.477	–1.751	70.591	–1.384	70.702	–1.373	71.503	–1.722	71.637
–1.547	70.479	–1.759	70.593	–1.380	70.704	–1.384	71.504	–1.724	71.641
–1.524	70.480	–1.751	70.594	–1.372	70.707	–1.379	71.506	–1.710	71.642
–1.491	70.482	–1.767	70.598	–1.374	70.710	–1.378	71.511	–1.682	71.648
–1.452	70.487	–1.758	70.600	–1.381	70.712	–1.364	71.512	–1.659	71.657
–1.420	70.488	–1.768	70.601	–1.372	70.714	–1.367	71.514	–1.629	71.662
–1.412	70.490	–1.768	70.603	–1.374	70.715	–1.373	71.519	–1.560	71.668
–1.369	70.492	–1.768	70.607	–1.382	70.717	–1.363	71.521	–1.550	71.670
–1.343	70.495	–1.774	70.608	–1.376	70.718	–1.368	71.522	–1.517	71.671
–1.334	70.497	–1.776	70.610	–1.376	70.721	–1.377	71.528	–1.515	71.675
–1.319	70.499	–1.777	70.611	–1.372	70.723	–1.366	71.529		

Table continued on following pages

Table 1. TYC 2402-0643-1 observations, ΔB, ΔV, ΔR_c, and ΔI_c, variable star minus comparison star, cont.

Δ*V*	*VHJD 2458800+*	Δ*V*	*VHJD 2458800+*	Δ*V*	*VHJD 2458800+*	Δ*V*	*VHJD 2458800+*	Δ*V*	*VHJD 2458800+*
–1.085	69.481	–0.943	70.492	–1.307	70.614	–0.942	70.731	–1.132	71.551
–1.059	69.483	–0.913	70.496	–1.316	70.616	–0.936	70.733	–1.142	71.553
–1.054	69.485	–0.902	70.498	–1.312	70.617	–0.959	70.735	–1.161	71.554
–1.033	69.486	–0.889	70.499	–1.313	70.619	–0.974	70.736	–1.190	71.558
–1.024	69.489	–0.884	70.501	–1.310	70.624	–0.981	70.738	–1.191	71.559
–0.988	69.491	–0.878	70.505	–1.318	70.625	–1.000	70.739	–1.200	71.561
–0.960	69.493	–0.874	70.507	–1.310	70.627	–1.025	70.742	–1.217	71.565
–0.967	69.494	–0.880	70.508	–1.308	70.628	–1.035	70.743	–1.221	71.566
–0.942	69.499	–0.874	70.510	–1.293	70.633	–1.051	70.745	–1.236	71.568
–0.936	69.501	–0.878	70.514	–1.295	70.634	–1.068	70.746	–1.242	71.570
–0.937	69.502	–0.877	70.515	–1.284	70.636	–1.089	70.749	–1.249	71.572
–0.956	69.504	–0.877	70.517	–1.285	70.637	–1.106	70.750	–1.252	71.573
–0.910	69.507	–0.882	70.518	–1.268	70.642	–1.128	70.752	–1.265	71.577
–0.921	69.508	–0.884	70.522	–1.267	70.643	–1.150	70.753	–1.272	71.578
–0.936	69.510	–0.886	70.524	–1.264	70.644	–1.152	70.756	–1.274	71.580
–0.938	69.512	–0.889	70.525	–1.257	70.646	–1.151	70.757	–1.284	71.584
–0.938	69.515	–0.890	70.527	–1.241	70.649	–1.162	70.758	–1.288	71.585
–0.939	69.516	–0.928	70.533	–1.246	70.651	–1.174	70.760	–1.290	71.587
–0.940	69.518	–0.945	70.535	–1.238	70.652	–1.185	70.762	–1.299	71.591
–0.935	69.523	–0.968	70.537	–1.232	70.654	–1.194	70.764	–1.301	71.593
–0.936	69.525	–0.979	70.538	–1.203	70.662	–1.212	70.765	–1.309	71.594
–0.933	69.526	–1.015	70.542	–1.196	70.663	–1.208	70.767	–1.326	71.600
–0.915	69.528	–1.041	70.544	–1.188	70.664	–1.222	70.769	–1.320	71.601
–0.912	69.533	–1.049	70.545	–1.186	70.666	–1.221	70.770	–1.329	71.603
–0.937	69.534	–1.069	70.547	–1.173	70.670	–1.223	70.772	–1.329	71.609
–0.931	69.536	–1.101	70.550	–1.150	70.672	–1.238	70.773	–1.338	71.611
–0.997	69.539	–1.111	70.552	–1.130	70.675	–1.248	70.776	–1.342	71.612
–1.013	69.541	–1.127	70.553	–1.082	70.679	–1.243	70.777	–1.329	71.621
–1.030	69.542	–1.142	70.555	–1.078	70.680	–1.244	70.778	–1.332	71.622
–1.052	69.544	–1.152	70.558	–1.064	70.682	–1.249	70.780	–1.322	71.624
–1.076	69.548	–1.167	70.559	–1.053	70.683	–1.074	71.480	–1.327	71.628
–1.096	69.549	–1.180	70.561	–1.032	70.686	–1.060	71.482	–1.323	71.629
–1.107	69.551	–1.185	70.562	–1.012	70.687	–1.052	71.483	–1.315	71.631
–1.114	69.553	–1.208	70.566	–0.994	70.689	–0.986	71.489	–1.306	71.634
–1.138	69.557	–1.213	70.568	–0.983	70.690	–0.981	71.491	–1.315	71.635
–1.162	69.558	–1.222	70.569	–0.959	70.693	–0.966	71.492	–1.301	71.637
–1.178	69.560	–1.227	70.570	–0.951	70.695	–0.939	71.497	–1.299	71.641
–1.180	69.562	–1.246	70.576	–0.935	70.696	–0.938	71.498	–1.280	71.643
–1.196	69.566	–1.250	70.577	–0.932	70.697	–0.943	71.500	–1.272	71.644
–1.214	69.567	–1.253	70.579	–0.930	70.700	–0.940	71.503	–1.266	71.648
–1.220	69.569	–1.264	70.580	–0.936	70.701	–0.944	71.505	–1.255	71.650
–1.231	69.571	–1.272	70.583	–0.936	70.703	–0.932	71.507	–1.253	71.651
–1.242	69.574	–1.281	70.585	–0.932	70.704	–0.941	71.511	–1.244	71.656
–1.240	69.576	–1.283	70.586	–0.920	70.708	–0.941	71.513	–1.248	71.657
–1.253	69.577	–1.290	70.588	–0.921	70.709	–0.942	71.514	–1.218	71.659
–1.246	69.579	–1.296	70.590	–0.925	70.711	–0.941	71.520	–1.201	71.662
–1.146	70.470	–1.302	70.592	–0.924	70.712	–0.947	71.521	–1.184	71.664
–1.140	70.471	–1.304	70.593	–0.923	70.715	–0.943	71.523	–1.187	71.666
–1.132	70.473	–1.306	70.595	–0.928	70.716	–0.955	71.528	–1.166	71.669
–1.121	70.475	–1.309	70.599	–0.920	70.717	–0.958	71.530	–1.160	71.670
–1.085	70.478	–1.312	70.600	–0.930	70.719	–0.953	71.531	–1.134	71.672
–1.065	70.479	–1.310	70.602	–0.931	70.722	–0.991	71.535	–1.122	71.675
–1.063	70.481	–1.312	70.603	–0.931	70.723	–1.012	71.537	–1.110	71.677
–1.047	70.482	–1.324	70.607	–0.926	70.724	–1.014	71.539	–1.085	71.678
–0.995	70.487	–1.316	70.609	–0.931	70.726	–1.056	71.542		
–0.986	70.489	–1.312	70.610	–0.934	70.728	–1.062	71.544		
–0.961	70.491	–1.319	70.612	–0.927	70.730	–1.084	71.545		

Table continued on following pages

Table 1. TYC 2402-0643-1 observations, ΔB, ΔV, ΔR_c, and ΔI_c, variable star minus comparison star, cont.

Δ*R*	*RHJD 2458800+*	Δ*R*	*RHJD 2458800+*	Δ*R*	*RHJD 2458800+*	Δ*R*	*RHJD 2458800+*	Δ*R*	*RHJD 2458800+*
–0.829	71.479	–1.018	71.640	–0.983	70.576	–0.677	70.707	–0.694	71.528
–0.817	71.480	–0.991	71.641	–0.984	70.577	–0.675	70.708	–0.688	71.530
–0.801	71.482	–0.982	71.643	–0.996	70.579	–0.675	70.709	–0.714	71.534
–0.757	71.488	–0.947	71.648	–1.004	70.582	–0.671	70.711	–0.726	71.536
–0.743	71.489	–0.908	71.656	–1.007	70.584	–0.667	70.713	–0.746	71.537
–0.719	71.491	–0.937	71.658	–1.013	70.585	–0.672	70.715	–0.779	71.541
–0.687	71.495	–0.922	71.661	–1.020	70.586	–0.670	70.716	–0.782	71.542
–0.689	71.497	–0.907	71.663	–1.023	70.589	–0.675	70.718	–0.803	71.544
–0.688	71.498	–0.896	71.664	–1.026	70.591	–0.675	70.720	–0.855	71.550
–0.687	71.502	–0.882	71.667	–1.027	70.592	–0.672	70.722	–0.870	71.551
–0.683	71.504	–0.864	71.669	–1.034	70.594	–0.672	70.723	–0.881	71.553
–0.682	71.505	–0.844	71.671	–1.033	70.598	–0.679	70.725	–0.900	71.556
–0.685	71.510	–0.813	71.674	–1.048	70.599	–0.676	70.727	–0.911	71.558
–0.683	71.511	–0.793	71.677	–1.037	70.600	–0.679	70.728	–0.916	71.560
–0.681	71.513	–0.899	70.468	–1.039	70.602	–0.678	70.730	–0.942	71.563
–0.691	71.518	–0.895	70.470	–1.048	70.606	–0.678	70.731	–0.950	71.565
–0.685	71.520	–0.868	70.472	–1.041	70.608	–0.695	70.734	–0.953	71.567
–0.695	71.522	–0.864	70.473	–1.048	70.609	–0.714	70.735	–0.966	71.569
–0.695	71.527	–0.849	70.476	–1.046	70.610	–0.719	70.737	–0.974	71.571
–0.694	71.528	–0.833	70.478	–1.049	70.613	–0.729	70.738	–0.972	71.572
–0.688	71.530	–0.822	70.480	–1.048	70.615	–0.759	70.741	–0.988	71.575
–0.714	71.534	–0.804	70.481	–1.046	70.616	–0.772	70.742	–0.987	71.577
–0.726	71.536	–0.762	70.486	–1.047	70.617	–0.792	70.744	–0.992	71.579
–0.746	71.537	–0.746	70.488	–1.038	70.623	–0.803	70.745	–0.992	71.582
–0.779	71.541	–0.724	70.489	–1.041	70.624	–0.827	70.748	–1.014	71.584
–0.782	71.542	–0.707	70.491	–1.048	70.626	–0.840	70.749	–1.016	71.586
–0.803	71.544	–0.670	70.495	–1.039	70.627	–0.860	70.751	–1.024	71.590
–0.855	71.550	–0.659	70.496	–1.024	70.631	–0.888	70.752	–1.040	71.592
–0.870	71.551	–0.645	70.498	–1.021	70.633	–0.888	70.754	–1.030	71.593
–0.881	71.553	–0.643	70.499	–1.018	70.634	–0.888	70.756	–1.039	71.598
–0.900	71.556	–0.634	70.504	–1.013	70.636	–0.903	70.757	–1.037	71.600
–0.911	71.558	–0.632	70.505	–1.003	70.640	–0.905	70.759	–1.054	71.601
–0.916	71.560	–0.630	70.507	–1.004	70.642	–0.915	70.761	–1.039	71.608
–0.942	71.563	–0.631	70.509	–0.995	70.643	–0.919	70.763	–1.056	71.609
–0.950	71.565	–0.632	70.512	–0.992	70.645	–0.936	70.764	–1.050	71.611
–0.953	71.567	–0.630	70.514	–0.980	70.648	–0.934	70.766	–1.050	71.619
–0.966	71.569	–0.635	70.515	–0.985	70.650	–0.949	70.768	–1.056	71.621
–0.974	71.571	–0.637	70.517	–0.974	70.651	–0.956	70.769	–1.037	71.622
–0.972	71.572	–0.633	70.521	–0.977	70.653	–0.959	70.771	–1.041	71.626
–0.988	71.575	–0.634	70.522	–0.941	70.660	–0.968	70.772	–1.048	71.628
–0.987	71.577	–0.639	70.524	–0.938	70.662	–0.975	70.774	–1.035	71.629
–0.992	71.579	–0.640	70.526	–0.932	70.663	–0.986	70.776	–1.016	71.633
–0.992	71.582	–0.669	70.532	–0.934	70.665	–0.986	70.777	–1.037	71.634
–1.014	71.584	–0.683	70.534	–0.919	70.669	–0.985	70.779	–1.025	71.636
–1.016	71.586	–0.701	70.535	–0.873	70.671	–0.829	71.479	–1.018	71.640
–1.024	71.590	–0.710	70.537	–0.883	70.672	–0.817	71.480	–0.991	71.641
–1.040	71.592	–0.756	70.541	–0.880	70.674	–0.801	71.482	–0.982	71.643
–1.030	71.593	–0.770	70.543	–0.837	70.678	–0.757	71.488	–0.947	71.648
–1.039	71.598	–0.781	70.544	–0.829	70.679	–0.743	71.489	–0.908	71.656
–1.037	71.600	–0.800	70.546	–0.822	70.680	–0.719	71.491	–0.937	71.658
–1.054	71.601	–0.832	70.549	–0.812	70.682	–0.687	71.495	–0.922	71.661
–1.039	71.608	–0.850	70.551	–0.777	70.685	–0.689	71.497	–0.907	71.663
–1.056	71.609	–0.863	70.552	–0.765	70.686	–0.688	71.498	–0.896	71.664
–1.050	71.611	–0.865	70.554	–0.753	70.688	–0.687	71.502	–0.882	71.667
–1.050	71.619	–0.893	70.557	–0.741	70.689	–0.683	71.504	–0.864	71.669
–1.056	71.621	–0.894	70.558	–0.708	70.692	–0.682	71.505	–0.844	71.671
–1.037	71.622	–0.904	70.559	–0.701	70.693	–0.685	71.510	–0.813	71.674
–1.041	71.626	–0.917	70.561	–0.676	70.695	–0.683	71.511	–0.779	71.675
–1.048	71.628	–0.937	70.565	–0.686	70.696	–0.681	71.513	–0.793	71.677
–1.035	71.629	–0.943	70.566	–0.672	70.699	–0.691	71.518		
–1.016	71.633	–0.955	70.568	–0.682	70.700	–0.685	71.520		
–1.037	71.634	–0.962	70.569	–0.682	70.702	–0.695	71.522		
–1.025	71.636	–0.982	70.575	–0.689	70.703	–0.695	71.527		

Table continued onnext page

Table 1. TYC 2402-0643-1 observations, ΔB, ΔV, ΔR_c, and ΔI_c, variable star minus comparison star, cont.

Δ*I*	*IHJD 2458800+*	Δ*I*	*IHJD 2458800+*	Δ*I*	*IHJD 2458800+*	Δ*I*	*IHJD 2458800+*	Δ*I*	*IHJD 2458800+*
–0.540	71.479	–0.727	71.636	–0.694	70.579	–0.403	70.708	–0.415	71.527
–0.518	71.481	–0.705	71.640	–0.709	70.582	–0.399	70.710	–0.403	71.529
–0.505	71.482	–0.678	71.642	–0.715	70.584	–0.398	70.711	–0.413	71.530
–0.453	71.488	–0.675	71.643	–0.718	70.585	–0.398	70.714	–0.432	71.534
–0.441	71.490	–0.667	71.647	–0.716	70.587	–0.398	70.715	–0.445	71.536
–0.426	71.491	–0.654	71.649	–0.723	70.589	–0.401	70.716	–0.464	71.538
–0.396	71.496	–0.630	71.656	–0.729	70.591	–0.406	70.718	–0.497	71.541
–0.396	71.497	–0.625	71.658	–0.730	70.592	–0.400	70.721	–0.522	71.543
–0.391	71.499	–0.619	71.661	–0.742	70.594	–0.409	70.722	–0.520	71.544
–0.403	71.502	–0.606	71.665	–0.740	70.598	–0.404	70.724	–0.574	71.550
–0.387	71.504	–0.571	71.668	–0.742	70.599	–0.407	70.725	–0.592	71.552
–0.398	71.506	–0.572	71.669	–0.747	70.601	–0.411	70.727	–0.588	71.553
–0.399	71.510	–0.592	70.469	–0.740	70.602	–0.412	70.729	–0.605	71.557
–0.395	71.512	–0.607	70.470	–0.754	70.606	–0.404	70.730	–0.619	71.558
–0.397	71.513	–0.596	70.472	–0.752	70.608	–0.420	70.732	–0.625	71.560
–0.405	71.519	–0.585	70.474	–0.756	70.609	–0.431	70.734	–0.640	71.564
–0.397	71.520	–0.557	70.477	–0.750	70.611	–0.440	70.735	–0.671	71.565
–0.393	71.522	–0.547	70.478	–0.751	70.613	–0.452	70.737	–0.652	71.567
–0.415	71.527	–0.540	70.480	–0.749	70.615	–0.461	70.738	–0.668	71.569
–0.403	71.529	–0.519	70.481	–0.752	70.616	–0.483	70.741	–0.672	71.571
–0.413	71.530	–0.472	70.486	–0.750	70.618	–0.494	70.743	–0.678	71.572
–0.432	71.534	–0.457	70.488	–0.744	70.623	–0.511	70.744	–0.692	71.576
–0.445	71.536	–0.438	70.490	–0.740	70.624	–0.523	70.745	–0.701	71.577
–0.464	71.538	–0.428	70.491	–0.739	70.626	–0.547	70.748	–0.696	71.579
–0.497	71.541	–0.387	70.495	–0.743	70.627	–0.553	70.749	–0.721	71.583
–0.522	71.543	–0.369	70.497	–0.725	70.632	–0.560	70.751	–0.707	71.584
–0.520	71.544	–0.362	70.498	–0.727	70.633	–0.580	70.752	–0.713	71.586
–0.574	71.550	–0.366	70.500	–0.725	70.635	–0.594	70.755	–0.726	71.590
–0.592	71.552	–0.357	70.504	–0.717	70.636	–0.603	70.756	–0.735	71.592
–0.588	71.553	–0.352	70.506	–0.709	70.641	–0.616	70.758	–0.730	71.593
–0.605	71.557	–0.359	70.507	–0.700	70.642	–0.626	70.759	–0.744	71.599
–0.619	71.558	–0.357	70.509	–0.699	70.643	–0.636	70.762	–0.748	71.600
–0.625	71.560	–0.359	70.513	–0.697	70.645	–0.646	70.763	–0.747	71.602
–0.640	71.564	–0.354	70.514	–0.687	70.649	–0.655	70.764	–0.755	71.608
–0.671	71.565	–0.359	70.517	–0.675	70.650	–0.661	70.766	–0.755	71.610
–0.652	71.567	–0.360	70.521	–0.673	70.651	–0.665	70.768	–0.751	71.611
–0.668	71.569	–0.365	70.523	–0.671	70.653	–0.672	70.769	–0.744	71.620
–0.672	71.571	–0.360	70.524	–0.647	70.661	–0.673	70.771	–0.735	71.621
–0.678	71.572	–0.375	70.526	–0.637	70.662	–0.684	70.772	–0.734	71.623
–0.692	71.576	–0.400	70.532	–0.633	70.664	–0.695	70.775	–0.734	71.627
–0.701	71.577	–0.407	70.534	–0.630	70.665	–0.688	70.776	–0.734	71.628
–0.696	71.579	–0.422	70.536	–0.601	70.670	–0.696	70.778	–0.725	71.630
–0.721	71.583	–0.430	70.537	–0.599	70.671	–0.702	70.779	–0.715	71.633
–0.707	71.584	–0.478	70.541	–0.590	70.672	–0.709	70.781	–0.715	71.634
–0.713	71.586	–0.494	70.543	–0.582	70.674	–0.540	71.479	–0.727	71.636
–0.726	71.590	–0.505	70.544	–0.553	70.678	–0.518	71.481	–0.705	71.640
–0.735	71.592	–0.520	70.546	–0.544	70.679	–0.505	71.482	–0.678	71.642
–0.730	71.593	–0.555	70.550	–0.528	70.681	–0.453	71.488	–0.675	71.643
–0.744	71.599	–0.564	70.551	–0.517	70.682	–0.441	71.490	–0.667	71.647
–0.748	71.600	–0.570	70.552	–0.486	70.685	–0.426	71.491	–0.654	71.649
–0.747	71.602	–0.576	70.554	–0.481	70.686	–0.396	71.496	–0.630	71.656
–0.755	71.608	–0.598	70.557	–0.463	70.688	–0.396	71.497	–0.625	71.658
–0.755	71.610	–0.607	70.558	–0.456	70.689	–0.391	71.499	–0.619	71.661
–0.751	71.611	–0.619	70.560	–0.429	70.692	–0.403	71.502	–0.606	71.665
–0.744	71.620	–0.628	70.561	–0.421	70.694	–0.387	71.504	–0.571	71.668
–0.735	71.621	–0.645	70.565	–0.415	70.695	–0.398	71.506	–0.572	71.669
–0.734	71.623	–0.655	70.567	–0.407	70.697	–0.399	71.510	–0.547	71.671
–0.734	71.627	–0.657	70.568	–0.402	70.699	–0.395	71.512	–0.525	71.674
–0.734	71.628	–0.665	70.570	–0.397	70.701	–0.397	71.513		
–0.725	71.630	–0.687	70.575	–0.398	70.702	–0.405	71.519		
–0.715	71.633	–0.685	70.576	–0.400	70.703	–0.397	71.520		
–0.715	71.634	–0.690	70.578	–0.394	70.707	–0.393	71.522		

Table 2. Information on the stars used in this study.

Star	*Name*	*R.A. (2000)* h m s	*Dec. (2000)*[1] ° ′ ″	*V*	*J–K*
V (Variable)	TYC 2402-0643-1 GSC 4547 0771 2MASS J05185809+3658060 ASAS J113031-0101.9 NSVS 4382530 [GGM2006] 6868894	05 18 58.0949883180	+36 58 06.076375043[1]	11.373[2]	0.467 ± 0.049[2]
C (Comparison)	GSC 2402 0273 3UC255-052567[3]	05 19 01.8633	+37 02 53.47[2]	12.07[3]	0.68[4]
K (Check)	GSC 2402 1209 3UC255-052413[3]	05 18 41.3125	+37 01 51.489[2]	12.36[2]	0.420 ± 0.046[2]

[1] *Gaia Collaboration (2006).* [2] *VizieR (Ochsenbein* et al. *2000).* [3] *UCAC3 (U.S. Naval Obs. 2012).* [4] *2MASS (Skrutskie* et al. *2006).*

Table 3. O–C Residuals for TYC 2402 0643 1.

	Epochs	*Cycles*	*Linear Residuals*	*Quadratic Residuals*	*Weight*	*Error*	*References*
1	51597.1893	–18202.5	0.0005	–0.0002	0.1	0.0007	Gettel et al. (2006) (ROTSE)
2	51597.1896	–18202.5	0.0008	0.0001	0.1	0.0001	Gettel et al. (2006) (ROTSE)
3	51607.1791	–18177.5	0.0008	0.0002	0.1	0.0001	Gettel et al. (2006) (ROTSE)
4	51597.3891	–18202.0	0.0005	–0.0002	0.1	0.0006	Gettel et al. (2006) (ROTSE)
5	51597.3894	–18202.0	0.0008	0.0001	0.1	0.0002	Gettel et al. (2006) (ROTSE)
6	51607.3789	–18177.0	0.0008	0.0002	0.1	0.0002	Gettel et al. (2006) (ROTSE)
7	57095.7750	–4441.5	–0.0109	–0.0033	0.1	0.0003	Pojmański (2002)
8	57390.8700	–3703.0	–0.0044	0.0021	0.1	0.0115	Pojmański (2002)
9	58033.9930	–2093.5	–0.0027	0.0012	0.1	0.0063	Pojmański (2002)
10	58161.8590	–1773.5	–0.0018	0.0015	0.1	0.0066	Pojmański (2002)
11	58870.5129	0.0	0.0000	–0.0005	1.0	0.0004	Present observations
12	58870.7136	0.5	0.0009	0.0003	1.0	0.0005	Present observations
13	58871.5125	2.5	0.0006	0.0000	1.0	0.0008	Present observations

Table 4. Light curve characteristics for TYC 2402 0643 1.

Filter	*Phase 0.000*	*Magnitude ± σ** *Min. I*	*Phase 0.25*	*Magnitude ± σ** *Max. I*
B		–1.302 ± 0.004		–1.776 ± 0.003
V		–0.877 ± 0.002		–1.314 ± 0.005
R		–0.633 ± 0.003		–1.047 ± 0.001
I		–0.399 ± 0.093		–0.752 ± 0.002
Filter	*Phase 0.500*	*Magnitude ± σ** *Min. II*	*Phase 0.75*	*Magnitude ± σ** *Max. II*
B		–1.375 ± 0.007		–1.756 ± 0.005
V		–0.933 ± 0.008		–1.336 ± 0.007
R		–0.676 ± 0.007		–1.053 ± 0.004
I		–0.399 ± 0.003		–0.754 ± 0.002

Filter	*Min. I–Max. I ± σ*	*Max. I–Max. II ± σ*	*Min. I–Min. II ± σ*
B	0.474 ± 0.010	–0.020 ± 0.018	0.073 ± 0.012
V	0.437 ± 0.013	0.022 ± 0.042	0.056 ± 0.011
R	0.414 ± 0.008	0.006 ± 0.008	0.043 ± 0.010
I	0.353 ± 0.006	0.002 ± 0.002	0.000 ± 0.097

**Magnitude is the variable star – comparison star magnitude.*

Table 5. B, V, R_c, I_c Wilson-Devinney program solution parameters.

Parameters	*Values*
λ_B, λ_V, λ_R, λ_I (nm)	440, 550, 640, 790
g_1, g_2	0.32
A_1, A_2	0.5
Inclination (°)	83.40 ± 0.13
T_1, T_2 (K)	5250, 5182 ± 2
Ω	2.2236 ± 0.0011
$q(m_1/m_2)$	0.2079 ± 0.0003
Fill-outs: $F_1 = F_2$ (%)	0.22 ± 0.01
$L_1/(L_1+L_2+L_3)_I$	0.8097 ± 0.0095
$L_1/(L_1+L_2+L_3)_R$	0.8106 ± 0.0083
$L_1/(L_1+L_2+L_3)_V$	0.8124 ± 0.0035
$L_1/(L_1+L_2+L_3)_B$	0.8154 ± 0.0045
JD_o (days)	2457870.51357 ± 0.00006
Period (days)	0. 39943 ± 0.00004
r_1/a, r_2/a (pole)	0.4909 ± 0.0006, 0.2430 ± 0.0011
r_1/a, r_2/a (side)	0.5356 ± 0.0009, 0.2538 ± 0.0013
r_1/a, r_2/a (back)	0.5605 ± 0.0012, 0.2932 ± 0.0026

Smartphone Astrophotography: A Useful Approach for Outreach and Education

Sara Bimo
York University, 4700 Keele Street, Toronto, Ontario M3J 1P3, Canada; bimosara@yorku.ca

Received February 18, 2020; revised April 24, 2020; accepted April 24, 2020

Abstract In this article, I describe my experiences with a somewhat neglected method of variable star observation: smartphone images. I outline the potential of smartphone images as a tool for astronomy education and argue that they are a uniquely effective way to draw in beginner observers (especially younger observers, amongst whom high-level smartphone usage is ubiquitous). I describe my methods in collecting images of two variable stars (δ Cephei and β Persei) with my smartphone, and how I used these data to make magnitude estimates and phase diagrams. I conclude with a note on the potential of smartphones as an educational tool, and outline some of the aspects that contribute to their appeal and usefulness.

1. Introduction

This past year, I have been working on a student project focused on making variable star observing more easily accessible. Like many outreach projects, it is, at heart, concerned with one question: how can astronomy (or, science in general) be made easy? In many ways, this is the million dollar question, and the many attempts to answer it have prominently featured across a variety of subjects, such as the philosophy of citizen science and the epistemology of science. One can almost convince oneself that making science "easy" is the missing piece required to solve many of the quandaries that plague those of us concerned with science outreach and related social issues; we can dream that it will promote the establishment of a scientifically literate and engaged public, which will, in turn, lead to a more effective and just society.

The question of whether easy and accessible science is indeed the solution to our ills is impossible to answer, but it nonetheless remains an intoxicating idea. It was the pursuit of this question that first introduced me to the ample history of amateur astronomers and variable star observing, and to the wealth of work done by organizations such as the AAVSO in connection to this same goal. Variable star astronomy seems to tick all the boxes for drawing in non-scientists; it incorporates the glamour and beauty of the stars, while genuinely providing a meaningful opportunity for amateurs to contribute to the greater enterprise of astronomy. In this article, I'll talk about my experiences with creating an "easy" astronomy resource for beginners, and how I believe smartphone camera photometry may be a more effective entry point to the field than the more commonly used methods of visual observing or DSLR camera observing.

2. The case for smartphone images

The project I previously mentioned involved the creation of a standalone tutorial for variable star observing in the form of an interactive and gamified app (this app is still in development and will be made available on the Google Play Store by August 2020, under the title "Variable Astronomy: A Do-It-Yourself Experiment"). Created in UNITY, a platform often used for video game development, the application was created with high school and university students in mind as the target audience, users who would most likely begin their intellectual journeys into astronomy by looking for resources online. On a basic level, the idea of the project was to guide people with absolutely no prior knowledge of astronomy through the process of a simple yet useful experiment in variable star observing. It began by teaching users how to collect data and make magnitude observations and concluded with a guide to creating phase diagrams from their data. It also informed users about how they could share their observations and engage with the wider astronomical community. My hope was that this application would be an effective way to create new amateur astronomers. As such, much of its success relied on it being, to put it simply, easy. Thus, while working on creating this resource, I imagined myself in the role of a salesman trying to recruit new clients into variable star observing.

In trying to find the easiest and fastest way to observe stars, I began by putting myself in the shoes of my target users, and experimented with various methods of observing. Of these, I reasoned that the most accessible (and least intimidating) is visual observing. After that, DSLR photometry is probably the second most appealing to complete beginners, with DSLR cameras being a reasonably common and familiar device. I also tried taking pictures with the camera on my smartphone, with little hope that the quality would be high enough to be able to make magnitude estimates.

To my surprise, these smartphone images ended up being the most convenient and effective method for a rough and tumble introduction to variable stars. As more experienced observers would have been able to tell me, there are certain hidden difficulties in visual observing that are easy to forget until you find yourself outside in your chosen observing spot, unsure of where to look and what to do next (Gaskell 1991). For example, after you've settled on a target star, you must use star maps, or planetarium apps to actually find it in the sky. This is sometimes easier said than done, especially in areas with high light pollution; you must allow your eyes to adjust to the night sky, and wait a while until you can accurately guess at the magnitude of your star. You also need to have memorized the positions and magnitudes of your reference stars–otherwise, you will have to refer back and forth between the sky and your star chart, running the risk of losing the position of your star and

wasting time as your eyes become disaccustomed. In addition, in harsher weather conditions, being outside for longer periods of time is quite difficult. For dedicated, passionate observers, these inconveniences are minor, and do not strongly affect the quality of the experience. But for complete beginners with little emotional attachment to or stake in the enterprise, the slightest difficulty may be enough to put them off the idea completely.

Cellphone photometry alleviates these inconveniences to a degree that may be enough to keep the more fickle observers interested. To begin with, when taking cell phone pictures, observers do not need to pinpoint the exact location of their target star. Knowing the vague position, perhaps guided by a general constellation that may be easier to immediately identify, is often good enough if several pictures in that field of view are taken. Observers can avoid staying outside for long periods of time, as well as preparing star charts and memorizing reference stars, by pulling their pictures up once in the comfort of their own homes and making their magnitude estimates in their own time, aided by any other resources they may find helpful. Furthermore, some of the urgency involved in making accurate estimates is eliminated by the fact that observers can just go out and take another cell phone picture if their first attempts do not go as planned. In this way, visual observing can be "tamed" enough for beginner observers to gain an entry into the science of variable star observing.

DSLR pictures offer some of these advantages, and also allow for observers to make magnitude estimate in their own time (Loughney 2010). However, in my experience, DSLR cameras are a more intimidating animal, and observers may be confused as to how exactly to adjust their cameras for optimal quality. Smartphone cameras tend to have less customizable settings, and as such are less daunting to beginners. Changing the ISO, white balance, and aperture is just a matter of tapping some icons on a screen.

DSLRs are also more cumbersome and thus more difficult to transport to your observing location, while many observers will already be carrying their cellphones with them wherever they go. DSLRs will also need a tripod, whereas you can get away with not using one for smartphone pictures (you may look silly resting your phone on nearby benches or walls to stabilize it, but the pictures will turn out well!) (Loughney 2010). Furthermore, when it comes to disseminating pictures, DSLRs must be hooked up to a computer and files must be transferred, whereas most smartphones will have built-in options for easily sharing pictures (Loughney 2010). This affects the social nature of observing: much of the fun of the experience comes from sharing findings with a wider community, or bragging to friends about how cool your pictures are. Smartphones lend themselves to this aspect of the activity, and are conducive to creating a sense of community.

While the quality of the smartphone photographs may not be good enough to do advanced photometry or highly accurate estimating, it is more than adequate to capture magnitude fluctuations in the more popular beginner stars (see Figure 1). For new observers, simply being able to see some kind of change in a star is a pivotal and impactful moment,

Figure 1. Image of the constellation Cepheus taken on at 8:13:00 p.m., February 19, 2019, in Toronto, Canada. δ Cephei, ζ Cephei, and ε Cephei are outlined by a black box. δ Cephei is the topmost star within this box. By using comparison stars, I estimated δ Cephei to have a visual magnitude of approximately 3.5.

as it can feel like a shift from passively stargazing to actually "doing science."

3. Method and results

I took my pictures in light-polluted downtown Toronto, and was able to capture fluctuations in δ Cephei and β Persei with my Samsung Galaxy S9. Newer Samsung series phones like mine often have a "pro" mode on their built-in cameras; while regular settings aren't sensitive enough for astrophotography, pro mode allows users to adjust their ISO, aperture, and shutter speed, focus settings, and white balance, similar to how one might on a DSLR camera (Samsung 2020). I used an ISO of 800 (the highest setting available on my phone), an aperture of f/1.5, and a shutter speed of 8 seconds, while setting my focus to manual mode and my white balance to 5500 K. While different types of phones vary in camera quality and level of modifiability, many will offer at least some of these advanced features. In order to ensure that my results could be achieved with a variety of smartphone models, I did some research into other popular phone models. iPhones, for example, don't have the "pro" function available on Samsungs, but can be tweaked with the help of third party applications that adjust these camera settings for you.

I took my pictures over a range of dates from October 2018 to March 2019, usually from a nearby schoolyard which offered some respite from the bright lights of the city. Despite poor seeing and frequent cloud coverage, my cell phone was able to capture stars as dim as 5.2 magnitude (I suspect that under more amenable conditions, even dimmer stars could be photographed).

I avoided making any unaided-eye magnitude estimates, and instead reviewed my pictures only after I returned home. There, I pulled up star charts for δ Cephei and β Persei and made my estimates by comparing with the reference stars that had also been captured in my pictures. For δ Cephei, I used ε Cephei and ζ Cephei, and for β Persei I used α Persei and ρ Persei (see Table 1 and Table 2). (Note: ρ Persei is a semiregular variable with 0.7 magnitude amplitude, which is a large enough variance to potentially affect the accuracy of visual estimates. If possible, chosen reference stars should not be variables with an amplitude larger than 0.5 magnitude). After collecting enough pictures to construct a somewhat sparse light curve for both of my target stars, I checked my magnitude estimates against others during the same time period by using the AAVSO's light curve generator (LCG, see Figure 2 and Figure 3). Happily, I found that my cell phone pictures resulted in a light curve quite similar to the one compiled by the LCG, and that my resulting phase diagrams matched up with previously constructed phase diagrams (Kafka 2020). All in all, I found that cell phone pictures resulted in reasonably accurate magnitude estimates, and were a great way to conduct a simple little experiment—one that has the potential to quickly and effectively introduce new observers to many aspects of variable star observing.

4. Conclusion

Perhaps the greatest strength of smartphones as an observing tool is their ubiquity and familiarity. Especially amongst younger generations, smartphones tend to be understood as an extension of our bodies–they act as a supplement to our memory and knowledge and extend the scope of our limited human abilities (Mutchler *et al.* 2011). And more often than not, they are always on our person. Much like visual observing, smartphone camera observing feels less like an adoption of new technology for the sake of doing complicated science and more like a natural process of casual observation and discovery, with common tools that in our immediate environment and readily at our disposal. In this way, the sense of old-fashioned adventure and playful discovery experienced with visual observing is

Table 1. δ Cephei smartphone image observations.

Julian Date	*Magnitude Estimate*	*Phase*
2458410.431	3.7	0.39
2458421.313	3.7	0.36
2458426.528	3.7	0.39
2458481.326	4.1	0.2
2458482.292	4.2	0
2458490.325	3.4	0.49
2458534.343	3.5	0.69

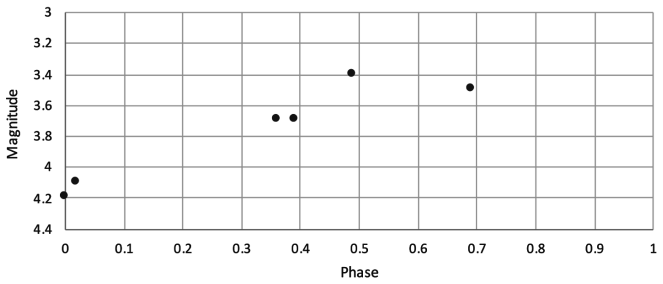

Figure 2. δ Cephei phase diagram.

Table 2. β Persei smartphone image observations.

Julian Date	*Magnitude Estimate*	*Phase*
2458410.431	2.0	0
2458421.313	2.1	0.79
2458426.528	2.0	0.6
2458481.303	3.0	0.69
2458481.354	2.5	0.71
2458482.292	2.0	1

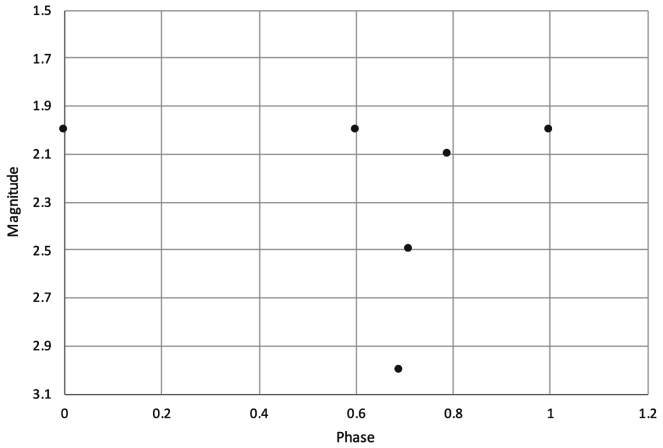

Figure 3: β Persei phase d+iagram.

preserved, with the added benefit of the higher convenience afforded by smartphones. In trying to "sell" newcomers on variable star observing and create the next generation of amateur and professional scientists, smartphones have great potential to not only briefly entice people into the world of variable astronomy, but to lay the groundwork for a deeper engagement that empowers new learners to perceive themselves as real astronomers who do real science.

Such outreach efforts are crucial in fundamentally changing the relationship between science and the public and blurring the line between experts and laypeople by democratizing access to scientific data and expertise. Through their ease of use and great potential for data collection, smartphone images make a valuable contribution to the wider project of science.

5. Acknowledgements

This work was done during my final year as an Astronomy and Astrophysics student at the University of Toronto. I wish to thank Professor John Percy for supervising this project, providing valuable guidance and support, and encouraging my work and continued interest in the outreach and education potential of variable star astronomy.

References

Gaskell, C. M. 1991, *J. Amer. Assoc. Var. Star. Obs.*, **20**, 41.

Kafka, S. 2020, variable star observations from the AAVSO International Database (https://www.aavso.org/aavso-international-database-aid).

Loughney, D. 2010, *J. Br. Astron. Assoc.*, **120**, 157.

Mutchler, L. A., Shim, J. P., and Ormond, D. 2011, in *Proceedings of the Seventeenth Americas Conference on Information Systems*, paper 418 (https://aisel.aisnet.org/amcis2011_submissions/418).

Samsung. 2020, What is Pro mode? (https://www.samsung.com/global/galaxy/what-is/promode/).

A Gallery of Sky Brightness Curves from the January 2019 Total Lunar Eclipse

Jennifer J. Birriel
J. Kevin Adkins
Department of Physics, Earth Science, and Space Systems Engineering, Morehead State University, 150 University Boulevard, Morehead, KY 40351; j.birriel@moreheadstate.edu, jkadkins@moreheadstate.edu

Andrea Bertolo
Regional Environmental Prevention and Protection Agency of Veneto, Via Ospedale Civile 24, Padova, Italy; andrea.bertolo@arpa.veneto.it

Rainer Ehlert
Citizen Scientist, Observatorio Real de 14, Cto. Real de Catorce #145, 78216 San Luis Potosí, San Luis Potosí, Mexico; rsfoto@rsfotografia.com

Michael McKeag
IDA Delegate, IDA Oregon Director, P.O. Box 130, Mosier, OR 97040; michael.mckeag@darksky.org

Salvador J. Ribas
Parc Astronomic Montsec - Ferrocarrils de la Generalitat de Catalunya, Cami del coll d'Ares s/n, E25691 Ager, Lleida, Spain; sjribas@parcastronomic.cat

Anthony Tekatch
Unihedron, 4 Lawrence Avenue, Grimsby, Ontario L3M 2L9, Canada; anthony@unihedron.com

Received January 19, 2020; revised March 24, April 21, 2020; accepted April 22, 2020

Abstract On the night of 20–21 January 2019, a total lunar eclipse occurred for all of the Americas and most of Africa and Western Europe. We present a gallery of night sky brightness curves taken during the eclipse from eleven locations distributed through the Americas and Western Europe. Each data set was acquired using Unihedron Sky Quality Meter (SQM) pointed at zenith. In most cases, it is easy to identify the eclipse signature for the partial and total eclipse phase. The penumbral phase is undetectable due to the increasing brightness at zenith as the lunar altitude increases. A site located near the Tropic of Cancer in Mexico displays the most unusual curve: as the moon emerges from totality, the lunar altitude is very near zenith resulting in a rapid increase in brightness. These results can serve as a reference for future lunar eclipse observations using an SQM device pointed at zenith. We use the data to determine the length of the totality phase, to compare totality brightness to each site's brightness on a clear, new moon night, and finally to estimate the size of Earth's umbral shadow. Ideal observation sites would be located in the mid-latitudes of either hemisphere. We suggest future eclipse observations with SQMs be accompanied by contemporaneous all-sky imaging and data from a cloud sensor and weather station at each site to better understand the effects of lunar altitude and clouds in the field of view of each individual SQM.

1. Introduction

During a lunar eclipse, the full moon passes through Earth's shadow and sky brightness decreases. At totality, the brightness of the sky should theoretically approach that of a new moon night under local conditions. Published photometric studies of night sky brightness during total lunar eclipses are rare (Birriel and Adkins 2019a). We present a collection of data taken with optically identical equipment during the 20–21 January 2019 total lunar eclipse from sites across the Americas and Western Europe. We compare and contrast data sets and make suggestions for future observations.

The total lunar eclipse of January 2019 was visible in its entirety—including the penumbral, partial, and total phases—across all of the Americas and the United Kingdom (e.g. https://www.timeanddate.com/eclipse/lunar/2019-january-21). Throughout most of Europe and western Africa the total lunar eclipse phase was visible but some areas missed portions of the penumbral and/or partial phases. Across the zone of totality, the entire eclipse lasted 5 hours, 11 minutes, and 33 seconds. The totality phase of the eclipse lasted 61 minutes and 58 seconds. The geometry of the eclipse is illustrated in Figure 1.

Prior to this, there exist only two published observations of night sky brightness acquired during a total lunar eclipse. Morton recorded sky brightness during the total lunar eclipse of July 6, 1982 (Morton 1983); he used the Lowell observatory 31-inch refractor to track a patch of sky 20 degrees above the moon, tracking at lunar speed. His sky brightness curve is symmetric in the visible band, which is not surprising, given that lunar altitude relative to the patch of sky did not change. Dvorak (2005) serendipitously recorded the night sky brightness of the October 27–28, 2004, total lunar eclipse while making

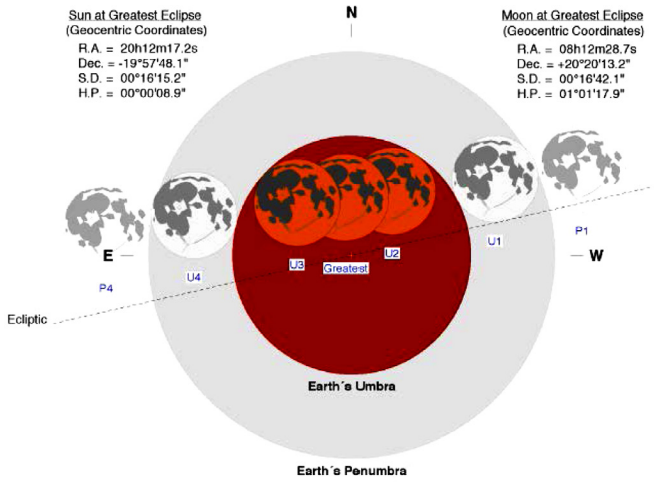

Figure 1. An illustration of the stages of the January 2019 total lunar eclipse. P1 indicates the start of the penumbral eclipse, U1 the start of the partial eclipse, and U2 the start of totality. U3 indicates the end of totality and the start of the partial eclipse. U4 signals the end of the partial phase and beginning of the penumbral phase. Finally, P4 indicates the end of the eclipse. This figure is reproduced here courtesy of Fred Espenak, www.EclipseWise.com.

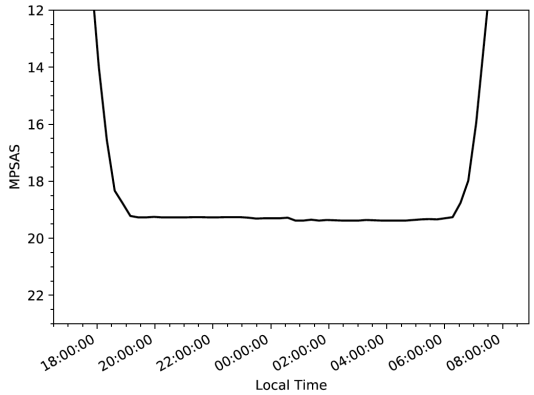

Figure 2. A clear, New Moon night at the Morehead, Kentucky observation site. These data were acquired on January 7–8, 2013, using the same SQM-LE that recorded the lunar eclipse data. These data were extracted from image plots of historical data (lost due to a hard drive failure) using the WEBPLOTDIGITIZER (Rohatgi 2019).

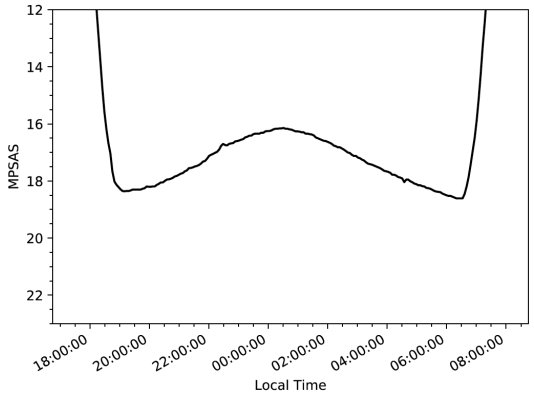

Figure 3. A clear Full Moon night at the Morehead, Kentucky observation site. These data were obtained January 26–27, 2013, using the same SQM-LE that recorded the lunar eclipse data. These data were extracted from image plots of historical data (lost due to a hard drive failure) using the WEBPLOTDIGITIZER (Rohatgi 2019).

Figure 4. An example SQM-LE installation; this is the Morehead, Kentucky site. It is located on the roof of a four-story building located away from light sources and shadowing from trees or buildings. The device is pointed at zenith.

CCD observations of the eclipsing binary QQ Cas.

Lunar eclipses occur when the moon is full. It is important to have an understanding of what sky brightness curves look like on both a full moon night and a new moon night. Figures 2 and 3 show the progression of night sky brightness at a mid-latitude location, in Morehead, Kentucky. (Recall that astronomical magnitude is an inverse scale, with lower numbers corresponding to greater brightness. Hence, we invert the y-axis in our plots so that the light curves are intuitive; a decrease on the plot corresponds to a decrease in sky brightness.) From Figure 2, a clear new moon night has a constant magnitude from the end of astronomical dusk to the start of astronomical dawn. Whereas on a full moon night, Figure 3, the night sky brightens until the moon reaches maximum altitude and then decreases as the moon's altitude decreases.

2. Instrumentation and observations

Unihedron Sky Quality Meters fitted with a lens (hereafter, SQM-L) are designed to perform wide-field photometric measurements of the night sky (Unihedron 2019) and have been completely characterized by Cinzano (2005, 2007). Each contains a TAOS TSL237S photodiode sensor and a HOYA CM-500 infrared blocking filter. SQM-Ls are designed to collect visible light from a cone centered at zenith. The SQM-L response to a point source, as a function of incidence angle, is bell-shaped, with a FWHM (full width at half maximum) of about 20 degrees. The response drops by a factor of 10 for a point source 19 degrees off-axis (Cinzano 2007). An onboard sensor provides temperature-corrected measurements of night sky brightness in magnitudes per square arcsecond (mpsas). Each device has a quoted uncertainty of ±0.1 mpsas.

The devices used in this study are the SQM-LU and SQM-LE. The SQM-LU is passively powered via a USB cable connected to a laptop that simultaneously controls the device

Table 1. SQM observation sites.

Location	*Contributor*	*Site Description/ Conditions*	*Visible Eclipse Phases*	*SQM Interval (min)*	*Device Type*
Borrego Springs, California	M. McKeag	Rural/Partly Cloudy	P1–P4	0.5	SQM-LU
San Luis Potosi, Mexico	R. Ehlert	Suburban/Clear	P1–P4	5.0	SQM-LE
Morehead, Kentucky	J. J. Birriel, J. K. Adkins	Suburban/Mostly Clear	P1–P4	2.0	SQM-LE
Grimsby, Ontario, Canada	A. Tekatch	Suburban/Overcast	P1–P4	5.0	SQM-LE
La Silla Observatory, Chile	I. Saviane	Pristine/Clear	P1–P4	3.0	SQM-LE
COU Station, Lleida, Spain	S. Ribas	Pristine/Fog and Stratus Clouds	P1–U4	0.7	SQM-LE
Montseny, Barcelona, Spain	S. Ribas	Rural/Clear	P1–U4	0.8	SQM-LE
Monte Baldo, Veneto, Italy	A. Bertolo	Rural/Fog and Partly Cloudy	P1–U4	5.0	SQM-LE
Montebello, Veneto, Italy	A. Bertolo	Suburban/Overcast	P1–U4	5.0	SQM-LE
Cima Ekar, Veneto, Italy	A. Bertolo	Rural/Overcast	P1–U4	5.0	SQM-LE
Passo Valles, Veneto, Italy	A. Bertolo	Rural/Clear	P1–U4	5.0	SQM-LU

and logs data. The SQM-LE is an Ethernet-enabled version; such a device is usually installed at a permanent location and connects to a data-logging computer. An example of a permanently mounted SQM-LE is provided in Figure 4. Table 1 summarizes the locations and other relevant information of each SQM used in this study.

The data presented here are not the result of a planned, coordinated observing campaign. Retrospectively, two of the authors (Birriel and Adkins) put out a call for data from SQM sites that had collected data on the night of the eclipse. For this reason, observing intervals are not the same. However, the differences in data collection intervals do not affect the analyses that follow.

3. Results

Each eclipse observation, Figures 5–13, is labeled with the stages of the eclipse, denoted in Figure 1, using the known time for each phase based on the eclipse's geometry. Lunar altitudes at U1 and U4 are indicated in the upper portion of each plot. Finally, figure captions include local weather conditions retrieved from archival data available from timeanddate.com website with weather data reported in 15-minute intervals provided by CustomWeather, Inc. (2019). The analyses that follow are informed by these regional weather conditions.

Inspecting Figures 5–13, the partial and total eclipse phases are generally easy to identify. Partial phases are visible as steep changes in brightness, in the regions U1–U2 and U3–U4. Likewise, the nearly horizontal segments between U2 and U3, where the sky brightness has the largest mpsas, represents the total phase. Figure 8 is the exception; this site was experiencing overcast conditions throughout the night of the eclipse. Even in overcast conditions sky brightness decreased by approximately 1 mpsas during totality, although one might miss such a signal if they were unaware of the eclipse. On the other hand, the penumbral eclipse is not definitively identifiable in any of the observations.

4. Discussion

The interpretation of data such as those presented here is not trivial. We discuss the effects of cloud and lunar altitude. We also examine the scientific usefulness of sky brightness obtained during total eclipses.

4.1. Clouds

Clouds can affect measurements in two distinct ways. In sites free of artificial light, clouds block natural light sources in the sky, and so passing clouds will result in increased mpsas measurements (Ribas *et al.* 2016). On the other hand, at light polluted sites clouds reflect artificial light back downward; this results in decreased mpsas measurements (Kyba *et al.* 2011). Humidity has similar effects on sky brightness (Pramudya *et al.* 2019).

In addition to either increasing or decreasing sky brightness (as noted above), clouds result in "jagged" or noisy SQM data. The data from Grimsby, Ontario, Figure 8, were obtained under overcast skies; note the data are rather "noisy" with brightness variations as large as almost ± 1 mpsas. On the other hand, the larger variations in sky brightness typical of a rising moon are absent and the signature of eclipse during totality is barely visible. At Borrego Springs, California, Figure 5, conditions were partly cloudy and these data also exhibit a fair amount of noise, but the signature of the rising full moon followed by the eclipse are clearly visible. The effects of passing clouds are also evident in Figures 9, 10, and 12.

The sites in Spain and Italy are particularly interesting because they are in geographic proximity to one another. Measurements from three of these sites, Figures 10b, 11, and 13, are consistent with a decrease in sky brightness as the Moon enters Earth's penumbral shadow. However, at a nearby site in Spain, Figure 10a, we again see a large brightening. This illustrates the impact of local cloud cover on sites in geographic proximity. The stratus clouds in this pristine location did not brighten the night sky (Ribas *et al.* 2016). Here, the sky darkens due to the presence of clouds and brightens when the clouds clear, allowing moonlight through. The bright spike at U1 in Figure 10a is an example of one such clearing in the sky. We see no large spike in Figure 10b which is nearby because local cloud cover is different. The same argument would apply to Figures 12a and 12b. We suggest that the small brightening that occurs at around 1:00 am local time in Figure 13 is also due to changes in local atmospheric conditions.

4.2. Lunar altitude

Zenith sky brightness increases with lunar altitude, as evident in Figure 3. Although each SQM points to zenith, the angular response of the device is small, but non-negligible, at angles between 60 and 20 degrees from zenith (Cinzano 2007);

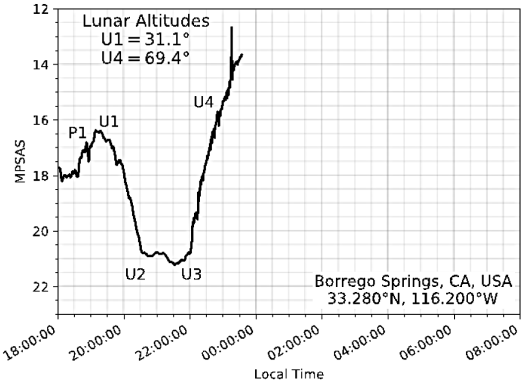

Figure 5. Borrego Springs, California: Local conditions on the night of the eclipse were partly cloudy with visibility of 10 miles and humidity averaging 80±2%. The spike just before midnight occurred when a wind gust blew the tripod over. Note here that the tail end of the first partial eclipse phase and the beginning portion of the second partial phase are difficult to distinguish from totality. The light curve is somewhat noisy and yet is quite dark: nearly 21 mpsas. Observations ended just before midnight at this site.

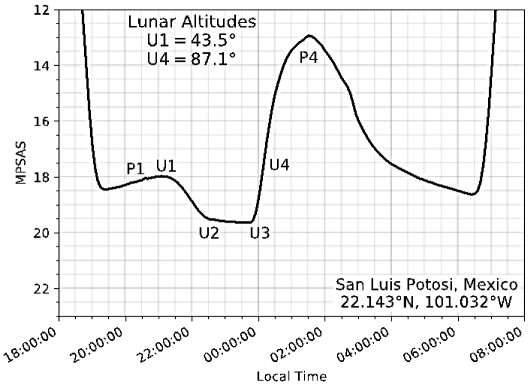

Figure 6. San Luis Potosi, Mexico: Local conditions on the night of the eclipse were clear with visibility of 10 miles and humidity averaging 70±10%. At this site, the lunar altitude is very near zenith as the partial eclipse ends, which is why the brightness increases so rapidly as the moon exits totality.

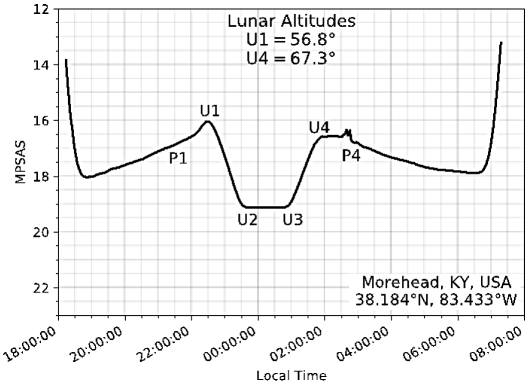

Figure 7. Morehead, Kentucky: Local conditions on the night of the eclipse were generally clear with visibility of 10 miles and humidity averaging 60±3%. According to timeanddate.com, around 9:50 p.m. there were some passing clouds, which explains the increased brightness (i.e. the bump) just as the partial eclipse begins (indicated by U1). The small feature around 2:50 a.m. is also likely due to atmospheric effects or wind.

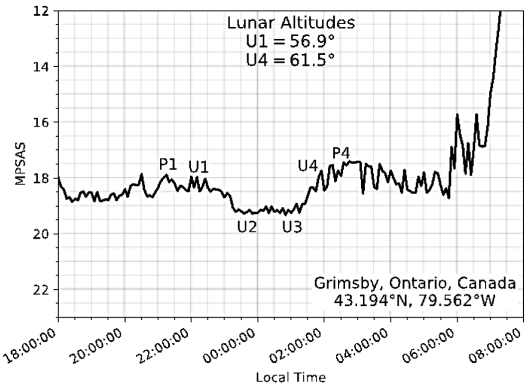

Figure 8. Grimsby, Ontario, Canada: Local conditions on the night of the eclipse were mostly cloudy to overcast with light snow, visibility of 1 mile or less, and humidity averaging 75±3%. Interestingly, here the eclipse is still seen in the sky brightness curve as a systematic decrease in sky brightness of roughly 1 mpsas.

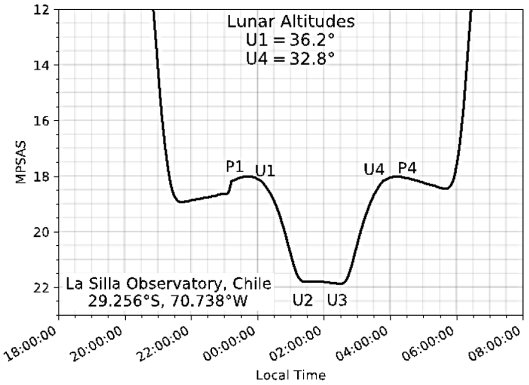

Figure 9. La Silla Observatory, Chile: Local conditions on the night of the eclipse were mainly clear with visibility of 6 miles and humidity averaging 86±5%. (These conditions are from ground stations.) The feature near 11:00 p.m. (23:00 hours) is not a discontinuity in data, but rather a smooth and sudden increase in brightness.

this effect is compounded by the fact that the sky behaves as a spherical diffuser. The effects of lunar altitude are very evident at the Mexico site, Figure 6. After totality ends and the moon moves into the penumbral shadow, there is a rapid increase in sky brightness from just over 17 mpsas to roughly 13 mpsas between the U4 and P4 stages. The lunar altitude at this site reaches 87 degrees, very near zenith. The brightness then decreases, as expected, when as the lunar altitude decreases during the second part of the night. (This same steep increase in brightness is visible in the data from California, Figure 5, where the lunar altitude is 69.4 degrees and increasing at the end of the partial eclipse phase, U4.)

During the penumbral phase of a lunar eclipse, one might expect to see a decrease in brightness, since the moon is moving into the penumbral shadow. This does appear to be the case the observation sites in Spain and Italy, see Figures 10b, 11, and 13. On the other hand, Figures 5–7, 9, and 12(a) exhibit a sky brightness that continues to increase between P1 and U1. Why might this happen? As the moon enters Earth's penumbral shadow, the moon continues to increase in altitude relative to zenith and is still a bright source, with surface brightness of approximately 4.0 mpsas when completely immersed in Earth's penumbra (Sekiguchi 1980). The effects of lunar altitude

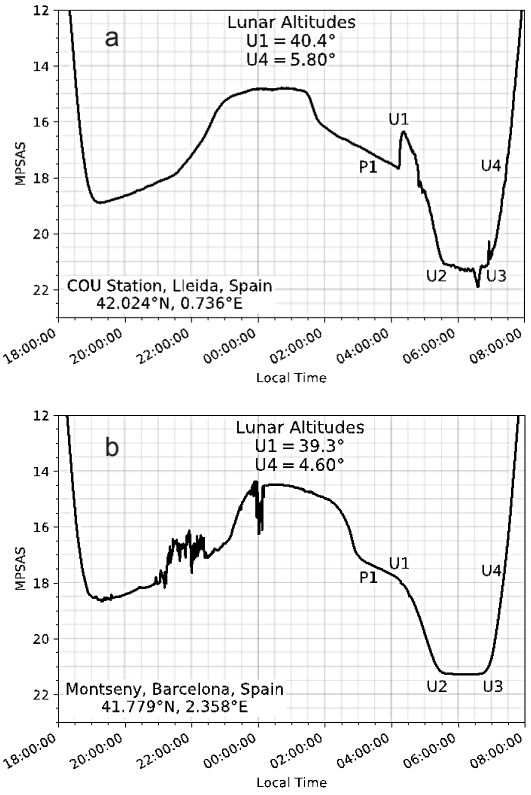

Figure 10. (a) COU Station, Lleida, Spain: Local conditions included higher humidity levels in some moments with appearance of stratus as a result of fog in the valley. (b) Montseny, Barcelona, Spain: Local conditions on the morning of the eclipse were clear and humidity averaging 80±2%. Note that at these locations, the sun begins rising as the partial eclipse is in progress.

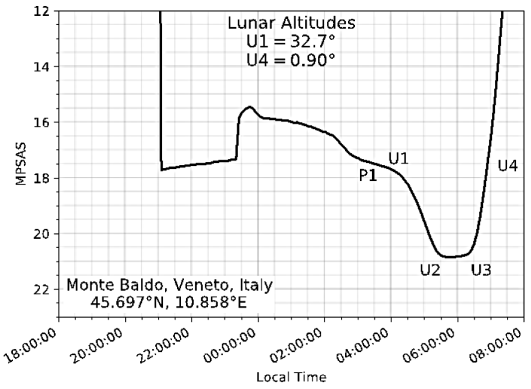

Figure 11. Monte Baldo, Vento, Italy: Local conditions on the morning of the eclipse included passing clouds and fog for ground level stations. Visibility ranged between 8 and 12 miles and humidity averaging 83±5%. At this location, the sun begins rising as the partial eclipse is in progress.

are visible in the eclipse record by Dvorak (2005), whose observations were derived from the region of sky surrounding QQ Cas and would also have been affected by changes in lunar altitude. On the other hand, Morton (1983) observed sky brightness in the region just above the moon while tracking at lunar rate and the observed sky brightness decreases smoothly as the penumbral eclipse begins.

Lunar altitude affects are likely the source of the asymmetry in the U1 and U4 phases in Figure 7. Morton (1983), whose observation technique would eliminate lunar altitude effects, reported a sky brightness curve that is symmetric on both sides

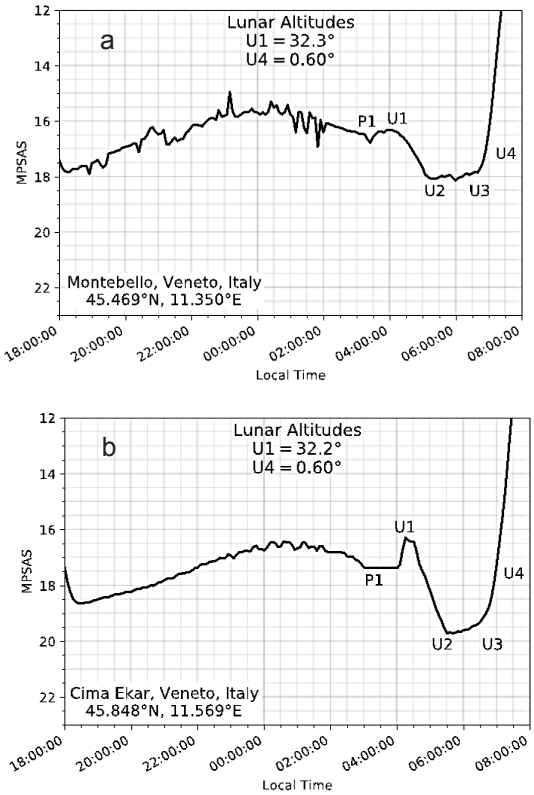

Figure 12. (a) Montebello and (b) Cima Ekar, Vento, Italy: Local conditions on the morning of the eclipse were overcast. Humidity was 81±6%. Notice that, like the Grimsby site, the eclipse is still visible despite overcast conditions but, like the other locations in Spain and Italy, the sun begins rising as the partial eclipse is in progress.

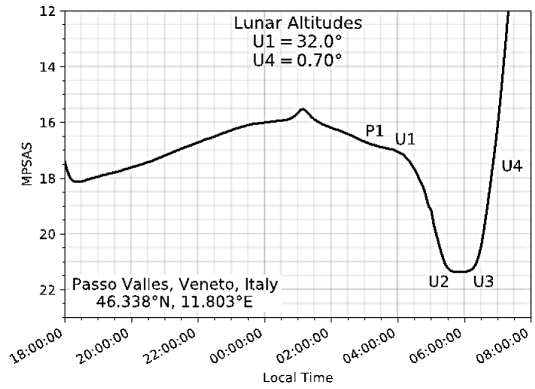

Figure 13. Passo Valles, Vento Italy: No weather data are available for this site during the hours of the eclipse. However, the hours before and after sky conditions are clear with visibility of 10 miles. The data are consistent with such conditions during the eclipse; note the smooth curve and the deep curve during partial and total eclipse phases with a totality brightness of roughly 22 mpsas. At this location, the sun begins rising as the partial eclipse is in progress.

of totality. On the other hand, Dvorak (2005), whose observation technique would have been affected by lunar altitude, also records a curve with U1 and U4 asymmetry.

4.3. Scientific value

We used SQM data plots to determine the duration of totality as observed at each location, see Table 2. The start and end of totality is measured on the plot by estimating where the curve is totally flat, and subsequently the associated times for U2 and

Table 2. Measured length of totality at each observation site.

Location	*Length of Totality* (min)*	*Comments*
Borrego Springs, California	80 ± 8	Full eclipse visible; cloudy
San Luis Potosi, Mexico	75 ± 8	Full eclipse visible; clear; Moon at zenith at U4
Morehead, Kentucky	65 ± 8	Full eclipse visible; mostly clear
Grimsby, Ontario, Canada	95 ± 8	Full eclipse visible; overcast
La Silla Observatory, Chile	70 ± 8	Full eclipse visible; clear
COU Station, Lleida, Spain	75 ± 8	Sun rising as total eclipse ends; fog and stratus cloud
Montseny, Barcelona, Spain	65 ± 8	Sun rising as total eclipse ends; clear
Monte Baldo, Veneto, Italy	50 ± 8	Sun rising as total eclipse ends; partly cloudy and fog
Montebello, Veneto, Italy	75 ± 8	Sun rising as total eclipse ends; overcast
Cima Ekar, Veneto, Italy	60 ± 8	Sun rising as total eclipse ends; overcast
Passo Valles, Veneto, Italy	35 ± 8	Sun rising as total eclipse ends; clear

**Length of totality corresponds to the duration of the U2–U3 event phases.*

Table 3. Comparison of night sky brightness values between a clear, new moon night and the extracted average brightness between U2 and U3.

Location	*Totality (mpsas)*	*New Moon (mpsas)*
San Luis Potosi, Mexico	19.6 ± 0.1	19.4 ± 0.3
Morehead, Kentucky	19.1 ± 0.1	19.3 ± 0.3
La Silla Observatory, Chile	21.8 ± 0.1	22.0 ± 0.3
COU Station, Lleida, Spain	21.3 ± 0.1	21.7 ± 0.4
Montseny, Barcelona, Spain	21.3 ± 0.1	20.8 ± 0.7
Monte Baldo, Veneto, Italy	20.6 ± 0.1	20.6 ± 0.3
Passo Valles, Veneto, Italy	20.9 ± 0.1	21.3 ± 0.3

Table 4. Measurement of the ratio of Earth's umbral diameter to the lunar diameter.

Location	*Measured Ratio*
Borrego Springs, California	2.2 ± 0.3
Morehead, Kentucky	1.9 ± 0.3
La Silla Observatory, Chile	2.0 ± 0.2

U3 are read from the axis. We report a conservative 8-minute uncertainty, one quarter of the scale marking on the x-axis, for each of these measurements to allow for variation in the estimation. Interestingly, a majority of the sites do not agree with the near 62-minute time of totality. Further investigation underscores the impact that weather can have on analysis results. For easy comparison, the third column in Table 2 presents the site's weather conditions and which eclipse phases were visible. Sites with unfavorable weather, and those where the sun rises as totality ends, result in large deviations from the known time of totality. Conversely, sites with clear weather, evidenced by smooth, continuous SQM plots, agree well with the known time of totality.

The depth of the eclipse in terms of SQM readings depends on lunar distance (which is the same for all sites) and local sky conditions including lunar altitude and local light pollution and is not particularly valuable. On the other hand, the SQM reading during totality should be similar to the sky brightness on a clear, new moon night; where possible we have made appropriate comparisons using an average value extracted between U2 and U3 from the data, see Table 3. Because clouds are known to increase sky brightness at light polluted sites, sites with clouds are excluded from the comparison. For the remaining sites, we find excellent agreement between totality and a new moon. For the uncertainties for the new moon night we assume a canonical value of ± 0.3 mpsas typically of seasonal variations (e.g. Plauchu-Frayn *et al.* 2017; Posch, Binder, and Puschnig 2018). The sites in Spain have long-term observations and we quote the known variations in season for these. Since totality measurements represent a single measurement these are subject only to the known SQM uncertainty of ± 0.1 mpsas (Cinzano 2007).

Birriel and Adkins (2019b) suggest a method to estimate the size of Earth's umbral shadow using sky brightness curves. We employ their method and present results in Table 4 for sites where the U1 through U4 phases are clearly identifiable. On average, Earth's umbral shadow has a diameter of 2.65 lunar diameters for central eclipses, those where the moon passes through the center of Earth's shadow. We find that the ratio of Earth's umbral diameter to the lunar diameter is in agreement between all sites. However, the values are collectively smaller than the known umbral diameter; this result is not unexpected since this eclipse is a non-central one (Birriel and Adkins 2019b).

What makes the most scientifically useful data set? Ideal sites are those with generally clear sky conditions and from which all phases of the eclipse, P1–P4, can be clearly identified. Mid-latitude sites are ideal while sites between the Tropics of Cancer and Capricorn would not provide much useful data. It is important that each site have contemporaneous sky and weather conditions available for interpretation of unusual features. (For example, Figure 9 exhibits a sudden brightening at around 11:00 p.m. local time, around the time the partial eclipse begins. It appears to be a discontinuity in data, but it is not. The sky was clear at this site and the lunar altitude was approximately 30.2 degrees which is just at the limit of the SQM's angular sensitivity. Is this effect the result of instrument sensitivity or changes in humidity or other atmospheric conditions? Without a detailed record of local sky conditions, we cannot say with certainty.) While archival weather data are useful, they are generally regional in nature. The ideal instrumental suite to accompany an SQM site would include an all-sky camera to monitor both clouds and the moon, a cloud sensor, and a weather

station (or data from the closest possible weather station, such as an airport).

5. Conclusions

We have presented measurements of night sky brightness during the January 20–21, 2019, total lunar eclipse as recorded by SQM-L devices at 11 different locations across the Americas and Western Europe. The data show the signature of the eclipse is generally quite distinct for the partial and total phases. On the other hand, the signature of the penumbral phase is more difficult to discern due to the combination of lunar altitude and the device's angular response at angles off zenith. Meaningful comparisons of data from different sites require detailed information regarding cloud cover, humidity, and lunar altitude. Interpretation of such light curves is paramount if one wishes to use these to extract information regarding eclipse phases and their duration. For example, estimating the size of Earth's umbral shadow requires identification of the U1 through U4 phases of the eclipse in a sky brightness curve recorded during a total eclipse.

Given the proliferation of SQM devices for light pollution research, this gallery should prove useful for future eclipse observations, and the authors propose coordinated observing campaigns for future lunar eclipses. Ideal observation sites would be located in the mid-latitudes of either hemisphere, where the lunar altitude does not exceed 70 degrees during the eclipse. Future SQM observers should collect data from the same site on both clear new moon nights and clear full moon nights, ensuring a baseline for comparison to the eclipse data. Those with access to a self-contained, autonomous SQM-LU-DL should select a dark sky site with high probability of a clear sky. It is also important that observers accurately synchronize all clocks (laptop, SQM, cameras, weather stations, and cloud sensors).

6. Acknowledgements

The authors wish to thank the La Silla Observatory Site Manager, Dr. Ivo Saviane, for his data contribution to this study. Additionally, we want to acknowledge that all of the data plots presented in this paper were created with the Matplotlib library in PYTHON (Hunter 2007). We thank Fred Espenak (www.EclipseWise.com) for allowing us to reproduce the geometry of the January 2019 eclipse (Figure 3). The authors also wish to thank the anonymous referee whose comments and suggestions improved both the readability and quality of this paper.

References

Birriel, J., and Adkins, J. K. 2019a, *J. Amer. Assoc. Var. Star Obs.*, **47**, 94.

Birriel, J., and Adkins, J. K. 2019b, *Amer. J. Phys.*, **87**, 994.

Cinzano, P. 2005, *ISTIL Internal Rep. No. 9*, v.1.4, 1.

Cinzano, P. 2007, *ISTIL Internal Rep. No. —*, v.0.9, 1.

CustomWeather, Inc. 2019, weather information (https://customweather.com/ (via https://www.timeanddate.com/weather)), accessed 12 December 2019.

Dvorak, S. 2005, *J. Amer. Assoc. Var. Star Obs.*, **34**, 72.

Hunter, J. D. 2007, *Comput. Sci. Eng.*, **9**, 90.

Kyba, C. C. M., Ruhtz, T., Fischer, J., and Hölker, F. 2011, PLoS One, 6, e17307 (https://journals.plos.org/plosone/article?id=10.1371/journal.pone.0017307).

Morton, J. C. 1983, *Obs.*, **103**, 24.

Plauchu-Frayn, I., Richer, M. G., Colorado, E., Herrera, J., Córdova, A., Ceseña, U., and Ávila, F. 2017, *Publ. Astron. Soc. Pacific*, **129**, 035003.

Posch, T., Binder, F., and Puschnig, J. 2018, *J. Quant. Spectrosc. Radiat. Transfer*, **216**, 56.

Pramudya, Y., Budi, K. S., Okimustava, and Muchlas. 2019, in *Journal of Physics Conference Series 1231*, issue 1, article id. 012004.

Ribas, S. J., Torra, J., Figueras, F., Paricio, S., and Canal-Domingo, R. 2016, *Int. J. Sustainable Lighting*, 18, 32.

Rohatgi, A. 2019, WEBPLOTDIGITIZER (https://apps.automeris.io/wpd).

Sekiguchi, N. 1980, *Moon and Planets*, **23**, 99.

Unihedron. 2019, Unihedron Sky Quality Meter (http://unihedron.com/projects/sqm-le/), accessed 28 December 2019.

Recent Maxima of 77 Short Period Pulsating Stars

Gerard Samolyk
P.O. Box 20677, Greenfield, WI 53220; gsamolyk@wi.rr.com

Received January 24, 2020; accepted January 24, 2020

Abstract This paper contains times of maxima for 77 short period pulsating stars (primarily RR Lyrae and δ Scuti stars). These data were determined from the CCD observations received by the AAVSO Short Period Pulsator Section in 2019.

1. Recent observations

The accompanying list (Table 1) contains times of maxima calculated from CCD observations made by participants in the AAVSO's Short Period Pulsator (SPP) Section. These observations were reduced by the writer using the PERANSO program (Vanmunster 2007).

The linear elements in the *General Catalogue of Variable Stars* (GCVS; Kholopov *et al.* 1985) were used to compute the O–C values for most stars. For a few exceptions where the GCVS elements are missing or are in significant error, light elements from another source are used: NT Cam (AAVSO VSX site, Watson *et al.* 2014), RZ Cap and DG Hya (Samolyk 2010), and V2416 Cyg (Samolyk 2018). The error estimate is included. Column F indicates the filter used.

Table 1 will be web-archived and made available through the AAVSO ftp site at ftp:ftp.aavso.org/public/datasets/gsamj481spp77.txt. The times of maximum for RR Lyr stars in Table 1, along with data from earlier AAVSO publications, are included in the GEOS database at: http://rr-lyr.irap.omp.eu/dbrr/.

In the case of LV UMa (Figure 1), the following light elements were calculated using a linear regression on the times of maxima listed in this paper:

$$\text{Time of maximum (JD)} = 2457040.8744 + 0.036999856 \cdot E \quad (1)$$
$$\pm 0.0009 \quad 0.000000023$$

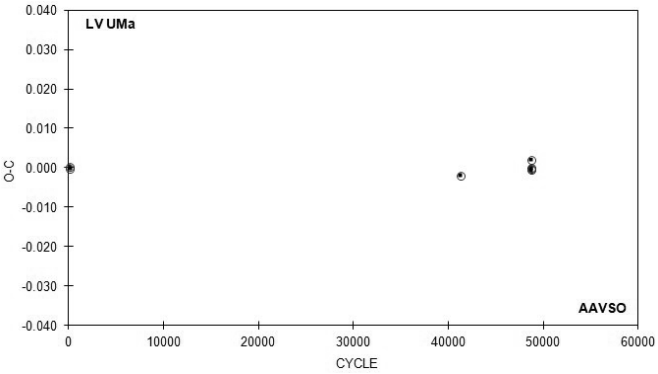

Figure 1. O–C plot for LV UMa using the light elements in Equation 1.

References

Kholopov, P. N., *et al.* 1985, *General Catalogue of Variable Stars*, 4th ed., Moscow.

Samolyk, G. 2010, *J. Amer. Assoc. Var. Stars*, **38**, 12.

Samolyk, G. 2018, *J. Amer. Assoc. Var. Stars*, **46**, 74.

Vanmunster, T. 2007, PERANSO period analysis software, http://www.peranso.com.

Watson, C., Henden, A. A., and Price, C. A. 2014, AAVSO International Variable Star Index (https://www.aavso.org/vsx).

Table 1. Recent times of maxima of stars in the AAVSO short period pulsator program.

Star	*JD (max) Hel. 2400000 +*	*Cycle*	*O–C (day)*	*F*	*Observer*	*Error (day)*	*Star*	*JD (max) Hel. 2400000 +*	*Cycle*	*O–C (day)*	*F*	*Observer*	*Error (day)*
SW And	58486.3076	91241	–0.5035	V	T. Arranz	0.0008	ZZ And	58803.5179	61268	0.0355	V	K. Menzies	0.0018
SW And	58497.3619	91266	–0.5062	V	T. Arranz	0.0007	AC And	58716.8670	14364	0.4626	V	G. Samolyk	0.0011
SW And	58696.8228	91717	–0.5134	V	G. Samolyk	0.0011	AC And	58732.5431	14386	0.4915	V	T. Arranz	0.0011
SW And	58752.5473	91843	–0.5161	V	T. Arranz	0.0007	AC And	58752.5019	14414	0.5355	V	T. Arranz	0.0019
SW And	58753.4312	91845	–0.5167	V	T. Arranz	0.0006	AC And	58757.3648	14421	0.4198	V	T. Arranz	0.0016
SW And	58755.6429	91850	–0.5164	V	T. Arranz	0.0006	AC And	58759.4823	14424	0.4035	V	T. Arranz	0.0021
SW And	58756.5278	91852	–0.5161	V	T. Arranz	0.0006	AC And	58764.5665	14431	0.5091	V	T. Arranz	0.0014
SW And	58757.4123	91854	–0.5162	V	T. Arranz	0.0005	AC And	58764.5671	14431	0.5097	V	G. Samolyk	0.0013
SW And	58759.6237	91859	–0.5161	V	T. Arranz	0.0008	AC And	58767.3571	14435	0.4547	V	T. Arranz	0.0019
SW And	58763.6035	91868	–0.5169	V	T. Arranz	0.0008	AC And	58769.4739	14438	0.4378	V	T. Arranz	0.0025
SW And	58765.3728	91872	–0.5167	V	T. Arranz	0.0006	AT And	58660.8096	26450	–0.0060	V	G. Samolyk	0.0016
SW And	58767.5834	91877	–0.5175	V	T. Arranz	0.0006	AT And	58697.8215	26510	–0.0090	V	K. Menzies	0.0025
SW And	58835.6926	92031	–0.5193	TG	G. Conrad	0.0015	AT And	58735.4573	26571	–0.0050	V	T. Arranz	0.0014
SW And	58846.3056	92055	–0.5210	V	T. Arranz	0.0007	AT And	58773.7018	26633	–0.0093	TG	G. Conrad	0.0025
XX And	58491.3159	26847	0.2861	V	T. Arranz	0.0015	AT And	58796.5331	26670	–0.0038	V	K. Menzies	0.0028
XX And	58716.8165	27159	0.2896	V	G. Samolyk	0.0015	DY And	58721.8293	37556	–0.1721	V	K. Menzies	0.0015
XX And	58803.5473	27279	0.2907	V	K. Menzies	0.0015	DY And	58825.5628	37728	–0.1695	V	K. Menzies	0.0019

Table continued on following pages

Table 1. Recent times of maxima of stars in the AAVSO short period pulsator program, cont.

Star	JD (max) Hel. 2400000 +	Cycle	O–C (day)	F	Observer	Error (day)
SW Aqr	58695.8633	73151	–0.0007	V	G. Samolyk	0.0012
SW Aqr	58738.5782	73244	–0.0010	V	T. Arranz	0.0009
TZ Aqr	58716.8037	37059	0.0141	V	G. Samolyk	0.0013
YZ Aqr	58747.6616	42366	0.0857	V	G. Samolyk	0.0017
BO Aqr	58802.6041	24756	0.2276	V	G. Samolyk	0.0018
BR Aqr	58786.5981	43892	–0.2320	V	G. Samolyk	0.0009
BR Aqr	58840.5692	44004	–0.2313	V	G. Samolyk	0.0012
CY Aqr	58724.6941	400015	0.0160	V	G. Samolyk	0.0003
CY Aqr	58724.7551	400016	0.0159	V	G. Samolyk	0.0003
CY Aqr	58724.8163	400017	0.0160	V	G. Samolyk	0.0004
CY Aqr	58724.8774	400018	0.0161	V	G. Samolyk	0.0004
CY Aqr	58753.3211	400484	0.0160	V	T. Arranz	0.0004
CY Aqr	58760.6461	400604	0.0163	V	G. Samolyk	0.0003
CY Aqr	58760.7073	400605	0.0165	V	G. Samolyk	0.0004
CY Aqr	58760.7679	400606	0.0160	V	G. Samolyk	0.0004
TZ Aur	58488.6658	98516	0.0170	V	G. Samolyk	0.0008
TZ Aur	58521.5675	98600	0.0181	V	T. Arranz	0.0008
TZ Aur	58533.3164	98630	0.0167	V	T. Arranz	0.0006
TZ Aur	58538.4076	98643	0.0162	V	T. Arranz	0.0008
TZ Aur	58540.3686	98648	0.0188	V	T. Arranz	0.0008
TZ Aur	58782.8129	99267	0.0165	V	G. Samolyk	0.0009
BH Aur	58486.7494	34500	0.0093	V	G. Samolyk	0.0009
BH Aur	58487.6641	34502	0.0118	TG	G. Conrad	0.0015
BH Aur	58489.4868	34506	0.0102	V	T. Arranz	0.0011
BH Aur	58750.8262	35079	0.0101	V	G. Samolyk	0.0009
BH Aur	58765.8772	35112	0.0101	V	G. Samolyk	0.0010
BH Aur	58782.7500	35149	0.0076	TG	G. Conrad	0.0017
BH Aur	58814.6788	35219	0.0101	V	K. Menzies	0.0009
RS Boo	58535.6384	44430	–0.0216	V	T. Arranz	0.0006
RS Boo	58541.6750	44446	–0.0224	V	T. Arranz	0.0006
RS Boo	58543.5623	44451	–0.0218	V	T. Arranz	0.0007
RS Boo	58554.8760	44481	–0.0283	V	G. Samolyk	0.0001
RS Boo	58558.6492	44491	–0.0285	V	T. Arranz	0.0006
RS Boo	58569.5932	44520	–0.0273	V	T. Arranz	0.0008
RS Boo	58572.6141	44528	–0.0251	V	T. Arranz	0.0007
RS Boo	58586.5782	44565	–0.0226	V	T. Arranz	0.0005
RS Boo	58594.5028	44586	–0.0221	V	T. Arranz	0.0006
RS Boo	58603.5572	44610	–0.0238	V	T. Arranz	0.0006
RS Boo	58606.5723	44618	–0.0274	V	T. Arranz	0.0006
RS Boo	58608.4604	44623	–0.0260	V	T. Arranz	0.0006
RS Boo	58609.5917	44626	–0.0267	V	T. Arranz	0.0006
RS Boo	58617.5151	44647	–0.0274	V	T. Arranz	0.0006
RS Boo	58628.4581	44676	–0.0273	V	T. Arranz	0.0005
RS Boo	58631.4774	44684	–0.0267	V	T. Arranz	0.0006
RS Boo	58634.4961	44692	–0.0267	V	T. Arranz	0.0006
RS Boo	58642.4217	44713	–0.0252	V	T. Arranz	0.0007
ST Boo	58530.9039	63233	0.1109	V	G. Samolyk	0.0009
ST Boo	58567.6206	63292	0.1124	V	T. Arranz	0.0007
ST Boo	58577.5785	63308	0.1137	V	T. Arranz	0.0007
ST Boo	58585.6660	63321	0.1114	V	T. Arranz	0.0009
ST Boo	58600.5983	63345	0.1087	V	T. Arranz	0.0008
ST Boo	58605.5750	63353	0.1071	V	T. Arranz	0.0010
ST Boo	58615.5288	63369	0.1043	V	T. Arranz	0.0008
ST Boo	58623.6140	63382	0.0997	V	T. Arranz	0.0009
ST Boo	58625.4820	63385	0.1008	V	T. Arranz	0.0008
ST Boo	58630.4560	63393	0.0965	V	T. Arranz	0.0009
ST Boo	58633.5660	63398	0.0950	V	T. Arranz	0.0007
ST Boo	58635.4343	63401	0.0965	V	T. Arranz	0.0009
ST Boo	58638.5423	63406	0.0930	V	T. Arranz	0.0008
ST Boo	58663.4283	63446	0.0874	V	T. Arranz	0.0009
SW Boo	58530.7109	31078	0.5246	V	T. Arranz	0.0009
SW Boo	58564.6062	31144	0.5271	V	T. Arranz	0.0009
SW Boo	58565.6326	31146	0.5264	V	T. Arranz	0.0009
SW Boo	58601.5824	31216	0.5292	V	T. Arranz	0.0009
SW Boo	58616.4785	31245	0.5330	V	T. Arranz	0.0008
SZ Boo	58493.9310	59014	0.0123	V	G. Samolyk	0.0012
SZ Boo	58582.8110	59184	0.0130	V	G. Samolyk	0.0011
TV Boo	58554.5299	108603	0.1307	V	T. Arranz	0.0018
TV Boo	58557.6285	108613	0.1037	V	T. Arranz	0.0008
TV Boo	58558.5646	108616	0.1022	V	T. Arranz	0.0009
TV Boo	58562.6563	108629	0.1306	V	T. Arranz	0.0015
TV Boo	58563.5852	108632	0.1218	V	T. Arranz	0.0013
TV Boo	58567.6274	108645	0.1007	V	T. Arranz	0.0011
TV Boo	58568.5700	108648	0.1057	V	T. Arranz	0.0019
TV Boo	58572.6602	108661	0.1326	V	T. Arranz	0.0012
TV Boo	58573.5946	108664	0.1293	V	T. Arranz	0.0014
TV Boo	58577.6381	108677	0.1095	V	T. Arranz	0.0011
TV Boo	58605.4507	108766	0.1044	V	T. Arranz	0.0010
TV Boo	58609.5285	108779	0.1189	V	T. Arranz	0.0021
TV Boo	58614.5222	108795	0.1116	V	T. Arranz	0.0016
TV Boo	58615.4541	108798	0.1059	V	T. Arranz	0.0013
TV Boo	58616.3896	108801	0.1037	V	T. Arranz	0.0009
TV Boo	58625.4529	108830	0.1028	V	T. Arranz	0.0009
TV Boo	58630.4816	108846	0.1305	V	T. Arranz	0.0015
TV Boo	58631.4200	108849	0.1312	V	T. Arranz	0.0014
TV Boo	58634.5226	108859	0.1082	V	T. Arranz	0.0014
TV Boo	58635.4553	108862	0.1033	V	T. Arranz	0.0011
TV Boo	58646.3942	108897	0.1026	V	T. Arranz	0.0009
TV Boo	58650.4885	108910	0.1336	V	T. Arranz	0.0016
TV Boo	58651.4196	108913	0.1270	V	T. Arranz	0.0013
TW Boo	58576.8510	59529	–0.1053	V	G. Samolyk	0.0011
TW Boo	58618.3702	59607	–0.1035	V	T. Arranz	0.0008
UU Boo	58488.9319	49033	0.3390	V	N. Simmons	0.0008
UU Boo	58590.8295	49256	0.3434	V	K. Menzies	0.0008
UY Boo	58598.8066	25755	0.8185	V	G. Samolyk	0.0010
UY Boo	58642.4266	25822	0.8325	V	T. Arranz	0.0021
UY Cam	58493.6629	85861	–0.0985	V	G. Samolyk	0.0026
UY Cam	58493.9287	85862	–0.0997	V	G. Samolyk	0.0042
UY Cam	58514.7618	85940	–0.0959	TG	G. Conrad	0.0031
UY Cam	58548.6824	86067	–0.0897	TG	G. Conrad	0.0032
UY Cam	58750.8281	86824	–0.0950	V	G. Samolyk	0.0027
NT Cam	58507.6967	84359	0.0240	V	G. Conrad	0.0011
NT Cam	58507.7778	84360	0.0226	V	G. Conrad	0.0023
NT Cam	58507.8685	84361	0.0310	V	G. Conrad	0.0011
RW Cnc	58529.5775	34673	0.2326	V	T. Arranz	0.0009
RW Cnc	58540.5311	34693	0.2422	V	T. Arranz	0.0014
RW Cnc	58551.4622	34713	0.2293	V	T. Arranz	0.0009
RW Cnc	58557.4839	34724	0.2318	V	T. Arranz	0.0009
RW Cnc	58562.4173	34733	0.2404	V	T. Arranz	0.0011
RW Cnc	58573.3612	34753	0.2404	V	T. Arranz	0.0018
RW Cnc	58585.3913	34775	0.2321	V	T. Arranz	0.0009
RW Cnc	58586.4864	34777	0.2328	V	T. Arranz	0.0011
TT Cnc	58518.6049	32965	0.1284	V	T. Arranz	0.0015
TT Cnc	58526.4944	32979	0.1296	V	T. Arranz	0.0015
TT Cnc	58535.5115	32995	0.1315	V	T. Arranz	0.0012
TT Cnc	58552.4218	33025	0.1384	V	T. Arranz	0.0009
TT Cnc	58565.3713	33048	0.1285	V	T. Arranz	0.0009
VZ Cnc	58493.8231	104261	0.0204	V	N. Simmons	0.0015
KV Cnc	58209.6143	10853	–0.0849	V	G. Samolyk	0.0015
KV Cnc	58210.6196	10855	–0.0836	V	G. Samolyk	0.0011
KV Cnc	58215.6385	10865	–0.0847	V	G. Samolyk	0.0010
KV Cnc	58554.5271	11540	–0.0461	V	T. Arranz	0.0034
KV Cnc	58594.6179	11620	–0.1153	V	G. Samolyk	0.0014
KV Cnc	58598.6396	11628	–0.1096	V	G. Samolyk	0.0015
SS CVn	58523.9042	39500	–0.3803	V	G. Samolyk	0.0015
RV Cap	58690.8487	55406	–0.1179	V	G. Samolyk	0.0011
RZ Cap	58688.7796	18214	0.0067	V	G. Samolyk	0.0018
VW Cap	58750.5996	106093	0.2134	V	G. Samolyk	0.0053
YZ Cap	58724.7574	54835	0.0402	V	G. Samolyk	0.0021
RR Cet	58782.7547	46293	0.0190	V	G. Samolyk	0.0011
RU Cet	58782.7381	32333	0.1359	V	G. Samolyk	0.0010
RV Cet	58730.8842	31468	0.2756	V	G. Samolyk	0.0021

Table continued on next page

Table 1. Recent times of maxima of stars in the AAVSO short period pulsator program, cont.

Star	*JD (max) Hel. 2400000 +*	*Cycle*	*O–C (day)*	*F*	*Observer*	*Error (day)*
RX Cet	58764.8121	32489	0.3402	V	G. Samolyk	0.0007
TY Cet	58849.6512	22932	–0.0185	V	G. Samolyk	0.0028
UU Cet	58795.6527	29018	–0.1818	V	G. Samolyk	0.0016
S Com	58566.6584	30536	–0.1162	TG	G. Conrad	0.0014
XX Cyg	58645.6352	105218	0.0032	V	G. Samolyk	0.0005
XX Cyg	58645.7712	105219	0.0044	V	G. Samolyk	0.0006
XZ Cyg	58645.8523	31121	–2.7584	V	G. Samolyk	0.0008
XZ Cyg	58660.7797	31153	–2.7654	V	G. Samolyk	0.0010
XZ Cyg	58679.4337	31193	–2.7794	V	T. Arranz	0.0006
XZ Cyg	58684.5659	31204	–2.7809	V	T. Arranz	0.0007
XZ Cyg	58685.4999	31206	–2.7803	V	T. Arranz	0.0006
XZ Cyg	58686.4348	31208	–2.7788	V	T. Arranz	0.0008
XZ Cyg	58690.6399	31217	–2.7740	V	G. Samolyk	0.0011
XZ Cyg	58692.5048	31221	–2.7759	V	T. Arranz	0.0007
XZ Cyg	58693.4373	31223	–2.7768	V	T. Arranz	0.0007
XZ Cyg	58698.5696	31234	–2.7782	V	T. Arranz	0.0007
XZ Cyg	58699.5035	31236	–2.7777	V	T. Arranz	0.0007
XZ Cyg	58700.4387	31238	–2.7759	V	T. Arranz	0.0008
XZ Cyg	58707.4406	31253	–2.7745	V	T. Arranz	0.0007
XZ Cyg	58712.5700	31264	–2.7788	V	T. Arranz	0.0008
XZ Cyg	58713.5021	31266	–2.7801	V	T. Arranz	0.0007
XZ Cyg	58797.4783	31446	–2.8099	V	K. Menzies	0.0009
XZ Cyg	58825.4843	31506	–2.8059	V	K. Menzies	0.0007
DM Cyg	58672.7967	38323	0.0959	V	G. Samolyk	0.0013
DM Cyg	58675.7342	38330	0.0944	V	G. Samolyk	0.0009
DM Cyg	58719.8183	38435	0.0932	TG	G. Conrad	0.0014
DM Cyg	58729.4769	38458	0.0950	V	T. Arranz	0.0008
DM Cyg	58750.4702	38508	0.0953	V	T. Arranz	0.0007
DM Cyg	58756.3489	38522	0.0960	V	T. Arranz	0.0009
DM Cyg	58758.4491	38527	0.0969	V	T. Arranz	0.0009
V2416 Cyg	58645.6336	90053	0.0000	V	G. Samolyk	0.0013
V2416 Cyg	58645.6896	90054	0.0001	V	G. Samolyk	0.0015
V2416 Cyg	58645.7467	90055	0.0013	V	G. Samolyk	0.0013
V2416 Cyg	58645.8019	90056	0.0006	V	G. Samolyk	0.0015
V2416 Cyg	58645.8567	90057	–0.0005	V	G. Samolyk	0.0014
RW Dra	58608.6486	43419	0.2444	V	G. Samolyk	0.0016
RW Dra	58617.5269	43439	0.2643	V	T. Arranz	0.0011
RW Dra	58632.6034	43473	0.2817	V	T. Arranz	0.0007
RW Dra	58633.4927	43475	0.2851	V	T. Arranz	0.0007
RW Dra	58636.5881	43482	0.2801	V	T. Arranz	0.0007
RW Dra	58660.4912	43536	0.2657	V	T. Arranz	0.0008
RW Dra	58668.4845	43554	0.2865	V	T. Arranz	0.0008
RW Dra	58676.4579	43572	0.2874	V	T. Arranz	0.0007
RW Dra	58684.4079	43590	0.2649	V	T. Arranz	0.0008
RW Dra	58699.4630	43624	0.2608	V	T. Arranz	0.0011
XZ Dra	58600.8965	34990	–0.1075	V	G. Samolyk	0.0016
XZ Dra	58679.5213	35155	–0.1047	V	T. Arranz	0.0009
XZ Dra	58689.5225	35176	–0.1100	V	T. Arranz	0.0008
XZ Dra	58700.4856	35199	–0.1063	V	T. Arranz	0.0009
XZ Dra	58701.4359	35201	–0.1090	V	T. Arranz	0.0005
XZ Dra	58709.5453	35218	–0.1000	V	T. Arranz	0.0007
XZ Dra	58710.4978	35220	–0.1005	V	T. Arranz	0.0008
XZ Dra	58711.4512	35222	–0.1001	V	T. Arranz	0.0008
XZ Dra	58712.4031	35224	–0.1012	V	T. Arranz	0.0007
XZ Dra	58730.5040	35262	–0.1072	V	T. Arranz	0.0011
XZ Dra	58731.4561	35264	–0.1081	V	T. Arranz	0.0011
SV Eri	58504.5982	32154	1.0798	V	G. Samolyk	0.0021
BB Eri	58523.5443	33276	0.3275	V	G. Samolyk	0.0015
BB Eri	58802.8001	33766	0.3332	V	G. Samolyk	0.0016
RR Gem	58488.5888	43120	–0.6493	V	T. Arranz	0.0009
RR Gem	58490.5723	43125	–0.6523	V	T. Arranz	0.0009
RR Gem	58493.7500	43133	–0.6531	V	G. Samolyk	0.0010
RR Gem	58499.7054	43148	–0.6574	V	R. Sabo	0.0006
RR Gem	58520.3643	43200	–0.6586	V	T. Arranz	0.0005
RR Gem	58522.3543	43205	–0.6552	V	T. Arranz	0.0007
RR Gem	58526.3259	43215	–0.6567	V	T. Arranz	0.0005
RR Gem	58527.5161	43218	–0.6584	V	T. Arranz	0.0005
RR Gem	58529.5085	43223	–0.6526	V	T. Arranz	0.0006
RR Gem	58537.4547	43243	–0.6526	V	T. Arranz	0.0009
RR Gem	58550.5612	43276	–0.6573	V	K. Menzies	0.0006
RR Gem	58551.3567	43278	–0.6564	V	T. Arranz	0.0007
RR Gem	58553.3459	43283	–0.6538	V	T. Arranz	0.0009
RR Gem	58558.5084	43296	–0.6563	V	T. Arranz	0.0008
RR Gem	58566.4553	43316	–0.6556	V	T. Arranz	0.0009
RR Gem	58568.4397	43321	–0.6578	V	T. Arranz	0.0006
RR Gem	58570.4237	43326	–0.6604	V	T. Arranz	0.0006
RR Gem	58572.4109	43331	–0.6597	V	T. Arranz	0.0006
RR Gem	58576.3841	43341	–0.6596	V	T. Arranz	0.0006
GQ Gem	58489.7505	49360	–0.2117	V	K. Menzies	0.0019
TW Her	58617.7149	92774	–0.0191	V	G. Samolyk	0.0007
TW Her	58655.6762	92869	–0.0199	TG	G. Conrad	0.0009
TW Her	58666.4669	92896	–0.0184	V	T. Arranz	0.0007
TW Her	58682.4501	92936	–0.0192	V	T. Arranz	0.0007
TW Her	58692.4405	92961	–0.0188	V	T. Arranz	0.0007
TW Her	58694.4377	92966	–0.0196	V	T. Arranz	0.0006
VX Her	58607.8138	80939	–0.0896	V	G. Samolyk	0.0006
VX Her	58647.4307	81026	–0.0901	V	T. Arranz	0.0007
VX Her	58657.4482	81048	–0.0908	V	T. Arranz	0.0006
VX Her	58659.7241	81053	–0.0918	TG	G. Conrad	0.0011
VZ Her	58524.8936	49363	0.0900	V	K. Menzies	0.0006
VZ Her	58598.8697	49531	0.0910	V	G. Samolyk	0.0007
AR Her	58576.8644	36431	–1.0727	V	G. Samolyk	0.0009
AR Her	58600.7949	36482	–1.1136	V	G. Samolyk	0.0019
AR Her	58604.5818	36490	–1.0869	V	T. Arranz	0.0015
AR Her	58614.4515	36511	–1.0878	V	T. Arranz	0.0009
AR Her	58628.5133	36541	–1.1268	V	T. Arranz	0.0009
AR Her	58629.4523	36543	–1.1279	V	T. Arranz	0.0009
AR Her	58636.5462	36558	–1.0844	V	T. Arranz	0.0012
AR Her	58638.4341	36562	–1.0766	V	T. Arranz	0.0009
AR Her	58642.6647	36571	–1.0763	V	G. Samolyk	0.0011
AR Her	58646.4136	36579	–1.0876	V	T. Arranz	0.0008
AR Her	58675.5536	36641	–1.0893	V	T. Arranz	0.0011
DL Her	58607.8264	34480	0.0696	V	G. Samolyk	0.0017
DL Her	58651.5980	34554	0.0607	V	T. Arranz	0.0009
DL Her	58657.5065	34564	0.0529	V	T. Arranz	0.0009
DL Her	58663.4226	34574	0.0528	V	T. Arranz	0.0017
DY Her	58554.8817	168978	–0.0336	V	R. Sabo	0.0008
DY Her	58608.8336	169341	–0.0348	V	G. Samolyk	0.0007
SZ Hya	58533.7696	33234	–0.2839	V	G. Samolyk	0.0029
SZ Hya	58539.6924	33245	–0.2707	V	G. Samolyk	0.0009
SZ Hya	58546.6719	33258	–0.2753	V	G. Samolyk	0.0011
SZ Hya	58553.6368	33271	–0.2946	V	G. Samolyk	0.0024
SZ Hya	58571.3831	33304	–0.2772	V	T. Arranz	0.0007
SZ Hya	58586.4212	33332	–0.2818	V	T. Arranz	0.0011
SZ Hya	58600.3970	33358	–0.2743	V	T. Arranz	0.0008
SZ Hya	58838.9297	33802	–0.2762	V	G. Samolyk	0.0015
UU Hya	58536.7642	36379	0.0127	V	G. Samolyk	0.0012
UU Hya	58561.3782	36426	0.0049	V	T. Arranz	0.0017
DG Hya	58508.8475	8133	0.0266	V	G. Samolyk	0.0017
DG Hya	58565.4188	8208	0.0297	V	T. Arranz	0.0015
DH Hya	58536.7866	55952	0.1153	V	G. Samolyk	0.0013
DH Hya	58576.3950	56033	0.1149	V	T. Arranz	0.0009
RR Leo	58488.7563	33584	0.1777	V	N. Simmons	0.0007
RR Leo	58530.8299	33677	0.1787	V	G. Samolyk	0.0008
RR Leo	58537.6154	33692	0.1783	V	T. Arranz	0.0008
RR Leo	58538.5196	33694	0.1777	V	T. Arranz	0.0007
RR Leo	58542.5919	33703	0.1785	V	T. Arranz	0.0007
SS Leo	58255.4028	26302	–0.1087	V	T. Arranz	0.0011
SS Leo	58542.8927	26761	–0.1108	V	G. Samolyk	0.0015
SS Leo	58602.3949	26856	–0.1112	V	T. Arranz	0.0009
SS Leo	58607.4042	26864	–0.1127	V	T. Arranz	0.0009
SS Leo	58628.7011	26898	–0.1115	TG	G. Conrad	0.0015

Table continued on next page

Table 1. Recent times of maxima of stars in the AAVSO short period pulsator program, cont.

Star	*JD (max) Hel. 2400000 +*	*Cycle*	*O–C (day)*	*F*	*Observer*	*Error (day)*	*Star*	*JD (max) Hel. 2400000 +*	*Cycle*	*O–C (day)*	*F*	*Observer*	*Error (day)*
ST Leo	58542.7743	64060	–0.0180	V	G. Samolyk	0.0008	DY Peg	58725.6683	195041	–0.0201	V	G. Samolyk	0.0005
TV Leo	58593.6646	32031	0.1330	V	G. Samolyk	0.0013	DY Peg	58725.7411	195042	–0.0202	V	G. Samolyk	0.0004
TV Leo	58604.4259	32047	0.1286	V	T. Arranz	0.0011	DY Peg	58725.8149	195043	–0.0193	V	G. Samolyk	0.0005
WW Leo	58553.7721	39266	0.0557	V	G. Samolyk	0.0019	DY Peg	58725.8877	195044	–0.0194	V	G. Samolyk	0.0006
WW Leo	58563.4172	39282	0.0553	V	T. Arranz	0.0017	DY Peg	58760.6740	195521	–0.0189	V	G. Samolyk	0.0006
AA Leo	58539.8018	31643	–0.1155	V	G. Samolyk	0.0013	DY Peg	58760.7456	195522	–0.0202	V	G. Samolyk	0.0005
U Lep	58090.7627	28786	0.0428	V	G. Samolyk	0.0008	DF Ser	58617.7145	66039	0.1086	V	G. Samolyk	0.0010
U Lep	58839.7039	30074	0.0427	V	G. Samolyk	0.0012	RV UMa	58508.9687	28700	0.1357	V	G. Samolyk	0.0014
SZ Lyn	58487.7238	168941	0.0356	V	G. Samolyk	0.0006	RV UMa	58553.9010	28796	0.1342	V	G. Samolyk	0.0015
SZ Lyn	58523.5247	169238	0.0377	V	G. Samolyk	0.0009	RV UMa	58559.5171	28808	0.1336	V	T. Arranz	0.0008
SZ Lyn	58523.6440	169239	0.0364	V	G. Samolyk	0.0008	RV UMa	58562.7938	28815	0.1339	V	G. Samolyk	0.0011
SZ Lyn	58523.7652	169240	0.0371	V	G. Samolyk	0.0009	RV UMa	58567.4719	28825	0.1314	V	T. Arranz	0.0009
SZ Lyn	58551.6082	169471	0.0365	V	G. Samolyk	0.0007	RV UMa	58603.5177	28902	0.1366	V	T. Arranz	0.0009
SZ Lyn	58558.3589	169527	0.0373	V	T. Arranz	0.0006	RV UMa	58604.4544	28904	0.1372	V	T. Arranz	0.0009
SZ Lyn	58571.6179	169637	0.0375	TG	G. Conrad	0.0013	RV UMa	58618.4960	28934	0.1370	V	T. Arranz	0.0008
SZ Lyn	58788.9464	171440	0.0415	V	G. Samolyk	0.0009	RV UMa	58626.4524	28951	0.1363	V	T. Arranz	0.0007
RR Lyr	58617.7053	27687	–0.5817	V	G. Samolyk	0.0011	RV UMa	58632.5381	28964	0.1373	V	T. Arranz	0.0008
RR Lyr	58662.4808	27766	–0.5887	V	T. Arranz	0.0009	RV UMa	58656.4049	29015	0.1330	V	T. Arranz	0.0008
RR Lyr	58675.5186	27789	–0.5889	V	T. Arranz	0.0009	AE UMa	58531.4938	266542	–0.0021	V	T. Arranz	0.0004
RR Lyr	58704.4228	27840	–0.5949	V	T. Arranz	0.0009	AE UMa	58531.5839	266543	0.0020	V	T. Arranz	0.0005
RZ Lyr	58598.8245	34065	–0.0704	V	G. Samolyk	0.0008	AE UMa	58539.5862	266636	0.0047	V	T. Arranz	0.0005
RZ Lyr	58683.6881	34231	–0.0730	TG	G. Conrad	0.0019	AE UMa	58539.6667	266637	–0.0008	V	T. Arranz	0.0004
RZ Lyr	58697.4919	34258	–0.0728	V	T. Arranz	0.0007	LV UMa	57040.8748	0	0.0004	V	V. Petriew	0.0011
AV Peg	58695.8042	38182	0.2014	V	G. Samolyk	0.0008	LV UMa	57040.9114	1	0.0000	V	V. Petriew	0.0011
AV Peg	58720.3972	38245	0.2008	V	T. Arranz	0.0008	LV UMa	58562.6026	41128	–0.0018	V	G. Samolyk	0.0048
AV Peg	58750.4573	38322	0.2020	V	T. Arranz	0.0008	LV UMa	58838.8826	48595	0.0002	V	G. Samolyk	0.0028
AV Peg	58754.3623	38332	0.2033	V	T. Arranz	0.0007	LV UMa	58838.9215	48596	0.0021	V	G. Samolyk	0.0019
AV Peg	58770.3656	38373	0.2012	V	T. Arranz	0.0006	LV UMa	58838.9560	48597	–0.0004	V	G. Samolyk	0.0018
BH Peg	58845.5806	30391	–0.1177	V	G. Samolyk	0.0023	LV UMa	58838.9933	48598	–0.0001	V	G. Samolyk	0.0015
DY Peg	58725.5956	195040	–0.0198	V	G. Samolyk	0.0004							

Recent Minima of 216 Eclipsing Binary Stars

Gerard Samolyk
P.O. Box 20677, Greenfield, WI 53220; gsamolyk@wi.rr.com

Received February 24, 2002; accepted February 24, 2002

Abstract This paper continues the publication of times of minima for eclipsing binary stars. Times of minima determined from observations received by the AAVSO Eclipsing Binaries Section from August 2019 through January 2020 are presented.

1. Recent observations

The accompanying list contains times of minima calculated from recent CCD observations made by participants in the AAVSO's eclipsing binary program. These observations were reduced by the observers or the writer using the method of Kwee and van Woerden (1956).

The linear elements in the *General Catalogue of Variable Stars* (GCVS, Kholopov *et al.* 1985) were used to compute the O–C values for most stars. For a few exceptions where the GCVS elements are missing or are in significant error, light elements from another source are used: CD Cam (Baldwin and Samolyk 2007), AC CMi (Samolyk 2008), CW Cas (Samolyk 1992a), DV Cep (Frank and Lichtenknecker 1987), Z Dra (Danielkiewicz-Krośniak and Kurpińska-Winiarska 1996), DF Hya (Samolyk 1992b), DK Hya (Samolyk 1990), EF Ori (Baldwin and Samolyk 2005), GU Ori (Samolyk 1985).

The light elements used for QX And, EK Aqr, MR Del, AQ Psc, and V1128 Tau are from (Kreiner 2004).

The light elements used for V1261 Cas, CW Cep, EM Cep, V2181 Cyg, V2610 Oph, VZ Psc, and V1241 Tau are from (Paschke 2014).

The light elements used for V1071 Per and V1092 Per are from the AAVSO VSX site (Watson *et al.* 2014). O–C values listed in this paper can be directly compared with values published in the *AAVSO Observed Minima Timings of Eclipsing Binaries* monographs. The standard error is included when available. Column F indicates the filter used. A "C" indicates a clear filter.

This list will be web-archived and made available through the AAVSO ftp site at ftp://ftp.aavso.org/public/datasets/gsamj481eb215.txt. This list, along with the eclipsing binary data from earlier AAVSO publications, is also included in the Lichtenknecker database administered by the Bundesdeutsche Arbeitsgemeinschaft für Veränderliche Sterne e. V. (BAV) at http://www.bav-astro.de/LkDB/index.php?lang=en.

References

Baldwin, M. E., and Samolyk, G. 2005, *Observed Minima Timings of Eclipsing Binaries No. 10*, AAVSO, Cambridge, MA.

Baldwin, M. E., and Samolyk, G. 2007, *Observed Minima Timings of Eclipsing Binaries No. 12*, AAVSO, Cambridge, MA.

Danielkiewicz-Krośniak, E, and Kurpińska-Winiarska, M., eds. 1996, *Rocznik Astron.* (SAC 68), **68**, 1.

Frank, P., and Lichtenknecker, D. 1987, *BAV Mitt.*, No. 47, 1.

Kholopov, P. N., *et al.* 1985, *General Catalogue of Variable Stars*, 4th ed., Moscow.

Kreiner, J. M. 2004, *Acta Astron.*, **54**, 207 (http://www.as.up.krakow.pl/ephem/).

Kwee K. K., and van Woerden, H. 1956, *Bull. Astron. Inst. Netherlands*, **12**, 327.

Paschke, A. 2014, "O–C Gateway" (http://var.astro.cz/ocgate/).

Samolyk, G. 1985, *J. Amer. Assoc. Var. Star Obs.*, 14, 12.

Samolyk, G. 1990, *J. Amer. Assoc. Var. Star Obs.*, 19, 5.

Samolyk, G. 1992a, *J. Amer. Assoc. Var. Star Obs.*, 21, 34.

Samolyk, G. 1992b, *J. Amer. Assoc. Var. Star Obs.*, 21, 111.

Samolyk, G. 2008, J. Amer. Assoc. Var. Star Obs., 36, 171.

Watson, C., Henden, A. A., and Price, C. A. 2014, AAVSO International Variable Star Index VSX (Watson+, 2006–2014; http://www.aavso.org/vsx).

Table 1. Recent times of minima of stars in the AAVSO eclipsing binary program.

Star	JD (min) Hel. 2400000 +	Cycle	O–C (day)	F	Observer	Standard Error (day)	Star	JD (min) Hel. 2400000 +	Cycle	O–C (day)	F	Observer	Standard Error (day)
RT And	58759.4502	28012	–0.0123	V	T. Arranz	0.0001	TU Boo	58666.7366	78944	–0.1645	V	S. Cook	0.0001
RT And	58844.3568	28147	–0.0112	V	T. Arranz	0.0001	TY Boo	58849.9572	76839.5	0.0615	V	G. Samolyk	0.0003
RT And	58849.3881	28155	–0.0114	V	T. Arranz	0.0001	TZ Boo	58673.7079	64075.5	0.0624	V	S. Cook	0.0006
UU And	58760.6869	11512	0.1073	V	G. Samolyk	0.0001	TZ Boo	58835.9543	64621.5	0.0583	V	G. Samolyk	0.0002
UU And	58848.3792	11571	0.1082	V	T. Arranz	0.0001	UW Boo	58871.9163	16390	–0.0067	V	K. Menzies	0.0002
WZ And	58734.7748	25677	0.0846	V	K. Menzies	0.0001	Y Cam	58799.6731	4791	0.4990	V	G. Samolyk	0.0001
WZ And	58865.5600	25865	0.0862	V	G. Samolyk	0.0002	AL Cam	58664.7611	24281	–0.0240	V	G. Samolyk	0.0002
XZ And	58712.8490	25592	0.1989	V	G. Samolyk	0.0001	CD Cam	58750.8303	7836	–0.0162	V	G. Samolyk	0.0002
XZ And	58825.5039	25675	0.1997	V	T. Arranz	0.0002	CD Cam	58854.7586	7972	–0.0169	V	G. Samolyk	0.0004
AB And	58743.5801	68197	–0.0481	V	K. Menzies	0.0001	RT CMa	58813.8154	24880	–0.7790	V	G. Samolyk	0.0001
AB And	58760.3403	68247.5	–0.0485	V	L. Corp	0.0001	SX CMa	58863.7570	18943	0.0305	V	G. Samolyk	0.0002
AB And	58761.3359	68250.5	–0.0486	V	T. Arranz	0.0002	TU CMa	58810.8325	28226	–0.0110	V	G. Samolyk	0.0001
AB And	58761.5018	68251	–0.0486	V	T. Arranz	0.0001	UU CMa	58853.8122	6580	–0.0658	V	G. Samolyk	0.0005
AB And	58782.5781	68314.5	–0.0475	V	G. Samolyk	0.0001	AC CMi	58795.9464	7861	0.0056	V	G. Samolyk	0.0001
AB And	58786.5609	68326.5	–0.0474	V	G. Samolyk	0.0002	AK CMi	58835.8620	27804	–0.0241	V	G. Samolyk	0.0001
AB And	58828.5435	68453	–0.0491	V	G. Samolyk	0.0001	TY Cap	58697.8101	9768	0.1005	V	G. Samolyk	0.0001
AD And	58764.7751	20039	–0.0541	V	G. Samolyk	0.0002	TY Cap	58723.4320	9786	0.1003	V	T. Arranz	0.0001
BD And	58770.4054	51432	0.0143	V	T. Arranz	0.0001	RZ Cas	58824.6540	13072	0.0789	V	G. Samolyk	0.0002
BD And	58783.3665	51460	0.0141	V	T. Arranz	0.0001	TV Cas	58762.4196	7812	–0.0306	V	T. Arranz	0.0001
BD And	58804.6594	51506	0.0135	V	K. Menzies	0.0001	TW Cas	58802.6392	11758	0.0183	V	G. Samolyk	0.0001
BX And	58697.8220	36336	–0.1067	V	G. Samolyk	0.0001	ZZ Cas	58719.6685	20331	0.0261	V	N. Simmons	0.0001
BX And	58750.9020	36423	–0.1067	V	G. Samolyk	0.0001	ZZ Cas	58719.6688	20331	0.0264	V	G. Samolyk	0.0001
BX And	58850.3487	36586	–0.1088	V	T. Arranz	0.0002	AB Cas	58750.7693	11732	0.1432	V	G. Samolyk	0.0001
DS And	58747.7152	22370	0.0042	V	G. Samolyk	0.0001	AB Cas	58757.6042	11737	0.1437	V	G. Samolyk	0.0001
DS And	58782.5792	22404.5	0.0053	V	G. Samolyk	0.0001	AB Cas	58802.7108	11770	0.1435	V	G. Samolyk	0.0002
DS And	58795.7164	22417.5	0.0057	V	G. Samolyk	0.0001	AB Cas	58828.6814	11789	0.1435	TG	G. Conrad	0.0002
QR And	58765.4643	34773	0.1634	V	T. Arranz	0.0003	CW Cas	58696.8679	53517.5	–0.1266	V	G. Samolyk	0.0001
QX And	58746.7036	15155.5	0.0069	V	K. Menzies	0.0002	CW Cas	58747.8862	53677.5	–0.1265	V	G. Samolyk	0.0002
QX And	58747.7352	15158	0.0080	V	G. Samolyk	0.0003	CW Cas	58748.6825	53680	–0.1274	V	K. Menzies	0.0001
QX And	58782.5576	15242.5	0.0019	V	G. Samolyk	0.0002	CW Cas	58763.3495	53726	–0.1281	V	T. Arranz	0.0001
QX And	58795.7496	15274.5	0.0044	V	G. Samolyk	0.0001	CW Cas	58763.5099	53726.5	–0.1272	V	T. Arranz	0.0002
RY Aqr	58757.6379	9119	–0.1468	V	G. Samolyk	0.0001	CW Cas	58763.6687	53727	–0.1278	V	T. Arranz	0.0001
CX Aqr	58725.8249	40059	0.0187	V	G. Samolyk	0.0001	CW Cas	58767.3355	53738.5	–0.1279	V	T. Arranz	0.0001
CZ Aqr	58719.7952	17790	–0.0675	V	G. Samolyk	0.0001	CW Cas	58767.4946	53739	–0.1283	V	T. Arranz	0.0001
EK Aqr	58788.5965	20515.5	0.0241	V	G. Samolyk	0.0003	CW Cas	58767.6544	53739.5	–0.1279	V	T. Arranz	0.0001
XZ Aql	58704.7696	7854	0.1810	V	G. Samolyk	0.0001	CW Cas	58795.7149	53827.5	–0.1274	V	G. Samolyk	0.0002
OO Aql	58697.5763	39630.5	0.0732	V	T. Arranz	0.0001	CW Cas	58850.3987	53999	–0.1288	V	T. Arranz	0.0002
OO Aql	58701.3774	39638	0.0734	V	T. Arranz	0.0001	DZ Cas	58824.5582	38719	–0.2157	V	G. Samolyk	0.0002
OO Aql	58701.6305	39638.5	0.0731	V	T. Arranz	0.0001	DZ Cas	58847.3186	38748	–0.2171	V	T. Arranz	0.0002
OO Aql	58704.4185	39644	0.0738	V	T. Arranz	0.0001	GT Cas	58725.6064	10497	0.2088	V	G. Samolyk	0.0003
OO Aql	58713.5412	39662	0.0743	V	T. Arranz	0.0001	IR Cas	58714.8135	24021	0.0155	V	G. Samolyk	0.0001
OO Aql	58719.3679	39673.5	0.0729	V	L. Corp	0.0001	IS Cas	58724.8525	16263	0.0733	V	G. Samolyk	0.0001
V342 Aql	58700.7644	5716	–0.0981	V	G. Samolyk	0.0002	IS Cas	58846.3914	16329	0.0724	V	T. Arranz	0.0003
V342 Aql	58707.5466	5718	–0.0977	V	T. Arranz	0.0002	KR Cas	58764.6070	8916	–0.1647	V	T. Arranz	0.0001
V342 Aql	58724.4985	5723	–0.1002	V	T. Arranz	0.0002	KR Cas	58769.5094	8917	–0.1665	V	T. Arranz	0.0002
V343 Aql	58696.7021	16401	–0.0487	V	G. Samolyk	0.0001	KR Cas	58823.4549	8928	–0.1680	V	T. Arranz	0.0002
V346 Aql	58718.4911	15185	–0.0151	V	T. Arranz	0.0001	MM Cas	58730.8746	20138	0.1227	V	G. Samolyk	0.0002
RX Ari	58799.6387	19814	0.0594	V	G. Samolyk	0.0001	MM Cas	58758.6810	20162	0.1259	V	S. Cook	0.0008
RX Ari	58865.5347	19878	0.0594	V	G. Samolyk	0.0004	MM Cas	58764.4716	20167	0.1241	V	T. Arranz	0.0001
SS Ari	58747.9008	48572	–0.4153	V	G. Samolyk	0.0001	MM Cas	58765.6284	20168	0.1224	V	G. Samolyk	0.0002
SS Ari	58765.7656	48616	–0.4143	V	G. Samolyk	0.0001	MM Cas	58844.4069	20236	0.1250	V	T. Arranz	0.0003
SS Ari	58813.6692	48734	–0.4179	V	G. Samolyk	0.0001	OR Cas	58802.6211	11714	–0.0336	V	G. Samolyk	0.0001
SS Ari	58848.3818	48819.5	–0.4178	V	T. Arranz	0.0003	OR Cas	58857.4315	11758	–0.0345	V	T. Arranz	0.0002
SS Ari	58849.3949	48822	–0.4196	V	T. Arranz	0.0002	OX Cas	58799.6637	7042	0.0769	V	G. Samolyk	0.0003
SX Aur	58810.9029	15411	0.0214	V	G. Samolyk	0.0002	PV Cas	58702.7366	10554.5	–0.0019	V	G. Samolyk	0.0001
TT Aur	58786.7243	28171	–0.0098	V	G. Samolyk	0.0002	PV Cas	58765.7533	10590.5	–0.0022	V	G. Samolyk	0.0001
AP Aur	58813.6836	28751	1.7709	V	G. Samolyk	0.0002	PV Cas	58782.3526	10600	–0.0323	V	T. Arranz	0.0001
EM Aur	58792.8964	15259	–1.1308	V	G. Samolyk	0.0003	PV Cas	58824.3641	10624	–0.0321	V	T. Arranz	0.0001
EM Aur	58805.6503	15266	–1.1308	TG	G. Conrad	0.0004	PV Cas	58852.3702	10640	–0.0335	V	T. Arranz	0.0002
EM Aur	58878.5264	15306	–1.1340	V	K. Menzies	0.0006	V364 Cas	58720.6914	15804.5	–0.0248	V	G. Samolyk	0.0001
EP Aur	58733.8709	54863	0.0170	V	G. Samolyk	0.0001	V364 Cas	58743.8369	15819.5	–0.0253	V	K. Menzies	0.0001
EP Aur	58810.7024	54993	0.0175	V	G. Samolyk	0.0001	V364 Cas	58761.5826	15831	–0.0249	V	T. Arranz	0.0002
HP Aur	58733.9041	11229.5	0.0758	V	G. Samolyk	0.0002	V375 Cas	58714.6895	16338	0.2816	V	G. Samolyk	0.0002
HP Aur	58765.9157	11252	0.0741	V	G. Samolyk	0.0001	V375 Cas	58760.3659	16369	0.2831	V	T. Arranz	0.0001
HP Aur	58780.8556	11262.5	0.0744	V	K. Menzies	0.0001	V375 Cas	58782.4669	16384	0.2834	V	T. Arranz	0.0001
HP Aur	58845.5939	11308	0.0747	V	G. Samolyk	0.0002	V375 Cas	58785.4151	16386	0.2848	V	T. Arranz	0.0002

Table continued on following pages

Table 1. Recent times of minima of stars in the AAVSO eclipsing binary program, cont.

Star	*JD (min) Hel. 2400000 +*	*Cycle*	*O–C (day)*	*F*	*Observer*	*Standard Error (day)*
V380 Cas	58712.6709	24363	–0.0762	V	G. Samolyk	0.0002
V380 Cas	58788.6803	24419	–0.0741	V	G. Samolyk	0.0001
V1261 Cas	58766.3422	14980	0.0113	V	T. Arranz	0.0002
V1261 Cas	58802.5963	15094	0.0129	V	G. Samolyk	0.0004
U Cep	58704.8302	5681	0.2243	V	G. Samolyk	0.0002
U Cep	58724.7774	5689	0.2271	V	G. Samolyk	0.0001
U Cep	58764.6660	5705	0.2269	V	G. Samolyk	0.0002
SU Cep	58712.8155	35930	0.0090	V	G. Samolyk	0.0002
SU Cep	58724.5309	35943	0.0062	V	T. Arranz	0.0001
WW Cep	58707.7082	21960	0.3572	V	S. Cook	0.0003
WW Cep	58730.7128	21975	0.3578	V	G. Samolyk	0.0001
WZ Cep	58786.5802	73653	–0.2071	V	G. Samolyk	0.0001
WZ Cep	58828.5327	73753.5	–0.2080	V	G. Samolyk	0.0001
XX Cep	58725.8888	5941	0.0293	V	G. Samolyk	0.0001
XX Cep	58765.6227	5958	0.0286	V	G. Samolyk	0.0001
XX Cep	58847.4304	5993	0.0299	V	T. Arranz	0.0004
CW Cep	58726.7053	8557	0.0093	V	S. Cook	0.0006
DK Cep	58697.6837	25466	0.0283	V	G. Samolyk	0.0001
DK Cep	58717.4022	25486	0.0287	V	T. Arranz	0.0001
DL Cep	58723.4653	15196	0.0680	V	T. Arranz	0.0002
DL Cep	58754.4431	15215	0.0667	V	T. Arranz	0.0001
DV Cep	58702.6373	10275	–0.0068	V	G. Samolyk	0.0002
EM Cep	58710.7493	23042	–0.0003	V	S. Cook	0.0004
NN Cep	58744.7047	6917	0.0057	V	S. Cook	0.0007
TT Cet	58813.6373	54054	–0.0854	V	G. Samolyk	0.0001
TW Cet	58824.6092	51921	–0.0363	V	G. Samolyk	0.0002
TW Cet	58855.6592	52019	–0.0378	V	S. Cook	0.0003
TX Cet	58810.6855	21230	0.0127	V	G. Samolyk	0.0001
RW Com	58835.8925	79266	0.0161	V	G. Samolyk	0.0001
RZ Com	58849.9108	70936.5	0.0573	V	G. Samolyk	0.0001
RZ Com	58871.9140	71001.5	0.0576	V	K. Menzies	0.0006
RW CrB	58724.6050	24742	0.0039	V	G. Samolyk	0.0002
V Crt	58849.9491	24860	–0.0006	V	G. Samolyk	0.0002
Y Cyg	58765.6863	16457.5	0.1200	V	G. Samolyk	0.0002
Y Cyg	58810.6302	16472.5	0.1190	V	G. Samolyk	0.0002
SW Cyg	58719.4408	3685	–0.3757	V	T. Arranz	0.0001
WW Cyg	58708.7102	5525	0.1505	V	S. Cook	0.0006
WW Cyg	58728.6178	5531	0.1515	V	G. Samolyk	0.0001
WW Cyg	58758.4778	5540	0.1515	V	T. Arranz	0.0001
WW Cyg	58811.5627	5556	0.1521	V	G. Samolyk	0.0001
ZZ Cyg	58725.4916	21834	–0.0768	V	T. Arranz	0.0001
ZZ Cyg	58811.6118	21971	–0.0770	V	G. Samolyk	0.0001
AE Cyg	58733.4507	14597	–0.0036	V	T. Arranz	0.0001
BR Cyg	58709.5559	12885	0.0014	V	T. Arranz	0.0001
CG Cyg	58739.3791	30602	0.0801	V	T. Arranz	0.0001
CG Cyg	58754.5270	30626	0.0806	V	K. Menzies	0.0001
CG Cyg	58763.3631	30640	0.0808	V	T. Arranz	0.0001
CG Cyg	58764.3102	30641.5	0.0811	V	L. Corp	0.0002
DK Cyg	58720.6873	44022.5	0.1288	V	G. Samolyk	0.0001
DK Cyg	58729.3960	44041	0.1297	V	T. Arranz	0.0001
DK Cyg	58729.6300	44041.5	0.1283	V	T. Arranz	0.0001
DK Cyg	58782.5841	44154	0.1298	V	G. Samolyk	0.0001
KR Cyg	58702.8054	35019	0.0250	V	G. Samolyk	0.0001
KV Cyg	58718.6037	10303	0.0636	V	T. Arranz	0.0002
KV Cyg	58738.4770	10310	0.0640	V	T. Arranz	0.0001
V387 Cyg	58704.6407	47954	0.0199	V	G. Samolyk	0.0001
V387 Cyg	58720.6549	47979	0.0192	V	G. Samolyk	0.0001
V387 Cyg	58749.4825	48024	0.0200	V	T. Arranz	0.0001
V388 Cyg	58731.4933	19531.5	–0.1291	V	T. Arranz	0.0002
V388 Cyg	58734.4942	19535	–0.1348	V	T. Arranz	0.0001
V388 Cyg	58763.7023	19569	–0.1340	V	G. Samolyk	0.0001
V456 Cyg	58725.7769	15501	0.0536	V	G. Samolyk	0.0001
V456 Cyg	58753.4037	15532	0.0534	V	T. Arranz	0.0001
V466 Cyg	58710.4663	21512.5	0.0075	V	T. Arranz	0.0001
V477 Cyg	58696.6738	6181.5	–0.5125	V	G. Samolyk	0.0001
V477 Cyg	58700.6668	6183	–0.0400	V	G. Samolyk	0.0002
V477 Cyg	58719.4408	6191	–0.0419	V	T. Arranz	0.0001
V477 Cyg	58754.6461	6206	–0.0415	V	K. Menzies	0.0001
V488 Cyg	58702.7983	52644	–0.2590	V	G. Samolyk	0.0002
V548 Cyg	58748.5520	7917	0.0265	V	K. Menzies	0.0001
V704 Cyg	58725.6288	36422	0.0387	V	G. Samolyk	0.0002
V704 Cyg	58726.4850	36423.5	0.0389	V	T. Arranz	0.0001
V704 Cyg	58765.5787	36492	0.0393	V	G. Samolyk	0.0002
V836 Cyg	58725.4554	21230	0.0241	V	T. Arranz	0.0001
V891 Cyg	58710.6650	12618	0.0525	V	S. Cook	0.0009
V1034 Cyg	58728.6160	16163	0.0212	V	G. Samolyk	0.0002
V2181 Cyg	58702.8163	13856.5	–0.005	V	G. Samolyk	0.0005
TT Del	58697.8379	4690	–0.1292	V	G. Samolyk	0.0001
TY Del	58726.4674	13237	0.0758	V	T. Arranz	0.0001
TY Del	58764.5846	13269	0.0769	V	G. Samolyk	0.0001
TY Del	58820.5687	13316	0.0780	V	G. Samolyk	0.0001
YY Del	58696.8529	19843	0.0124	V	G. Samolyk	0.0001
YY Del	58752.3695	19913	0.0125	V	T. Arranz	0.0001
YY Del	58756.3350	19918	0.0126	V	T. Arranz	0.0001
BW Del	58747.7951	13599	0.4778	V	S. Cook	0.0007
FZ Del	58730.4746	34992	–0.0297	V	T. Arranz	0.0001
FZ Del	58820.5439	35107	–0.0298	V	G. Samolyk	0.0001
MR Del	58726.4139	11934.5	–0.0089	V	L. Corp	0.0003
Z Dra	58720.6678	6539	–0.0052	V	G. Samolyk	0.0002
BH Dra	58764.6101	10315	–0.0039	V	G. Samolyk	0.0001
SV Equ	58756.7385	21991.5	–0.2000	V	S. Cook	0.0009
SV Equ	58759.8245	21995	–0.1975	V	S. Cook	0.0017
TZ Eri	58840.6529	6303	0.3603	V	G. Samolyk	0.0001
YY Eri	58840.7240	53683.5	0.1688	V	G. Samolyk	0.0002
YY Eri	58848.2796	53707	0.1693	V	L. Corp	0.0007
YY Eri	58856.6387	53733	0.1696	V	G. Samolyk	0.0001
SX Gem	58849.7049	29131	–0.0590	V	G. Samolyk	0.0002
TX Gem	58849.7652	13929	–0.0418	V	N. Simmons	0.0003
TX Gem	58849.7653	13929	–0.0417	V	G. Samolyk	0.0002
WW Gem	58747.8997	26469	0.0233	V	G. Samolyk	0.0001
WW Gem	58799.8883	26511	0.0239	V	G. Samolyk	0.0001
AF Gem	58765.8803	25415	–0.0701	V	G. Samolyk	0.0001
AL Gem	58810.9103	23349	0.1010	V	G. Samolyk	0.0002
SZ Her	58746.5466	20636	–0.0347	V	K. Menzies	0.0001
TT Her	58680.7276	20486	0.0417	V	S. Cook	0.0006
AK Her	58684.4300	39139	0.0200	V	L. Corp	0.0001
CC Her	58697.6523	10974	0.3307	V	G. Samolyk	0.0001
DI Her	58712.7078	1562	–0.0022	V	G. Samolyk	0.0003
HS Her	58712.6643	8276.5	–0.0005	V	G. Samolyk	0.0006
LT Her	58697.6401	16551	–0.1613	V	G. Samolyk	0.0002
DF Hya	58835.8644	48541.5	0.0146	V	G. Samolyk	0.0001
DF Hya	58854.8748	48599	0.0152	V	G. Samolyk	0.0001
DK Hya	58869.8147	30706	–0.0003	V	G. Samolyk	0.0002
SW Lac	58712.6827	41897.5	–0.0689	V	G. Samolyk	0.0001
SW Lac	58740.7484	41985	–0.0663	V	G. Samolyk	0.0001
SW Lac	58760.3120	42046	–0.0667	V	T. Arranz	0.0002
SW Lac	58760.4704	42046.5	–0.0686	V	T. Arranz	0.0002
SW Lac	58760.6337	42047	–0.0657	V	T. Arranz	0.0002
SW Lac	58847.3865	42317.5	–0.0679	V	L. Corp	0.0003
VX Lac	58746.6804	12553	0.0887	V	K. Menzies	0.0001
VX Lac	58747.7553	12554	0.0891	V	G. Samolyk	0.0001
AR Lac	58704.6414	8628	–0.0518	V	G. Samolyk	0.0002
AW Lac	58700.8042	28067	0.2169	V	K. Menzies	0.0001
CM Lac	58728.5994	19756	–0.0038	V	G. Samolyk	0.0001
CM Lac	58749.4597	19769	–0.0045	V	T. Arranz	0.0001
CO Lac	58696.6732	20206.5	–0.0154	V	G. Samolyk	0.0001
CO Lac	58719.8053	20221.5	–0.0165	V	G. Samolyk	0.0001
CO Lac	58740.6522	20235	0.0106	V	G. Samolyk	0.0001
CO Lac	58785.3777	20264	0.0121	V	T. Arranz	0.0002
DG Lac	58829.5547	6490	–0.2380	V	G. Samolyk	0.0002
GX Lac	58719.7942	2985	–0.0432	V	G. Samolyk	0.0002
T LMi	58850.8224	4455	–0.1333	V	K. Menzies	0.0004

Table continued on next page

Table 1. Recent times of minima of stars in the AAVSO eclipsing binary program, cont.

Star	JD (min) Hel. 2400000 +	Cycle	O–C (day)	F	Observer	Standard Error (day)
Z Lep	58763.8929	31538	–0.2018	V	G. Samolyk	0.0001
RR Lep	58792.9179	31041	–0.0446	V	G. Samolyk	0.0001
RY Lyn	58828.7076	11109	–0.0171	V	G. Samolyk	0.0002
EW Lyr	58702.6433	16525	0.2987	V	G. Samolyk	0.0002
FL Lyr	58711.4488	9407	–0.0021	V	T. Arranz	0.0001
FL Lyr	58750.6558	9425	–0.0019	V	G. Samolyk	0.0002
β Lyr	58631.85	745	2.62	B	G. Samolyk	0.02
β Lyr	58631.86	745	2.63	R	G. Samolyk	0.02
β Lyr	58631.87	745	2.63	V	G. Samolyk	0.02
β Lyr	58638.34	745.5	2.64	B	G. Samolyk	0.02
β Lyr	58638.35	745.5	2.65	R	G. Samolyk	0.02
β Lyr	58638.37	745.5	2.67	V	G. Samolyk	0.02
RU Mon	58802.8688	4759	–0.1464	V	G. Samolyk	0.0001
RW Mon	58838.8935	13199	–0.0909	V	G. Samolyk	0.0001
AT Mon	58795.8844	15864	0.0111	V	G. Samolyk	0.0002
BB Mon	58869.7498	43931	–0.0040	V	G. Samolyk	0.0002
RZ Oph	58705.58	63	–0.26	V	G. Samolyk	0.03
RZ Oph	58705.58	63	–0.25	R	G. Samolyk	0.04
RZ Oph	58705.60	63	–0.24	B	G. Samolyk	0.04
RZ Oph	58705.61	63	–0.22	I	G. Samolyk	0.05
V501 Oph	58719.6319	28729	–0.0101	V	G. Samolyk	0.0001
V508 Oph	58670.4300	39409	–0.0260	V	L. Corp	0.0001
V508 Oph	58719.7348	39552	–0.0265	V	S. Cook	0.0003
V839 Oph	58704.6604	44636	0.3324	V	G. Samolyk	0.0002
V2610 Oph	58713.4240	14873	–0.0390	V	L. Corp	0.0003
EF Ori	58813.8160	3991	0.0094	V	G. Samolyk	0.0003
EQ Ori	58788.9419	15664	–0.0379	V	G. Samolyk	0.0002
ER Ori	58799.8263	40560.5	0.1483	V	G. Samolyk	0.0001
ET Ori	58788.8165	33761	–0.0033	V	G. Samolyk	0.0001
FR Ori	58810.8572	35043	0.0463	V	G. Samolyk	0.0001
FZ Ori	58854.7375	37077	–0.0240	V	G. Samolyk	0.0002
GU Ori	58813.8758	33449.5	–0.0713	V	G. Samolyk	0.0001
U Peg	58714.8600	59243.5	–0.1724	V	G. Samolyk	0.0001
U Peg	58755.5228	59352	–0.1734	V	L. Corp	0.0001
U Peg	58820.5472	59525.5	–0.1736	V	G. Samolyk	0.0001
TY Peg	58800.5501	5934	–0.4674	V	G. Samolyk	0.0001
UX Peg	58730.7328	11851	–0.0023	V	G. Samolyk	0.0001
BB Peg	58704.8210	41329	–0.0327	V	G. Samolyk	0.0001
BB Peg	58724.7037	41384	–0.0326	V	G. Samolyk	0.0001
BB Peg	58739.7061	41425.5	–0.0325	TG	G. Conrad	0.0002
BB Peg	58743.6826	41436.5	–0.0326	V	K. Menzies	0.0001
BB Peg	58795.5573	41580	–0.0334	V	G. Samolyk	0.0001
BB Peg	58840.5651	41704.5	–0.0326	V	G. Samolyk	0.0002
BG Peg	58714.8620	6752	–2.4214	V	G. Samolyk	0.0002
DI Peg	58763.7306	19060	0.0144	V	G. Samolyk	0.0001
DI Peg	58845.5899	19175	0.0148	V	G. Samolyk	0.0001
GP Peg	58740.8563	17940	–0.0568	V	G. Samolyk	0.0002
Z Per	58730.7175	4277	–0.3508	V	G. Samolyk	0.0001
Z Per	58828.5151	4309	–0.3550	V	G. Samolyk	0.0002
RT Per	58752.8584	29876	0.1161	V	K. Menzies	0.0001
RV Per	58795.9517	8487	0.0075	V	G. Samolyk	0.0001
ST Per	58702.7796	6142	0.3209	V	G. Samolyk	0.0001
ST Per	58763.6939	6165	0.3239	V	G. Samolyk	0.0001
ST Per	58824.6046	6188	0.3234	V	G. Samolyk	0.0001
ST Per	58869.6261	6205	0.3235	V	G. Samolyk	0.0003
XZ Per	58828.7450	13304	–0.0728	V	G. Samolyk	0.0001
IT Per	58802.8299	19182	–0.0442	V	G. Samolyk	0.0002
IT Per	58816.6392	19191	–0.0385	V	K. Menzies	0.0004
IU Per	58754.7758	15336	0.0029	V	K. Menzies	0.0001
V432 Per	58718.8316	71052	0.0297	V	G. Samolyk	0.0001
V432 Per	58840.7237	71431	0.0669	V	G. Samolyk	0.0002
V1071 Per	58048.7974	–0.5	0.0040	V	V. Petriew	0.0005
V1071 Per	58048.9733	0	0.0000	V	V. Petriew	0.0003
V1092 Per	58046.8419	0	0.0000	V	V. Petriew	0.0003
β Per	58799.7128	4589	0.1399	V	G. Samolyk	0.0002
Y Psc	58811.6336	3499	–0.0261	V	G. Samolyk	0.0001
RV Psc	58788.7141	62108	–0.0669	V	G. Samolyk	0.0002
RV Psc	58869.5968	62254	–0.0669	V	G. Samolyk	0.0002
UV Psc	58755.5457	17826	–0.0220	V	L. Corp	0.0001
UV Psc	58843.3706	17928	–0.0240	V	L. Corp	0.0003
VZ Psc	58764.3228	57154.5	0.0028	V	L. Corp	0.0004
VZ Psc	58782.4854	57224	0.0080	V	T. Arranz	0.0003
VZ Psc	58783.3937	57227.5	0.0019	V	T. Arranz	0.0001
VZ Psc	58783.5270	57228	0.0045	V	T. Arranz	0.0002
AQ Psc	58755.5196	13152	–0.0016	V	L. Corp	0.0002
UZ Pup	58869.7413	17935.5	–0.0107	V	G. Samolyk	0.0002
U Sge	58698.5271	12296	0.0204	V	T. Arranz	0.0001
V505 Sgr	58712.7072	12048	–0.1201	V	G. Samolyk	0.0001
BS Sco	58715.7153	2547	0.0559	V	S. Cook	0.0024
V701 Sco	58730.8119	19893	–0.0126	V	S. Cook	0.0018
U Sct	58747.5874	14952	–0.0254	V	S. Cook	0.0009
RW Tau	58763.8870	4724	–0.2964	V	G. Samolyk	0.0001
RZ Tau	58763.8396	50730	0.0951	V	G. Samolyk	0.0001
TY Tau	58824.7000	34930	0.2774	V	G. Samolyk	0.0001
WY Tau	58764.9144	30837	0.0656	V	G. Samolyk	0.0001
AC Tau	58869.5547	6476	0.1912	V	G. Samolyk	0.0002
CT Tau	58724.8888	19976	–0.0723	V	G. Samolyk	0.0002
CT Tau	58849.5862	20163	–0.0721	V	G. Samolyk	0.0001
EQ Tau	58740.8242	54277.5	–0.0429	V	G. Samolyk	0.0001
EQ Tau	58748.8459	54301	–0.0429	V	K. Menzies	0.0001
EQ Tau	58762.8403	54342	–0.0438	V	K. Menzies	0.0001
V781 Tau	58854.3448	43430	–0.0505	V	L. Corp	0.0006
V1128 Tau	58843.3165	20772	–0.0045	V	L. Corp	0.0002
V1128 Tau	58848.3560	20788.5	–0.0036	V	L. Corp	0.0005
V1241 Tau	58872.7791	38069	–0.0116	V	S. Cook	0.0006
V Tri	58746.8696	58565	–0.0072	V	K. Menzies	0.0001
V Tri	58878.5417	58790	–0.0064	V	K. Menzies	0.0002
X Tri	58740.8598	16714	–0.1005	V	K. Menzies	0.0001
X Tri	58740.8599	16714	–0.1004	V	G. Samolyk	0.0001
X Tri	58849.6707	16826	–0.1016	V	G. Samolyk	0.0001
X Tri	58859.3853	16836	–0.1023	V	T. Arranz	0.0001
RS Tri	58743.8788	10898	–0.0584	V	K. Menzies	0.0002
RV Tri	58746.8651	16869	–0.0428	V	K. Menzies	0.0001
TY UMa	58813.8076	54383	0.4384	V	G. Samolyk	0.0002
VV UMa	58828.7236	18932	–0.0911	V	G. Samolyk	0.0001
XZ UMa	58838.8398	10366	–0.1553	V	G. Samolyk	0.0002
ZZ UMa	58810.7254	9942	–0.0015	V	G. Samolyk	0.0001
ZZ UMa	58849.8125	9959	–0.0018	V	G. Samolyk	0.0001
AF UMa	58799.7761	6087	0.6388	V	G. Samolyk	0.0002
W UMi	58702.7266	14708	–0.2224	V	G. Samolyk	0.0005
W UMi	58719.7420	14718	–0.2186	V	G. Samolyk	0.0002
AW Vul	58713.6525	15411	–0.0352	V	G. Samolyk	0.0001
AW Vul	58735.4274	15438	–0.0345	V	T. Arranz	0.0001
AX Vul	58810.5630	6893	–0.0395	V	G. Samolyk	0.0002
AY Vul	58795.5174	6678	–0.1793	V	G. Samolyk	0.0002
BE Vul	58723.5997	11992	0.1071	V	G. Samolyk	0.0002
BE Vul	58762.4004	12017	0.1067	V	T. Arranz	0.0001
BO Vul	58734.6806	11689	–0.0131	V	K. Menzies	0.0001
BO Vul	58810.5696	11728	–0.0130	V	G. Samolyk	0.0001
BS Vul	58740.6154	32500	–0.0354	V	G. Samolyk	0.0001
BS Vul	58810.5825	32647	–0.0361	V	G. Samolyk	0.0002
BT Vul	58746.5743	20456	0.0071	V	K. Menzies	0.0001
BU Vul	58704.8083	44238	0.0130	V	G. Samolyk	0.0001
CD Vul	58740.6113	18197	–0.0015	V	G. Samolyk	0.0002
ER Vul	58746.3511	26592.5	0.0219	V	L. Corp	0.0004

35,000 Radial Velocities for 348 Stars from the Tennessee State University Automatic Spectroscopic Telescope

Joel A. Eaton
7050 Bakerville Road, Waverly, TN 37185; eatonjoel@yahoo.com

Received March 27, 2020; revised April 22, 2020; accepted April 27, 2020

Abstract This paper presents radial velocities from a robotic telescope for stars that mainly have solar-type spectra (neutral iron-peak elements). These stars are mainly spectroscopic binaries, many of which are variables of various sorts. Data for such stars have measured random errors of roughly 0.1 km/s. We also publish velocities for a number of hotter stars for which the uncertainties are greater. The measured velocities are given in three electronic files at the AAVSO ftp site (ftp://ftp.aavso.org/public/datasets) as the .tar file AST-RVs-JAAVSO-481.tar). There are also .jpg plots of the data, electronic lists of the stars, and a FORTRAN program for extracting data for a particular star from the data files. The data cover roughly the Julian Dates 2452800–2455100 (09 June 2003–25 September 2009).

1. Introduction

While I was in the Center of Excellence for Information Systems at Tennessee State University I designed and built a two-meter robotic telescope (2-m AST) with a high-dispersion spectrograph for monitoring the velocities and line strengths of primarily cool stars. During this time (JD 2452800–2455100 (09 June 2003–25 September 2009)) I used that telescope to observe two groups of stars: 1) a group of bright cool giants in a synoptic (monitoring) program, and 2) a group of spectroscopic binaries being observed with the Georgia State University interferometer. These programs were intended to be a service to the astronomical community. This paper puts the velocities of those stars into the public record.

2. Extracting velocities from the observations

The observations consisted of echelle spectra (R ≈ 30,000) covering the wavelength range 5000–7100 Å taken with the TSU 2-m Automatic Spectroscopic Telescope at Fairborn Observatory in Washington Camp, Arizona (Eaton and Williamson 2004a, 2004b, 2007). These data were reduced at the observatory with a pipeline procedure using an echelle reduction program based on one we got from Jeff Hall of Lowell Observatory, which Williamson rewrote in C to run on our LINUX computers. We copied the resulting files back to Tennessee over the Internet every morning, knitted the separate orders of the echelle into a single array of intensity vs. (a continuous) wavelength, and archived the results.

To extract velocities from these spectra, we used lists of strong photospheric lines in the spectra, which we represented as delta functions, and cross correlated them with the observed spectrum as a function of velocity shift. We then fit the resulting cross-correlation function (CCF) with a Gaussian to get a velocity.

The initial zero point for the velocities came from observations of ~270 Th-Ar calibration lines measured at the beginning and end of the night. We corrected this velocity for drift during the night by measuring the shift of ~31 telluric O_2 lines available in each individual spectrum, in the range 6870–6924 Å, again calculating a CCF and fitting it with a Gaussian to get a velocity shift. So the wavelengths, hence velocities, are dependent on Th-Ar lines to establish the wavelengths of various echelle orders with respect to one another and telluric lines to correct for drifts during the night from such sources as thermal changes in the CCD and optical components of the spectrograph.

Most of the stars monitored by the AST have solar-type spectra dominated by neutral lines of iron-peak elements. For these we used a list of 128 strong metallic lines in the spectrum of the Sun, mostly Fe I, at the wavelengths given by Moore *et al.* (1966). For a few somewhat warmer stars, we used a list (ε Aur) containing 37 lines, mostly of singly-ionized species; for β Ori (Rigel), a list of 33 lines; for early B stars, a list (γ Peg) of 34 lines of He I and various singly and doubly-ionized metals; and for the few stars with spectra dominated by molecules, we picked a single spectrum of the star and used it as a cross-correlation mask to give velocities relative to that spectrum. For these other three classes, the wavelengths are from various publications of Charlotte Moore (1945, 1965, 1967, 1970). Table 1 gives the wavelengths used for these mask spectra and for the telluric O_2 lines.

The velocities given here are on the system I have just described, based on the wavelengths in Table 1. However, it may be useful for combining these velocities with others from different instruments to provide a transformation to a system defined by velocity standards, this following the philosophy used to define the UBV system (Johnson and Morgan 1953). We have done this for the stars with solar-type spectra (see Eaton and Williamson 2007 section 4.1) by using 23 IAU "standards," the closest thing we could find to a group of stars defining a velocity scale. From this analysis, the AST gives velocities 0.35 ± 0.09 km s^{-1} more negative than the canonical IAU values, so we would add 0.35 km s^{-1} to our measured values to bring them onto the IAU system.

From an analysis of the variation of sharp-lined stars with the most constant velocities, the random error of a single measured velocity is of the order of 0.1 km s^{-1}. This uncertainty, 0.10–0.11 km s^{-1}, should apply for those stars for which the solar mask spectrum is appropriate, namely those with moderately sharp lines of spectral type F to middle M. For the warmer stars (ε Aur, β Ori, and γ Peg mask spectra), the uncertainties

are naturally greater and remain unknown because there were not enough data to analyze them.

For the double-lined spectroscopic binaries (SB2s), I used an interactive program to mark and isolate the two components in the CCF, first the weaker one and then the stronger minus the velocity range marked for the weaker line, then fit their separate profiles with Gaussians to get the velocities. Obviously this approach does not work for severely blended lines near conjunction. Also, many of these SB2s are RS CVn-type stars with decidedly blocky, non-Gaussian profiles, so the uncertainties are much larger than for single stars.

The stars observed are listed in three tables: Table 2 for those in the synoptic program and the GSU binaries, Table 3 for various double-lined spectroscopic binaries, and Table 4 for the cool stars dominated by molecular lines. These tables list (1) HD number, (2) V, (3) (B–V), (4) the number of radial velocities, (5) a symbol indicating the line list used: blank for the Solar list, "eps" for the singly-ionized species chosen for ε Aur, "**" for β Ori, and "*" for γ Peg, (6) the spectral type from *The Bright Star Catalogue* (Hoffleit and Jaschek 1982), (7) the star's common name, and (8) notes, such as variable type or some other star type.

3. The archive

The actual data are available from the AAVSO ftp archive as a single tar file (AST-RVs-JAAVSO-481.tar at ftp://ftp.aavso.org/public/datasets/) containing the files listed in Table 5. Of these, there are four text files duplicating Tables 1–4 of the text and three electronic-only files giving the measured radial velocities. The FORTRAN program may be used to extract data from these latter three files. The .tar file of plots contains plots of the velocities, hd*.jpg, that may be displayed with MICROSOFT FILE EXPLORER, or an equivalent program, to preview the data. The two data files for stars with only one line component list the Heliocentric Julian Date – 2,400,000, radial velocity in km s^{-1}, and HD number in (F11.4,F8.2,I8) format; that for SB2, HJD – 2,400,000,RV1,RV2,HD no., in (F11.4,2F8.2,I8) format.

Some of these stars have been analyzed in published papers based on most of the data given here. Table 6 lists these.

4. Acknowledgements

This research was supported over the years by grants from NASA and the NSF to Tennessee State University and by State funding to the Center of Excellence.

References

Bruntt, H., *et al.* 2008, *Astrophys. J.*, **683**, 433.
Eaton, J. A. 2008, *Astrophys. J.*, **681**, 562.
Eaton, J. A., Henry, G. W., and Odell, A. P. 2008, *Astrophys. J.*, **679**, 1490.
Eaton, J. A., and Shaw, F. G. 2007, *Astron. J.*, **133**, 2669.
Eaton, J. A., and Williamson, M. H. 2004a, in *Advanced Software, Control, and Communication Systems for Astronomy*, eds. H. Lewis, G. Raffi, Proc. SPIE 5496, SPIE Digital Library, Bellingham, WA, 710.
Eaton, J. A., and Williamson, M. H. 2004b, *Astron. Nachr.*, **325**, 522.
Eaton, J. A., and Williamson, M. H. 2007, *Publ. Astron. Soc. Pacific*, **119**, 886.
Evans, N. R., Berdnikov, L., Gorynya, N., Rastorguev, A., and Eaton, J. 2011, *Astron. J.*, **142**, 87.
Fekel, F. C., Boden, A. F., Tomkin, J., and Torres, G. 2009, *Astrophys. J.*, **695**, 1527.
Handler, G., *et al.* 2009, *Astrophys. J., Lett.*, **698**, L56.
Hoffleit, D., and Jaschek, C. 1982, *The Bright Star Catalogue. Fourth revised edition. (Containing data compiled through 1979)*, Yale University Observatory, New Haven, CT.
Johnson, H. L., and Morgan, W. W. 1953, *Astrophys. J.*, **117**, 313.
Marsden, S. C., Berdyugina, S. V., Donati, J.-F., Eaton, J. A., and Williamson, M. H. 2007, *Astron. Nachr.*, **328**, 1047.
Moore, C. E. 1945, *Contrib. Princeton Univ. Obs.*, No. 20, 1.
Moore, C. E. 1965a, *Selected Tables of Atomic Spectra, Atomic Energy Levels and Multiplet Tables—Si II, Si III, Si IV*, National Bureau of Standards, National Standard Reference Series (NSRDS-NBS) 3 (Sec. 1), NBS, Washington, D. C.
Moore, C. E. 1965b, *Selected Tables of Atomic Spectra, Atomic Energy Levels and Multiplet Tables—Si I*, National Bureau of Standards, National Standard Reference Series (NSRDS-NBS) 3 (Sec. 2), NBS, Washington, D. C.
Moore, C. E. 1970, *Selected Tables of Atomic Spectra, Atomic Energy Levels and Multiplet Tables—C I...C VI*, National Bureau of Standards, National Standard Reference Series (NSRDS-NBS) 3 (Sec. 3), NBS, Washington, D. C.
Moore, C. E., Minnaert, M.G.J., and Houtgast, J. 1966, *The Solar Spectrum 2935* Å *to 8770* Å, National Bureau of Standards Monograph No. 61, U. S. Government Printing Office, Washington, D. C.
Moravveji, E., Guinan, E. F., Shultz, M., Williamson, M. H., and Moya, A. 2012, *Astrophys. J.*, **747**, 108.
Tomkin, J., and Fekel, F. C. 2008, *Astron. J.*, **135**, 555.

Table 1. Lines used to compute cross-correlations.

Lines used for stars with solar-type spectra

5446.591	Ti I (3)	5701.557	Fe I (209)	6056.013	Fe I (1259)	6261.106	Ti I (104)	6475.632	Fe I (206)
5446.924	Fe I (15)	5706.008	Fe I (1183)	6062.856	Zr I (3)	6265.141	Fe I (62)	6481.878	Fe I (109)
5455.624	Fe I (15)	5711.095	Mg I (8)	6065.494	Fe I (207)	6280.622	Fe I (13)	6482.809	Ni I (66)
5472.713	Ti I (107)	5763.002	Fe I (1107)	6085.257	Ti I (69)	6290.974	Fe I (1258)	6493.788	Ca I (18)
5497.526	Fe I (15)	5782.136	Cu I (2)	6086.288	Ni I (249)	6297.799	Fe I (62)	6494.994	Fe I (168)
5501.477	Fe I (15)	5790.990	Cr I (7)	6108.125	Ni I (45)	6327.604	Ni I (44)	6518.373	Fe I (342)
5505.889	Mn I (4)	5847.006	Ni I (44)	6111.078	Ni I (230)	6335.337	Fe I (62)	6546.252	Ti I (102)
5506.791	Fe I (15)	5852.228	Fe I (1178)	6122.226	Ca I (3)	6344.155	Fe I (169)	6569.224	Fe I (1253)
5525.552	Fe I (1062)	5853.688	Ba II (2)	6136.624	Fe I (169)	6355.035	Fe I (342)	6572.795	Ca I (1)
5528.418	Mg I (9)	5866.461	Ti I (72)	6137.702	Fe I (207)	6358.687	Fe I (13)	6574.252	Fe I (13)
5543.199	Fe I (926)	5867.572	Ca I (46)	6141.727	Ba II (2)	6366.491	Ni I (230)	6575.037	Fe I (206)
5543.944	Fe I (1062)	5883.814	Fe I (982)	6162.180	Ca I (3)	6393.612	Fe I (168)	6581.218	Fe I (34)
5562.716	Fe I (626)	5892.883	Ni I (68)	6166.440	Ca I (20)	6400.009	Fe I (916)	6586.319	Ni I (64)
5567.400	Fe I (209)	5899.304	Ti I (72)	6170.516	Fe I (1260)	6400.323	Fe I (13)	6592.926	Fe I (268)
5569.631	Fe I (686)	5930.191	Fe I (1180)	6173.341	Fe I (62)	6408.026	Fe I (816)	6593.884	Fe I (168)
5572.851	Fe I (686)	5934.665	Fe I (982)	6180.209	Fe I (269)	6411.658	Fe I (816)	6625.039	Fe I (13)
5576.099	Fe I (686)	5956.706	Fe I (14)	6191.186	Ni I (45)	6419.956	Fe I (1258)	6643.638	Ni I (43)
5581.979	Ca I (21)	5965.835	Ti I (154)	6191.571	Fe I (169)	6421.360	Fe I (111)	6663.448	Fe I (111)
5588.764	Ca I (21)	5975.353	Fe I (1017)	6200.321	Fe I (207)	6430.856	Fe I (62)	6677.997	Fe I (268)
5590.126	Ca I (21)	6013.497	Mn I (27)	6215.149	Fe I (1018)	6439.083	Ca I (18)	6710.323	Fe I (34)
5594.471	Ca I (21)	6020.186	Fe I (1178)	6216.358	V I (19)	6449.820	Ca I (19)	6717.687	Ca I (32)
5598.497	Ca I (21)	6021.803	Mn I (27)	6219.287	Fe I (62)	6450.179	Co I (37)	6743.127	Ti I (48)
5601.286	Ca I (21)	6024.068	Fe I (1178)	6230.736	V I (19)	6462.570	Ca I (18)	6750.164	Fe I (111)
5624.558	Fe I (686)	6027.059	Fe I (1018)	6232.648	Fe I (816)	6462.749	Fe I (13)	6945.210	Fe I (111)
5627.642	V I (37)	6039.736	V I (34)	6233.201	V I (20)	6469.192	Fe I (168)		
5641.448	Fe I (1087)	6042.104	Fe I	6237.328	Si I (28)	6471.668	Ca I (18)		

Lines Used for Warmer Stars (ε Aur)

4991.969	S II (7)	5041.024	Si II (5)	5320.723	S II (38)	5639.977	S II (14)	6402.247	Ne I (1)
5001.479	Ca II (15)	5047.738	He I (47)	5428.655	S II (38)	5640.346	S II (11)	6578.050	C II (2)
5009.567	S II (7)	5055.980	Si II (5)	5432.797	S II (6)	5647.020	S II (14)	6582.880	C II (2)
5014.045	S II (15)	5169.033	Fe II (42)	5453.855	S II (6)	5875.685	He I (11)	6678.152	He I (46)
5015.678	He I (4)	5234.625	Fe II (49)	5473.614	S II (6)	5978.930	Si II (4)		O II (85)?
5018.440	Fe II (42)	5276.002	Fe II (49)	5509.705	S II (6)	6347.110	N II (46)	7065.177	He I (10)
5032.434	S II (7)	5316.615	Fe II (49)	5606.151	S II (11)	6371.370	Si II (2)		

Lines for Early B Stars (γ Peg)

4921.929	He I (48)	5015.671	He I (4)	5243.313	Fe III (113)	5676.020	N II (3)	6347.091	Si II (2)
4994.358	N II (24,64)	5045.088	N II (4)	5432.770	S II (6)	5679.560	N II (3)	6371.359	Si II (2)
5005.145	N II (19,6)	5047.736	He I (47)	5453.836	S II (6)	5696.615	Al III (2)?	6402.245	Ne I (1)
5007.316	N II (24)	5143.477	C II (16)	5639.995	S II blend?	5722.723	Al III (2)	6578.030	C II (2)
5009.540	S II (7)	5145.160	C II (16)	5647.004	S II (14)	5739.762	Si III (4)	6582.850	C II (2)
5010.620	N II (4)	5151.080	C II (16)	5659.950	S II (11)	5833.920	Fe III (114)?	6678.149	He I (46)
5014.045	S II (15)	5156.100	Fe II	5666.620	S II (11)	5875.685	He I (11)		

Telluric O2 Lines for Velocity Calibration

6870.946	6876.715	6889.903	6904.117	6919.002
6871.285	6877.637	6892.369	6905.023	6923.369
6872.247	6879.928	6893.300	6908.534	6924.164
6872.843	6883.833	6896.037	6909.431	
6873.798	6885.754	6896.965	6913.200	
6874.653	6886.743	6899.954	6914.090	
6875.590	6888.948	6900.868	6918.122	

Table 2. Stars with solar–type spectra.

HD	V	(B–V)	N	CCF[a]	SP	Name	Notes
352	6.22	1.38	226		K2 III	5 Cet = AP Psc	SB1
571	5.04	0.40	110	eps	F2II	22 And	σ = 0.93
886	2.83	–0.23	1674	*	B2 IV	γ Peg	β Cep
1522	3.56	1.20	96		K1.5III	ι Cet	σ = 0.16
2261	2.37	1.09	41		K0III	α Phe	
3627	3.28	1.28	10		K3III	δ And	SB1
4502	4.06	1.12	229		K1IIe	ζ And	SB1; RS CVn
4656	4.43	1.50	124		K5III	δ Psc	σ = 0.24
5665	8.92	0.96	9		K		
6286	8.24	0.96	319		G2 V	BE Psc	SB1; RS CVn
6833	6.77	1.14	20		G9II		σ = 0.14
6860	2.06	1.58	221		M0IIIa	β And	σ = 0.24
7308	7.63	1.59	10		K5II		
7318	4.68	1.04	18		K0III	φ Psc	
7640	8.46	0.60	14		G		
7672	5.43	0.87	31		G5IIIe	39 AY Cet	
8556	5.92	0.37	93		F3V	HR 404	SB
8890	2.02	0.60	679		F7Ib–II	α UMi = Polaris	Cepheid
9053	3.41	1.57	32		M0IIIa	γ Phe	SB
9312	6.78	0.93	29		G5		
9352	5.70	1.52	61		K0Ib+B9V	HR 439	
9828	8.74	1.28	13		K0		SB1
9927	3.57	1.28	63		K3–III	υ Per	σ = 0.20
9939	6.99	0.91	45		K0I		SB1
10588	6.32	0.86	9		G8III–IV	HR 503	SB1
11353	3.74	1.13	28		K0III	ζ Cet	SB1
11636	2.64	0.13	21		A5V	β Ari	SB1
11909	5.11	0.90	12		K1Vp	ι Ari	SB1
12533	2.26	1.37	83		K3–IIb	γ^1 And	σ = 0.24
12641	5.96	0.83	31		G5II–III	61 Cen	SB1
12642	5.62	1.59	154		M1 //I		σ = 0.24
12923	6.29	0.89	19		K0	HR 616	SB1
12929	2.00	1.15	167		K2IIIab	α Ari	σ = 0.13
13974	4.90	0.58	105		G0.5V	δ Tri	SB1
14214	5.60	0.59	289		G0.5IV	HR 672	SB1
14985	8.83	1.23	20		K2		SB1
16620	4.82	0.43	34		F5V	ε Cet	SB1 σ = 0.27
16909	8.30	1.07	17		K		SB1?
17094	4.20	0.18	29		F0IV	μ Cet	δ Sct
17433	6.76	0.96	104		K0	VY Ari	SB1; RS CVn
17709	4.53	1.56	86		K7III	17 Per	
18778	5.91	0.17	104	eps	A7III–IV	HR 906	SB1; σ = 0.33
18884	2.53	1.64	150		M1.5IIIa	α Cet	LPV; σ = 0.26
19058	3.39	1.65	94		M4II	ρ Per	LPV; σ = 1.01
19476	3.80	0.98	69		K0III	κ Per	SB1?
20084	5.62	0.87	19		G3IIp+	HR 965	
20210	6.25	0.29	49		A1m	V423 Per	SB1
20394	8.74	1.07	16		G9III		SB1
20902	1.82	0.47	196		F5Ia	α Per	
21018	6.40	0.82	28		G5III	HR 1023	
21120	3.62	0.88	31		G6III	o Tau	SB1
21552	4.36	1.35	54		K3III	σ Per	
21754	4.14	1.11	92		K0Iab	5 Tau	SB1
22649	5.12	1.67	169		S3	BD Cam	SB1; symbiotic
22905	6.35	0.86	37		G8/K0III	HR 1120	SB1
23249	3.52	0.92	15		K0III–IV	δ Eri	RS CVn
25408	7.62	1.16	18		C5,3	UV Cam	Carbon star
25604	4.36	1.07	119		K0III	37 Tau	σ = 0.15
26630	4.14	0.94	54		G0Ib	μ Per	SB1
26673	4.71	1.01	71		G5Ib+A2V	52 Per	SB
27697	3.76	0.99	26		K0III	δ^1 Tau	SB1
28394	7.01	0.47	25		F8V		SB1
29094	4.25	1.18	46		K4III+...	58 Per	SB1
29139	0.85	1.54	147		K5III	α Tau	LPV?; σ = 0.23
29317	5.09	1.08	11		K0III	3 Cam	Cepheid
30050	7.79	0.65	461		Am+K0 IV	RZ Ari	SB1; RS CVn
30197	5.99	1.22	18		K4III	HR 1517	SB1

Table continued on following pages

Table 2. Stars with solar–type spectra, cont.

HD	*V*	*(B–V)*	*N*	*CCF[u]*	*SP*	*Name*	*Notes*
30282	7.51	0.95	6		F0	AW Per	Cepheid
31398	2.69	1.52	172		K3II	ι Aur	σ = 0.23
32068	3.75	1.25	494		K4II+B8V	ζ Aur	SB1; ζ Aur
32357	6.25	0.95	446		K0 III	12 BM Cam	SB1; RS CVn
33254	5.43	0.24	25		A2m	16 Ori	SB1
33856	4.45	0.19	36		K0.5III	ρ Ori	SB1
34029	0.08	0.80	117		G5IIIe+?	α Aur = Capella	SB1; RS CVn
34085	0.12	–.03	1626	**	B8Ia	β Ori = Rigel	
34334	4.55	1.28	8		K2.5IIIb	16 Aur	SB1
36167	4.71	1.57	150		K5III	31 CI Ori	σ = 0.20
36389	4.38	1.92	149		M2Iab–Ib	119 CE Tau	SRV
36859	6.28	1.56	24		K0	HR 1878	SB1
38099	6.33	1.48	30		K4III	V1197 Ori	Ellipsoidal var
39801	0.50	1.85	331		M1–2Ia–Iab	α Ori	
41116	4.16	0.87	649		G7III	1 Gem	SB1
42995	3.28	1.61	129		M3III	η Gem	SRV
43039	4.35	1.02	105		G8.5IIIb	κ Aur	σ = 0.14
43282	7.76	1.31	31		G5II		SB1
43821	6.24	0.84	30		K0	HR 2259	SB1
43905	5.33	0.40	149		M6III	45 Aur	SB1
43930	7.64	1.07	33		K1V	260 Ori	SB1; RS CVn
44478	2.88	1.64	159		M3IIIab	μ Gem	LPV
44537	4.91	1.97	78		K5–M0I	ψ^1 Aur	
44762	3.85	0.85	38		G7II	δ Col	SB1
44990	5.98	1.22	607		G3 Iab+A0	T Mon	SB1; Algol bin
45168	6.33	1.02	39		G9III	HR 2317	SB1
45910	6.74	0.23	361		gK+B2 III	AX Mon	SB1
46407	6.27	1.12	41		G9.5III	HR CMa	SB1; Algol
48329	2.98	1.40	228		G8Ib	ε Gem	σ = 0.32
49293	4.48	1.12	38		K0IIIa	18 Mon	SB1
51956	7.52	0.76	39		F8I		var RV
52973	3.79	0.79	200		F7–G3Ib	ζ Gem	Cepheid
54716	4.90	1.45	97		K4III–II	63 Aur	
55496	8.40	0.90	35		GII(Ba*)		HV*; σ = 0.31
55751	5.35	1.19	174		K2II	HR 2729	σ = 0.20
58972	4.34	1.44	93		K3III	γ CMi	SB1
59148	5.02	1.12	24		K2III	65 Gem	SB1
59643	8.01	2.18	58		R9	NQ Gem	symbiotic
59693	6.8	1.1	37		K0Ibp	U Mon	RV Tau; H-α em; shallow lines
59878	6.52	0.96	35		K0II–III	HR 2879	SB1
60414	4.97	1.37	40		M2III	KQ Pup	H-α em
60522	4.06	1.54	139		M0III–II	υ Gem	
61421	0.40	0.43	60		F5IV–V	α CMi	SB1
61994	7.08	0.67	28		G6V		SB1
62044	4.28	1.12	665		K1 III	σ Gem	SB1; RS CVn
62345	3.57	0.93	205		G8IIIa	κ Gem	SB
62509	1.14	1.00	175		K0IIIb	β Gem	σ = 0.12
62522	7.03	0.54	12		F5		noisy
62721	4.88	1.49	33		K4III	81 Gem	SB1
65339	6.02	0.16	9	eps	A2p		α^2 CVn var
66216	4.94	1.14	31		K2III	χ Gem	SB1
68256	6.2	0.6	33		G5V	ζ^2 Cnc	SB1
69148	5.73	0.88	8		G8III	OS UMa	SB1; Algol
69267	3.52	1.48	223		K4III	β Cnc	σ = 0.21
73974	6.92	0.96	41		K0II		SB1
74442	3.94	1.08	148		K0III–IIIb	δ Cnc	σ = 0.14
74874	3.38	0.68	192		G5III	ε Hya	SB1; BY Dra
75289	6.36	0.58	33		F9V	HR 3497	HPM*; σ = 0.11
75958	5.57	0.86	11		G6III	6 UMa	SB1
76294	3.11	1.00	175		G9II–III	ζ Hya	σ = 0.14
76943	3.97	0.44	64		F5V	10 UMa	SB1; σ = 0.38
77247	6.86	0.99	25		G7III	PV UMa	SB1
77912	4.54	1.03	16		G7IIa	HR 3612	σ = 0.18
78362	4.65	0.34	47		Am	τ UMa	SB1
78515	5.15	0.97	38		G9III	ξ Cyg	SB1
78712	5.95	1.67	115		M6 IIIS	RS Cnc	SRV
79096	6.77	0.77	46		G9V	π^1 Cnc	SB1; peculiar velocities

Table continued on following pages

Table 2. Stars with solar–type spectra, cont.

HD	V	(B–V)	N	CCF[a]	SP	Name	Notes
79910	5.24	1.19	56		K2III	23 Hya	SB1
80493	3.13	1.52	164		K7IIIab	α Lyn	σ = 0.22
81025	6.37	0.87	26		G2III	HR 3725	SB1; double
81797	1.98	1.44	247		K3II–III	α Hya	σ = 0.20
81809	5.40	0.62	45		G2V	HR 3750	SB1
82674	6.26	1.17	48		K2III	HR 3805	SB1
83240	5.01	1.04	44		K1III	10 Leo	SB1
84441	2.98	0.80	242		G1II	ε Leo	σ = 0.13
85622	4.59	1.19	34		G5Ib	m Vel = HR 3912	SB1
88284	3.61	1.01	48		K0III	λ Hya	SB1
89758	3.05	1.59	138		M0III	μ UMa	SB1
90537	4.22	0.89	39		G9IIIb	β LMi	SB?; noisy σ = 0.14
92214	4.91	0.90	53		G8III	φ^3 Hya	SB1
93813	3.11	1.25	190		K2III	ν Hya	σ = 0.18
94363	6.12	0.90	52		K0III+...	HR 4249	SB1
95689	1.79	1.07	28		G9III+A7	α UMa	SB1
96833	3.01	1.15	115		K1III	ψ UMa	σ = 0.15
97528	7.31	0.12	103		A1+K0	TT Hya	SB1; Algol bin
97907	5.32	1.20	45		K3III	73 Leo	SB1
98231	4.41	0.59	40		G0V	ξ UMa A	SB1
99028	4.00	0.35	53	eps	F4IV	ι Leo	SB1; σ = 0.20
99967	6.32	1.27	29		K0V	EE UMa = HR 4430	SB1
101013	6.12	1.07	33		G9III	HR 4474	SB1
101606	5.70	0.46	33		F4V	62 UMa	SB1
102212	4.03	1.51	175		M1IIIab	ν Vir	LPV
102509	4.54	0.51	49		F8III+A7V	DQ Leo	SB1; RS CVn
102928	5.64	1.03	48		K0III	HR 4544	SB1
105981	5.67	1.43	44		K4III	4 Com	SB1
105982	6.74	1.00	38		K0III		SB1
106760	5.00	1.15	33		K0.5IIIb	HR 4668	SB1
110024	5.49	0.96	48		G9III	26 Com	SB1
112048	6.45	1.09	70		K0	HR 4896	SB1
112300	3.38	1.58	169		M3III	δ Vir	σ = 0.40
112769	4.78	1.56	154		M1IIIb	36 Com	
113226	2.83	0.94	176		G8IIIab	ε Vir	σ = 0.11
115521	4.80	1.67	168		M2IIIa	σ Vir	var
116594	6.44	1.07	39		K0III	HR 5053	SB1
119458	5.99	0.85	28		G5III	HR 5161	SB1
120064	5.97	0.52	37		F6IV–V	3 Boo	SB1
120539	4.93	1.40	44		K4III	6 Boo	SB1
121370	2.68	0.58	49		G0IV	ε Boo	SB1
121844	7.89	1.13	40		K1III		SB1
122223	4.34	0.57	51		F6II	υ^2 Cen	SB1
122563	6.20	0.90	55		F8IV	HR 5270	σ = 0.39
124547	4.81	1.39	13		K3III	4 UMi	SB1
124897	0.04	1.23	201		K1III	α Boo	σ = 0.21
125351	4.81	1.05	29		K0III	A Boo	SB1
127665	3.58	1.30	129		K3III	ρ Boo	σ = 0.20
129132	6.14	0.37	53		G0V	HR 5472	SB; spectra noisy
129333	7.61	0.79	22		G0V	EK Dra	BY Dra
129989	2.70	1.00	153		K0II–III	ε Boo	
131511	6.00	0.84	23		K2V	DE Boo	SB1; RS CVn
133208	3.50	0.97	76		G8IIIa	β Boo	flare star; σ = 0.16
133640	4.76	0.65	125		G2	44 i Boo C	Brightest comp.; σ = 0.16
134320	5.67	1.25	31		K2III	46 Boo	SB1
137052	4.93	0.41	57		F5IV	ε Lib	SB1
137107	5.58	0.58	34		G2V	η CrB	SB1
139195	5.26	0.94	37		K0IIICNs	16 Ser	SB1
140538	5.86	0.68	94		G2.5V	ψ Ser	HPM*; σ = 0.11
142267	6.10	0.60	43		G0V	39 Ser	SB1
144889	6.19	1.36	31		K4III	HR 6005	SB1
145206	5.40	1.45	38		K4III	HR 6016	SB1
145849	5.64	1.37	15		K3III	HR 6046	SB1
145931	5.87	1.45	70		K4II+F6–8V	HR 6050	σ = 0.21
146051	2.74	1.58	171		M0.5III	δ Oph	
147395	6.61	1.56	24		M2III		SB1
147508	7.38	1.35	42		K2		SB1

Table continued on following pages

Table 2. Stars with solar–type spectra, cont.

HD	*V*	*(B–V)*	*N*	*CCF[a]*	*SP*	*Name*	*Notes*
148783	5.04	1.52	77		M6III	g Her	SRV
148856	2.77	0.94	146		G7IIIa	β Her	SB1
150050	6.72	1.30	61		K0 III		σ = 0.18
150680	2.8	0.0	40		G0 IV–V	ζ Her	SB1
155410	5.08	1.29	12		K3III	HR 6388	SB1
156014	3.48	1.44	237		M5Ib–II	α Her	
156283	3.16	1.44	96		K3IIab	π Her	σ = 0.24
157999	4.34	1.50	158		K2II	σ Oph	σ = 0.23
158614	5.31	0.72	47		G9IV–V	HR 6516	SB1; σ = 0.25
158837	5.59	0.81	41		G8III	HR 6524	SB1
159181	2.79	0.98	80		G2Ib–IIa	β Dra	σ = 0.20
160346	6.52	0.96	41		K3V		SB1
161471	3.02	0.47	54	eps	F2Iae	ι[1] Sco	emission-line star
161832	6.68	1.39	13		K3III+...	V826 Her	SB1
162338	7.19	0.46	21		G0		SB1; σ = 0.58
162596	6.32	1.13	40		K0	HR 6659	SB1
162714	6.18	1.33	43		F8Iab	Y Oph	Cepheid
163506	5.47	0.33	28	eps	F2Ibe	89 Her	post–AGB
163770	3.86	1.39	81		K1IIa	θ Her	σ = 0.24
164058	2.23	1.52	69		K5III	γ Dra	σ = 0.19
164975	4.66	0.33	51		F7.2Ib	W Sgr	Cepheid
165195	7.34	1.29	47		F6/7p	V256 Oph	LPV?
165341	4.03	0.86	41		K0V	70 Oph	BY Dra; σ = 0.14
168532	5.29	1.56	30		K4Iab	105 Her	SB1
168723	3.26	0.94	168		K2IIIab	η Ser	
169156	4.67	0.95	33		G9IIIb	ζ Sct	SB1
169690	5.67	0.85	92		G8III–IV+?	V2291 Oph = HR6902	SB1
169985	5.21	0.50	42		G0III+...	59 Ser	SB1
170153	3.55	0.49	17		F7Vvar	χ Dra	SB1
170547	6.28	0.93	38		G8II–III	HR 6940	SB1
170829	6.50	0.79	75		G8IV	HR 6950	SB1
172831	6.14	1.00	37		K0.5III	HR 7024	SB1
172865	6.94	0.79	19		G5III–IV		SB1; σ = 0.13
173093	6.3	0.42	54		F7 V		SB1
173297	7.47	0.86	103		F8 Ib–II	V350 Sgr	Cepheid
173764	4.22	1.12	197		G4II+B9.5	β Sct	SB1
174208	6.00	1.60	37		K2Ib	HR 7083	SB1
175515	5.58	1.04	25		G9III	HR 7135	SB1
175865	4.13	1.59	23		M5III	13 R Lyr	SRV
176155	5.31	0.54	61		F5Iab	FF Aql	Cepheid
176411	4.03	1.06	43		K1III	ε Aql	SB1
178428	6.07	0.70	70		G5V	HR 7260	SB1
180809	4.36	1.26	47		K0II	θ Lyr	σ = 0.15
181330	6.81	1.82	14		K5		SB1
181391	5.00	0.92	104		G8III	f Aql	SB1
182593	7.00	1.15	6		K0		SB1
182989	7.4	0.3	124		F5	RR Lyr	RR Lyr
183344	6.37	0.95	28		F8Ib–II	U Aql	Cepheid
183439	4.44	1.50	119		M0III	α Vul	
183864	7.38	1.18	24		G2I		SB1
183912	3.08	1.13	192		K3II+B0.5V	β Cyg	
185662	7.37	1.48	16		K2		SB1
186791	2.72	1.52	229		K3II	γ Aql	
187076	3.82	1.41	190		M2II+A0V	γ Sge	SB1; ζ Aur
187299	7.17	1.53	30		G5Ia0–Ia		SB1
187929	3.88	0.74	218		F6Iab	η Aql	Cepheid
188507	6.74	1.55	23		K4II–II		SB1
188727	5.72	0.88	29		G5Ib	S Sge	RV Tar var
188981	6.28	1.06	45		K1III	HR 7612	SB1
189319	3.47	1.57	123		M0III	γ Sge	σ = 0.27
189340	5.88	0.58	31		F8V		SB? σ = 0.16
190658	6.41	1.68	28		M2.5III	V1472 Aql	SB1; SRV?
192577	3.79	1.28	376		K3 Ib+B2	31 Cyg	SB1; ζ Aur
192713	5.15	1.06	161		G3Ib–II	22 Vul	SB1; ζ Aur
192876	4.24	1.07	155		G3Ib	α[1] Cap	σ = 0.22
192909	3.98	1.55	548		K3Ib+B3V	32 Cyg	SB1; ζ Aur
193370	5.18	0.61	7		F5Ib	35 Cyg	SB1

Table continued on next page

Table 2. Stars with solar–type spectra, cont.

HD	V	(B–V)	N	CCF[a]	SP	Name	Notes
193495	3.08	0.79	194		K0II+...	β[1] Cap	SB1
193664	5.93	0.60	22		G3V		HPM*; σ = 0.08
194184	6.10	1.39	30		K3III	HR 7799	SB1
194215	5.86	1.10	44		G8II–III	HR 7801	SB1
194317	4.43	1.33	71		K3III	39 Cyg	SB
196093	4.61	1.60	129		K2Ib+B3V	47 Cyg	SB1
196321	4.89	1.60	138		K5II	70 Aql	SB?
196574	4.33	0.96	45		G7.5III	l Aql	SB1
196795	7.88	1.23	32		K5Va	OQ Del	SB1; BY Dra
197345	1.25	0.09	134	eps	F2Iae	α Cyg	σ = 1.92
197752	4.93	1.18	16		K2III	30 Vul	SB1
197989	2.46	0.99	146		K0III	ε Cyg	SB?
200428	7.69	0.91	28		G5		SB1
200905	3.72	1.65	66		K4–5Ib–II	ξ Cyg	σ = 0.38
201251	4.55	1.57	40		K4Ib–IIa	63 Cyg	σ = 0.21
201626	8.13	1.07	22		R5–CH		SB?; CH star
202109	3.20	0.99	94		G8III–IIIa	ζ Cyg	SB1
202448	3.95	0.50	41		G6II+B9.5V	α Equ	SB1
203504	4.09	1.11	23		K1III	1 Peg	HPM*; σ = 0.14
203631	7.60	1.59	19		K5		SB1
204075	3.75	1.00	31		G4Ib	ζ Cap	SB1
204724	4.57	1.62	107		M1III	2 Peg	σ = 0.33
204867	2.91	0.83	155		G0Ib	β Aqr	σ = 0.22
206778	2.39	1.53	235		K2Ib	ε Peg	LPV
206859	4.34	1.17	115		G5Ib	9 Peg	σ = 0.21
207098	2.83	0.28	34	eps	F0mF2III	δ Cap	SB; Algol bin
208816	5.18	1.55	34		M2Iape+B8	VV Cep	SB1; ζ Aur
209750	2.96	1.04	162		G2Ib	α Aqr	σ = 0.25
209813	6.96	1.05	41		K0III...	HK Lac	SB1; RS CVn, noisy
210745	3.35	1.57	53		K1.5Ib	ζ Cep	
211388	4.13	1.46	72		K3II–III	1 Lac	σ = 0.23
212943	4.78	1.04	125		K0III	35 Peg	σ = 0.16
213306	3.75	0.40	79		F5Ib–G2I	δ Cep	Cepheid
213310	4.36	1.68	104		M0II+B8V	5 Lac	
213389	6.43	1.17	35		K2III	V350 Lac	SB1; RS CVn
213428	6.16	1.07	20		K0III	HR 8580	SB1
213429	6.17	0.52	33		F7V	HR 8581	SB1
215182	2.94	0.80	81		G2II–III	η Peg	SB1
215648	4.20	0.49	199		F6III–IV	ξ Peg	σ = 0.13
216131	3.48	0.93	97		G8III	μ Peg	σ = 0.12
216489	5.64	1.12	960		K1III	IM Peg	RS CVn
216946	4.95	1.78	111		K5Ib	V424 Lac	LPV
217014	5.49	0.67	144		G2.5IVa	51 Peg	double?; σ = 0.11
217188	7.43	1.01	25		K0III	AZ Psc	SB1; RS CVn
217476	5.00	1.42	37	eps	G4 0++B1	V509 Cac	SB1; ζ Aur?
217580	7.46	0.95	27		K3V		SB1
217906	2.42	1.67	168		M2.5II–III	β peg	LPV
219615	3.69	0.92	126		K0III	γ Psc	σ = 0.11
219834	5.19	0.79	26		G6/G8IV	94 Aqr	SB1
221170	7.71	1.09	20		G2 IV		σ = 0.13
222107	3.82	1.08	217		G8III	λ And	SB1; RS CVn
222516	6.99	0.43	13		F5		σ = 0.38
224014	4.54	1.22	72		G2 0e	ρ Cas	
224935	4.41	1.63	165		M3III	YY Psc	30 Psc Var
225212	4.94	1.63	195		K3Ibv	3 Cet	σ = 0.37
500001	8.26	0.72	67		G5IV	LX Per	SB1; RS CVn

[a]*Note (column 5): "eps", line list for ε Aur; "**", line list for β Ori; "*", line list for γ Peg.*

Table 3. Double-lined spectroscopic binaries.

HD	*V*	*(B–V)*	*N*	*SP*	*Name*	*Notes*
483	7.17	0.63	53	G2III		SB2
5516	4.40	0.94	13	G8III	η And	SB2
17841	8.4	0.8	33	K		SB2
22468	5.91	0.85	149	G9V	V711 Tau	RS CVn
64096	5.16	0.60	41	G2V	9 Pup	SB2
66751	6.5	0.6	15	F8V		SB2; hpm*
93765	6.06	0.34	69	F3V	44 LMi	SB2
157948	8.10	0.76	22	G5		SB2
166285	5.69	0.47	25	F5V	HR 6797	SB2
202275	4.49	0.50	31	F5V	δ Equ	SB2
205539	6.25	0.36	133	F0IV		SB2 Fekel *et al.* (2009)
206301	5.18	0.65	159	G2V	BY Cap	SB2; wk 2. line; RS CVn
210334	6.13	1.0	535	G2 IV+F	AR Lac	RS CVn
214608	6.83	0.55	32	F9V		SB2
214686	6.89	0.51	85	F7V		SB2 Tomkin and Fekel (2008)
218738	7.91	0.90	60	K0Ve	KZ And	SB2 BY Dra
219113	7.44	1.0	385	K4 IV-V+F	SZ Psc	SB2 RS CVn

Table 4. Stars with molecular lines.

HD	*V*	*(B–V)*	*N*	*CCF*	*SP*	*Name*	*Notes*
14386	3.04	1.42	141	self	M7IIIe	o Cet = Mira	Mira
16115	8.15	1.21	57	self	C2,3		C star; sig = 0.59
39816	6.70	2.00	82	self	M6.5IIIe	U Ori	Mira
132813	4.71	1.47	7	self	M4.5III	RR UMi	LPV; treat as M star
141850	7.1	1.39	82	self	M7IIIe	R Ser	Mira
182040	7.00	1.02	90	self	C1,2		CH star
223075	5.04	2.70	61	self	CII...	TX Psc	var C star

Table 5. Files Included in AST-RVs-JAAVSO-481.tar.

File Name	*Contents*
AST-RVs T1 LineLists.txt	Lines used to measure the radial velocities.
AST-RVs T2 SOLAR.txt	ASCII table of stars with single-lined photospheric spectra.
AST-RVs T3 SB2.txt	ASCII table of double-lined spectroscopic binaries.
AST-RVs T4 MOLEC.txt	ASCII table of stars with dominant molecular spectra.
AST-RVs ET1 SOLAR-RVs.txt	Data table of radial velocities for single-lined stars with solar-type photospheric spectra.
AST-RVs ET2 SB2-RVs.txt	Data table of radial velocities for double-lined binaries.
AST-RVs ET3 MOLEC-RVs.txt	Data table of radial velocities for stars with molecular spectra.
AST-RVs plots.tar	Plots (hd*.jpg) of the RVs vs. JD or phase for all the stars.
extract-RVs-for-HD.f	A FORTRAN program for extracting the velocities for a star, specified by its HD number, from the archive files.

Table 6. Published papers related to the data presented in this paper.

HD	*Name*	*Reference*
352	5 Cet	Eaton (2008)
886	γ Peg	Handler *et al.* (2009)
8890	α UMi = Polaris	Bruntt *et al.* (2008)
32068	ζ Aur	Eaton *et al.* (2008)
34085	β Ori = Rigel	Moravveji (2012)
45910	AX Mon	Eaton (2008)
97528	TT Hya	Eaton (2008)
173297	V350 Sgr	Evans *et al.* (2011)
205539		Fekel *et al.* (2009)
216489	IM Peg	Marsden *et al.* (2007)
192577	31 Cyg	Eaton *et al.* (2008)
192909	32 Cyg	Eaton *et al.* (2008)
192713	22 Vul	Eaton and Shaw (2007)
214686		Tomkin and Fekel (2008)

Abstracts of Papers and Posters Presented at the 108th Annual Meeting of the AAVSO, Held in Las Cruces, New Mexico, October 18–21, 2019

50th Anniversary of the Moon Landing, Personal Stories from Inside the Mission Control Center

Gordon Myers
5 Inverness Way, Hillsborough, CA 94010-7214; gordonmyers@hotmail.com

This July we celebrated the 50th anniversary of landing on the moon. It was a momentous accomplishment. In just twelve years we went from launching our first satellite to Armstrong stepping onto the lunar surface. Why did we go? What drove the decision for President Kennedy to announce such a challenging goal? How did the technology of that era—so antiquated when we look back today—enable us to achieve the goal? The presentation will take us back to 1950s America and the shock of Russia's early space achievements. It will describe how the U.S. developed the technology to get us to the moon and you'll hear personal stories describing what it was like working in the Mission Control Center

Novae Erupting within Symbiotic Binaries: Getting Ready for Coming Fireworks

Ulisse Munari
Vicolo dell'Osservatorio 5, Padova, I-35122, Italy; ulisse.munari@oapd.inaf.it

In a classical nova, once launched at high speed the ejecta continue their expansion unimpeded in the surrounding void forever. If the nova occurs on a WD orbiting within the thick wind of a cool giant or a Mira, i.e. in a symbiotic binary, the ejecta slam onto the pre-existing circumstellar material and are rapidly decelerated, with consequent emission of very high energy GeV gamma-rays and a lot of other awesome exotica. But this is just one of many different types of outbursts that a symbiotic binary may undergo, including a final one as a Type Ia Supernova, offering endless opportunities for fun as well as intriguing science to the keen observer. I'll review the nature of symbiotic binaries and of their outbursts in particular, and if we—as a global pro/am community—are truly ready for the anticipated coming ones. I'll do that primarily from the perspective of the advanced amateurs, those who carry out fully transformed multi-band photometry and master pro-level spectroscopy.

The Frontiers of RR Lyrae and Cepheid Variable Star Research

Karen Kinemuchi
Apache Point Observatory, P.O. Box 59 2001, Apache Point Road, Sunspot, NM 88349; kinemuchi@apo.nmsu.edu

I will present highlights of the RRL/Cep 2019 Conference: Frontiers of Classical Pulsators—Theory and Observations, held in Cloudcroft, New Mexico. This conference is a biannual gathering of astronomers to discuss our favorite stars, the RR Lyrae and Cepheids. With datasets coming from a variety of ground and space based projects, new discoveries as well as new questions are formed for classical pulsator science. In my overview, I will briefly cover some of these exciting results from the conference.

Applying Transformations

George Silvis
194 Clipper Road, Bourne, MA 02532-3525; gasilvis@gmail.com

Applying transformation coefficients to your photometric data corrects your magnitudes to the desired standard system (e.g., Johnson-Cousins BVRI). It can also be used to move a near-BVR system like that of a DSLR to the standard BVR. This presentation describes the concepts and reviews how transform coefficients are derived and applied. And most importantly, how they affect your data! It will showcase a new VPHOT feature to show how easy it is to work the transformation process into your workflow. You will walk out of the meeting ready to transform your observations to generate more accurate magnitudes.

O–C Diagrams

Gary Billings
P.O. Box 263, Rockyford, Alberta T0J 2R0, Canada; obs681@gmail.com

The O–C ("observed minus computed") diagram is a simple concept: fit the observational data with a model and examine the quality of the fit. That is, for all the observed datapoints, such as the times of eclipses of an eclipsing binary star, or times of maximum of a pulsator, subtract the times the model would predict, and then plot those "residuals" of the model fit. This allows one to magnify the residuals and study them. Patterns in the residuals may explain how the system has changed, how the model should be adjusted, or whether a different form of model should be used. This discussion presents the concept, describes the mathematical procedure and techniques to calculate this term, and provides specific examples to explain what certain patterns mean in the study of eclipsing binary systems.

AAVSO Bright Star Monitor Update

Ken Menzies
Mike Nicholas
address correspondence to Ken Menzies, 318A Potter Road, Framingham, MA 01701; kenmenstar@gmail.com

The purpose of the AAVSO Bright Star Monitor Section is to provide members with observational resources and encouragement to perform research, prepare scientific papers, and enhance their photometry skills. It supports the AAVSO Mission of global observing, promoting science research and public outreach. The AAVSO Bright Star Monitor (BSM) telescopes are a subset of the larger AAVSOnet network which are located at sites around the world. Each BSM site is equipped with a small refractor, a high grade astronomical camera (SBIG CCD / ZWO CMOS), and standard Astrodon photometric filters. They are operated robotically and are locally supported by AAVSO member volunteers. Each telescope can perform precise photometric measurements of the sky's relatively bright stars, those in the range of 3 to 13 V magnitude. It is free to use by all AAVSO members.

Czech Pulsational and Exoplanetary Group

Marek Skarka
Mendlovo nam. 13, Brno, 60300, Czech Republic; marek.skarka@gmail.com

The observation of variable stars has a long tradition in the Czech Republic. I will briefly introduce the activities within the Czech Variable Stars and Exoplanet Section of the Czech Astronomical Society. However, I will mainly focus on introducing a newly established group dedicated to the observation of pulsating stars and exoplanets that was founded in cooperation with citizen astronomers and students at the Masaryk University, Brno. I would like to attract the attention of American observers and will show how our project can benefit from a joint effort.

An Introduction to Observing Sections

Bert Pablo
AAVSO, 49 Bay State Road, Cambridge, MA 02138; hpablo@aavso.org

I will present a comprehensive overview of the observing sections which exist at the AAVSO and how you can be more involved.

R Aqr—the 2022 Eclipse Has Started!

Lee Anne Willson
5326 Springbrook Drive, Ames, IA 50014; lwillson@iastate.edu

The R Aqr symbiotic system consists of a Mira variable plus a companion that is presumably a white dwarf. Most of the time the light curve shows the pulsation of the Mira. However, every 44 years there is an event that distorts the light curve for about six cycles. Around 1978 this event reduced the brightness of the system while leaving the pulsation period of the Mira unchanged. In 1934 there was a dimming of maximum and a brightening of minimum. In 1981 Willson, Garnavich, and Mattei (*IBVS* 1961) proposed that the reason for the dimming is a partial eclipse of the Mira by an opaque source, and that the system has a 44-year orbital period, with a predicted next eclipse centered on 2022. In the interim, an orbit has been derived by Gromadzki and Mikołajewska (2009, *A&A* 495, p. 931); this has an eccentric orbit (e = 0.25) with periastron and eclipse occurring at nearly the same time, and with an orbital period of 43.6 years. A low minimum about three years ago prompted an alert to AAVSO members that has resulted in excellent coverage of the last three cycles, including BVRI photometry. The current cycle is so far depressed by about 2 magnitudes, again with normal light curve shape for the Mira. In addition, the R and I colors are also down by about the same amount, consistent with an opaque object eclipsing the Mira. For the eclipse to last six years and block more than 80% of the light means we are looking at a large structure. Is it an accretion disk around the companion, or an opaque flow between the two stars? Will this event include a brightening of minimum or just a depression of the light curve? The stars are too widely separated for Roche lobe overflow, but the Mira, with period 386 days, is expected to have a heavy wind, and this could lead to enhanced accretion near periastron. This poster will include our analysis of the light curve and discussion of possible models for the ongoing event in this unique system.

The Challenges of Updating VSX in the Survey Era

Sebastián Otero
AAVSO, 49 Bay State Road, Cambridge, MA 02138; sebastian@aavso.org

Keeping the world's largest variable star database up to date is not a trivial task. Even when one may think that in the internet era information is readily available everywhere to everyone, although that might sound true, reality is very far from that ideal. The VSX Team struggles with different problems every day in order to improve the quality and completeness of our metacatalogue. In this talk we highlight examples of the problems we find every day when dealing with large (or not so large) datasets—lack of information, formatting issues, evidently wrong information as a result of automated analysis (wrong periods, wrong types), blending due to a large pixel size resulting in incorrect identifications or spurious variability due to light contamination, and more. We also discuss the increasing number of sources that should be checked and the time and resources involved in such enormous task. We finally showcase the good things that may happen when dealing with these datasets, like correcting wrong identifications that were adopted for decades, or receiving new discoveries of interesting variable stars that are submitted to VSX by people like you.

How to Use VSX

Sebastián Otero
AAVSO, 49 Bay State Road, Cambridge, MA 02138; sebastian@aavso.org

VSX is one of the key tools of the AAVSO. One of the things that makes it special is that anybody anywhere can contribute to it. It is a living database with the aim of showing up-to-date information on variable stars. In this workshop we will describe the data you can find in VSX and will show you different ways in which you can contribute to make it more complete and accurate.

Human and Environmental Effects of Light Pollution

Mario Motta
19 Skipper Way, Gloucester, MA 01930-14; mmotta@massmed.org

As a past AAVSO president, I share the AAVSO's concern for preserving dark skies, and I have been active in light pollution (LP) issues for over 30 years. When I was elected and served for 8 years to the American Medical Association's (AMA) council on science and public health, I was able to initiate AMA reports that eventually became and remain AMA policy on light pollution as a public health issue. I have now been elected to the AMA Board of Trustees, and will present current AMA policy on LP issues. This policy has dramatically altered the initial environmentally toxic plans for widespread LED light conversion worldwide. The inherent energy efficiency of LED lighting makes the push for conversion on purely economic reasons for many municipalities and states. The lower energy use results in a lower air pollution burden as much of the energy produced is based on fossil carbon fuels. Taxes to pay for this energy use are proportionally reduced as well. Furthermore, maintenance costs are reduced due to longer LED lamp life. Not all LED light is optimal, however, when used as street lighting. The design of the lighting fixture can result in glare if designed improperly, and thus create a road hazard condition. In some white LED lighting the color spectrum produces too much blue wavelength. This contributes to disability glare as this scatters more in the human eye. Excessive blue at night suppresses the hormone Melatonin with subsequent deleterious health effects. The excessive blue spectrum is particularly environmentally problematic to many nocturnal species. 60% of animals are nocturnal and potentially are affected adversely by exposure to nighttime electrical lighting. Thus there are significant human and environmental concerns in regards to short wavelength LED emission. I will present the data and resources for use by AAVSO members to make use this information for LP advocacy.

Period Changes and the Evolution of Type II Cepheids

Horace A. Smith
Wayne Osborn
Grzegorz Kopacki
Pradip Karmakar
Barton Pritzl
Nathan De Lee
Charles Kuehn
Aaron LaCluyze
Katie Rabidoux
address correspondence to Horace A. Smith, 2406 Burcham Drive, East Lansing, MI 48823; smith@pa.msu.edu

Type II Cepheids are believed to be evolved, low-mass stars. Observed rates of period change for these variables provide important tests for theoretical models of their evolution. If we consider those short-period type II Cepheids (sometimes called BL Her stars) which are metal-poor, we find that observed rates of period change are broadly consistent with predictions that they are stars evolving from the blue horizontal-branch toward the asymptotic red giant branch. There are, however, irregular variations in the rates of period change that are not predicted theoretically, and some of the details of the evolutionary models do not always match observations. Longer-period type II Cepheids (called W Virginis stars) have sometimes been understood to be stars undergoing loops to the blue from the asymptotic red giant branch caused by thermal pulse instabilities. However, not all theoretical models predict such loops. Some W Virginis variables exhibit period changes consistent with those from the loop models, but others show more irregular period fluctuations.

Modeling Cepheid Variable Stars Using the Open-Source MESA Code

Joyce A. Guzik
Ebraheem Farag
Jakub Ostrowski
Nancy Evans
Hilding Neilson
Sofia Moschou
Jeremy Drake
address correspondence to Joyce A. Guzik, 432 Pruitt Avenue, White Rock, NM 87547; joyceannguzik@gmail.com

Cepheid variable stars are core helium-burning stars of around 4 to 15 solar masses that show radial pulsations with typical periods of a few days to a few weeks, and magnitude variations of a few tenths to up to 2 magnitudes per pulsation cycle. Cepheids are well within the reach of amateur observers, with over 200 Galactic Cepheids brighter than 10th magnitude, and have been the target of numerous AAVSO observations. Cepheids show a period-luminosity relation, discovered by Henrietta Leavitt in 1908, that has been used to determine distances within the Galaxy and to galaxies beyond the Milky Way. Cepheids are also a laboratory to test stellar interior

physics, such as nuclear reaction rates for helium burning, turbulence models, and opacities, under conditions not easily accessible in laboratories on Earth. Current problems in Cepheid research include the discrepancy between the Hubble constant derived from the Cepheid period-luminosity relation and that derived from cosmic microwave background observations, and the discrepancy between Cepheid masses derived from pulsation periods or binary dynamics and that derived using stellar evolution models. Here we will show how the open-source MESA (Modules for Experiments in Stellar Astrophysics) code (Paxton *et al.* 2011, 2013, 2015, 2018, 2019, http://mesa.sourceforge.net/) can be used to explore Cepheid evolution. We will also show results using the new radial stellar pulsation (RSP) capability in MESA to model the hydrodynamics of Cepheid envelopes during their pulsations, and simulate light curve and radial velocity variations. We will compare models with observations of Cepheids with well-known properties such as δ Cep, α UMi (Polaris), and V1334 Cyg. These stellar modeling capabilities are accessible to anyone with a laptop computer, following the directions in the MESA tutorial for installation, and starting with the examples in the MESA test suite.

Variable Stars in the LSST Era

Ardis Herrold
1321 W. Desert Dew Place, Oro Valley, AZ 85737; amacio@comcast.net

The Large Synoptic Survey Telescope (LSST) will usher in new opportunities for variable star research and observing beginning in late 2022. LSST will detect a wide range of transient events, from optical counterparts of gamma-ray bursts to long term monitoring of your favorite type of variable star in six bands. The LSST Education and Public Outreach team will develop the main access to data and information for teachers and students, science enthusiasts, and amateur astronomers. We want to hear from you—what kind of data and alerts are you most interested in, and what will you do with them?

The Denouement of the Galactic Novae

Frederick M. Walter
Department of Physics and Astronomy, Stony Brook Univeristy, Stony Brook, NY 11794-3800; frederick.walter@stonybrook.edu

AAVSO photometry of hundreds of galactic novae over the past century has added immeasurably to our understanding of the the nova mechanism—a thermonuclear runaway on the surface of a white dwarf star accreting from a binary companion. But in most cases we know little about the progenitor systems. Most galactic novae quickly fade back into that oblivion from which they came, nevermore to be observed. As they fade, astronomers, professionals and amateurs alike, often lose interest (and the ability to study the fading systems). I posit that many novae deserve to be be scrutinized far longer than is often the case. After the novae fade, the central source (a hot white dwarf plus an accretion disk) may be revealed. Long term monitoring reveals details of the break-up of the nova shell, and of the progenitor system. I will take examples from the Stony Brook/SMARTS nova program, which has followed over 100 novae spectroscopically and photometrically since 2003. I will stress how high quality amateur observations, both photometric and spectroscopic, can assist in elucidating the true nature of the galactic novae, where they came from, and how they get where they are going.

Period Change Behavior of the Eclipsing Binary LS Persei

Gary Billings
P.O. Box 263, Rockyford, Alberta T0J 2R0, Canada; obs681@gmail.com

LS Persei is an Algol-type eclipsing binary star, with a 2.9-day period and a documented instance of a period decrease. I have extended the record of times of minima backwards by more than 50 years using the photographic plate collection at Harvard College Observatory, and up to the present using CCD observations. The extended O–C curve shows an overall concave-downward trend, corresponding to a continuous period decrease ($\dot{P} = -2.3 \times 10^{-8}$), and an additional nearly sinusoidal variation. The former may be caused by mass transfer from the more massive to the less massive star of the pair. A cause for the nearly sinusoidal variation is less clear.

Planning a Visual Observing Program

Michael Cook
9 Laking Drive Newcastle, ON L1B 1M5, Canada; michael.cook@newcastleobservatory.ca

This "How-to Hour" presentation is designed to provide a discussion of principles, procedures, and skills that can be understood and utilized by amateurs to advance their practice of variable star photometry. It is presented by experienced observers who will describe the techniques needed to answer questions that all of us may ask and struggle with when advancing through our avocation. This presentation identifies and explains the fundamental principles of visual observing including: 1. How to select targets, 2. How to find them, 3. How to pick comparison stars, 4. How to compare targets and comparison stars, 5. How to measure with the eye, binoculars, telescope, and 6. How to report.

First Discovery of the Galactic Plane eXoplanet Survey: GPX-1b, a Transiting 15 M_{Jup} Companion to a Rapidly Rotating F-type Star

Paul Benni
Artem Burdanov
Eugene Sokov
Khalid Barkaoui
GPX follow-up team
SOPHIE team
Vadim Krushinsky
address correspondence to Paul Benni, 3 Concetta Circle, Acton, MA 01720; pbenni@verizon.net

We announce the discovery of GPX-1b, a 15 M_{Jup} transiting hot Jupiter/brown dwarf companion to a rapidly rotating 12 V mag F-type star on a 1.7-day orbit. This object is scientifically interesting as its mass is close to the brown dwarf—gas giant planet mass transition, being close to the lower mass range of brown dwarfs (13–80 M_{Jup}) where 13 M_{Jup} is the lower limiting mass for thermonuclear fusion of deuterium. The closest short period bright transiting brown dwarf systems that are < 13 V mag and are of similar mass as GPX-1b are WASP-18b and HATS-70b, which have a mass just below the 13 M_{Jup} limit. GPX-1b currently would be the brightest transiting brown dwarf system just above the 13 M_{Jup} limit and thus a favorable target for atmospheric characterization.

From Gaia DR2, star T_{eff} = 6420 K, and R_{sol} = 1.6. Preliminary planet/brown dwarf characteristics: R_{Jup} = 1.5, M_{Jup} = 15 (SOPHIE RV spectroscopy), 10 mmag transit depth, 2.1 hour transit duration, with an orbital period of 1.745 days. More data to follow pending publication. The GPX survey is designed to search high density star fields that other surveys, such as WASP, HATNet, XO, and KELT would find challenging due to blending of transit-like events. The GPX survey telescope is a wide-field telescope (Celestron RASA, 279 mm f/2.2, based in Acton, MA) on a Losmandy Titan mount, and configured with a FLI ML16200 camera. The resultant image resolution of GPX is about 2 arcsec/pixel compared to 13.7–23 arcsec/pixel of the aforementioned surveys and the TESS space telescope exoplanet survey. GPX evolved from the Kourovka Planet Search (KPS) prototype survey and consequent discovery of KPS-1b, a transiting hot-jupiter, using the same RASA survey telescope.

While the Galactic Plane eXoplanet (GPX) Survey primary goal is to search for exoplanet transits, many unreported variable stars are also discovered. One very interesting 14.7 Vmag star (survey name GPX-TF16E-48), was previously reported to VSX as NEV239, a W Ursae Majoris-type eclipsing variable (EW) in Cassiopeia, with a period of 0.297545 d (7.141 hr). Follow-up with first a C14 telescope, then later with larger aperture telescopes, reveals a box-like transit ~10 minutes in duration, with sharp 50-sec ingress and egress. Spectroscopic follow-up revealed that the primary companion of the system is a K7 dwarf star, with no spectral features of the second companion. Interestingly, depths of eclipses show unusual spectral energy distribution: the deepest transit depth ~60 mmag occurs in red wavelength (SDSS r and R_c bands) filters. We assume that the eclipsing body is a white dwarf and its calculated magnitudes are 19.2, 17.3, and 18.3 for SDSS g, r, and I bands, respectively. Such SED cannot be described by a black body model of the white dwarf, but is in agreement under the assumption that the eclipsed body is red. Or more strictly, the eclipsed body is red on one side that we can see immediately before and after the eclipse. We assume that this increase of the flux in red bands corresponds to strong H-alpha emission, but suitable narrow spectral features are not seen in the spectrum. The primary variability of the tidally distorted primary K7 dwarf star is about 180 mmag, whereas the asymmetric primary and secondary peaks seem to be slowly changing in peak-to-peak magnitude and shape over a period of months, possibly due to hot or cold spots. The primary K star mass is estimated to be 0.63 M_{sol} and radius 0.65 R_{sol}, with a T_{eff}=4070 K. The companion white dwarf mass is estimated to be 0.72 M_{sol}, with a radius of 0.013 R_{sol}. There is some preliminary evidence suggesting that the white dwarf is a low accretion rate polar, which is being further explored at this time.

Note: The authors for the first part of this presentation are Benni, Burdanov, Sokov, Barkaoui, GPX follow-up team, SOPHIE team. The authors for the second part of this presentation are Benni, Krushinsky, Burdanov, Barkaoui, GPX follow-up team.

Update on Professor and Student Survey of NSV RR Lyrae Variable Stars

Melanie Crowson
David Syndergaard
address correspondence to Melanie Crowson, P.O. Box 7327, Wesley Chapel, FL 33545; scopegal617@gmail.com

RR Lyrae variable stars are dynamic and important because they provide insight into how stars form and evolve. These variables are considered especially significant to many studies due to their short periods and high brightness contrasts. The purpose of this project was to add to the body of knowledge on potential RR Lyrae-type variable stars by providing a general survey of magnitude fluctuations over the course of one year for four possible RR Lyrae stars, thus adding further measurements to the known database. Surveying the distribution of some of these bodies supplies evidence as to the contributing elements that may impact their life cycles; in particular, their galactic coordinates were back-dropped to their light curves in this examination. Also, there is a minor absence of magnitude information on many variables in the photometric blue filter, so the project was conducted using primarily the Johnson B filter with supplemental V filter data as well. It is with this compilation of data on RR Lyraes that astronomers can better understand them, and so the following paper discusses the authors' photometric observations of four suspected RR Lyrae stars and whether they should remain in this category.

SPP Observing Section

Melanie Crowson
P.O. Box 7327, Wesley Chapel, FL 33545; scopegal617@gmail.com

Short period pulsating (SPP) variable stars represent an important stage of stellar evolution, and include the classes of W Virginis and other Cepheids, δ Scuti, and RR Lyrae, as main sequence stars begin their journey away from that path. This brief presentation will introduce these star categories, their importance, and some key features. It will also highlight the new observing section on the AAVSO's website covering SPPs and the tools available there. Variable star observing can be done by any who wants to make observations and use them to help further science. As such, AAVSO is dedicated to advancing this area of astronomical research by welcoming all to participate in variable star astronomy.

Transform Computations

George Silvis
194 Clipper Road, Bourne, MA 02532-3525; gasilvis@gmail.com

We understand that it is important to transform our photometric data, but the computations can be complex. Too often the presentations of how to do this are "tldr" (too long, didn't read). And they often just cover the trivial case of two filters. I'll present how transformation is done in the Transform Applier application (TA) and in the VPHOT implementation of TA. I'll show how the computation can be generalized to even an EXCEL spreadsheet.

A New Study of the Variable Star Population in the Hercules Globular Cluster (M13; NGC 6205)

Dan J. Deras
A. Arellano Ferro
C. Lazaro
I. H. Bustos Fierro
J. H. Calderon
S. Muneer
Sunetra Giridhar
address correspondence to Dan J. Deras, Cerrada Tenayuca 228, A201, Ciudad de Mexico, CDMX 3310, Mexico; dderas@astro.unam.mx

We present the results from VI CCD time-series photometry of the globular cluster M13 (NGC 6205). From the Fourier decomposition of the light curves of RRab and RRc stars we found an average metallicity of [Fe/H]zw = –1.58 ± 0.09. The distance to the cluster was estimated as 7.1 ± 0.1 kpc from independent methods related to the variable star families RR Lyrae, SX Phe, and W Virginis, from the luminosity of the theoretical ZAHB and from the orbit solution of a newly discovered contact binary star. The RR Lyrae pulsation modes are segregated by the red edge of the first overtone instability strip in this OoII-type cluster. A membership analysis of 52,800 stars in the field of the cluster is presented based on Gaia-DR2 proper motions which enabled the recognition of 23,070 likely cluster members, for 7,630 of which we possess VI photometry. The identification of member stars allowed the construction of a clean CMD and a proper ZAHB and isochrone fitting, consistent with a reddening, age, and distance of 0.02 mag, 12.6 Gyrs and 7.1 kpc, respectively. We report seven new variables; one RRc, two SX Phe, three SR, and one contact binary. V31 presents double-mode nature and we confirm V36 as RRd. Fifteen variable star candidates are also reported. The analysis of eighteen stars in the field of the cluster, reported as RR Lyrae in the Gaia DR2 database reveals that at least seven are not variable. We noted the presence of a high velocity star in the field of the cluster.

Variable Stars in Palomar 13: an Evaporating Globular Cluster

Mario Alberto Yepez Rivera
Armando Arellano Ferro
Klaus-Peter Schröder
S. Muneer
Sunetra Giridhar
Christine Allen
address correspondence to Mario Alberto Yepez Rivera, Aile 420, Pedregal de santo domingo, coyoacan, Ciudad de Mexico 4369, Mexico; myepez@astro.unam.mx

We present new CCD V I photometry of the distant globular cluster Pal 13. Fourier decomposition of the light curves of the three cluster member RRab stars lead to estimations of [Fe/H] = –1.65, and a distance of 23.67 ± 0.57 kpc. Light and color near minimum phases for RRab stars lead to an estimate of E(B−V) = 0.104 ± 0.001. A V / (V−I) color-magnitude diagram, built exclusively with likely star members, shows consistency with the above parameters and an age of 12 Gyrs. A search of variable stars in the field of view of our images revealed the variability of a red giant cluster member and of three probably non-member stars: two RRab stars and one W Virginis star or CW. The GAIA proper motions of member stars in Pal 13 show a significant scatter, consistent with the scenario of the cluster being tidally stripped.

AAVSO Contributions to Year 1 of TESS

Dennis Conti
141 E. Bay View Drive, Annapolis, MD 21403; dennis_conti@hotmail.com

During the first year of TESS, the AAVSO has materially contributed to the success of the ground-based observations that were needed to detect false positives, as well as help confirm candidate exoplanets. This talk will review these contributions, which have included: training and qualification of members to formally participate in the TESS Follow-up Program (TFOP), the development of software tools to help the TFOP members determine if any nearby eclipsing binaries (NEBs) were the cause of false detections, the development of best practices,

and the development of the guidelines used by TFOP members to submit their observations.

The Exoplanet Transit Survey and the AAVSO

Robert Zellem
Anya Biferno
Ethan Blaser
Alexandra Iterralde
Kyle Pearson
John Engelke
address correspondence to Robert Zellem, 4800 Oak Grove Drive, Pasadena, CA 91109; Robert.T.Zellem@jpl.nasa.gov

The amount of uncertainty in the ephemerides of confirmed planets can grow increasingly large over time. Therefore, it is critical that these uncertainties be reduced via regular maintenance since future atmospheric characterization studies will be conducted using the precious resources of future space telescopes, such as JWST. This talk will discuss a community-wide program that leverages the small telescope resources of amateur astronomers, small universities, and community colleges to conduct ground-based follow-up observations to reduce such uncertainties. This project—the Exoplanet Transit Survey (ETS)—will include a partnership with the AAVSO that will provide ETS with a base of qualified AAVSO exoplanet observers, as well as the AAVSO Exoplanet Database for archiving the follow-up observations.

The New Mittelman Observatory—A Professional Quality Robotic Telescope

Arne Henden
106 Hawkins Pond Road, Central Harbor, NH 03226; ahenden@gmail.com

David Mittelman, before his untimely passing, acquired the 95-cm Princeton University Boller and Chivens telescope. This has been converted into an f/4 Newtonian system and installed next to New Mexico Skies. Refurbishment efforts are nearly complete, and the telescope is available on a shared-risk basis with a 4k × 4k CCD camera and photometric filters. Other instrument ports may support a spectrograph and a lucky imaging camera in the future, as well as a visual eyepiece. Photos of the refurbishment effort and some first-light images will be presented.

Dorrit Hoffleit, Raymond Berg, and the "Unnamed Fleming Variables": An Epilogue

Kristine Larsen
286 Francis Street, New Britain, CT 6053; larsen@ccsu.edu

At the 1997 AAVSO Annual Meeting, Dorrit Hoffleit brought to the attention of the organization fourteen of Williamina Paton Fleming's variable star discoveries that still had insufficient data to merit classification in the *General Catalogue of Variable Stars* (GCVS) and urged further investigation of these stars. In follow-up presentations the author reported on the official status of these stars in VSX (incorporating both AAVSO and ASAS observations) as well as offered a new period for one of them. A tentative suggestion was offered for highly experienced visual observer Ray Berg's (BEB) follow-up observations in 1998 in which three of these stars (WX Ret, CL Hyi, NSV 3379) demonstrated relative stability even though further observations show variability on the order of a full magnitude or more. In this final follow-up presentation to this earlier work, ASAS-SN data are included, resulting in further determinations concerning the nature of the four remaining suspected variables (NSV 3379, NSV 7645, NSV 11792, NSV 12993) as well as a final explanation for Berg's 1998 visual observations of non-variability in the three aforementioned stars.

Long-time Observations of Visual Solar Observers

Rodney H. Howe
3343 Riva Ridge Drive, Fort Collins, CO 80526; ahowe@frii.com

Presented by Kristine Larsen

A summary of the history and procedures of the AAVSO Solar Section is provided. Statistical analysis shows that although there has been no clear change in the reporting behavior over the last 90 years, there is a statistically significant shift during times of extrema in the sunspot cycle (maxima and minima). Implications for the relative sunspot number are discussed.

PYTHON Pipeline to Simultaneously Extract Exoplanet and Variable Star Data from TESS Ground-based Followup Observations

Isobel Snellenberger
Madelyn Madsen
Matt Craig
address correspondence to Matt Craig, 1104 7th Avenue South, Moorhead, MN 56563; mcraig@mnstate.edu

As part of continuing from preparation for collecting data as part of the TESS ground-based follow-up network, we have been developing software using PYTHON to produce the data products needed for a TESS submission. We are now able to produce a photometry measurement table, a light curve, a seeing profile, and a field image with apertures with the software we have written. A new feature is the ability to generate a table reporting variable star observations in the field of a TESS exoplanet to the AAVSO. One goal is to make this software compatible with ASTROIMAGEJ, so that the user can, for example, do photometry and generate TESS reports in ASTROIMAGEJ but generate AAVSO variable star reports using this software.

PYTHON for Variable Star Astronomy: A Status Report

Matt Craig
Isobel Snellenberger
Madelyn Madsen
address correspondence to Matt Craig, 1104 7th Avenue South, Moorhead, MN 56563; mcraig@mnstate.edu

This review presents the current state of efforts to leverage software developed in part by large institutions like the Space Telescope Science Institute for use by AAVSO members. Over the past two years substantial progress has been made in providing an image viewer, image reduction tools, aperture photometry, differential photometry, and color corrections. The amount of code specific to AAVSO functionality is reasonably small, with most of the critical code part of the Astropy project. In addition, there are new educational materials available for people new to using PYTHON for image calibration. Perspectives of two relatively new users of the software are included.

Student Involvement in Exoplanet Science

Pat Boyce
3540 Carleton Street, San Diego, CA 92106; pat@boyce-astro.org

With the ability of small telescopes to conduct reasonably good exoplanet observations and with the "best practices" of conducting such observations now fairly well established, research-grade exoplanet observing can now be done down to the high school level. This talk will review a program that has been successful in training students to perform high-quality, exoplanet observations for the TESS Subgroup 1 and ETS in the future. The AAVSO CHOICE courses on Exoplanet Observing are a key step in their training.

Examples of Variable Stars found in the GNAT/MOTESS Variable Star Catalog

Roy A. Tucker
Eric R. Craine
Adam L. Kraus
address correspondence to Roy A. Tucker, 5500 West Nebraska Street, Tucson, AZ 85757; gpobs@mindspring.com

Images acquired in the course of asteroid search efforts by the MOTESS instrument (Moving Object and Transient Event Search System) are being processed by a computerized photometric pipeline to reveal new variable star candidates. The initial processing of the first survey, conducted during 2000–2001, revealed approximately 26,000 variable star candidates in the brightness range of tenth to eighteenth magnitude, easily within the range of amateurs with modest-sized telescopes and CCD cameras. We present examples of light curves yielded by later follow-up observations. The MG1-VSC provides a rich source of many different types of variable stars that can keep variable star observers busy for many years.

Measuring Decay Timescales of Downflows in Solar Flare Footpoints: Testing the One-minute Theory

Alexander K. Beltzer-Sweeney (NSO/San Diego Mesa College)
Elizabeth Butler
Adam Kowalski
Gianna Cauzzi
address correspondence to Alexander K. Beltzer-Sweeney, 5191 68th Street, San Diego, CA 92115; a.beltzer.sweeney@gmail.com

In 1989 George Fisher found analytically that chromospheric downflows in flare footprints should slow down to background detection levels within ~1 minute regardless of the initial energy injected. We set to test this theory by measuring downflows in flare kernels that were observed by the IRIS satellite between 2014 and 2017. The GOES classification system was used as a proxy for the energy of the nonthermal electron beam that is thought to heat the flare footprint. The redshift evolution of a Mg II triplet line was measured in twenty-six C, M, and X class flares to determine the timescale of deceleration of the chromospheric plasma in response to explosive flare heating. Two different methods for measuring the decay of the redshift as a function of time, bisector and gaussian, were used to test the robustness of the inferred downflow gas velocities across the wide variety of flares. Results of the analysis show that downflow velocities reached 30~50 km/s, which is consistent with previous results with a derived Mach number of 4~5. The times of half-maximum velocity were found to be between 15~30 seconds, indicating a rapid slowing. At later times, the Mg II line profiles exhibit prolonged redshifts with inferred speeds of 5 to 7 km/s.

High-precision Radial Velocity Measurements of Classical Cepheids

Richard I. Anderson
ESO, Karl Schwarzschild Str. 2, Garching b. München 85748, Germany; randerso@eso.org

I will review the surprising new insights into the nature of classical Cepheid variables that have been enabled by radial velocity measurements precise enough to measure the speed of a human walking. Following a brief overview of Cepheid properties, I will focus on two celebrities: first on the prototype, δ Cephei, and its secret companion that can only be detected indirectly, and then on α UMi (the North Star, Polaris), which is both the nearest Cepheid variable and whose detailed astrophysical explanation remains a mystery.

Erratum: Methods for O–C (Observed Minus Computed) Diagrams and for the Determination of Light Elements of Variable Stars with Linear and Second Order Polynomial Ephemerides

Roy Andrew Axelsen
P. O. Box 706, Kenmore, Queensland 4069, Australia; reaxelsen@gmail.com

In the article "Methods for O–C (Observed Minus Computed) Diagrams and for the Determination of Light Elements of Variable Stars with Linear and Second Order Polynomial Ephemerides" (*JAAVSO*, 2014, **42**, 451–460), Table 2 was given incorrectly. The correct content for Table 2 is given below.

The author would like to thank AAVSO member-observer Pradip Karmakar, of Kolkata, India, for bringing the error to his attention.

Table 2. Times of maximum of RS Gru from 1952 to 1988, epochs (number of cycles, with only the rounded values shown) and O–C values. The times of maximum are those published by Rodriguez *et al.* (1995). The calculations, employing formulae (1) and (2) of the present paper, use 2447464.7095 HJD as the initial time of maximum (Rodriguez *et al.* 1995) and 0.14701131 d as the initial period (McNamara and Feltz 1976).

Max.	*TOM (HJD)*	*Epoch E (Rounded)*	*O–C*	*Primary Source**
1	2434325.2940	–89377	0.014354	1
2	2434573.4510	–87689	0.016263	1
3	2436756.5710	–72839	0.018309	2
4	2436760.5380	–72812	0.016004	2
5	2436801.5540	–72533	0.015848	3
6	2436853.3030	–72181	0.016867	3
7	2441538.4027	–40312	0.013129	4
8	2441538.5490	–40311	0.012417	4
9	2441610.4379	–39822	0.012787	4
10	2441611.3200	–39816	0.012819	4
11	2441611.4677	–39815	0.013508	4
12	2441612.3493	–39809	0.013040	4
13	2441915.4856	–37747	0.012019	4
14	2442687.5892	–32495	0.012218	5
15	2443355.4610	–27952	0.011637	6
16	2443355.6092	–27951	0.012826	6
17	2443360.4584	–27918	0.010653	6
18	2443360.6050	–27917	0.010241	6
19	2447464.7095	0	0.000000	7
20	2447468.5324	26	0.000606	7
21	2447468.6793	27	0.000495	7
22	2447472.6489	54	0.000789	7

**Primary sources: 1. Hoffmeister (1956); 2. Oosterhoff and Walraven (1966); 3. Kinman (1961); 4. Dean* et al. *(1977); 5. McNamara and Feltz (1976); 6. Balona and Martin (1978); 7. Rodriguez* et al. *(1995).*